UNIVERSITÀ DEGLI STUDI DI PARMA
FACOLTÀ DI SCIENZE MATEMATICHE FISICHE E NATURALI

Dottorato in Scienze Chimiche
XXIII ciclo (2008 - 2010)

CHARGE AND ENERGY TRANSFER IN FUNCTIONAL MOLECULAR MATERIALS: SPECTROSCOPY AND MODELS

Coordinatore
Prof. Alberto Girlando

Tutor
Prof. Anna Painelli
Prof. Alberto Girlando

Dottorando
Luca Grisanti

2011

Contents

***DA* chromophores beyond the two state approach** 14

Interacting polar chromophores 43

List of Abbreviations

CT	charge transfer
D / A	electron donor/acceptor (group)
D / A	energy donor/acceptor (molecule)
LE	localized excitation
NLO	nonlinear optics
ph/e-ph	phonon/electron-ph
mv/e-mv	molecular vibration/electron-mv
PES	potential energy surface
OPA	one-photon absorption
TPA	two-photon absorption
TPEF	two-photon excited fluorescence
GM	Göppert-Mayer units ($1\mathrm{GM}=10^{-50}\cdot \mathrm{cm}^{4}\cdot \mathrm{s}\cdot \mathrm{photon}^{-1}$)
mf	mean field

gs, *g*	ground state
a. u.	arbitrary units
ET	energy transfer
RET	resonant energy transfer
(N)IR	(near) infrared
XRD	X ray diffraction
MO	molecular orbital
HF	Hartree Fock
INDO	intermediate neglect of differential overlap
INDO/S, ZINDO	INDO with spectroscopic parametrization
CI	configuration interaction
CIS	single excited configuration interaction
HOMO	highest occupied molecular orbital
LUMO	lowest unoccupied molecular orbital
PCM	polarizable continuum model
(TD)DFT	(time dependent) density functional theory
RMA	rigid molecule approximation
QHLD	quasi harmonic lattice dynamics

Introduction

The progress in chemical synthesis and the development of new organic and inorganic molecular systems is playing an important role in scientific and technological innovation. Molecular-based materials are in demand for the development of new electronic and photonic devices [1, 2, 3] but also for a wealth of other applications including, to cite a few, drug delivery [4], in vivo optical microscopy [5], microfabrication [5, 6, 7], photodynamic therapy [8, 9, 10]. In particular, fundamental biological processes involve functional molecules, as best demonstrated by light harvesting complexes exploited in the photosynthetic process [11, 12]. A thorough understanding of these processes will unveil some fundamental mechanism of life, offering at the same time important clues for the optimal engineering of molecular- based devices [13]. The low cost and the large availability of the organic precursors, and the possibility to build structures with unlimited complexity and finely tuned properties make molecular functional materials extremely appealing from a fundamental and applicative point of view. Functional behaviour is accompanied in molecular materials by low weight and mechanical flexibility opening the way to applications that are precluded to more common inorganic and crystalline materials used in the electronic industry. Bio-compatibility makes molecular materials useful in life-science, biological and medical applications [8, 4].

Functional molecular materials are by definition *smart* materials: they are able to respond in a qualitative different way to wide range of external perturbation: temperature, light, pressure, magnetic and electric field, etc. [3, 14, 15, 16, 17]. Smart behaviour is related to the intrinsic non-linearity of the material responses to applied perturbations that, in its extreme manifestation, lead to switchable materials.

To fully exploit the promise of molecular functional materials, the physics that governs their complex behaviour must be thoroughly understood, with the aim, on one side, to optimize the materials for current needs, on the other side to guide the synthesis of new materials showing brand new behaviour. This thesis offers a contribution to the rationalization of the properties of several families of molecular functional materials. Systems of interest range from organic and organometallic chromophores and multichromophores, valence tautomeric systems, bistable molecular materials, organic semiconducting crystals. Phenomena of interest range from linear and non-linear optical spectra, charge transfer and charge transport processes, energy transfer, multistability. Different systems with distinctively different properties have been investigated adopting a variety of techniques, including spectroscopic measurements, theoretical models and computational approaches.

Spectroscopic techniques include standard absorption and fluorescence spectroscopic measurements mainly in solution. Special skills were developed in low-temperature and in frozen solution spectroscopic measurements, including fluorescence anisotropy. From the theoretical perspective large emphasis was put in the development of essential state model to describe low-energy linear and non-linear spectra of CT chromophores and multichromophores. Essential state models adopt a minimal basis to describe electronic degrees of freedom of CT chromophores just accounting for the charge-resonance that dominate the low-energy physics of these systems. Thanks to this minimal choice for the electronic structure, essential state models can describe fairly accurately the coupling of electrons with molecular vibrations and can be extended to account for the interaction with the solvent. In a bottom-up modeling strategy, essentials state models developed for chromophores in solution offer the basis to construct more complex models for systems where several chromophores interact via electrostatic forces, including multichromophoric assemblies and molecular crystals.

Essential state models are semiempirical and a careful analysis of experimental data is the basis for their definition. Their actual exploitation requires the development of *ad hoc* numerical codes, that can deal with electron-vibration coupling either adopting the adiabatic approximation or in truly non-adiabatic approaches. The codes are simple for simple systems, but become more and more complex and demanding as long as the number of slow degrees of freedom (either molecular vibrations or polar solvation coordinates) increases. Essentials states models were also the basis to build models for bistable molecular crystals, where the cooperative nature of the interactions was captured via a mean-field treatment of electrostatic intermolecular interactions. Quantum chemical calculations were exploited is several cases to support essential state models, and an original implementation of an INDO code was developed to attack in a new perspective two important and timely issues: charge transport in organic molecular crystals and energy transfer between organic chromophores.

This extensive and multifaceted work was often done in collaboration with other groups. Notable in this respect are the collaborations with two Italian groups expert in the synthesis of organic and organometallic chromophores and multichromophores, Prof. D. Roberto ("Università degli Studi di Milano") e Dr. S. Quici (CNR - Milano); with an Italian group expert in non-linear optical spectroscopy (Prof. C. Ferrante, "Università di Padova"). Another national collaboration was active with the group of Bologna University. The group has a well recognised expertise in optical spectroscopy of organic crystals (Prof. Brillante) and in theoretical model for the structural and vibrational properties of organic crystals (Prof. Della Valle and Venuti). Joining these expertise with the expertise of the host research group in modelling electronic and electron-vibration coupling in molecular materials was instrumental to attack the complex problem of the in charge transport in organic semiconductors. Particularly important have been two international collaborations. The first with the group of Prof. J. Veciana (Barcellona), that has a well recognized expertise in the synthesis and characterisation of molecular functional materials, has been supported by "EU-NOE MAGMANET". I spent 6 weeks in Barcelona and PhD student from there spent two months in our laboratory. The second international collaboration was with the group of Prof. S. Pati (Bangalore) that is a recognized expert in the theoretical description of molecular functional materials. In the framework of this collaboration, supported by the Executive Program of Scientific and Technological cooperation between the Italian Republic and the Republic of India 2008-2010, I spent a month in the laboratory of Prof. Pati.

The thesis is organized as follow. The first chapter is mainly devoted to CT chromophores and multichromophores. Essential state models are presented and exploited to describe optical spectra of several donor-acceptor (*DA*) chromophores and bichromophoric assemblies in solution. Essential state models for *DA* chromophores were already developed in the host laboratory [18, 19] and successfully applied to many systems [20, 21, 22, 23]. Here special emphasis is put on specific *DA* chromophores which spectral behaviour calls for some extension of the basic model to account for the presence of several low-energy excitations and/or for additional slow degrees of freedom. Interchromophore interactions are at the hearth of models for bichromophoric systems, and have been extensively investigated in the framework of the bottom-up modelling strategy. Extended models demand for extended spectroscopic characterization and the technique of fluorescence anisotropy, recently implemented in the host laboratory, proved extremely successful in this context.

Chapter two describe a class of organic and metallorganic *DA* compounds that, with respect to the typical *DA* chromophores described in Chapter 1, are characterized by a low degree of conjugation between the *D* and *A* groups and therefore by weak CT absorption band occurring in the near-infrared spectral region. This family of chromophores is particularly promising for bistability [24]. A bottom-up modeling strategy is adopted to model bistable molecular crystals of *DA* chromophores. The work starts with a detailed analysis of optical spectra of the *DA* dye in solution to extract the relevant molecular model that is then used to build models for interacting chromophores in the crystal. The calculation of electrostatic intermolecular interactions is based on an original implementation of quantum chemical calculations, where a constant electric field is imposed to force the molecule in one of the resonating structure and hence evaluate the relevant charge distribution. A mean-field treatment of electrostatic intermolecular interactions then proves that bistability can be induced in crystals of *DA* chromophores via a careful balance of inter and intramolecular energies. The model is validated via a quantitative comparison with temperature-dependent Mössbauer spectra for a specific system. The model, originally developed from crystal of neutral *DA* chromophores is then extended to treat crystal of DA^+ molecular ions. This non-trivial extension suggests that the electrostatic interaction between the DA^+ ion and the counterion offers a powerful tool to drive the system in the bistability region. While mainly devoted to bistability, chapter 2 touches upon other problems as well. Among them we point at the discussion of the role of bridge in $D\ \pi\ A$ chromophores. Finally preliminary results are discussed about a new family of *DA* chromophores showing an intriguing and complex physics that includes bistability in solution, dimerization equilibria and the formation of mixed-valence dimers.

In chapter three we describe a computational tool to evaluate the electron - phonon couplings in organic molecular material. The method, which involves a semiempirical quantomechanic approach, fully accounts for the mixing between intramolecular and intermolecular (lattice) vibrations. The method is applied to the case of rubrene, which presents many low frequency vibrations that potentially couples with low frequency lattice phonons.

In chapter four, a short review of the resonance energy transfer mechanism is given and an original computational method based on INDO/S calculation of configuration interaction matrix elements is proposed. The computational scheme is then tested on a few pairs of organic chromophores.

Chapter 1

CT chromophores and multichromophores: essential state models and spectroscopic behaviour

In this chapter we focus attention on optical spectra of charge transfer (CT) chromophores and multichromophores. CT chromophores are an interesting class of π -conjugated molecules decorated with electron donor (D) and acceptor (A) groups. In these molecules π conjugated electrons guarantee for low-lying excitations and large transition dipole moments, and therefore large (hyper)polarizabilities. These interesting properties are further amplified by the presence of D and A groups that lower the energy of CT states. Indeed the low energy physics of CT chromophores is governed by CT degrees of freedom, a feature exploited in the host laboratory to develop essential state models for optical spectra of CT chromophores [25].

CT chromophores represent a vast family of molecules: the simplest structure has a D and an A group joint by a π-conjugated bridge. These polar structures, also known as push-pull chromophores, have been quite extensively investigated for their large NLO properties [26, 17]. Their low-frequency absorption transition has a CT character and its large solvatochromism is well known [27]. More complex and highly symmetrical chromophores include quadrupolar, $D\pi A\pi D$ or $A\pi D\pi A$, and octupolar (DA_3 or AD_3) chromophores [28, 29, 30]. In all cases the low energy physics of these dyes is governed by CT processes and their optical spectra can be accurately described in terms of essential state models [25]. Specifically, polar dyes resonate between two structures, $DA \longleftrightarrow D^+A^-$, and the essential state model just accounts for two electronic basis states [18]. Quadrupolar dyes can instead be described based on three electronic states [21], while four basis states are essential to describe octupolar dyes [22]. The interaction with the solvent and with molecular vibrations are introduced in essential state models, leading to a fairly accurate description of solution spectra [31, 32, 33, 21, 34, 35, 36].

The same essential state models lead themselves quite naturally to describe multichromophoric assemblies [25, 37, 38, 23], where different CT chromophores interact via electrostatic forces. Essential state models have been developed in the host laboratories in the last 15 years and have been quite successfully applied to many chromophores and multichromophores. However, in an effort to extend the library of molecules described in terms of essential state models, a few intriguing examples of chromophores have been encountered for which a detailed description of optical spectra requires some extension of the basic essential state model. In this chapter I will discuss a few examples of polar dyes where an extension of the two state model is in order, as well as a few examples of multichromophoric species.

1.1 Essential state description of a DA chromophore

The low energy physic of DA chromophore is governed by the resonance $DA \longleftrightarrow D^+A^-$. The minimal model for their electronic structure then accounts for two basis state: the neutral $|DA\rangle$ state and the zwitterionic $|D^+A^-\rangle$ state [18, 19, 39, 33]. The Hamiltonian reads:

$$\mathscr{H}_{el} = \begin{pmatrix} 0 & -\tau \\ -\tau & 2z_0 \end{pmatrix} \tag{1.1}$$

where $2z_0$ represents the energy difference between the two structures and τ is the mixing element. The same Hamiltonian is conveniently rewritten using a couple of operators:

$$\hat{\rho} = \begin{pmatrix} 0 & 0 \\ 0 & 1 \end{pmatrix} \qquad \hat{\sigma} = \begin{pmatrix} 0 & 1 \\ 1 & 0 \end{pmatrix} \qquad \mathscr{H}_{el} = 2z_0\hat{\rho} - \tau\hat{\sigma} \tag{1.2}$$

The solution of the electronic 2 × 2 Hamiltonian is exact, and the ground and the excited state are:

$$|g\rangle = \sqrt{1-\rho}\,|DA\rangle + \sqrt{\rho}\,|D^+A^-\rangle \qquad (1.3)$$

$$|e\rangle = -\sqrt{\rho}\,|DA\rangle + \sqrt{1-\rho}\,|D^+A^-\rangle \qquad (1.4)$$

where ρ is the expectation value in the ground state of the $\hat{\rho}$ operator and corresponds to the degree of charge transferred from D to A (also called *ionicity*), that can vary from 0 to 1. The ρ value only depends on z_0 and τ:

$$\rho = \frac{1}{2}\left(1 - \frac{z_0}{\sqrt{{z_0}^2 + \tau^2}}\right) \qquad (1.5)$$

Molecules in a state characterised by $\rho \ll 0.5$ ($\rho \sim 0$) are in neutral regime. Molecules with $\rho \gg 0.5$ ($\rho \sim 1$) are in the ionic regime. Figure 1.1 shows the $\rho(z_0)$ curves calculated for a few τ values.

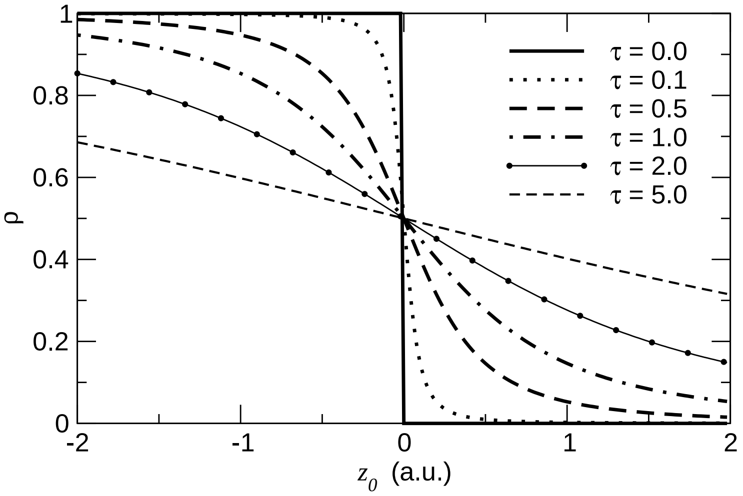

Figure 1.1: *The z_0 dependence of ρ for different τ values. Notice that the mixing element τ is responsible for the smoothness of the $\rho(z_0)$ curve. For $\tau = 0$ the system can only be found at $\rho = 0$ or $\rho = 1$, and states with intermediate ionicities are only possible for finite τ.*

According to the original idea of Mulliken [40], we neglect all matrix elements of the dipole moment operator except μ_0, the dipole moment in the D^+A^- state. The dipole moment operator then reads:

$$\hat{\mu} = \mu_0 \hat{\rho} \qquad (1.6)$$

All spectroscopically relevant quantities can be easily expressed as a function of ρ, as follows:

$$\mu_{ge} = \mu_0 \sqrt{\rho\,(1-\rho)} \tag{1.7}$$

$$\omega_{ge} = \frac{\tau}{\sqrt{\rho\,(1-\rho)}} \tag{1.8}$$

The ρ dependence of μ_{ge} and ω_{ge} is shown in fig. 1.2. The permanent ground and excited state dipole moments are:

$$\mu_g = \mu_0 \rho \qquad \mu_e = \mu_0 (1-\rho) \tag{1.9}$$

The solvatochromism is governed by the mesomeric dipole moment:

$$\Delta\mu = \mu_e - \mu_g = \mu_0\,(1-2\rho) \tag{1.10}$$

In particular, for a pure electronic model, the absorption solvatochromism is determined by $\mu_g \Delta\mu$ and emission solvatochromism by $\mu_e \Delta\mu$.

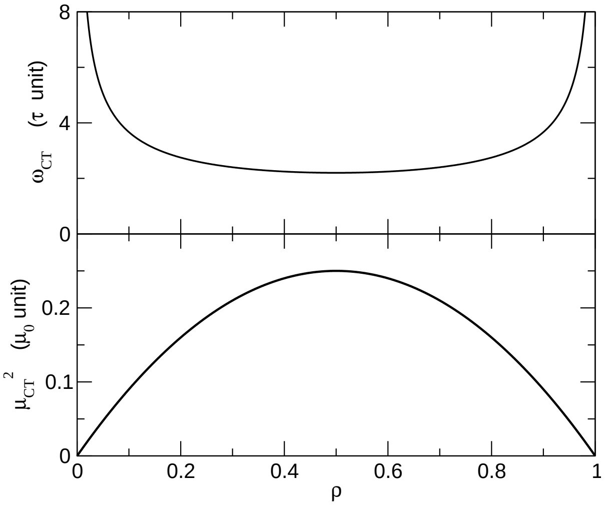

Figure 1.2: *Calculated frequency (upper panel) and square of the transition dipole moment (lower panel) of the CT transition, as a function of ρ. At $\rho \sim 0$ (largely neutral molecules) or $\rho \sim 1$ (largely ionic molecules) the transition frequency is very sensitive the ρ.*

The complete description of optical spectra of a *DA* chromophore requires the introduction of molecular vibrations. We account for a single effective coordinate q that linearly modulates the diagonal energy z_0 (Holstein coupling).

The total Hamiltonian then reads [33]:

$$\begin{aligned}\mathscr{H} &= \mathscr{H}_{el} + \mathscr{H}_{ph} + \mathscr{H}_{e-ph} \\ &= 2z_0\hat{\rho} - \tau\hat{\sigma} + \frac{{\omega_v}^2}{2}\left(q^2 + p^2\right) - g\sqrt{2\omega_v}q\hat{\rho} \qquad (1.11)\end{aligned}$$

where the p is the momentum associated to the q coordinate. ω_v is the vibrational frequency and g is the electron-phonon (e-ph) coupling constant: $g = \frac{1}{\sqrt{2\omega_v}}\left(\frac{\partial z_0}{\partial q}\right)_{q_{eq}}$. The strength of the coupling is conveniently measured by $\varepsilon_v = \frac{g^2}{\omega_v}$, i.e. the vibrational relaxation energy.

In the *adiabatic* approximation the vibrational kinetic energy is neglected and q becomes a classical coordinate. In this approximation the total Hamiltonian: $\mathscr{H}_{adiab} = 2\left(z_0 - \sqrt{\frac{\omega_v}{2}}gq\right)\hat{\rho} - \tau\hat{\sigma} + \frac{1}{2}{\omega_v}^2q^2$ can be easily solved as a two state electronic Hamiltonian with a q dependent z_0. The adiabatic solution leads to q dependent $|g\rangle$ and $|e\rangle$ states and to q dependent energies, that describe the potential energy surfaces (PES), as shown in the right panel of figure 1.3. The vibrational problem can be solved on each PES to find relevant vibrational eigenstates. As it can be seen in fig. 1.3, the two basis state have harmonic PES with the same curvature, but the PES resulting from the diagonalization are anharmonic and show different curvature. The solution of the vibrational problem becomes trivial if the harmonic approximation is enforced, i.e. if the anharmonic PES for the g and the e state are approximated by parabolic surfaces. The exact solution of the adiabatic anharmonic problem is possible, but numerically cumbersome.

To deal with the problem in a non adiabatic picture it is useful to introduce raising and lowering operators ($\hbar = 1$) in order to express $\hat{q}$ and $\hat{p}$:

$$\hat{q} = \frac{1}{\sqrt{2\omega_v}}\left(\hat{a}^\dagger + \hat{a}\right) \qquad (1.12)$$

$$\hat{p} = i\frac{1}{\sqrt{2\omega_v}}\left(\hat{a}^\dagger - \hat{a}\right) \qquad (1.13)$$

Equation 1.11 can be rewritten:

$$\begin{aligned}\mathscr{H} &= \mathscr{H}_{el} + \mathscr{H}_{ph} + \mathscr{H}_{e-ph} \\ &= 2z_0\hat{\rho} - \tau\hat{\sigma} + \omega_v\left(\hat{a}\hat{a}^\dagger + \frac{1}{2}\right) - g\left(\hat{a}^\dagger + \hat{a}\right)\hat{\rho} \qquad (1.14)\end{aligned}$$

The total Hamiltonian matrix is then written on the basis obtained as the direct product of the two electronic basis states ($|DA\rangle$ and $|D^+A^-\rangle$) times the eigenstates of the harmonic oscillator described by $\mathscr{H}_{ph} = \omega_v\left(\hat{a}\hat{a}^\dagger + \frac{1}{2}\right)$. The resulting basis set is infinite and is truncated accounting for just the lowest N states

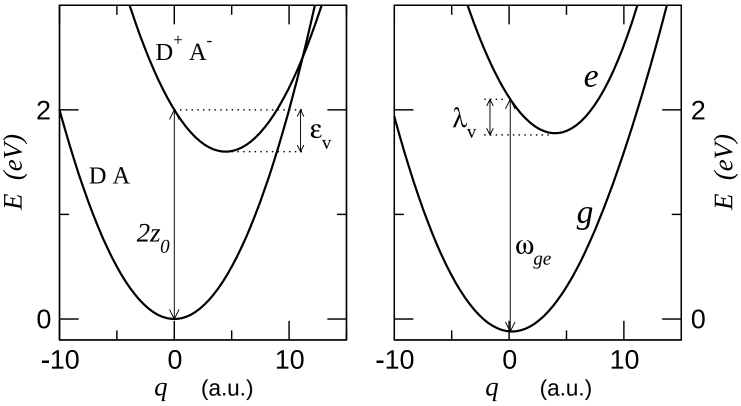

Figure 1.3: *Left: the q-dependent energies of the two electronic basis states. Right: adiabatic eigenstate PESs obtained from the diagonalization of Hamiltonian in equation (1.11). The figure is obtained for* $z = 1$ *eV,* $\tau = 0.5$ *eV,* $\omega_v = 0.2$ *eV and* $\varepsilon_v = 0.4$ *eV. In the left panel,* ε_v *marks the vibrational relaxation energy relevant to the basis states, while* λ_v *in the right panel, shows the same quantity (i.e. the vibrational relaxation energy) for the adiabatic eigenstates.*

of the harmonic oscillator. Numerically exact solutions are obtained by diagonalising the Hamiltonian matrix on a basis with large enough N as to ensure convergence of the relevant results.

So far we have described an isolated chromophore: to complete the picture we have to account for the interaction between the molecule and its environment. The simplest approach starts studying the molecule in solution. Ignoring all specific effects, we adopt the a *reaction field* model. A solvent around a polar solute generates an electric field F_R that is proportional to the dipole moment of the solute: $F_R = r\langle\mu\rangle$. There are two contributions to the reaction field:

$$F_R = F_{R,el} + F_{R,or} = r_{el}\langle\mu\rangle + r_{or}\langle\mu\rangle \tag{1.15}$$

The first contribution accounts for the polarisation of the electronic cloud of solvent molecules around the polar solute. It is related to very fast degrees of freedom (the energy of typical electronic excitations of the solvent, in the UV region) and can be treated in the anti-adiabatic approximation, leading to a renormalisation of the electronic model parameters, τ and z_0. $F_{R,el}$ is related only to the refractive index of the solvent, and in view of the minor variability of the refractive index of common organic solvents, we assume that the renormalized τ and z_0 parameters are essentially solvent independent.

The second contribution, $F_{R,or}$, is present only in polar solvent and is due to the reorientation of the polar solvent molecules around the polar solute. This term is characterised by a much slower dynamics compared to the relevant degrees of freedom and can be accounted for in the adiabatic approximation. We define the solvent relaxation energy $\varepsilon_{or} = \frac{1}{2} r_{or} \mu_0^2$ and introduce an effective solvation coordinate $f = f_{or}\mu_0$, so that the complete Hamiltonian reads:

$$\mathscr{H} = \mathscr{H}_{el} + \mathscr{H}_{ph} + \mathscr{H}_{e-ph} - f\hat{\rho} + \frac{1}{4\varepsilon_{or}} f^2 \tag{1.16}$$

The parameter ε_{or} is directly related to the solvent polarity. Polar solvents have large relaxation energies and large value of ε_{or}, while apolar solvents have $\varepsilon_{or} = 0$. ε_{or} is the only parameters that determines the evolution of the spectral properties of the chromophore increasing the solvent polarity, and fully accounts for solvatochromism.

In eq. 1.16 the Hamiltonian is parametrically dependent on the solvation coordinate f. The relevant energies describe the potential energy surface (PES) with respect to the f coordinate, with minima centred at the equilibrium value for f, $f_{eq} = 2\varepsilon_{or}\langle\rho\rangle$. We treat f as a classical coordinate, so that states around the minimum along each PES are populated with probability $p_c(f)$ according to the Boltzmann law:

$$p_c\left(f_j\right) = \frac{\exp\frac{E_c(f_j)}{kT}}{\int p_c\left(f'\right) \mathrm{d}f'} \tag{1.17}$$

where c refer to the electronic considered state ($c = g, e$).

Therefore to calculate the properties (including optical spectra) of chromophore in solution, we diagonalise the f dependent $\mathscr{H}$ in eq. 1.16 for different f values and calculate the f dependent property of interest. Ensemble properties are finally obtained summing up on a grid of f values and weighting relevant contributions according to the Boltzmann distribution. Along these lines it become obvious that polar solvation is responsible for inhomogeneous broadening of optical spectra. Since ε_{or} determines the curvature of the f dependent PES, as in eq. 1.16, polar solvents results in larger broadening, while apolar solvents ($\varepsilon_{or} \approx 0$) corresponds to steep surface with a very deep minimum. Of course the distribution is different for absorption and fluorescence spectra: for absorption spectra the solvent feels the field generated by the the ground state dipole and the distribution has to be calculated based on the ground-state PES; for fluorescence, the solvent relaxes after excitation, and the distribution has to be calculated based on the excited-state PES.

We underline that in the calculation of optical spectra one must assign a specific lineshape to each transition, calculated at each F value. In particular we

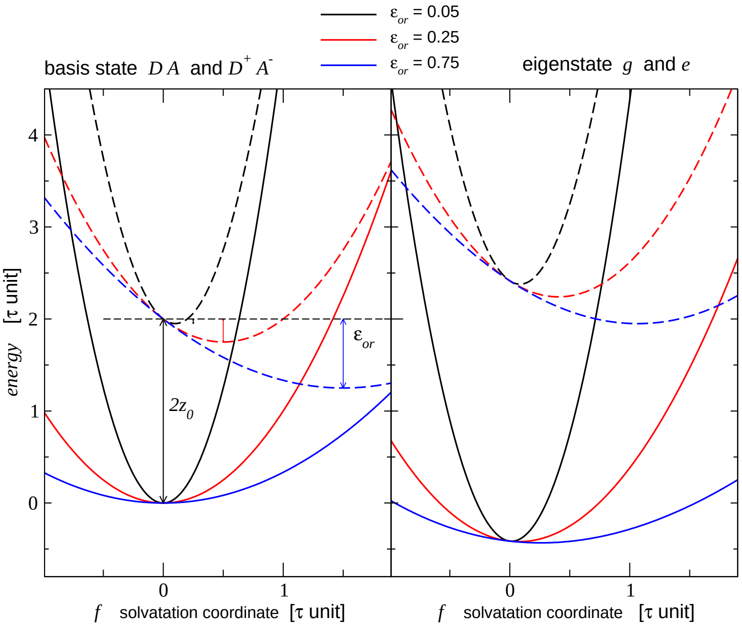

Figure 1.4: *Energy as a function of the orientational solvation coordinate, calculated for model parameter* $z_0=1$ *(and* $\varepsilon_v = 0$*), with all energies in unit of* τ*. On the left panel the basis states (called diabatic); on the right the eigenstates (adiabatic states). The dashed lines refer to the excited state energy. It can be noticed the effect of the increase of the solvation relaxation energy* ε_{or} *in determining the curvature and the position of the minima (the more polar is the state, the more shifted is the equilibrium position*

assign either a Gaussian line to each vibronic band, calculated for each f with a fixed width Γ, independent on the solvent polarity. An estimate of Γ can be obtained from the width of the vibronic lines in non polar solvents. In polar solvents, summing over spectra calculated at different f leads to inhomogeneous broadening of the bands.

The detailed procedure to calculate linear and non-linear spectra is explained in appendix sect. B.1.1.

1.2 Essential state models for chromophore and multichromophore

Essential state models account for a minimal set of electronic states and thanks to this simplification, they offer a way to treat in good detail the coupling of electronic and vibrational degrees of freedom and the effects of polar solvation. Essential state models are semi-empirical models: model parameters must be extracted from the experiment. Most often the parameters are extracted from the analysis of linear optical spectra and from their solvent dependence. Linear and non linear spectra can be calculated with the guessed parameters and the results compared with the experimental one, in a procedure similar to a fit.

Because solvent effects are explicitly accounted for, in essential state approaches the model for the solute molecule is strictly solvent independent. The essential molecular model resulting from the analysis of solution spectra can then be used to describe the same chromophore in different environments. This is the basis for the so called bottom-up approach modelling strategy to describe multichromophoric assemblies [20, 23, 25], molecular films [32], or crystals [24, 41].

Adopting solvent-independent molecular parameters largely reduces the number of free parameters with respect to standard treatments based on the Marcus-Hush or Jortner models [42, 43, 44, 45, 46]. As it will be underlined in several cases in this chapter, despite of the reduction of free parameters, the calculated spectra satisfactorily reproduce experimental data, confirming the validity of the model. Moreover, the global fit of optical spectra in solvents of different polarity allows for a reliable partitioning of the relaxation energy into a vibrational and a solvation contribution, a delicate issue in the Marcus-Hush treatment where spectra measured in different solvents are analysed separately.

DA chromophores beyond the two state approach

The two state model described in sect. 1.1 is a simple and effective model, that has been successfully applied to describe several families of push–pull chromophores. It reproduces linear and non-linear properties of *DA* chromophore in solution and in more complex environments. However, the two-state approximation is quite dramatic and in some experimental systems it must be relaxed. In this chapter we discuss two examples:

- an organic ligand that is well described as a *DA* chromophore, but that upon complexation on Zn^{2+} show an interesting enhancement of the TPA intensity that cannot be explained in a two state model (see sect. 1.3)
- an organic chrysenic-like *DA* compound whose spectra show a competition between a CT and a localised transition (see sect. 1.4)

Indeed another example of an improved description of a *DA* molecule beyond the two state model will described the next chapter, when the role of bridge state is discussed with reference to two chromophores of interest for bistability (see sect. 2.1.7).

1.3 Terpyridine-based ligand and the related Zn-complex

Fig. 1.5 shows the chemical structure of an organic terpyridine–based ligand **T** and of its Zinc complex **[ZnT]**. The ligand itself is a push-pull chromophore where the terpyridine group acts as an electron-acceptor, while the amino group is the electron-donor. In the complex the Zinc is coordinated to the acceptor group, leading to a much stronger acceptor character of the complexated terpyridine group. Here we combine an essential state model description and a bottom up modelization approach. This work has been done in collaboration with the group of D. Roberto of the University of Milano (Italy) that developed the synthesis of the two compounds, while the nonlinear characterisation (two-photon absorption) was performed by the group of Prof. C. Ferrante of the University of Padova (Italy). Our group is responsible for collecting optical linear spectra, and for the theoretical model [47].

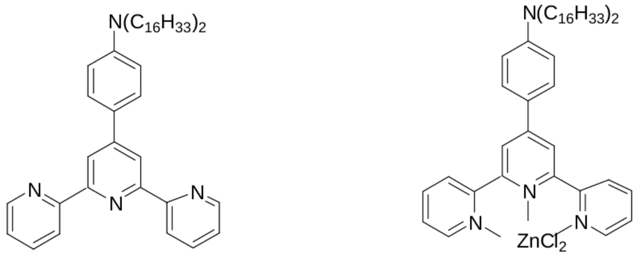

T **[ZnT]**

Figure 1.5: *Studied terpyridinic ligand and the related Zinc complex*

1.3.1 Ligand: spectroscopy and two state model

Fig. 1.6 (upper panels) reports experimental spectra of the ligand **T**. Panel (a) shows linear absorption and fluorescence spectra collected in solvents of different polarity; panel (b) shows TPA spectra collected in CH_2Cl_2. Table 1.1 summarizes main spectroscopic data. Linear spectra were collected in our laboratory, according to the procedures described in the appendix sect. A.1. The experimental procedures adopted for fluorescence quantum yield (FQY) and TPA measurements done in Padova are explained in appendix A.2.

Table 1.1: *Experimental data for **T** in cyclohexane, toluene and dichloromethane.*

solvents	λ_{abs}/nm (ϵ/M^{-1}cm^{-1})	λ_{fluo}/nm (FQY)	λ_{TPA}/nm (σ_{TPA}/GM)
cyclohexane	348	377	
toluene	358	413	
dichloromethane	362 (21300±500)	474 (0.27±0.03)	730 (96±12)

One-photon absorption (OPA) and fluorescence spectra were collected in cyclohexane (CH) , toluene and dichloromethane. Since **T** exhibits very low solubility in CH, for this solvent the spectrum reported in fig. 1.6(a) is not the absorption spectra but the fluorescence excitation spectrum (see caption of fig. 1.6). As expected for a largely neutral polar chromophores, **T** shows a weakly solvatochromic absorption while fluorescence spectra exhibit a stronger solvatochromism. The TPA band exactly overlaps the linear absorption band (fig. 1.6(b)), as expected for asymmetric molecules.

The two-state model presented in the previous section applies very well to **T**, as demonstrated by calculated spectra shown in panels (c) and (d) of Figure 1.6, The spectra have been obtained with model parameters in table 1.2 (for details about the calculation of linear and two-photon spectra see appendix B.2). The results are very good: not only transition energies, but also the evolution of absorbance and fluorescence band shape with solvent polarity are well reproduced. The TPA spectrum is also reproduced quantitatively with the same parameters: in particular we notice that both the molar extinction coefficient of OPA and the TPA cross section are in good agreement with the experimental data. We underline that six parameters of the model (η, $\sqrt{2}t$, μ_0, ε_v, ω_v and the intrinsic linewidth of the vibronic transition, Γ) are solvent-independent, while only one (ε_{or}) changes with solvent polarity.

1.3.2 Optical spectra of [ZnT]: the need for an extension of the model

The complexation of **T** on ZnCl$_2$ has interesting consequences in optical spectra, as seen in Figure 1.7 (Table 1.3 summarizes experimental data). Absorption and fluorescence spectra are red-shifted with respect to the ligand and the molar extinction coefficient increases by a factor ~1.2, while the cross section of

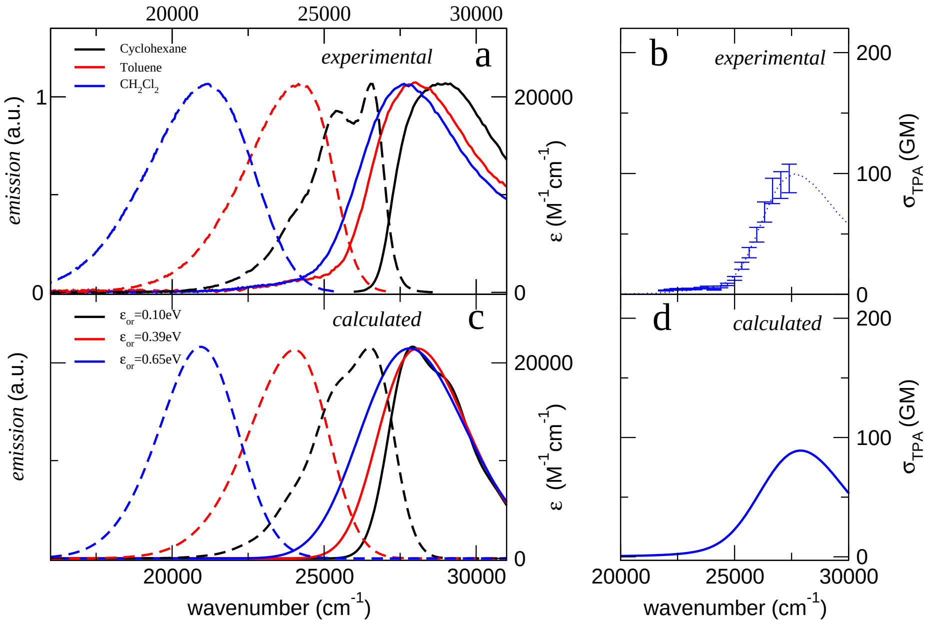

Figure 1.6: *Top panels: experimental spectra of* ***T****. Panel a: continuous and dashed lines refer to absorption and fluorescence, respectively.* ***T*** *hardly dissolves in CH, and in the OPA spectrum a very weak band appears in the low-energy region that can be assigned to the complexation of* ***T*** *with traces of metallic ions in solution. To overcome this problem, the fluorescence excitation spectrum is shown (black continuous line, in arbitrary units). The molar extinction coefficient was measured in* CH_2Cl_2 *and spectra collected in other solvents are normalised to this value. Panel c: TPA spectrum in Göppert-Mayer (symbols and errors bars) and OPA spectrum (arbitrary units, dotted line) collected in* CH_2Cl_2*. Bottom panels: Spectra calculated for* ***T*** *by the two-state model using the parameters reported in Table 1.2*

Table 1.2: *Model parameters for **[ZnT]** and for **T**: the molecular parameters relevant to the **T** ligand (*τ*,* z_0*,* μ_0*,* ω_v*,* ϵ_v *and* Γ*) are rigidly transferred from the two-state model to the three state model (common values, upper part of the table). In the central part of the table are shown the parameters entering only the three-state model for **[ZnT]** and in the last part the solvent parameters for both molecules .*

molecular parameter	**T**	**[ZnT]**
z_0/eV	1.54	
τ/eV	0.95	
μ_0/D	20.5	
ε_v/eV	0.20	
ω_v/eV	0.17	
Γ/eV	0.065	
x_0/eV		2.28
t'/eV		0.77
μ'_0/D		8.6
$\alpha\mu_0$/D		36.9
solvent parameter	**T**	**[ZnT]**
ε_{or}/eV cyclohexane	0.10	
toluene	0.39	0.13
dichloromethane	0.62	0.27

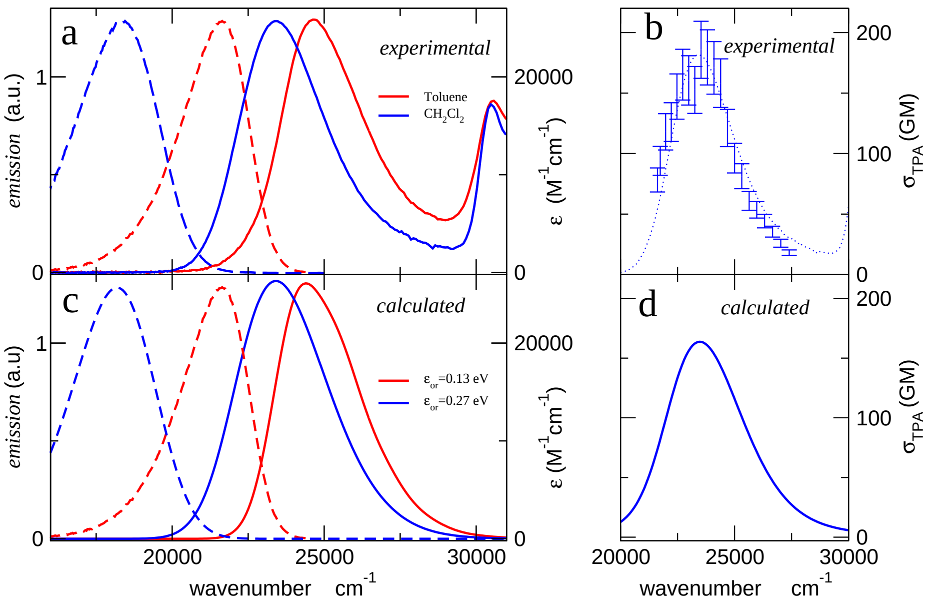

Figure 1.7: *Top panels: experimental spectra of* ***[ZnT]****. Panel a: continuous and dashed lines refer to absorption and fluorescence, respectively. The molar extinction coefficient was measured in* CH_2Cl_2 *and spectra collected in other solvents are normalises to this value. Panel c: TPA spectrum in GM (symbols and error bars) and OPA spectrum (arbitrary units, dotted line) collected in* CH_2Cl_2*. Bottom panels: Spectra calculated for* ***[ZnT]*** *by the three-state model using the parameters reported in Table 1.2*

Table 1.3: *Experimental data for **[ZnT]** toluene and dichloromethane.*

solvent	λ_{abs}/nm (ϵ/M^{-1}cm^{-1})	λ_{fluo}/nm (FQY %)	λ_{TPA}/nm (σ_{TPA}/GM)
toluene	405	463	
dichloromethane	427 (25700±400)	549 (0.48±0.05)	847 (186±24)

two-photon absorption increases by a factor of ~2 with respect to **T** [47]. Linear optical properties of **[ZnT]** can be rationalised in the two state picture: upon complexation with the Lewis acid group ZnCl$_2$, the acceptor strength of the terpyridine group increases lowering the energy of D^+A^-, and therefore decreasing the z_0 value. As a results ρ increases justifying the red shift of the absorbance and fluorescence bands as well as the the weak increase of the absorption intensity. But when we tried to reproduce the increase seen in the TPA cross section, the two state model fails completely: in fact we obtain an amplification of the TPA cross section not larger than 1.2. The reason for the failure of the two-state model for **[ZnT]** has to be ascribed to the presence of a higher-energy state, that contributes to the TPA response, while barely affecting the low-energy state involved in OPA.

Then we model **[ZnT]**, again in an essential-state picture, as a DAA_v specie, where A_v is a virtual acceptor that mimics the ZnCl$_2$ group. This leads to three resonating structures:

$$D\,A\,A_v \longleftrightarrow D^+A^-A_v \longleftrightarrow D^+A\,A_v^-$$

that define three basis states. In agreement with the two-state model, the states $|D\,A\,A_v\rangle$ and $|D^+A^-A_v\rangle$ are separated in energy by $2z_0$ and the mixing element is $-\tau$. The energy gap between $D^+A^-A_v$ and $D^+A\,A_v^-$ is $2(x_0 - z_0)$, and the two states are mixed by $-\tau'$, as sketched in Figure 1.8. The corresponding Hamiltonian is:

$$\mathscr{H}_{el} = \begin{pmatrix} 0 & -\tau & 0 \\ -\tau & 2z_0 & -\tau' \\ 0 & -\tau' & 2x_0 \end{pmatrix} \tag{1.18}$$

$|D^+A\,A_v^-\rangle$ is a virtual high-energy state ($x_0 > z_0$), that, being not directly coupled with the neutral state $|D\,A\,A_v\rangle$, marginally affects the ground state. On the other hand, $|D^+AA_v^-\rangle$ significantly contributes to the first excited state, leading to a sizeable increase of the dipole moment of the first excited state,

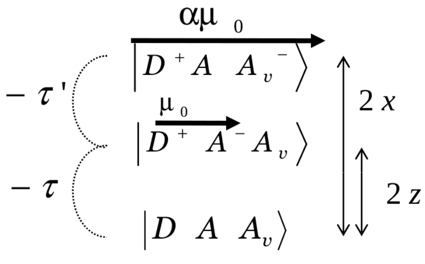

Figure 1.8: *The three basis states for* ***[ZnT]***

and hence of $\Delta\mu = \mu_e - \mu_g$. The OPA intensity is proportional to the squared transition dipole moment (μ_{ge}^2) between the ground state and the excited state, and is barely affected by the presence of the virtual state. On the other hand, the TPA cross section is proportional to $(\Delta\mu)^2\,\mu_{ge}^2$, so that a sizeable increase of the TPA response is expected as a result of complexation, as experimentally observed [47].

Before starting the detailed analysis of optical spectra of the **[ZnT]** complex, the role of the virtual state on the intensity of OPA and TPA spectra is discussed in more detail. Colour maps in Figure 1.9 show the OPA (top panel) and the TPA intensities (bottom panel) calculated as a function of z_0 (half the energy gap between $D\,A\,A_v$ and $D^+A^-A_v$) and of $x_0 - z_0$ (half the energy gap between $D^+A^-A_v$ and $D^+A\,A_v^-$, figure 1.8), for the three state model in Eq. 1.19. Both the mixing elements are set to 1 ($\tau = \tau' = 1$) and the dipole moment of $D^+A\,A_v^-$ is set to $2\mu_0$, twice the dipole moment of $D^+A^-A_v$. For $x_0 - z_0 \gg \tau'$ the virtual state becomes irrelevant, and one regains the two-state model. In particular for small values of z_0, $\rho \rightarrow 0.5$ and according to equation 1.7 (and fig. 1.9) the transition dipole moment is very large, so that the OPA intensity is high. Increasing z_0, the system becomes more neutral, ρ decreases, and OPA decreases as well. Anyway, the presence of the virtual excited state never affects the OPA intensity significantly. On the contrary, the TPA intensity strongly depends on the energy of the virtual state, and, as shown in the bottom panel of Figure 1.9, it increases when the virtual excited states approaches the first excited state. These predictions suggest that the three-state model can explain the experimental observations.

For a more detailed modelling of the **[ZnT]** complex, molecular vibrations and polar solvation are introduced, along similar lines as previously discussed for the two-state model. Again, only one effective molecular coordinate is coupled to the electronic transition, with frequency ω_v and relaxation energy ε_v.

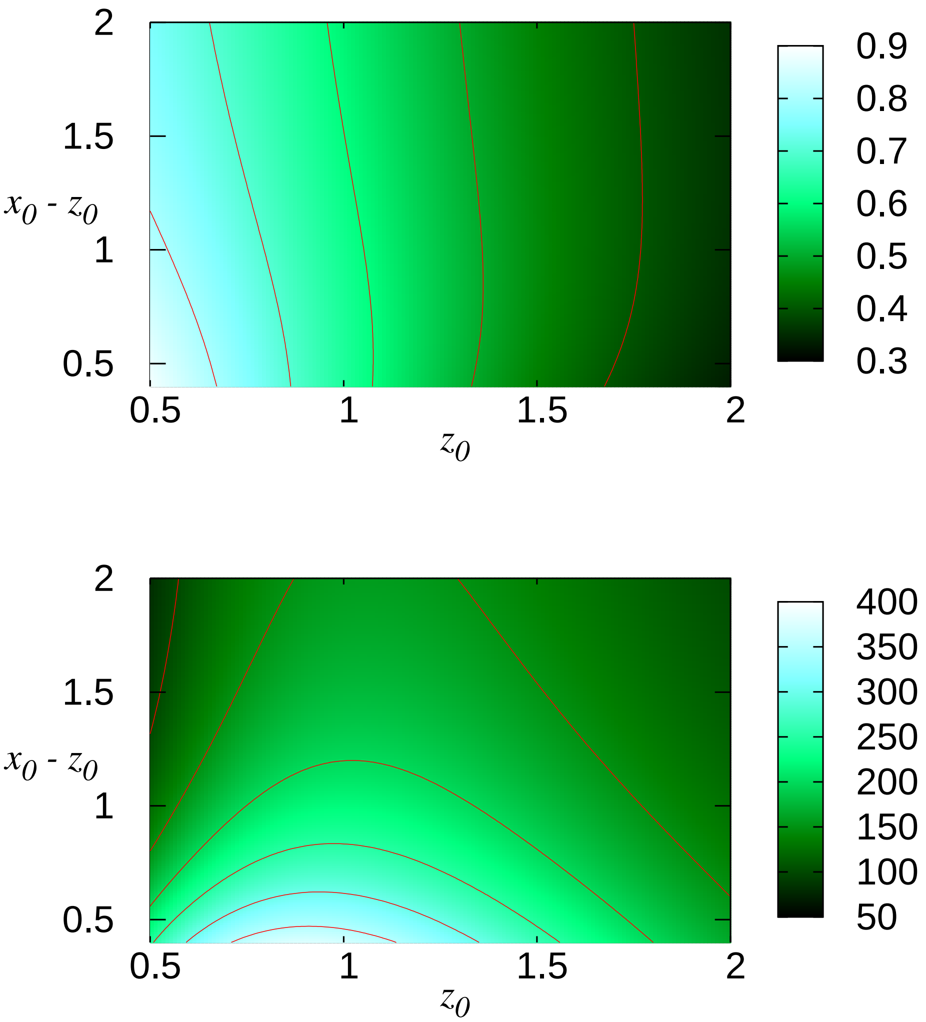

Figure 1.9: *Results of the three-state electronic model with* $\tau = \tau' =$ *1 eV,* $\mu_0 =$ 20*D and* $\alpha =$ *2. Colour maps show the OPA intensity as calculated oscillator strength (top panel) and TPA intensity in GM estimated at the maximum of the TPA band (bottom panel) as function of* z_0 *and* $x_0 - z_0$ *for the first electronic state, using the three-state model The red contour lines mark the equispaced levels, with increments 0.1 and 50GM in the top and bottom panel, respectively. This refers to pure electronic problem (*$\varepsilon_{or} = 0$ *and* $\varepsilon_v = 0$*). Effective width was introduced to estimate numerically the cross section:* Γ_{eff}*=0.16 eV .*

We assume for the $|D^+A\,A_v^-\rangle$ state the same coupling as for the $|D^+A^-A_v\rangle$ state. The electronic and vibrational Hamiltonian then reads:

$$\mathcal{H}_{el} + \mathcal{H}_{e-ph} + \mathcal{H}_{ph} = \begin{pmatrix} 0 & -\tau & 0 \\ -\tau & 2z_0 - \omega_v \sqrt{2\varepsilon_v} q & -\tau' \\ 0 & -\tau' & 2x_0 - \omega_v \sqrt{2\varepsilon_v} q \end{pmatrix} + \frac{1}{2} {\omega_v}^2 \left(q^2 + p^2\right) \tag{1.19}$$

The reaction field approach is followed to account for polar solvation. Because of the coordination with the polar $ZnCl_2$ we account for its permanent dipole moment introducing a parameter μ'. Moreover to measure the dipole length of $|D^+AA_v^-\rangle$ we introduce a parameter α ($\alpha > 1$ on physical basis) so that the dipole moment operator reads:

$$\hat{\mu} = \begin{pmatrix} \mu' & 0 & 0 \\ 0 & \mu' + \mu_0 & 0 \\ 0 & 0 & \mu' + \alpha\mu_0 \end{pmatrix} \tag{1.20}$$

We notice that μ' does not affect OPA and TPA intensities (it does not enter the transition dipole moments nor the mesomeric dipole moment), but it is responsible for a larger solvatochromism of absorption bands with respect to **T**. With this hypothesis for the dipole moments, the three-state Hamiltonian reads:

$$\mathcal{H} = \mathcal{H}_{el} + \mathcal{H}_{e-ph} + \mathcal{H}_{ph} + \frac{1}{\mu_0}\hat{\mu} f + \frac{1}{4\varepsilon_{or}} f^2 \tag{1.21}$$

As for two state model we treat f as a classical variable. For fixed f the $\mathcal{H}$ in Equation 1.21 defines a coupled electron-vibration problem that is numerically diagonalised on a non-adiabatic basis. The spectra are calculated as described in appendix B.

The number of parameters entering the three-state model is large and to reduce the number of freely adjustable parameters we exploit the bottom-up modelling strategy and transfer all relevant parameters from the two-state model of a free ligand **T** to the description of the ligand unit within the complex. Table 1.2 summarizes all parameters entering **T** and **[ZnT]** model. Molecular parameters τ, z_0, μ_0, ω_v, ε_v and Γ in the first part of the table, are common to the two molecules. Solvent relaxation energies are smaller than those reported for **T**, a fact that can be rationalised in terms of the smaller dimension of the solute cavity for **T** than for **[ZnT]**. Calculated spectra are reported in the bottom panels of fig. 1.7. The agreement with experimental data is very good: band shapes, transition energies and intensities (molar extinction coefficients and the TPA cross section) are well reproduced.

Quite interestingly the three-state model actually accounts for the inductive effects predicting a red-shift of the optical transition without the need to empirically re-adjust z_0. The third state $D^+AA_v^-$ included in the model, can be defined as a virtual state in the sense that it marginally affects the ground state and linear spectral properties. However it does enter with sizeable weight the first excited state, leading to an increase of the dipole moment of the first excited state, and hence to an amplification of the TPA response, where $\sigma_{\mathrm{TPA}} \propto \mu_{ge}^2(\mu_g - \mu_e)^2$ (see appendix B). This mechanism is general, and can be extended to different systems: attaching a virtual acceptor or a virtual donor to a push-pull chromophore is expected to sizeable increase its TPA response.

1.4 Annine: CT vs localized excitations

In collaboration with S. Quici (CNR-Milano), D. Roberto (University Milano) and C. Ferrante (Padova) we have investigated a family of chrysene derivative molecules. The molecular structure of these molecules in fig. 1.10 is characterized by an extendend π framework, that in virtue of its rigidity lead to good photostability. The properties of molecules in this family have been already object of some investigation [48, 49].

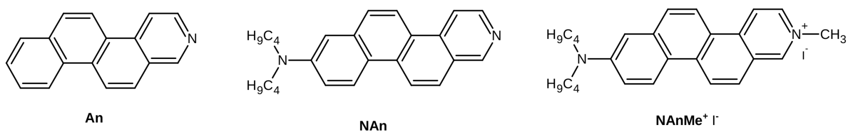

Figure 1.10: *Chemical structures of the molecules discussed in this section*

An is an heterocyclic substituited chrysene in which the carbon in position 2 is substituited with a nitrogen atom, obtaining the corresponding 2-azachrisene and increasing the acceptor strength of the substituted ring. **An** represent the reference compound. Adding an electron donor group on the opposite side of the fused ring structure, we obtain the 8-N,N-dibutylamino-2-azachrysene (**NAn**), as in figure 1.10, that represent an interesting *DA* chromophore. The third compound, **NAnM$^+$**, from which the family name ANNINE comes (ANellated benzene rings hemicyaNINE), is obtained by methylation of the pyridinic nitrogen, resulting in a strong increase of the acceptor strength. We describe in detail the properties of **NAn**, the parallel study of **An** and **NAnMe$^+$** is mainly realized to support our analysis of **NAn**.

1.4.1 Optical properties of An

We study the compound **An** (2-azachrisene, show in figure 1.10) in order to support the physical interpretation of the **NAn** spectra, that will be described later. Absorption and fluorescence emission and fluorescence excitation spectra of **An** are measured in cyclohexane, toluene, CH_2Cl_2 and DMSO.

We encounter some difficults related to the poor solubility of **An** in almost all solvents, an to its the tendency to form aggregates and/or excimers [50]. Fluorescence excitation spectra are helpful in this respect. Anyway, in diluite solutions and/or after sonication and filtration a set of reliable spectra was obtained, except for cyclohexane. Results are shown in figure 1.11. The presence of a bad baseline for toluene, as well as the unresolved low energy side of the emission spectra can be due to formation of aggregates and excimers.

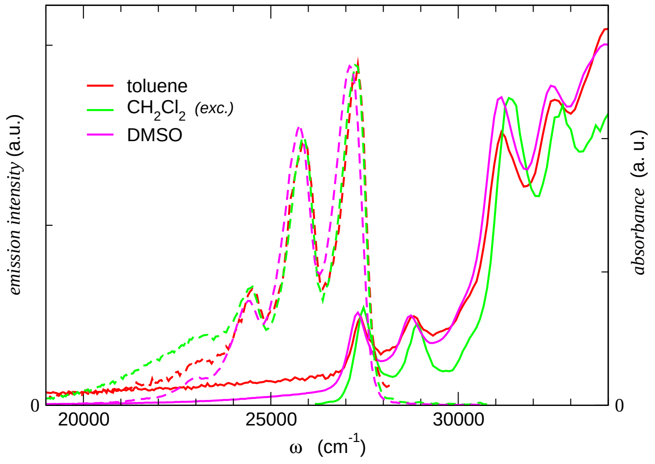

Figure 1.11: *Experimental absorption and fluorescence of* ***An*** *in three solvent. For* CH_2Cl_2 *the excitation spectra is shown instead of the absorption.*

Anyway, spectra in fig. 1.11 show the typical behaviour expected for organic conjugated fused ring chromophores, with $\pi \rightarrow \pi^*$ excitations with narrow and well resolved vibronic structure. The negligible effect of the solvent polarity on optical spectra, showing no broadening and no solvatochromism upon increasing solvent polarity, confirms the localized nature of the excitations and the emission.

1.4.2 Optical properties of NAn

Linear optical spectra (absorbtion and fluorescence) of **NAn** were collected in solvents of different polarities: cyclohexane, toluene, CH_2Cl_2 and DMSO. Molar extinction coefficient and FQY were also measured in CH_2Cl_2 and DMSO. Spectra are shown in fig. 1.12 e 1.13 and spectroscopic quantities are summarized in tables 1.4 and 1.5. The absorption spectrum is characterized by three systems of transitions (see fig. 1.12):

- a weak absorption **I** at ~ 410 nm, that is well resolved in nonpolar solvent
- a band at about 350-360 nm (**II**), with a distinct solvatochromic behaviour
- a strong peak at ~ 300 nm (**III**)

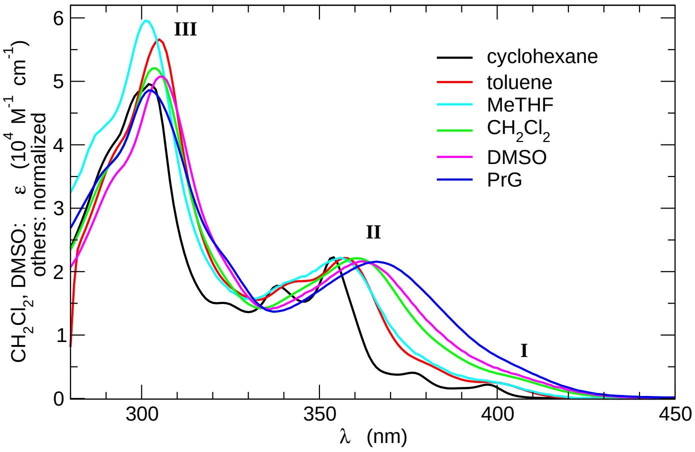

Figure 1.12: *Experimental absorption spectra of* ***NAn*** *in different solvents.*

We are mainly interested in the low energy portion of the spectra, and specifically on feature **I** and **II**: fig. 1.13 collects the relevant region of absorption spectra in 1.12 and the fluorescence spectra, including two more solvent used for fluorescence anisotropy measurements (see below): propilenic glycole (PrG) and 2-methyl-tethrahydrofurane (MeTHF). **I** is difficult to locate in polar solvents, where it partly overlaps with **II**. Both absorption and fluorescence are well resolved in apolar solvent, with a clear vibronic structure. Fluorescence shows a marked solvatochromism. In nonpolar solvent the 0-0 vibronic peaks of absorption and emission coincide.

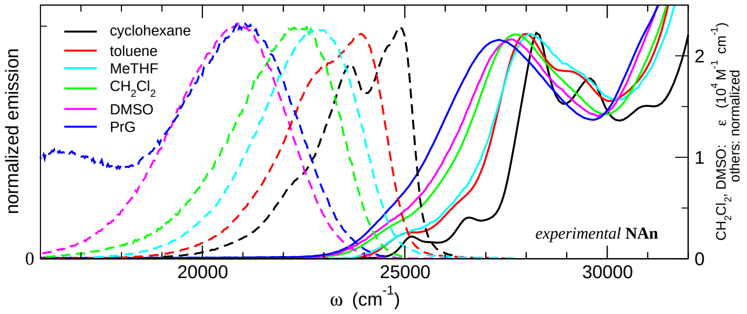

Figure 1.13: *Low energy portion of the experimental absorption spectra and fluorescence spectra of* ***NAn*** *in different solvents.*

Table 1.4: *Experimental data for absorption and the TPA of* ***NAn****, with absorption maxima and molar extinction coefficient ϵ, and TPA maximum and cross section in DMSO*

	I	**II**	
solvent	λ_{abs}/ nm (ϵ/M^{-1}cm^{-1})	λ_{abs}/ nm (ϵ/M^{-1}cm^{-1})	λ_{TPA}/ nm (σ_{TPA} / GM)
cyclohex.	397 [0-0] 376 [0-1]	353 [0-0] 338 ([0-1]	
toluene	~400 [0-0] ~385 [0-1]	357 [0-0] ~341 [0-1]	
MeTHF	400	356	
CH_2Cl_2	~ 407 (~ 3000)	361 (22000)	
PrG	~ 410	439	
DMSO	~ 410 (~ 3000)	362 (21500)	730 (100)

Table 1.5: *Experimental data for fluorescence of* ***NAn****: emission maxima and fluorescence quantum yeald (FQY).*

solvent	λ_{em} / nm	FQY
cyclohexane	402 [0-0] 424 [0-1]	
toluene	418 [0-0] ~437 [0-1]	
MeTHF	439	
CH_2Cl_2	467	0.23
PrG	476	
DMSO	481	0.47

We notice that room T spectra in PrG shown a double band fluorescence, with a weaker peak at lower frequency that disappear in the frozen solvent (see below). Frozen solution of MeTHF show a similar but less pronounced behaviour, with a very weak and resolved emission redshifted respect to the main one. The room T emission in MeTHF does not show this feature. The investigation of this phenomenon, that is possibly due to some excited state dynamic and relaxation processes [51, 52, 53], is beyond the aim of this work and requires time dependent techniques not available at present in our laboratory.

Absorption spectra of **NAn** do not resemble typical spectra of *DA* chromophores. In fact the lowest energy transition is definitely too weak for a CT transition, while feature **II**, lying higher in energy, has both the intensity and the solvatochromic behaviour typical of a CT transition. On the other hand, fluorescence shows an increasing CT character when going from the apolar solvent (in which it overlaps with LE absorption) to polar solvents where spectra has the typical strong solvatochromism of dipolar emission from CT state.

At the same time, we notice that the absorption **I** and more generally the absorption and fluorescence spectra profile of **NAn**, as in fig. 1.13 in non polar solvents strongly resemble to the absorption and fluorescence bandshapes in **An** (see fig. 1.11). It is then tempting to assign feature **I** in absorption spectra to a localized excitation i.e. an excitation involving the azo-chrysene π skeleton.

Since the investigated sistem has a low energy physics involving more than one excited state and possibly the transition dipole moments is oriented along different directions, emission and fluorescence excitation anisotropy spectra were recorded in glassy solution of propilenic glycole (PrG) at 200K and 2-methyl-tethrahydrofurane (MeTHF) at 77K. A detailed description of theoretical and practical aspects of anisotropy measurements can be found in the appendix A.4 and B.3.1, respectively.

The anysotropy excitation profile is pretty rich in both solvents and it reaches the limiting 0.4 value in the low energy side of the spectra, corresponding to an (almost) complete alignment of excitation and emission dipoles, then the anisotropy decreases in a “plateau” region at 350–390 nm. The main difference between the two solvents is in the anisotropy value in the plateau region, where for the more polar solvent (PrG) $r \sim 0.3$, while in MeTHF $r \sim 0.2$.

The experimental excitation and emission spectra in frozen PrG and MeTHF are shown together with anisotropies in fig. 1.14. The spectra exhibit important differences from room T spectra: in spite of the different polarities, absorption (excitation) and emission spectra in PrG and MeTHF are peaked at a similar wavelenght. Moreover, the emission spectra are weakly shifted compared to room T spectra.

Anysotropy results confirm the presence of more than one excitation, and actually reveal that the emission in frozen solvent occur always from the lowest energy state, the one responsible for the absorption at 400-420 nm, because in both solvents the r value tend to 0.4 at the red edge of the absorption spectra profile.

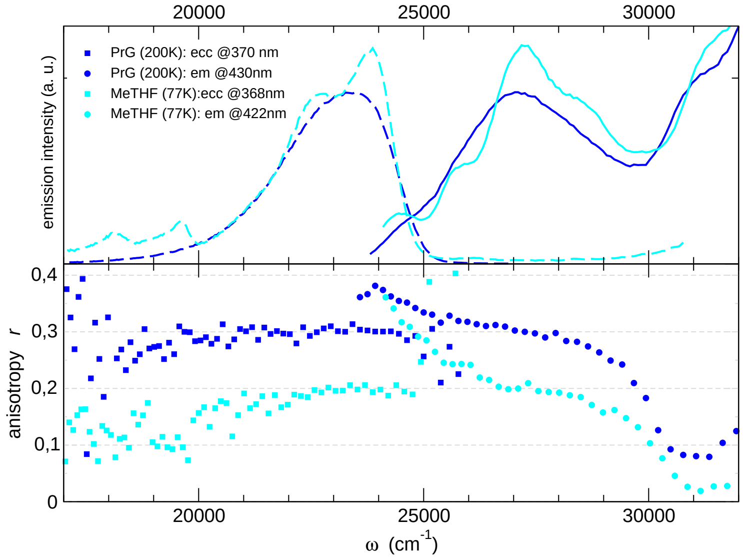

Figure 1.14: *Spectral properties of frozen solution of* ***NAn****in PrG (deep blue) and MeTHF (light blue). Top panel shows fluorescence excitation spectra (continuos line) and fluorescence spectra (dashed lines). Data in the legend refers to anysotropy spectra, while the excitation and detection wavelenght for emission and excitation spectra are respectively 430 nm and 399 nm (PrG), 422 nm and 368 nm (MeTHF).*

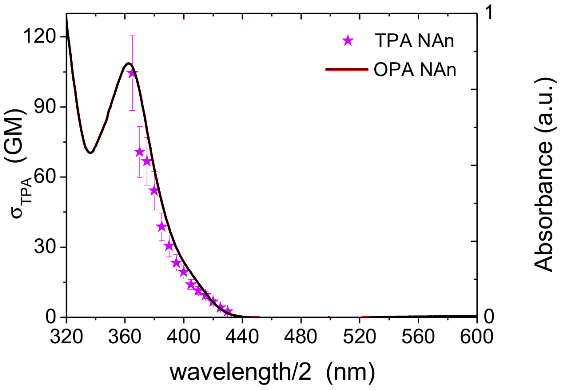

Figure 1.15: *Experimental TPA spectra (stars) and the normalized OPA for* ***NAn*** *in DMSO.*

Experimental TPA spectra

Two photon absorption (TPA) spectra were measured in Padova by the group of Ferrante for the **NAn** (and for the **NAnM**$^+$, see following section) in DMSO solution. The experimental TPA spectra is shown in fig. 1.15, along with the OPA spectra for comparison. The experimental results are summarized together with OPA in table 1.4. Even if the TPA band is not complete due to experimental limitations in the short wavelenght side, the maximum of TPA and OPA coincide, as expected for asymetric dyes.

1.4.3 CT and localized transition and the failure of the standard two-state approach

A complex experimental picture

To describe optical spectra of **NAn** we must account for two excited states, close in energy. One is responsible for the CT transition and corresponds to the band **II** in absorption spectra, while the other can be identified as a *localized excitation* (LE), i.e. essentially a $\pi \rightarrow \pi^*$ transition, similar to the lowest energy feature observed in **An** and corresponding to the absorption **I**.

In absorption the feature **I** is always lower in energy than **II** even if, upon increasing the solvent polarity, **II** lowers in energy until in partially overlaps **I**. But the large solvatochromism of fluorescence spectra suggests a CT character of the lowest excited state (the fluorescent state). This apparent contraddiction can be resolved assuming that in polar solvents the nature of the first excited state changes from LE to CT as long as the system relaxes after the excitation.

Semiempirical INDO/S calculations

To validate our hypothesys and to support the definition of the dipole moment operator in the essential state model we perform semiempirical calculations (ArgusLab package [54]). Calculation refers to the in vacuo molecule optimized at AM1 semiempirical level of theory, while the excited state calculations were performed with the INDO/S hamiltonian with CI (40 occupied MOs by 40 virtual MOs as space for the excited configurations).

We define the *DA* direction as parallel to the x axis; the y direction is perpendicular to x in the molecular plane (see fig. 1.16). The transition dipole moments calculated for the first excitations of **An** and **NAn** are shown in fig. 1.17. In the **NAn** the three lowest energy transitions computed as polarized are not along the main dipolar (*DA*) direction but the transition dipole moment form a small angle with the y axis. At the same time an intense transition is found at higher energy (the large transition dipole moment in the figure 1.17), mainly along the CT direction. This transition is not found among the (low energy) transitions for **An**, and is identified as the CT transition. For **NAn** the angle formed by the the average of the first transitions and the following CT-like is about 50-70 degrees.

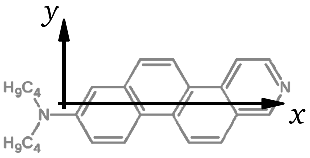

Figure 1.16: *Axis definition for **NAn** and related molecules.*

1.4.4 A three state model for the two transitions in NAn

We define a model for **NAn** including three electronic basis state: $|D\ \pi\ A\rangle$, $|D^+\pi\ A^-\rangle$, and $|D\ \pi^*A\rangle$. The first two state ideally account for the CT transition, and correspond to the two states of the essential state model for *DA* dyes (see sect. 1.1). The $|D\ \pi^*A\rangle$ state represents the local excitation. We assume again an energy $2z_0$ for the $|D^+\pi\ A^-\rangle$, mixed by an element $-\tau$ with the neutral

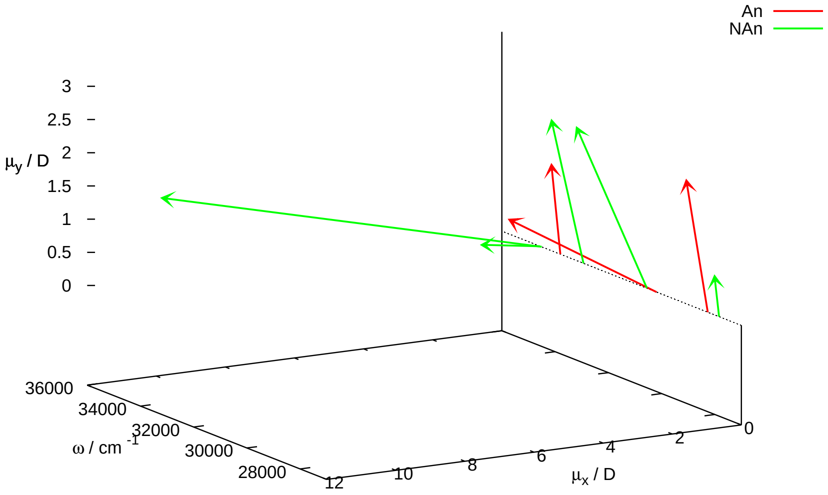

Figure 1.17: *INDO/S calculated transition dipole moment for* ***An*** *(red) and* ***NAn*** *(green). On the x axis the excitation energies (cm^{-1}), while the other two axis refer the two components of the transition dipole moments: on y axis the x component (parallel to DA direction) and on the z axis the y component. z components are negligible.*

state. The $|D\ \pi^* A\rangle$ state has energy $2y_0$, and for this state we account for the coupling $(-\beta)$ only with the nearby zwitterionic state, while neglect any direct coupling with $|D\pi\ A\rangle$. The relevant hamiltonian is:

$$\mathscr{H}_{el} = \begin{pmatrix} 0 & -\tau & 0 \\ -\tau & 2z_0 & -\beta \\ 0 & -\beta & 2y_0 \end{pmatrix} \tag{1.22}$$

On this basis the $\hat{\rho}$ operator, measuring the weight of the zwitterionic state, is:

$$\hat{\rho} = \begin{pmatrix} 0 & 0 & 0 \\ 0 & 1 & 0 \\ 0 & 0 & 0 \end{pmatrix} \tag{1.23}$$

The definition of the dipole moment operator is crucial in this model. We assign a large dipole moment, μ_0, to the zwitterionic $|D^+\pi\ A^-\rangle$, directed along the x direction. Moreover we define a non-vanishing off-diagonal element, $\mu_* = \langle D\ \pi\ A\ |\hat{\mu}| D\ \pi^* A\rangle$ to account for the finite intensity of the LE transition. This dipole forms an angle $\varphi \sim 50 \div 70°$ with the x DA direction. This choice is in agreement with the orientations of the transition dipole moment for the lowest transitions in fused ring aromatic compounds, suggested by the quantum chemical calculation (see sect 1.4.3. The two components of the dipole moment then reads:

$$\mu_x = \begin{pmatrix} 0 & 0 & \mu_* \cos(\varphi) \\ 0 & \mu_0 & 0 \\ \mu_* \cos(\varphi) & 0 & 0 \end{pmatrix} \tag{1.24}$$

$$\mu_y = \begin{pmatrix} 0 & 0 & \mu_* \sin(\varphi) \\ 0 & 0 & 0 \\ \mu_* \sin(\varphi) & 0 & 0 \end{pmatrix} \tag{1.25}$$

As with the two state model we define a vibrational coordinate q (and the relative momentum p), linearly coupled respect to the $|D^+\pi\ A^-\rangle$ state. We set the frequency of this moleculear vibration equal to ω_v and assume a relaxation energy ε_v. Thus the adiabatic hamiltonian is:

$$\mathscr{H}_{el+ph} = \begin{pmatrix} 0 & -\tau & 0 \\ -\tau & 2z_0 - \omega_v\sqrt{2\varepsilon_v}q & -\beta \\ 0 & -\beta & 2y_0 \end{pmatrix} + \frac{1}{2}\omega_v q^2 \tag{1.26}$$

To reproduce the vibrational structure observed in non-polar solvent in the LE band, we define a second vibrational coordinates q_* (and momentum p_*) for the coupling with $|D\pi^*A\rangle$, with frequency and vibrational relaxation energy ω_{v*} and ε_{v*}. This coordinate does not add much to the physical description of the system apart from a better reproduction of the structure of the LE band. The total adiabatic hamiltonian reads:

$$\begin{aligned}\mathscr{H}_{el+2ph} &= \begin{pmatrix} 0 & -\tau & 0 \\ -\tau & 2z_0 - \omega_v\sqrt{2\varepsilon_v}q & -\beta \\ 0 & -\beta & 2y_0 - \omega_{v*}\sqrt{2\varepsilon_{v*}}q_* \end{pmatrix} \\ &\quad + \frac{1}{2}\omega_v q^2 + \frac{1}{2}\omega_{v*}q_*^2 \end{aligned} \tag{1.27}$$

We expect $\mu_0 \gg \mu_*$, moreover we neglect the permanent dipole moment associated with $|D\pi^*A\rangle$, therefore the solvation model reduces to the one relevant to the standard two state model. We define an effective solvation coordinate along the CT direction (x component) with a relaxation energy ε_{or}. The resulting total hamiltonian then is:

$$\mathscr{H} = \mathscr{H}_{el+2ph} - f\hat{\rho} + \frac{1}{4\varepsilon_{or}}f^2 \tag{1.28}$$

The equation 1.27 represents a coupled electro-vibrational hamiltonian that will be actually solved in a non adiabatic approach over the basis obtained by the direct product of the three electronic states times n states associated at the harmonic oscillator relevant to q, times n_* states of the harmonic oscillator relevant for q_*. The general procedure for the calculation of absorption, fluorescence and anisotropy spectra is described in appendix B.1.1 and B.3.1.

1.4.5 Results

The calculated absorption and fluorescence spectra at ambient conditions are shown in figure 1.18, and the corresponding three-state model parameters are listed in the table 1.6. The agreement between calculated spectra and experimental data is really good, particularly in view of the relative simplicity of the proposed model, with respect to the complex spectroscopic behaviour observed. In particular, we successfully reproduce all the spectroscopical peculiarities of **NAn**. The absolute intensity of the two transitions, as well as the fluorescence solvatochromism and the marked loss of vibrational structure upon increasing solvent polarity are correctly reprodueced.

Spectra in fig. 1.18 have been obtained via non-adiabatic diagonalization, however, to better undertstand the physics at the base of the anomalous spectral behaviour on **NAn**, we make resort to the adiabatic approximation and plot the

Table 1.6: *The three-state model parameters for* ***NAn*** *used to calculate optical properties in fig. 1.18*

molecular parameter	**NAn**
z_0 / eV	1.51
t / eV	1.07
y_0 / eV	1.46
β / eV	0.04
μ_0 / D	19.6
μ_* / D	0.85
φ / °	50
ε_v / eV	0.28
ω_v / eV	0.18
ε_{v*} / eV	0.15
ω_{v*} / eV	0.14
Γ / eV	0.075

solvent parameter		**NAn**
ε_{or} / eV	cyclohexane	0.0
	toluene	0.40
	MeTHF	0.50
	dichloromethane	0.55
	DMSO	0.65
	PrG	0.70

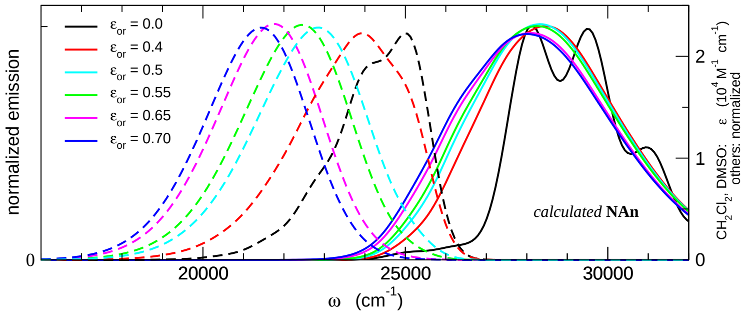

Figure 1.18: *Calculated absorption and fluorescence, parameters in table 1.6, value for ε_{or} in the legend are listed as in the experimental data of fig. 1.13*

PES relevant to the three electronic states. For graphical reason at this stage we neglect the q_* coordinate and its coupling to electrons setting $\varepsilon_* = 0$ and renormalizing y_0 to 1.37 eV to relocate the energy of the localized state in the proper position.

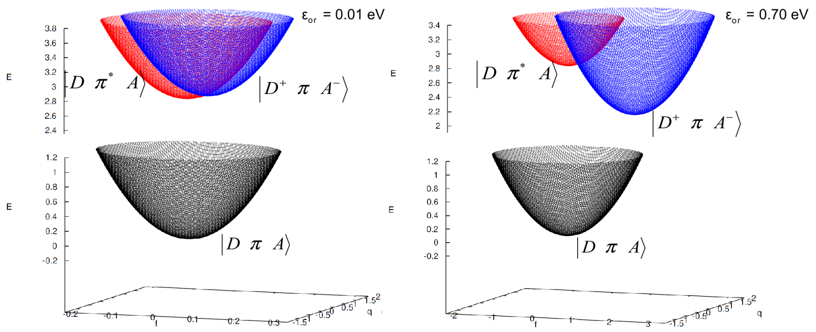

Figure 1.19: *f,q dependent PES for the three basis state. Left: apolar solvent, right: polar solvent. Parameters are the same in the table 1.6, but with ε_{v*} (ω_{v*} is then irrelevant), and a renormalized $y_{0,eff} = 1.37$.*

Figure 1.19 shows the PES relevant for the basis (diabatic) states in a slightly polar ($\varepsilon_{or} = 0.01$ eV) and in strongly polar ($\varepsilon_{or} = 0.70$ eV) solvent. In the first case the states $|D\ \pi^* A\rangle$ and $|D^+\pi\ A^-\rangle$ are very close in energy, while the polar solvent largely stabilizes the zwitterionic state.

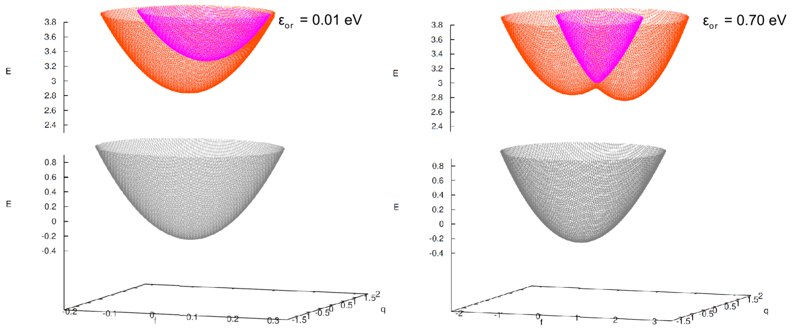

Figure 1.20: *Calculated f,q dependent PES for the three adiabatic eigenstate. Left: apolar solvent, right: polar solvent. Parameters as defined in the caption of fig. 1.19.*

Figure 1.20 shows the corresponding adiabatic PES. In the slightly polar solvent the lowest energy PES corresponds to a state that strongly resemble $|D\ \pi^{*}A\rangle$, while the second PES has a CT character. The lowest excitation always corresponds to the LE state both in absorption and in fluorescence. The situation is very different in a strongly polar solvent, where the first excited state PES describes either a LE or a CT state in different regions of the q, f plane. Specifically absorption occurs "on the vertical" from the equilibrium position relevant to the ground state. In this point the lowest excitation has a dominant LE character, while the higher excitation corresponds to a CT state. The absorption spectrum then has a weak marginally solvatochromic absorption band (corresponding to feature **I**), and an higher energy intense absorption (feature **II**), which CT character is demonstrated by its important solvatochromism. However, after excitation the system relaxes and moves toward the global minimum of the excited state PES where the state aequires a dominant CT character (see fig.1.21): in polar solvents fluorescence occurs from the CT state, even if in absorption the lowest excitation has an LE character. Of course the situation is different in frozen solvent, where the solvent cannot relax after the solute excitation. In frozen solvent, quite irrespective of the solvent polarity we expect that fluorescence always occurs from the LE state. First excited state PES are reported in fig. 1.21 too, using contours to clarify the position of the minima.

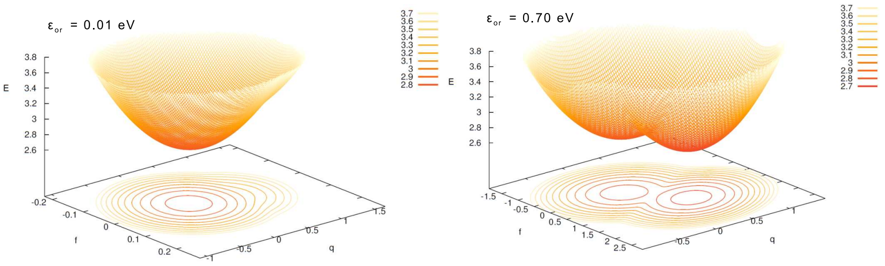

Figure 1.21: *Calculated f,q dependent PES and relative contourn of the first excited state. Left: apolar solvent, right: polar solvent. Parameters as defined in the caption of fig. 1.19.*

We are now in the position to calculate the anisotropy excitation and emission spectra. The temperature has to be set properly for the anisotropy calculation. We set $T = 90$K in MeTHF, corresponding to the glassy transition temperature of the solvent. In propylnenic glycole, we set $T = 200$K. ([55] and see appendix A.3.1).

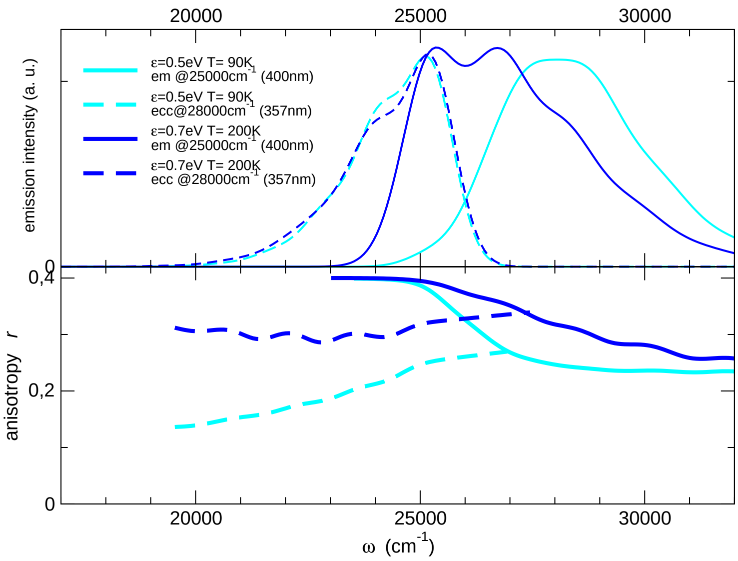

Figure 1.22: *Calculated absorbance and fluorescence of* ***NAn****, to be compared with experimental data in fig 1.14 (same symbols are used in both figures).*

Calculated anisotropies in fig. 1.22 compare very well with experimental spectra in fig. 1.14, and the different anisotropies observed for the two solvents in the plateau region is nicely reproduced in the calculation. Some problem is encountered in reproducing the position of the excitation spectra in PrG, but the complete agreement with the experimental spectra recorded in frozen solvent is a tricky problem, because one should account for the T-dependence of the solvent refractive index and dielectric constant, leading to T dependent model parameters.

The peculiar excited state properties, in term of energies and polar character, make **NAn** an interesting example of excited state *inversion*. that can occur any time there are a CT and localized excited states close in energy. This is the first time that the optical properties of a class of chrysene-like compounds is analyzed and understood in a detailed way. In spite of the highly nontrivial picture we succeded in understanding the physics governing low energy optical spectra of this chromophore.

With the same model and the same parameters listed before (table 1.6) we have calculate TPA spectra, reported with the OPA in figure 1.23. Again the level of agreement with experimental data is good. Indeed the presence of a low energy state is correctly accounted for, as confirmed by the low energy side

Table 1.7: *Experimental data for **NanMe**$^+$ in different solvents. For the dichloromethane and the toluene the absorption maxima refer to the fluorescence excitation spectra and for the toluene the emission maximum is estimated by the maximum due to the monomer contribution (spectra not shown).*

solvents	λ_{abs}/nm^a (ϵ/M^{-1}cm^{-1})^a	λ_{fluo}/nm^a (FQY)^b	λ_{TPA}/nm^a (σ_{TPA}/GM)^a
toluene	425	~ 513	
dichloromethane	502	621	
DMSO	440 (24000)	493 (0.38)	920 (285)

of the TPA band.

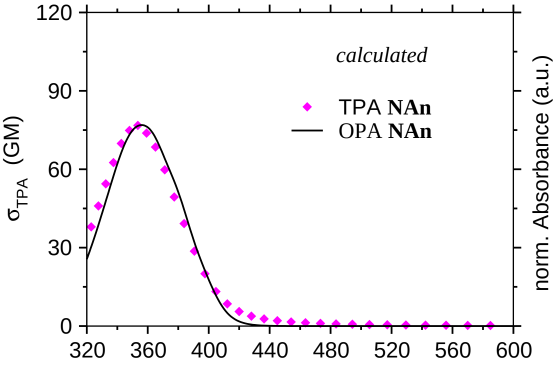

Figure 1.23: *Calculated TPA spectra (circle) and the normalized calculated OPA.*

1.4.6 Experimental properties of NAnMe$^+$

Absorption and emission spectra of **NAnMe**$^+$, show in fig. 1.24, have been recorded in toluene, CH_2Cl_2 and DMSO, and a clear tendency to aggregate was found in the first two solvents. In CH_2Cl_2 the aggregation behaviour has been investigated in a bit quantitative way, and a sistematic concentration dependence of the absorption maxima (redshift increasing concentration) has been found. Anyway, in CH_2Cl_2, the aggregate does not fluoresce (the shape of the emission spectra does not depend on the concentration neither on the excitation

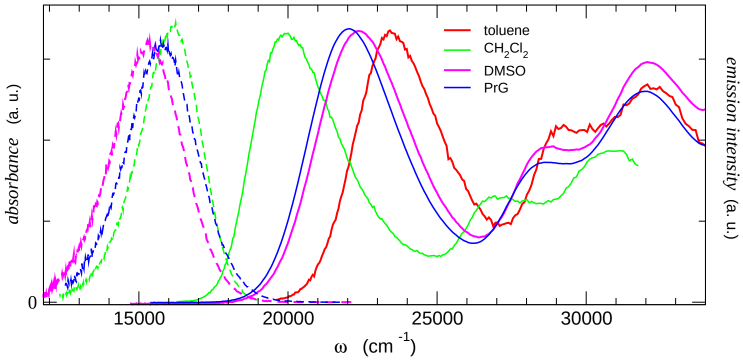

Figure 1.24: *Experimental absorption (fluorescence excitation for toluene and CH_2Cl_2) (right) and fluorescence spectra (left) of **NAnMe**$^+$ in different solvents.*

wavelenght). The fluorescence excitation spectra are then helpful to extract an absorption-like profile that is shown in fig. 1.24, instead of the absorption. In toluene both the aggregate and the molecule contribute to emission, and the first has non-negligible contribution even in diluite solutions. For this solvent, acceptable excitation spectra (shown in fig. 1.24) have been recorded. Spectroscopic data are listed in table 1.7.

Excitation and emission anisotropies measured in PrG at 200K, are reported in fig. 1.25 and shows an almost constant value of $r \sim 0.4$. TPA spectra of DMSO solutions were also recorded in Padova, and are shown in fig. 1.26. Notice that there is a significant increase in the TPA cross section compared to **NAn**.

The methylation of the pyridine-N of **NAn** leads to an enhancement of the strength of the acceptor group and absorption and fluorescence spectra are red shfited with respect to **NAn** (see fig. 1.24). The $|D^+\pi A^-\rangle$ state is now lower in energy than any local excited state and both fluorescence and absorption spectra are related to the CT transition. The measured anisotropy spectra for **NAnMe**$^+$confirms this interpretation.

NAnMe$^+$ is a charged molecule, and the standard dipolar approach for the solvent effects does not work for molecular *DA* ions. We therefore do not attempt to rationalize the solvathocromism of **NAnMe**$^+$. This in fact would require accounting for both a monopolar and a dipolar component to the reaction field, leading to a too large proliferation of adjustable parameters.

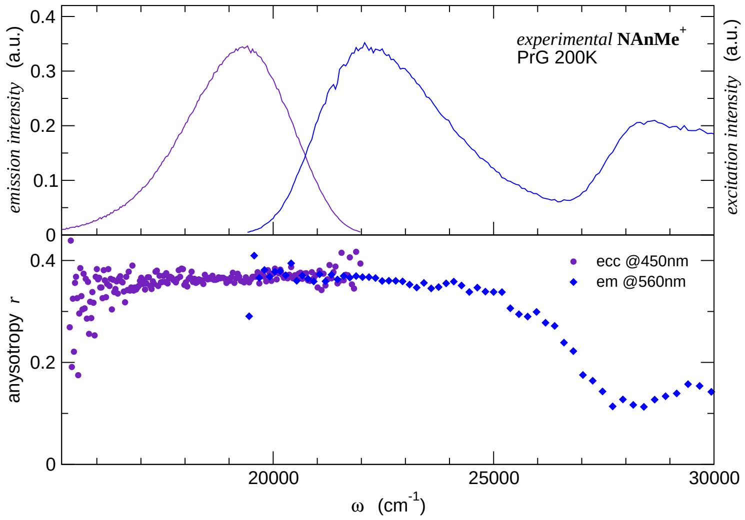

Figure 1.25: *Experimental excitation (right) and emission (left) anisotropies (bottom) and spectra (top) of **NAnMe**$^+$ in glassy solution in PrG. The excitation and emission wavelenght reported are the same for the anisotropy and for the spectra.*

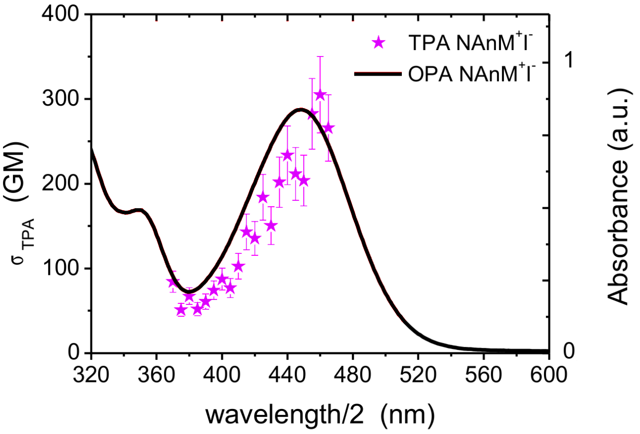

Figure 1.26: *Experimental TPA spectra (stars) and the normalized OPA for **NAn** in DMSO.*

Interacting polar chromophores

Essential state models for CT chromophores apply very well to describe the physics of systems where several chromophores interact via electrostatic forces. In the next chapter we describe interacting CT chromophores in molecular crystals, here we discuss instead optical spectra of multichromophoric systems and, more specifically, of two bichromophoric species.

The idea is to describe interacting chromophores starting from the modelization and the comprehension of the monomeric unit, and then introduce an appropriate model for the interactions. The properties of the bichromophore are not trivial: the geometry and the amount of the interaction heavily affect the property of the bichromophore and in some cases produce important effect.

DA chromophore are extensively investigated for their NLO responses. More recently, attention moved to multipolar structures where the presence of multiple D or A groups in symmetrical structures can affect NLO responses [21, 22, 36]. The interest in aggregates and multichromophoric systems arises from the possibility to synthesize TPA efficient and comparatively simple molecular units: their organisation in supramolecular structures can be exploited to cooperatively enhance the TPA response via specific interactions [25, 56].

The first example discussed is a substituted bipyridine system that will be interpreted as a dimer of the corresponding stilbazole chromophore. The second example is offered by a family of substituted spirobifluorenes, that are modelled as dimers of the relevant fluorene units.

1.5 Dimers of polar chromophores in solution: stilbazole and bipyridine

Stilbazole **S**, in fig.1.27, is a substituted pyridine, and its dimer is formed by connecting the two pyridine rings into a bipyridine structure $\mathbf{S}_2$ (fig. 1.27). These two molecules represent an interesting model system to check how interchromophore interactions affect experimental linear and nonlinear properties [57]. This work has been done in collaboration with the group of the group of D. Roberto (Milano University), which synthesized the molecules, and C. Ferrante (Padova University) which measured TPA spectra of both molecules and the fluorescence quantum yield (FQY). The Padova group is also responsible for some

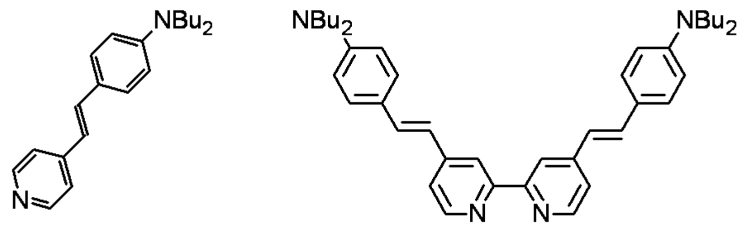

S **S$_2$**

Figure 1.27: *Studied molecules **S** and **S**$_2$*

ab initio and TD-DFT calculations. Computational results will be compared with our essential-state ones.

1.5.1 Stilbazole: the two state model at work

Experimental spectra of **S** are shown in the upper panel of fig. 1.28, and main spectroscopic data are summarized in table 1.8. The solvent dependent absorption and fluorescence spectra of **S** show the typical behaviour expected for a *DA* dye. In particular both absorption and fluorescence bands move to the red with

Table 1.8: *Experimental data for **S** in cyclohexane, toluene, dichloromethane and DMSO.*

solvents	λ_{abs}/nm (ϵ/M^{-1}cm^{-1}) *osc. strength f*	λ_{fluo}/nm (FQY %)^b	λ_{TPA}/nm (σ_{TPA}/GM)
cyclohexane	388 [0-0] 372 [0-1]	401 [0-0] 424 [0-1]	
toluene	379	439	
dichloromethane	387 (36100 ± 1400) *0.74*	472 (0.029 ± 0.004)	774 (190 ± 34)
DMSO	390	493	

^{b} standard: Fluorescein (in H_2O at pH > 11)
and Rhodamine B (in methanol)

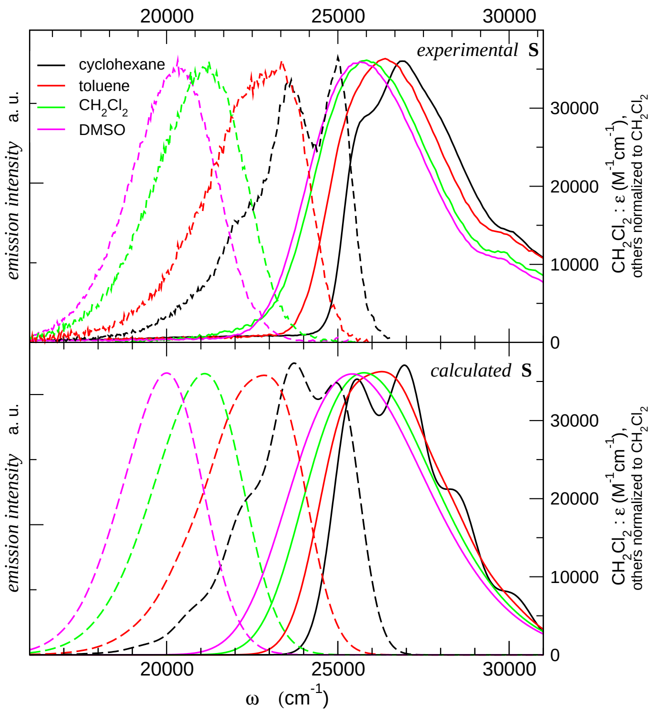

Figure 1.28: *Experimental (top) and calculated (bottom) linear spectra for molecule* ***S*** *in different solvents. Parameter shown in table 1.9 together with bipyridine ones.*

increasing solvent polarity with a larger effect on fluorescence, as expected for chromophores with a largely neutral ground state ($\rho < 0.1$).

We then apply our two state model as discussed in the sect. 1.1 to calculate linear absorption and fluorescence spectra and TPA spectra. Figures 1.28 (lower panel) shows that the essential state model reproduces well the evolution with the solvent polarity of absorption and fluorescence spectra, confirming the validity of the model and leading to a reliable set of parameters, reported in Table 1.9. The model for **S** derived from the analysis of OPA and fluorescence spectra applies to the calculation of TPA spectra, in Fig. 1.29, leading to very good results without the need to introduce any additional parameter.

The shift of the fluorescence spectra with increasing solvent polarity is reproduced particularly well. Some difficulties in reproducing the absorption experimental spectra occur in cyclohexane: because of the presence of higher energy localized transitions (that are beyond the scope of the two state model), the

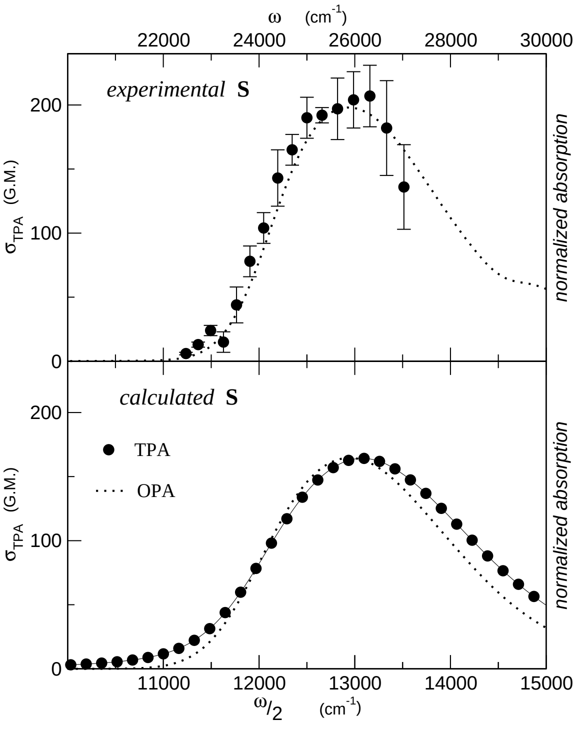

Figure 1.29: *Experimental (top) and calculated (bottom) TPA spectra for molecule* ***S*** *in CH_2Cl_2. Parameter shown in table 1.9 together with bipyridine ones.*

high-energy side of the spectra is different from the experimental one. This results in a distorted vibronic profile.

1.5.2 Interacting dipolar chromophore: bipyridine

An electronic four state model

We model the bipyridine molecule as a pair of N,N- dibutylstylbazole molecules connected by the two pyridine unit, neglecting the π-conjugation in the bipyridinic bond. We follow the bottom-up approach and transfer the information obtained from the analysis of optical spectra of **S** to the description of $\mathbf{S}_2$. The two electronic basis states for each stilbazole chromophore leads to a minimal electronic model for the bipyridine unit accounting for four electronic states, that actually reflect the two independent CT processes in the dimer. Thus the four basis states describe the state where both monomers are in the neutral state $|D\,A\,A\,D\rangle$, the two degenerate states where either one of the two species is zwitterionic, $|D^+A^-A\,D\rangle$ and $|D\,A\,A^-D^+\rangle$, and the state where both species are zwitterionic: $|D^+A^-A^-D^+\rangle$. On this basis, we define two operators that directly measure the degree of CT on each chromophore:

$$\hat{\rho}_1 = \begin{pmatrix} 0 & 0 & 0 & 0 \\ 0 & 1 & 0 & 0 \\ 0 & 0 & 0 & 0 \\ 0 & 0 & 0 & 1 \end{pmatrix} \qquad \hat{\rho}_2 = \begin{pmatrix} 0 & 0 & 0 & 0 \\ 0 & 0 & 0 & 0 \\ 0 & 0 & 1 & 0 \\ 0 & 0 & 0 & 1 \end{pmatrix} \tag{1.29}$$

thus $\langle\rho_1\rangle$ and $\langle\rho_2\rangle$ are the ionicities relevant to the two chromophores. The electronic Hamiltonian is the sum of the two Hamiltonians relevant to each chromophore (eq. 1.1) plus a term accounting for the electrostatic interaction $V\hat{\rho}_1\hat{\rho}_2$:

$$\mathscr{H}_{el} = \begin{pmatrix} 0 & -\tau & -\tau & 0 \\ -\tau & 2z_0 & 0 & -\tau \\ -\tau & 0 & 2z_0 & -\tau \\ 0 & -\tau & -\tau & 4z_0 + V \end{pmatrix} \tag{1.30}$$

V measures the electrostatic interaction energy between the two units, when both of them are in the zwitterionic state (electrostatic interactions involving neutral molecules are negligible).

The dipole moment operator for the bipyridine is defined with reference to the structure shown in figure 1.30, and it is the vector sum of the dipole moments of the two molecular arms. Thus, the electronic dipole has two com-

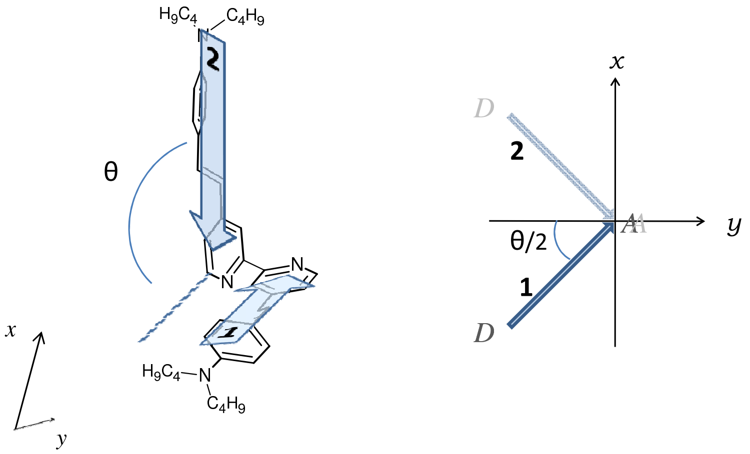

Figure 1.30: *Scheme for the geometrical arrangement of the dipoles in* $\boldsymbol{S}_2$

ponents, along the x and y directions $\hat{\mu} = \hat{\mu}_x \check{i} + \hat{\mu}_y \check{j}$, with

$$\hat{\mu}_x = \mu_0 \sin\left(\frac{\theta}{2}\right)(\hat{\rho}_1 - \hat{\rho}_2) \qquad \hat{\mu}_y = \mu_0 \cos\left(\frac{\theta}{2}\right)(\hat{\rho}_1 + \hat{\rho}_2) \tag{1.31}$$

Geometrical arrangement and strength of the interaction

We first analyse the role played by the geometry (i.e. the θ angle in fig. 1.30) and by the extent of the interaction (i.e. the magnitude of V). To start with let us consider the electronic problem, neglecting vibration and solvation coordinates. The diagonalization of eq. 1.30 leads to four eigenstates. The lowest energy eigenstate is the ground state g, then one expects a pair of excited states e_1 and e_2 corresponding to states where only one molecular arm is excited (one-exciton states) and, finally, the highest energy state describes the systems where both molecules are excited (two-exciton state). The two one-exciton states are obviously degenerate in the non-interacting ($V = 0$) system. When the two chromophore interact the two states split. This is the main effect of the parameter V, as can be seen in fig. 1.31.

The interaction identified as electrostatic is repulsive ($V > 0$), so that the *in-phase* combination of the two one-excitation states is higher in energy than the *out-of-phase* combination. The angle θ affects relative intensities of the OPA and TPA processes, shown in figure 1.32. In particular: varying the angle θ we can distribute the intensity on the lower or on the higher energy transition of the exciton pair. In the “cisoid” conformation ($\theta \approx 0$) only the *in-phase* one photon

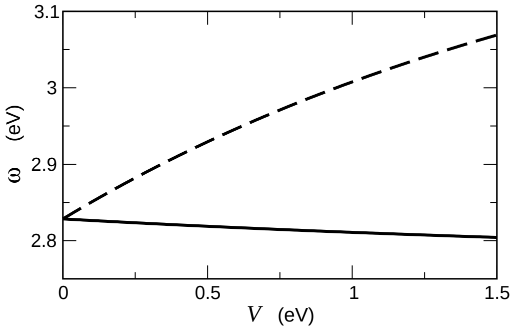

Figure 1.31: *The effect of the interaction parameter V on the first two excitation energies. Dashed line: lower energy transition $g \rightarrow e_1$. Cont. line: higher energy transition $g \rightarrow e_2$. Results refer to the electronic Hamiltonian in eq. 1.30 with $z_0 = \tau = 1$ eV*

excitation is optically active, i.e. the oscillator strength concentrates on the high energy state. In the "transoid" conformation ($\theta \approx 180$) the lowest energy transition is instead optically active. At intermediate angles both transitions are active.

The TPA process is a third order phenomenon and exhibits different symmetry rules. The lower energy state is not TPA-active for $\theta \approx 0$ or $\theta \approx 180$, while the higher energy state has maximum TPA intensities in these limits. The total OPA intensity is essentially V independent in this model, while increasing of V leads to a moderate increase of σ_{TPA} at large angles. This basic concepts are important to rationalize experimental data.

Vibrational and solvent degrees of freedom

We introduce two independent coordinates q_1 and q_2 relevant to the two chromophores, with momentum p_1 and p_2.The total Hamiltonian reads $\mathscr{H} = \mathscr{H}_{el} + \mathscr{H}_{ph} + \mathscr{H}_{e-ph}$, where $\mathscr{H}_{el}$ is the electronic Hamiltonian in eq. 1.30, and $\mathscr{H}_{ph}$ and $\mathscr{H}_{e-ph}$ are the vibrational Hamiltonians and the electron-molecular vibration coupling Hamiltonians:

$$\mathscr{H}_{ph} = \frac{1}{2}{\omega_v}^2\left(\hat{q_1}^2 + \hat{p_1}^2 + \hat{q_2}^2 + \hat{p_2}^2\right) \tag{1.32}$$

$$\mathscr{H}_{e-ph} = -g\sqrt{2\omega_v}\left(\hat{q_1}\hat{\rho}_1 + \hat{q_2}\hat{\rho}_2\right) \tag{1.33}$$

where ε_v is the vibrational relaxation energy (as defined in sect. 1.1) and $g = \sqrt{\omega_v \varepsilon_v}$. In the occupation number approach the effective coupled molecular

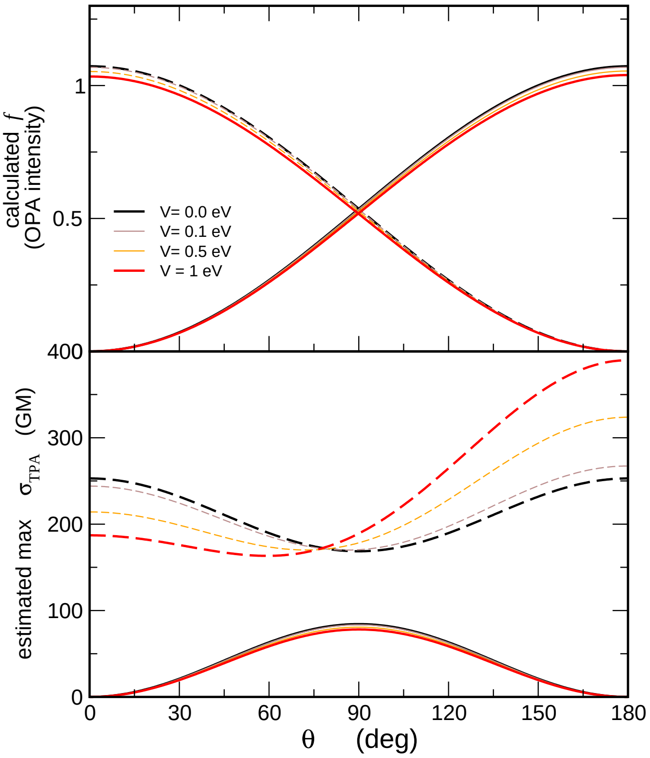

Figure 1.32: *The effect of the geometry and of the strength of the interaction on the OPA (upper panel) and TPA (lower panel) intensities for one-exciton states. Dashed line: lower energy transition $g \rightarrow e_1$. Cont. line: higher energy transition $g \rightarrow e_2$ This refers to pure electronic problem ($\varepsilon_{or} = 0$ and $\varepsilon_v = 0$) with $z_0 = \tau = 1eV$, $\mu_0 = 20D$. Effective width was introduced to estimate the cross section: Γ_{eff}=0.16 eV .*

vibrations then read:

$$\mathscr{H}_{ph} + \mathscr{H}_{e-ph} = \sum_{j=1,2} \omega \left(\hat{a}_j \hat{a}_j^\dagger + \frac{1}{2} \right) - g \left(\hat{a}_j^\dagger + \hat{a}_j \right) \hat{\rho}_j \tag{1.34}$$

We consider two independent reaction fields, each one responding to the dipole moment on each molecular arm: $\hat{\mu}_1 = \mu_0 \hat{\rho}_1$ and $\hat{\mu}_2 = \mu_0 \hat{\rho}_2$. Thus two independent solvation coordinates are defined f_1 and f_2, and the solvation Hamiltonian is:

$$\mathscr{H}_s = -f_1 \hat{\rho}_1 - f_2 \hat{\rho}_2 + \frac{1}{4\varepsilon_{or}} \left({f_1}^2 + {f_2}^2 \right) \tag{1.35}$$

The f_1 and f_2 coordinates are treated as classical coordinates and the total Hamiltonian $\mathscr{H} = \mathscr{H}_{el} + \mathscr{H}_{ph} + \mathscr{H}_{e-ph} + \mathscr{H}_s$ is defined on a two-dimensional grid of f_1 and f_2 values. On each point of the grid the Hamiltonian $\mathscr{H}(f_1, f_2)$ describing the coupled electronic and vibrational problem is diagonalized on the non-adiabatic basis. Spectra are calculated following the procedures in appendix B.

It is interesting to notice that the PES associated with the emitting state has a double minima structure in the (f_1, f_2) plane, and then the related Boltzmann distribution has two peaks, in correspondence of the two indistinguishable minima $(f_{eq1,e}, f_{eq2,e})$ and $(f_{eq2,e}, f_{eq1,e})$, where $f_{eqi,e} = 2\varepsilon_{or} \langle \rho_i \rangle_e$ is the equilibrium value for the effective solvent coordinate in the i-th arm cavity and e is the emitting state. In other terms, the solvent degrees of freedom induce symmetry breaking, localizing the excitation in one of the two arms. Absorption goes towards a delocalized exciton state, but fluorescence comes from a state where the excitation is localized on a single arm.

1.5.3 Optical spectra for bipyridine along bottom-up modelling

The experimental absorption and fluorescence spectra of the $\mathbf{S}_2$ in four solvents are shown in fig. 1.33 (top panel), and spectral data are collected in table 1.10. Compared to **S**, $\mathbf{S}_2$ spectra are redshifted, but the solvatochromic behaviour and bandshapes are very similar. In the calculation of the spectra all parameters relevant to the chromophoric unit are transferred from the model for **S** developed above, with the only exception of z_0, the energy difference between $|D^+A^-\rangle$ and $|DA\rangle$ that is expected to decrease in the bichromophoric specie because of the increase of the strength of the acceptor group (effect of second pyridinic group as substituent attached). Therefore the spectra are calculated tuning z_0, V and

Table 1.9: *Model parameters for **S** and for **S**$_2$.*

molecular parameter	**S**	**S**$_2$
z_0/eV	1.35	1.28
τ/eV	1.07	
μ_0/D	23.5	
ε_v/eV	0.38	
ω_v/eV	0.18	
Γ/eV	0.075	
V / eV		0.3
θ / deg.		180
solvent parameter	**S**	**S**$_2$
ε_{or}/eV cyclohexane	0.05	
toluene	0.23	
dichloromethane	0.48	
DMSO	0.69	

Table 1.10: *Experimental data for **S**$_2$ in cyclohexane, toluene, dichloromethane and DMSO.*

solvents	λ_{abs}/nm (ϵ/M^{-1}cm^{-1}) *osc. strength f*	λ_{fluo}/nm (FQY %)^b	λ_{TPA}/nm (σ_2/GM)
cyclohexane	396 [0-0] 379 [0-1]	431 [0-0] 408 [0-1]	
toluene	395	446	
dichloromethane	400 (67500 ± 7700) *1.40*	497 (7.9 ± 0.2)	800 (370 ± 50)
DMSO	407	527	

^{b}standards same as reported in table 1.8

θ, while keeping all other model parameters fixed to the values obtained from the essential state analysis of optical spectra of **S**.

The top panel of figure 1.33 shows the OPA and fluorescence spectra of $\mathbf{S}_2$ calculated in four solvents. The spectra are red shifted compared to **S**. This has two concurrent origins: (*a*) the increase of the acceptor strength; (*b*) the interaction between chromophore. Calculated OPA and fluorescence spectra in Figure 1.33 (bottom panel) reproduce very well experimental data. The fluorescence bandshapes, including the loss of vibrational structure going in polar solvent is nicely reproduced.

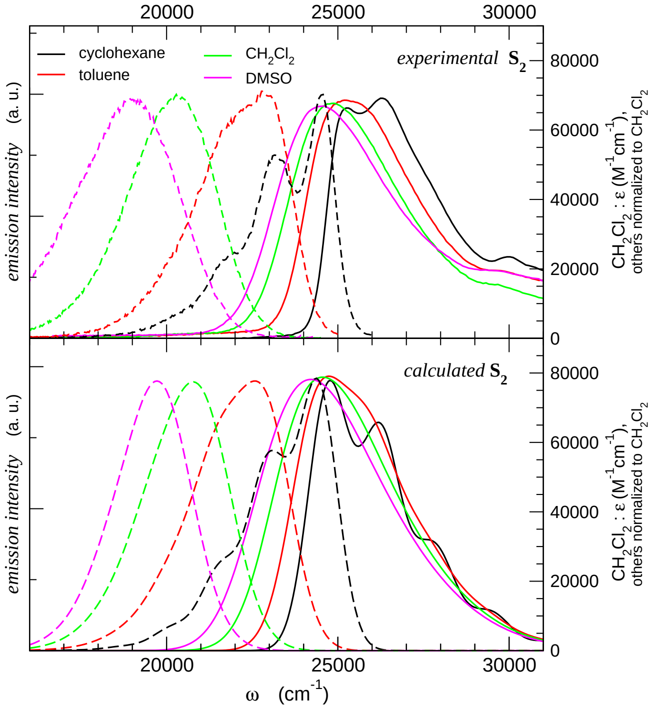

Figure 1.33: *Experimental (top) and calculated (bottom) spectra for* $\mathbf{S}_2$ *in different solvents. Parameters from table 1.9, with* $\varepsilon_{or} = 0.48$ *eV, as relevant to* CH_2Cl_2*.*

Lower panel of figure 1.34 shown the calculated TPA spectrum of $\mathbf{S}_2$ in CH_2Cl_2 together with the calculated TPA spectrum of the monomer **S** in the same solvent. Experimental TPA spectra of **S** and $\mathbf{S}_2$ are reported for comparison in the upper panel. Calculated TPA cross section of $\mathbf{S}_2$ perfectly agree with the experimental result, and the increase in σ_{TPA} going from the monomer to the bichromophore is correctly reproduced.

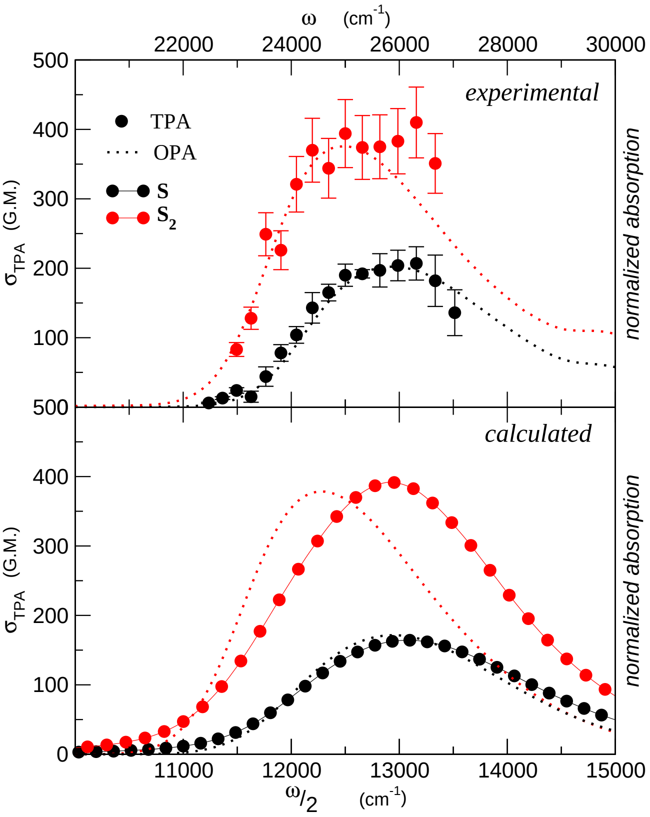

Figure 1.34: *Experimental (top) and calculated (bottom) TPA spectra for **S** (red) and* $\boldsymbol{S}_2$ *(black) in dichloromethane. Spectra are calculated with parameters listed in the table 1.9. Normalized OPA (experimental and calculated) is also shown for comparison (dotted lines).*

Excitation pair in S_2: splitting and relative intensities

For reasonable V values, the splitting between the two exciton states is very small and calculated spectra show a minor θ-dependence. In figure 1.35 calculated linear and non linear spectra are shown for different θ values; the parameter are the one for $\mathbf{S}_2$ in dichloromethane, as listed in table 1.9. For θ going from 180° to 0° the OPA band moves to the blue by $\sim$ 1000 cm^{-1}, and the intensity of both OPA and TPA decreases by a factor ~0.8 and ~0.9, respectively (the increase in the OPA only concern the maximum of the extinction molar coefficient, while the total oscillator remains constant). Because the splitting is not really appreciable in any experimental OPA spectra it is difficult to extract reliable θ values from the comparison with absorption experimental data.

For **S** OPA and TPA frequency always coincide, but apparently this does not occur for $\mathbf{S}_2$ (see top panel of fig 1.34). The blueshift of the experimental TPA maximum with respect to the OPA suggests $\theta \approx 180°$. Unfortunately, the observed blueshift is very small (comparable with experimental uncertainties), and cannot be taken as a strong proof of $\theta = 180°$. However, the transoid conformation is also supported by the large FQY measured for $\mathbf{S}_2$, which is not compatible with $\theta \sim 0°$, where the lowest energy excitation would be optically forbidden, leading to a non fluorescent specie. On the other hand $\theta \sim 180$ °, i. e. a transoid configuration, is also supported by chemical intuition, based on the structures found for bipyridine in solid state [58, 59], as well as by the theoretical calculation discussed in sect. 1.5.4). We then assume $\theta = 180$ in the description of $\mathbf{S}_2$.

1.5.4 Ab initio and TDDFT calculated absorption and TPA properties

In collaboration with the group of professor Ferrante (Padova University), our essential state results have been compared with results from ab initio and TDDFT calculations [57]. Calculation were run on the dimethylamino derivative, instead of the n-buthylamino group. The ground state geometries and excitation energies of **S** and $\mathbf{S}_2$ are investigated through ab-initio quantum-chemical calculations (HF, 6-311G(d,p) as basis set) both in vacuum and in CH_2Cl_2, using PCM model to take in account for solvent effect. Excited state energies and transition dipole moments were calculated in the CIS approach, while only for the excitations from ground state (the ones relevant for the absorption) TDDFT was also used.

The results for **S** are similar for vacuum and CH_2Cl_2 calculation, and the

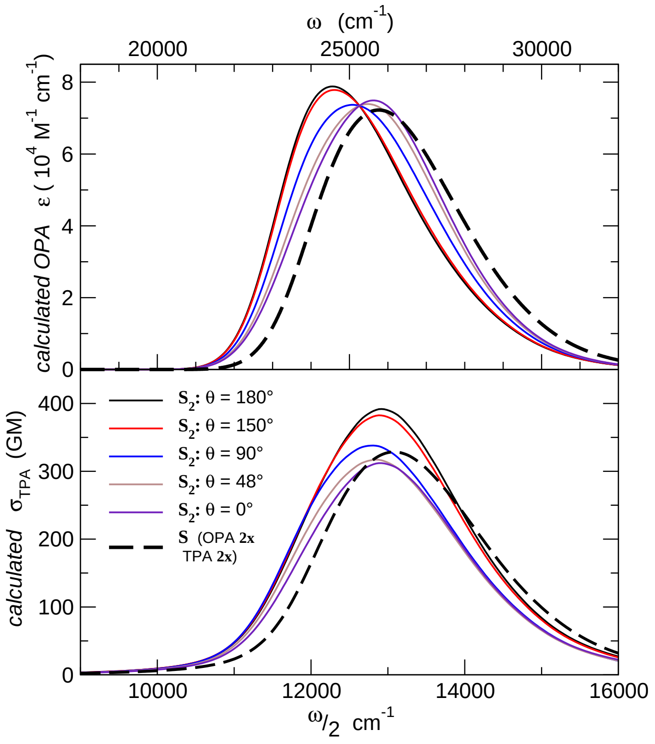

Figure 1.35: *Calculated OPA(top) and TPA (bottom) spectra for molecule* $\boldsymbol{S}_2$ *at different* θ *values (for comparison the results in* $\boldsymbol{S}$ *is also shown, dashed line). Parameters are the one for dichloromethane shown in table 1.9*

Table 1.11: *Calculated OPA and TPA for* $\boldsymbol{S}$ *and* $\boldsymbol{S}_2$ *in dichloromethane [57].* f *is here the calculated oscillator strength.*

		OPA		TPA
	excitation	CIS	TDDFT	CIS
		λ_{abs}/nm $(f)^a$	λ_{abs}/nm $(f)^a$	λ_{TPA}/nm (σ /G.M.)
S	$g \rightarrow e$	264 *(1.28)*	364 *(0.86)*	264 (43)
S_2 dd	$g \rightarrow e_1$	271 *(2.78)*	380 *(1.95)*	271 (0.4)
	$g \rightarrow e_2$	266 *(0.004)*	370 *(0.0004)*	266 (88)
S_2 du	$g \rightarrow e_1$	272 *(1.00)*	376 *(0.79)*	272 (8.4)
	$g \rightarrow e_2$	266 *(1.70)*	367 *(0.77)*	266 (13)

electronic densities involved in the HOMO-LUMO transition (responsible in **S** for the lowest energy transition with a 81% contribution), confirm a CT process from the donor amino to the acceptor (pyridine) group. Geometry optimization for $\mathbf{S}_2$ must account for the possible rotation around the single C – C bond connecting the two arms. The global minimum is observed at a dihedral angle of 180° (called **dd** conformation), and a shallow relative minimum at 48° is also found (called **du**) at 0.17 eV higher in energy, so that only the former transoid conformation is appreciably populated at room temperature.

The HOMO/HOMO-1 and LUMO/LUMO+1 pairs are quasi-degenerate, and the former pair show similar electronic densities as the HOMO of **S**. HOMO and HOMO-1 are confined in the two arms of the dimer. On the opposite, LUMO and LUMO+1 are somewhat delocalized on the whole molecule with a concentration of electron density on the central bipyridine group, which acts as an electron-acceptor for both arms.

The first excited state transition of **S** gives rise in $\mathbf{S}_2$ to two almost degenerate transitions for both conformations of dimer. These transitions are dominated by contributions from the HOMO → LUMO+1 (42%) and from the HOMO-1 → LUMO (30%) (**dd**). All the results are listed in the table 1.11 TD-DFT and CIS methods correctly predict that **S** shows only one low energy electronic state with a strong charge transfer character, whereas $\mathbf{S}_2$ in both **dd** and **du** conformations, possesses two electronic states with similar energies. Both methods agree with the experiment suggesting a red shift (approximately 1000 cm^{-1}) of the first excitation in going from **S** to $\mathbf{S}_2$. The calculations confirm our excitonic prediction about the intensity distribution between the first two excited states. In particular, the ab-initio calculations predict a small energy difference between the two states (in the range 600–800 cm^{-1}), difficult to detect experimentally.

CIS method overestimates excitation energies for both molecules, whereas TDDFT leads to better results. The theoretical ratio of the oscillator strengths between dimer and monomer for both CIS and TDDFT is in agreement with the experimental results. CIS was also used to calculate the TPA spectrum: the absolute value of the TPA cross sections predicted by the CIS calculations is four time smaller than the corresponding experimental value. Anyway, the estimated ratio of the TPA cross section in $\mathbf{S}_2$ with respect to **S** confirms the idea that the dominant conformation is the one with $\theta = 180°$. Finally the numerical simulation correctly predicts the red shift of the absorption maxima with increasing solvent polarity.

1.5.5 Bottom up essential state modelling and ab initio results in calculating spectral properties and to understand the role of the interaction

The bottom-up approach makes direct use of the parameters determined from the analysis of optical spectra of the single molecular unit and then requires just the addition of a few parameters to describe interaction between the two units. The agreement with experimental spectra is particularly striking in view of the reduced number of adjustable model parameters required to describe in a unique and coherent picture linear and non-linear optical spectra of **S** and **S**$_2$ accounting not only for their intensity and frequency, but also for the band-shape, and solvation effects. The redshift of **S**$_2$ spectra can have different origins: it may be due to the delocalization among the two **S**-moieties that form the dimer through the bipyridine bridge, a phenomenon accounted for in the essential state model by a decreased z_0, to efficiently describe the increased acceptor strength of the pyridinic ring. Moreover it can results from the electrostatic interaction between the two chromophores leading to an exciton splitting and a red-shift of the lowest energy excitation. The electron density calculation suggests that some amount of delocalization contributes to the red shift. The explicit inclusion of the delocalization in the essential state model would lead to a six-state electronic Hamiltonian that could be easily dealt with from a computational perspective. However the resulting model would require the introduction of several additional microscopic parameters, whose quantitative definition is problematic in the lack of additional experimental data.

The absolute values for the TPA cross sections estimated by the essential state model agree very well with the experimental results. The essential state model does not predict major variations of the TPA cross section for **S**$_2$ as a function of θ between the two **S**-moieties, in contrast to the CIS method that has predicts a large reduction of the TPA intensity going from the **dd** conformation (corresponding to θ =180°) to the **du** conformation (θ =48°). The two-photon absorption frequencies and cross sections are calculated only with the CIS method and, the quantitative determination of the TPA cross section is poor. This is perhaps the worst results, and confirms the fact that conventional ab-initio approach usually fail in accurately describing high order non-linear responses. Anyway, calculations still capture the TPA trend from the monomer to the dimer. In these respect the essential state model gives a more refined tool for the description of the OPA and TPA properties of dimer, starting form the experimental knowledge of the OPA and fluorescence of monomer in solvent with different polarity, and accounting for excitonic interactions among the single molecular units.

The essential state model does a fair job in reproducing both qualitatively and quantitatively the OPA and TPA features for both compounds, and delivers a tool that allows the prediction of the OPA and TPA properties of multichromophores. The two different theoretical strategies can be seen as complementary, since numerical simulations can provide useful information on the molecular structure, that are then used in the choice of some parameters (vibrational or conformational degrees of freedom) used by the essential state model.

1.6 Dipolar DA fluorenes and related spirobifluorenes: bichromophores beyond the electrostatic interactions

In this section we discuss optical properties of a series of fluorene substituited on one side with the strong acceptor NO_2 and on the other side with a donor group (structures **1a** to **5a** in fig. 1.36) and the corresponding spirobifluorene derivatives (structures **1** to **5** in fig. 1.36).

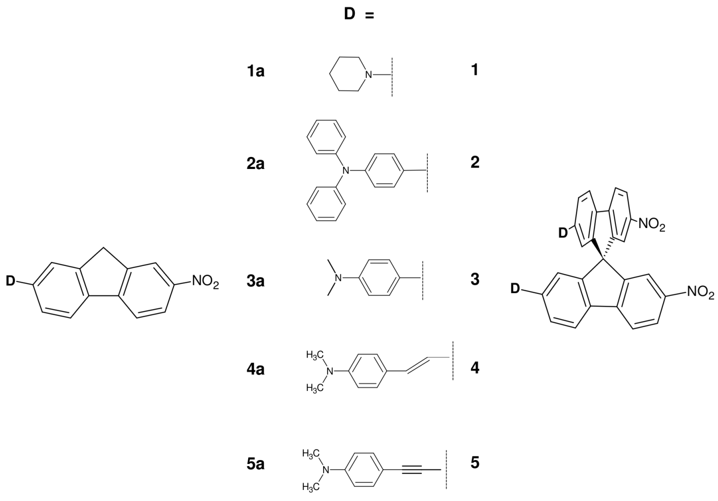

Figure 1.36: *Studied DA Fluorene molecules* ***na*** *(left) and related spirobifluorene* ***n*** *(right).*

Spirobifluorenes have been object of interest since date, in virtue of the peculiar interaction between the two perpendicularly oriented extended π systems connected by the sp^3 C (or Si) atom of the spiro-linkage. [60, 61]. The two molecular units couple, as a results of the electrostatic and exchange interactions, like the overlap between π orbitals of the two connected unit (*spiroconjugation*).

In all cases an important role is played by symmetry. In particular, in highly symmetric systems both electrostatic and exchange contributions to the interaction vanish and the only important interaction rises by vibronic Herberg-Teller coupling [62]. In asymmetric systems inter-unit charge tranfer has been suggested to explain the photophysical properties [63, 64]. Optical properties have been commonly studied to investigate the physics of spiroconjugation and to understand the excited states behaviour [65]. The interaction has been suggested as a source of amplification of non-linear optical properties [66].

This work has been done in collaboration with Dr. Quici (CNR of Milan). Quici group is responsible for the synthesis of the five pairs of molecules, in fig. 1.36 [67].

Here we present experimental optical spectra of these systems and their rationalization in terms of bottom up modeling approach that suggests a possible interpretation of the spiro-interaction. We will refer to the fluorene molecules with ***n*a** and to the spirobifluorene molecules as ***n*** (see fig. 1.36). All throught the section we also refer to the fluorene – spirobifluorene pair labeling the number follow by a star, for istance **1*** will refer to both **1a** and **1**.

1.6.1 Experimental optical properties

For all the molecules in fig. 1.36 absorption and fluorescence spectra were collected in different solvents, and two chosen pairs **1*** and **4*** were investigated in more detail, collecting fluorescence anisotropy spectra in frozen solvents. All compounds are stable in solution. Solubility is generally good, especially in chlorinated solvents, while reduced solubility is observed for **3***, **4*** and **5*** in apolar solvent.

Figure 1.37 and 1.38 show the spectroscopic behaviour of the five pairs **1*** to **5*** in ciclohexane and in CH_2Cl_2, respectively. For **1*** and **4*** the molar extinction coefficients were measured in toluene. Quantitative spectra for **1*** and **4*** are reported in fig. 1.39 and summarized in table 1.12. Spectra in other solvents (decaline, chloroform, 2-MeTHF) can be found in the upper panels of fig. 1.43 and 1.44, for compounds **1a** and **1** respectively, and in the upper panels of fig. 1.45 and 1.46, for compounds **4a** and **4**. The fluorescence quantum yield has been measured in different solvents and the results are summarized in table 1.13.

All compounds exhibit normal solvatocrhomism with absorption and fluorescence bands red shifting upon increasing solvent polarity. The vibronic structure of the CT absorption is unresolved in all solvents. The fluorescence is generally intense in non-polar solvents (see fluorescence quantum yields in tab. 1.13), but it is absent or very weak in polar solvents (in CH_2Cl_2at room T **1*** is the only detectable fluorescences). The Stoke shift is large even in apolar solvent, and no overlap is found between the 0–0 transitions in absorption and fluorescence. The molar extinction coefficient doubles going from the fluorene compound to the corresponding spirobifluorene.

Going from the fluorene ***na*** to the spirobifluorene ***n*** compound both absorption and fluorescence bands redshift. In particular, two limit cases are observed: the pair **4*** and **5*** show a shift of about 1000 cm^{-1}, while in **1*** the shift from **1a** to **1** is negligible. The pairs **1*** and **4***, representing the lower and the upper limit of the observed shift were chosen for a more detailed spectroscopic study.

Table 1.12: *Experimental data for absorption of **1*** and **4***in some solvents and molar extinction coefficient in toluene.*

solvents	λ_{abs}/nm ($\epsilon/M^{-1}cm^{-1}$)			
	1a	**1**	**4a**	**4**
ciclohexane	392	395	414	428
toluene	408 (20400)	411 (39400)	427 (32300)	436 (64600)
CH_2Cl_2	419	422	428	437

Table 1.13: *Experimental fluorescence data and fluorescence quantum yield in some solvent.*

solvents	λ_{em}/nm *(FQY)*			
	1a	**1**	**4a**	**4**
cyclohexane	454 [0-0] 479 [0-1] *(0.03)*	453 [0-0] 478 [0-1] *(0.02)*	474 [0-0] 506 [0-1] *(0.70)*	484 [0-0] 516 [0-1] *(0.62)*
toluene	547 *(0.65)*	536 *(0.09)*	599 *(0.45)*	612 *(0.27)*
CH_2Cl_2	683 *(<0.01)*	$\sim$ 667 *(0.06)*		

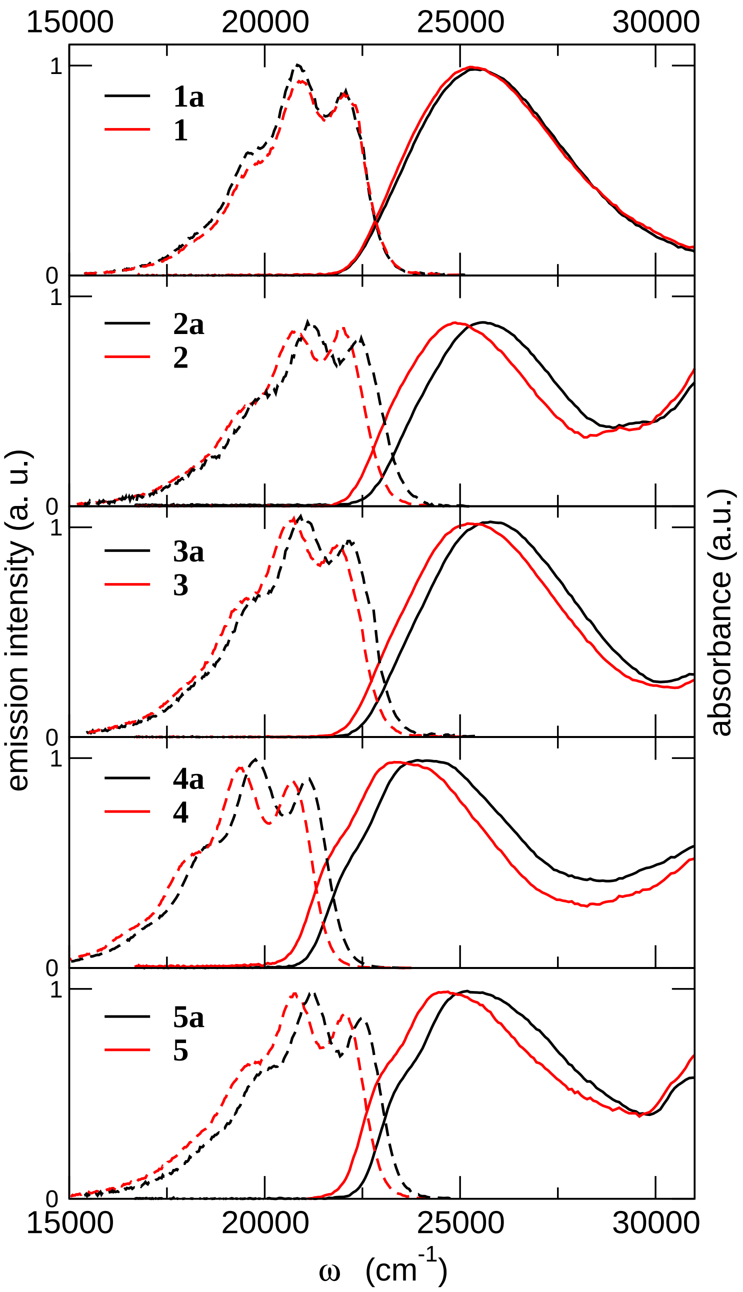

Figure 1.37: *Absorption spectra (cont. lines) and fluorescence spectra (dashed lines) of* ***na*** *(black line) and* ***n*** *(red lines) in cyclohexane.*

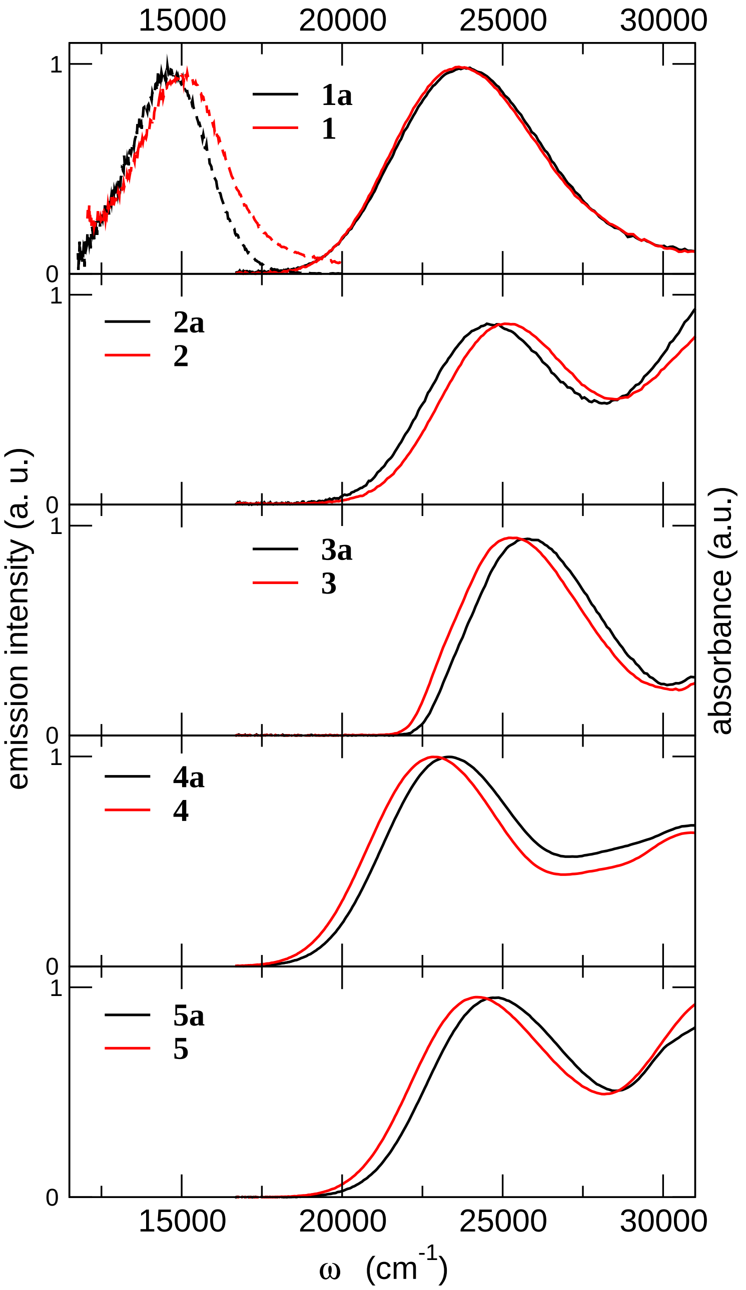

Figure 1.38: *Absorption spectra (cont. lines) and fluorescence spectra (dashed lines) of* **na** *(black line) and* **n** *(red lines) in* CH_2Cl_2. *Measurement of fluorescence were only possible in the pair* ***1****, *being very weak for the other compounds.*

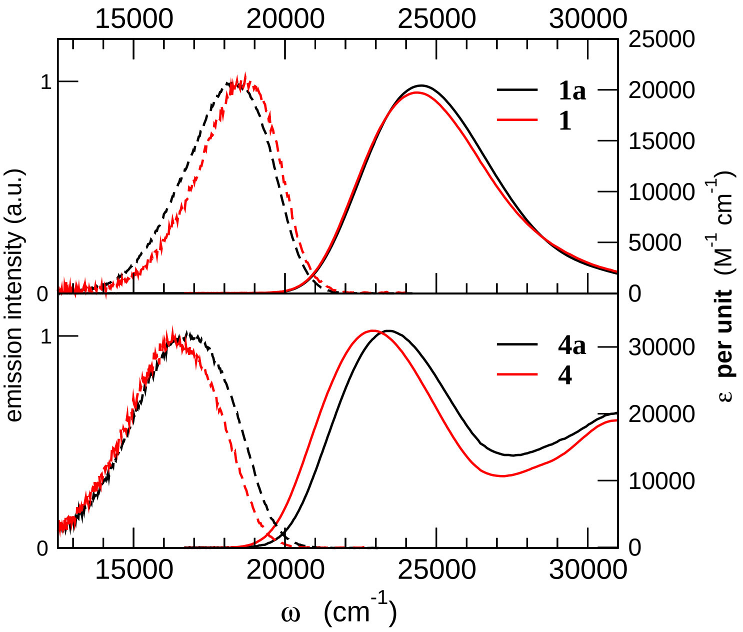

Figure 1.39: *Quantitative absorption spectra (cont. lines) and normalized fluorescence spectra (dashed lines) of* ***1a*** *and* ***4a*** *(black line, upper and lower panels respectively) and* ***1*** *and* ***4*** *(red lines, upper and lower panels respectively) in toluene.*

1.6.2 Modeling fluorenes and spirobifluorenes: a bottom-up approach

The fluorene monomers are regular *DA* chromophores and the two-state model, presented in sect. 1.1, is expected to work for these dyes. However, experimental data show a large Stokes shift also in non polar solvents as well as in frozen solvents (see below). The model presented in sect 1.1, predict vanishing Stokes shift in non-polar solvent as well as in frozen solvents. The large Stokes shift observed for the *DA* chromophores in fig. 1.36 can be ascribed to the presence of slow degrees of freedom, related to some low-frequency internal conformational modes. This is consistent with the observation of unresolved absorption bands in apolar solvent, in spite of well resolved fluorescence spectra [33].

Two state review: adding a conformational broadening

The internal mode can be modeled in principle as a classical slow coordinate [33], as done for the solvent degrees of freedom. We assume that this conformational mode tunes the effective overlap between the occupied orbital(s) localized on the donor group and the unoccupied orbital(s) localized mainly on the acceptor group. In the two state model this corresponds to assume that the coupling with this low degree of freedom modulates the τ, the hopping element from the donor to the acceptor. This is described by a classical coordinate u, with relaxation energy ε_{int}. The relevant term in the hamiltonian reads:

$$\mathscr{H}_{int} = -u\hat{\sigma} + \frac{1}{4\varepsilon_{int}}u^2 \tag{1.36}$$

where $\hat{\sigma}$ is the operator defined in eq. 1.2. The total hamiltonian now depends on *two* slow coordinates, and it can be written as:

$$\begin{aligned}\mathscr{H}(f,u) &= \mathscr{H}_{el} + \mathscr{H}_{ph} + \mathscr{H}_{e-ph} \\ &\quad + \mathscr{H}_{solv}(f) + \mathscr{H}_{int}(u) \\ &= \mathscr{H}_{el} + \mathscr{H}_{ph} + \mathscr{H}_{e-ph} \\ &\quad - f\hat{\rho} + \frac{1}{4\varepsilon_{or}}f^2 - u\hat{\sigma} + \frac{1}{4\varepsilon_{int}}u^2 \end{aligned} \tag{1.37}$$

where $\mathscr{H}_{el}$, $\mathscr{H}_{ph}$, $\mathscr{H}_{e-ph}$ have been defined in the sect. 1.1. The hamiltonian 1.37 is diagonalized on the (f,u) grid. The spectra calculated in each point of the grid are then summed up weighting for the relevant Boltzmann probability, following the procedure described in appendix C.

A minimal electronic model for spirobifluorenes

In the bottom up modeling approach to spirobifluorenes we neglect any CT process between the two fluorene moieties so that the electronic model is defined on the basis of four states, direct product of the two states relevant to each fluorene unit:

$$\begin{array}{rlllll} |N\rangle = & | \; D & A & D & A & \rangle \\ |Z_1\rangle = & | \; D^+ & A^- & D & A & \rangle \\ |Z_2\rangle = & | \; D & A & D^+ & A^- & \rangle \\ |W\rangle = & | \; D^+ & A^- & D^+ & A^- & \rangle \end{array}$$

Coherently with the two state model, the energy of the degenerate basis states $|Z_1\rangle$ and $|Z_2\rangle$ is $2z_0$, while $|W\rangle$ has energy $4z_0 + V$, where V measures the interaction between the chromophore in the zwitterionic state.

It is convenient to define the following operators on the chosen basis:

$$\hat{\rho}_1 = \begin{pmatrix} 0 & 0 & 0 & 0 \\ 0 & 1 & 0 & 0 \\ 0 & 0 & 0 & 0 \\ 0 & 0 & 0 & 1 \end{pmatrix} \qquad \hat{\rho}_2 = \begin{pmatrix} 0 & 0 & 0 & 0 \\ 0 & 0 & 0 & 0 \\ 0 & 0 & 1 & 0 \\ 0 & 0 & 0 & 1 \end{pmatrix} \tag{1.38}$$

$$\hat{\delta}_1 = \begin{pmatrix} 0 & 1 & 0 & 0 \\ 1 & 0 & 0 & 0 \\ 0 & 0 & 0 & 1 \\ 0 & 0 & 1 & 0 \end{pmatrix} \qquad \hat{\delta}_2 = \begin{pmatrix} 0 & 0 & 1 & 0 \\ 0 & 0 & 0 & 1 \\ 1 & 0 & 0 & 0 \\ 0 & 1 & 0 & 0 \end{pmatrix} \tag{1.39}$$

The operator $\hat{\delta}_1$ and $\hat{\delta}_2$ correspond to the two state off-diagonal operator $\hat{\sigma}$, rewritten on the bichromophoric basis. In close analogy with the two state model the expectation value of $\hat{\rho}_1$ and $\hat{\rho}_2$ represent the degree of charge transferred in the chromophore 1 and 2. The electronic hamiltonian then read

$$\mathscr{H}_{el} = 2z_0(\hat{\rho}_1 + \hat{\rho}_2) - \tau(\hat{\delta}_1 + \hat{\delta}_2) + \hat{\rho}_1\hat{\rho}_2 V \tag{1.40}$$

In spirobifluorene the relative orientations of the two chromophoric unit is locked, so that the two chromophores are exactly perpendicular and aligned according to the x and y axis of a reference frame, as sketched in fig. 1.40.

The dipole moment operator is the vectorial sum of the dipole moment operators relevant to the two fluorene units. According to fig. 1.40 the dipole moment operator has then two components:

$$\hat{\mu}_x = \mu_0\hat{\rho}_1 \qquad \hat{\mu}_y = \mu_0\hat{\rho}_2 \tag{1.41}$$

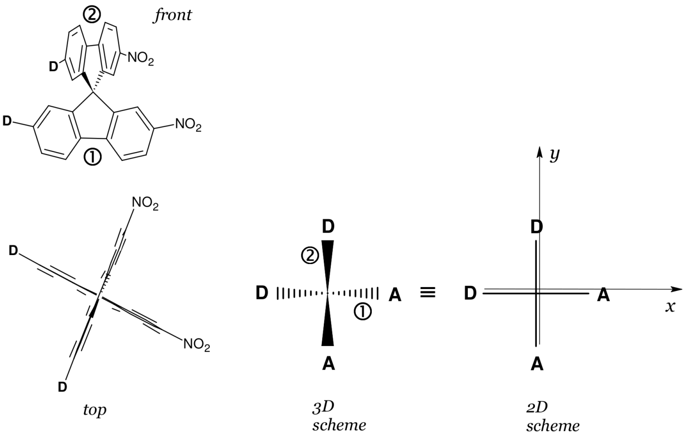

Figure 1.40: *Scheme of the spirobifluorene molecular structure and the relevant description for the four state model.*

Spiroconjugation: from six state model to four state model with negative V

According to the essential state model the V interaction should describe classical electrostatic interchromophore interactions. If we assume the geometrical setting of figure 1.40 and we locate the charges $(+1)$ on the center of the donor and (-1) on the center of the acceptor groups, it is easy to find that $V = 0$ by simmetry. However, the two chromophores are not strictly linked in corrispondence of their charge centroids, and a geometrical parameter accounting for this asymmetry can be introduced according to the scheme on the right in figure 1.41. With this generalization the electrostatic energy results (atomic unit):

$$V = \frac{1}{r_0}\left(\frac{1}{\sqrt{2}\alpha_D} + \frac{1}{\sqrt{2}\alpha_A} - \frac{2}{\sqrt{\alpha_A^2 + \alpha_D^2}}\right) \tag{1.42}$$

where α_A and α_D are the fraction of the chromophore length on the side of the acceptor, and on the side of the donor, respectively. Obviously $\alpha_A + \alpha_D = 1$, and the V from eq. 1.42 is always positive. Calculated $V(\alpha)$ values are shown in fig. 1.41.

The prediction $V > 0$ contradicts the experimental observation of a red shift of optical spectra when going from the fluorene to the spirobifluorene compounds. In fact, in a spirobifluorene frame the two one-exciton states are both

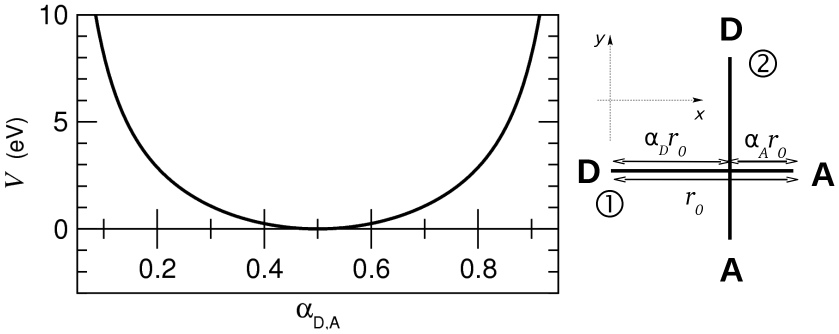

Figure 1.41: *Left: calculated electrostatic interaction* $V(\alpha_D)$ *(or equivalently* $V(\alpha_A)$*) with the expression in eq. 1.42 setting the DA distace* $r_0 = 10$ *Å.* α_D *and* α_A *are chosen according to the scheme on the right.*

OPA allowed with the same intensity, with no appreciable excitonic splitting for reasonable V value. Therefore, since $V > 0$ produces effects similar to those discussed in 1.5.2 (see fig. 1.31), it will never results in a redshift of the average of the two one-exciton transitions in the bichromophoric unit. This suggests that some delocalization and electronic exchange effects contribute in stabilizing the spiro-derivative. Setting up a complete model accounting for conjugation effect between the fluorene units is certainly possible, but the resulting model would require a very large number of model parameters, whose precise definition becomes arbitrary. At the same time, the similarity of ***na*** and ***n*** spectra suggests that delocalization effects are minor, and an increase of model complexity and parameters is not actually justified by experimental data. We therefore stick on the four-state model but with an effective V that implicitely accounts for both electrostatic and delocalization effects.

To support this concept we shortly introduce a six-state electronic model that explicitely account for delocalization, and check if a negative V (as to include delocalization effects) in a four-state model, produces similar results. For the six- state model we assume that two more electronic basis states appear, related to the possible hopping of electrons between the donors (associated to an hopping term $-t_D$) or between the acceptors ($-t_A$), belonging to the two different arms. The electronic basis state then are:

$$\begin{array}{rlllll} |N\rangle = & | \; D & A & D & A & \rangle \\ |Z_1\rangle = & | \; D^+ & A^- & D & A & \rangle \\ |Z_2\rangle = & | \; D & A & D^+ & A^- & \rangle \\ |W\rangle = & | \; D^+ & A^- & D^+ & A^- & \rangle \\ |Y_1\rangle = & | \; D^+ & A & D & A^- & \rangle \\ |Y_2\rangle = & | \; D & A^- & D^+ & A & \rangle \end{array}$$

we can assume that this two “crossed” CT states $|Y_1\rangle$ and $|Y_2\rangle$ are located at an energy $2z_0 + U$, where U accounts for the different energies of the normal and crossed CT state. On the basis of chemical intuition we expect $U > 0$. The relevant hamiltonian for the six-state model is:

$$\mathscr{H}_{el} = \begin{pmatrix} 0 & -\tau & -\tau & 0 & 0 & 0 \\ -\tau & 2z_0 & 0 & -\tau & -t_A & -t_D \\ -\tau & 0 & 2z_0 & -\tau & -t_D & -t_A \\ 0 & -\tau & -\tau & 4z_0 + V & 0 & 0 \\ 0 & -t_A & -t_D & 0 & 2z_0 + U & 0 \\ 0 & -t_D & -t_A & 0 & 0 & 2z_0 + U \end{pmatrix} \tag{1.43}$$

The dipole moment in this six-state model frame is defined in term of the scheme on the right in fig. 1.41. For simplicity here we set $\alpha_D = \alpha_A = \frac{1}{2}$, so that the dipole moment operators result:

$$\mu_x = \mu_0 \begin{pmatrix} 0 & 0 & 0 & 0 & 0 & 0 \\ 0 & 1 & 0 & 0 & 0 & 0 \\ 0 & 0 & 0 & 0 & 0 & 0 \\ 0 & 0 & 0 & 1 & 0 & 0 \\ 0 & 0 & 0 & 0 & \frac{1}{2} & 0 \\ 0 & 0 & 0 & 0 & 0 & \frac{1}{2} \end{pmatrix} \qquad \mu_y = \mu_0 \begin{pmatrix} 0 & 0 & 0 & 0 & 0 & 0 \\ 0 & 0 & 0 & 0 & 0 & 0 \\ 0 & 0 & 1 & 0 & 0 & 0 \\ 0 & 0 & 0 & 1 & 0 & 0 \\ 0 & 0 & 0 & 0 & \frac{1}{2} & 0 \\ 0 & 0 & 0 & 0 & 0 & \frac{1}{2} \end{pmatrix} \tag{1.44}$$

Right panel of figure 1.42 show the dependence of the transition energies and dipole moments for the two lowest excitations, calculated with the above Hamiltonian with $z_0 =$, 1.4 and $\tau = 1.80$ and either $t_D = t_A = 0.1\tau$ (continuos line) and $t_D = t_A = 0.25\tau$ (dashed lines). In both cases the energy of the lowest transition increases upon increasing U while the energy of the second transition decreases so that increasing U leads to a decresing energy gap between the two excitations. This behaviour is similar to that expected for a system described by a four state model (Hamiltonain in eq. 1.40) with negative V, as shown in the left panel of fig. 1.42. In particular we see that the behaviour of transition dipole

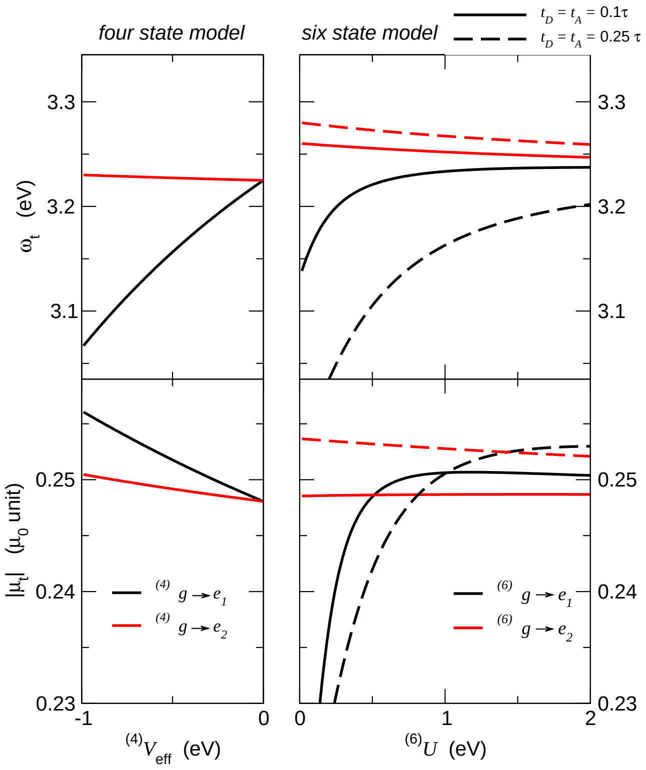

Figure 1.42: *Transition energies (upper panels) and transition dipole moments (lower panels) for the two lowest transitions relevant to a spirobichromophore. Left panels show results of the four-state model in eq. 1.40 as a function of (negative) V. Right panels show the same quantities for the six-state model in eq. 1.43, for two different $t_{D,A}$ parametrization as shown in the legend. For both model the electronic parameter are $z_0 = 1.4$ eV and $\tau = 0.80$ eV.*

moments is also similar in the two models provided that U is large enough as to correspond to a small negative V.

Therefore we will describe spirobifluorenes adopting the simplified four electronic state model in eq. 1.40 with a negative V value that accounts in an effective way for two competing effects: the electrostatic interactions between the two chromophores (leading to a negligible or positive contribution) and the spiroconjugation (leading to a negative contribution).

The four-state model: molecular vibrations and slow degrees of freedom

Building on the electronic model in eq. 1.40 we now define the complete model for spirobifluorenes accounting for the coupling to molecular vibrations, conformational coordinates and polar solvation.

Molecular vibrations are introduced accounting for a single effective coupled mode on each arm, described by the coordinates q_1 and q_2 and momenta p_1 and p_2 (see sect. 1.5.2). The electron phonon coupling is described by the relaxation energy ε_v or equivalently by $g = \sqrt{\omega_v \varepsilon_v}$, where ω_v is the vibrational frequency. To describe polar solvation we introduce two ortogonal and independent reaction fields f_x and f_y relevant to the two *DA* arms. The solvent relaxation energy is ε_{or}. To be consistent with the two state model description we introduce a conformational degree of freedom on each molecular arm, described by the coordinates u_1 and u_2, with relaxation energy ε_{int}.

The total hamiltonian then reads:

$$\begin{aligned}
\mathscr{H} \quad = \quad & 2z_0(\hat{\rho}_1 + \hat{\rho}_2) + (\hat{\delta}_1 + \hat{\delta}_2)\tau + \hat{\rho}_1 \hat{\rho}_2 V \\
& - \left(f_x + g\sqrt{2\omega} q_1\right) \hat{\rho}_1 - \left(f_y + g\sqrt{2\omega} q_2\right) \hat{\rho}_2 \\
& - u_1 \hat{\delta}_1 - u_2 \hat{\delta}_2 \\
& + \frac{1}{2}\omega_v^2 \left(q_1^2 + q_2^2 + p_1^2 + p_2^2\right) \\
& + \frac{1}{4\varepsilon_{or}} \left(f_x^2 + f_y^2\right) + \frac{1}{4\varepsilon_{int}} \left(u_1^2 + u_2^2\right)
\end{aligned} \tag{1.45}$$

This hamiltonian depends on four slow coordinates $\mathscr{H}\left(f_x, f_y, u_1, u_2\right)$. Then we define a grid on the f_x, f_y, u_1 and u_2 degrees of freedom and, on each point of the grid, we are left with a problem described by 4 electronic states coupled to 2 vibrational modes. This problem is solved in a non-adiabatic way diagonalizing on each point of the grid the Hamiltonian matrix written on the basis obtained as the direct product of the four electronic states times the $n \times n$ states of the two harmonic oscillators. Once the matrix is diagonalized, spectra are calculated on each point of the grid as described in appendix B and finally total spectra are obtained summing over the contributions from all points in the grid weighted by the relevant Boltzmann probability. Calculation were run with a large number of phonon state: $n = 12$. This is due to the relatively high e-mv coupling, and is required to get realiable anisotropy spectra (see below). With $n = 12$, the relevant hamiltonian matrix to be diagonalized is has a leading dimension of $4 \cdot 12^2 = 576$. The diagonalization has to be performed at each value of the four dimensional $\left(f_x, f_y, u_1, u_2\right)$ grid for room T absorption and fluorescence spectra.

1.6.3 Results

The four-state model described above has been applied to **1** and **4**. A bottom-up modeling strategy is adopted and the two-state molecular parameters derived from the analysis of relevant fluorene molecules in table 1.14 and 1.15 are rigidly transferred to describe the same unit in the spirobifluorene bichromophore. Model parameters and calculated spectra refers to four solvents: decalin, toluene, MeTHF, choloroform. Decalin and MeTHF were studied as relevant for the anisotropy measurements.

Parameters for the pair **1*** are listed in table 1.14. The corresponding calculated absorption and fluorescence spectra (lower panel), together with the corresponding experimental spectra (upper panels), are shown in the fig. 1.43 and 1.44 for compounds **1a** and **1** respectively. For the pair **4*** the parameters are listed in table 1.15. The corresponding calculated absorption and fluorescence spectra (lower panel), together with the corresponding experimental spectra (upper panels), are shown in the fig. 1.45 and 1.46 for compounds **4a** and **4** respectively. Fluorescence in both **4a** and **4** is observed only in apolar solvent.

The agreement between experimental and calculated spectra is generally very good. In particular, accounting for the internal degree of freedom we are able to reproduce the differences in the resolution of the vibrational structure in absorption and fluorescence, as well as the large Stokes shift, observed also in apolar solvent for **1a**.

In the spirobifluorene **1** the interaction V is set equal to 0. In fact, experimental spectra of **1a** and **1** are practically superimposed, suggesting negligible interaction between the two fluorene units. At room temperature, when $V = 0$, calculated fluorescence and absorption spectra of the fluorene *DA* monomer and the corresponding spirobifluorene result identical apart for a factor 2 in the absorption intensity, ratio that is actually observed in the experimental molar extinction coefficients (see table 1.12). When $V = 0$ the calculation of the spectra account for the possibility to have degenerate single-exciton states, and the

Table 1.14: *The model parameters for **1a** and for **1**: the molecular and the solvent parameters relevant are transferred from the two-state model to the four state model (common values, upper part of the table). In the central part of the table are shown the parameters for the **1** model only and in the last part the solvent parameters for both molecules. For the anisotropy calculation in glassy MeTHF:* $z_0 = 1.15$ *eV and* $T = 90K$.

molecular parameter		**1a**	**1**
z_0/eV		1.28	
τ/eV		0.90	
μ_0/D		18.5	
ε_{int}/eV		0.08	
ε_v/eV		0.40	
ω_v/eV		0.19	
Γ/eV		0.05	
V/eV			0.0
solvent parameter		**1a**	**1**
ε_{or}/eV	decalin	0.02	
	toluene	0.25	
	MeTHF	0.40	
	chloroform	0.7	

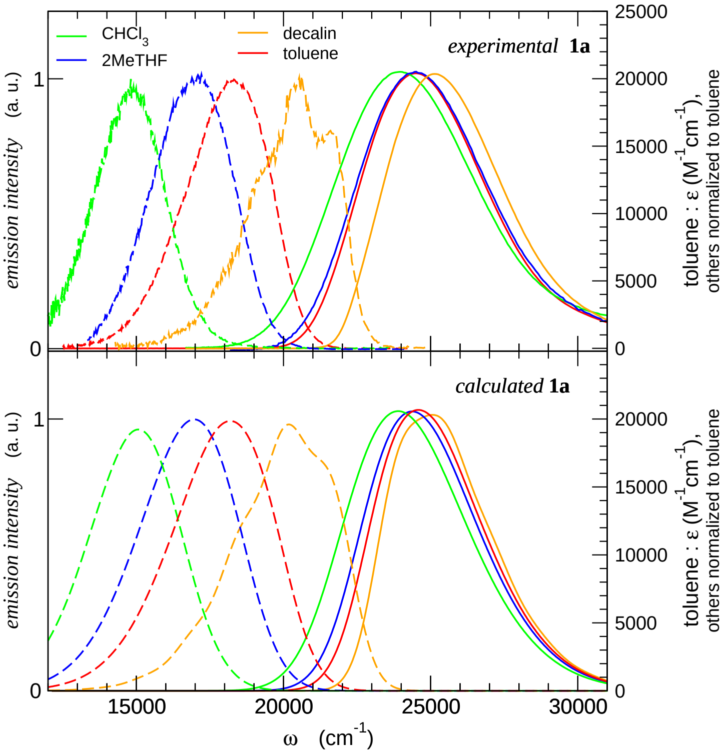

Figure 1.43: *Experimental (top) and calculated (bottom) absorption (right) and fluorescence (left) for fluorene **1a**. Parameters in tab. 1.14.*

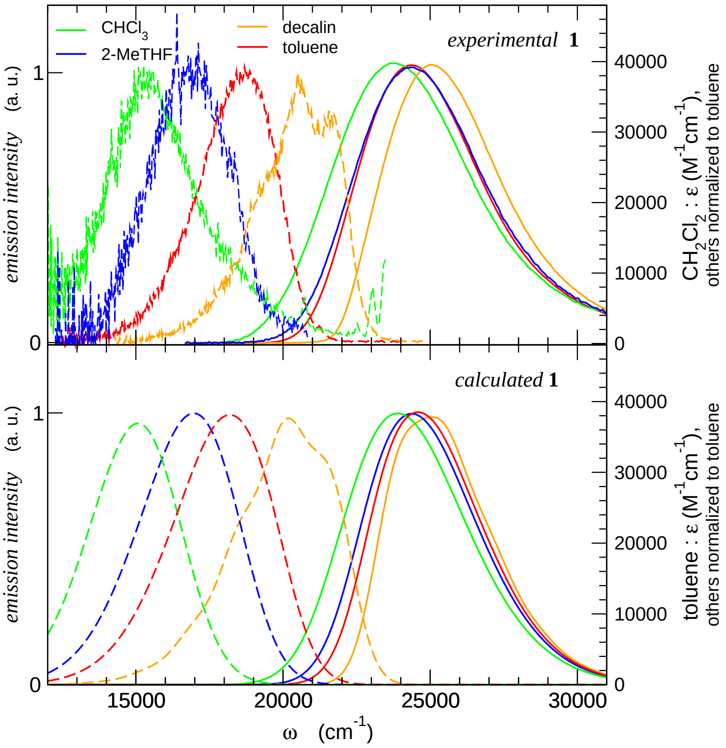

Figure 1.44: *Experimental (top) and calculated (bottom) absorption (right) and fluorescence (left) for spirofluorene **1**.Parameters in tab. 1.14.*

Table 1.15: *The model parameters for **4a** and for **4**: the molecular and the solvent parameters relevant are transferred from the two-state model to the four state model (common values, upper part of the table). In the central part of the table are shown the parameters for the **4** model only and in the last part the solvent parameters for both molecules. For the anisotropy calculation in glassy MeTHF* $z_0 = 1.15$ *and* $T = 90K$.

molecular parameter		**4a**	**4**
z_0/eV		1.27	
τ/eV		0.84	
μ_0/D		26	
ε_{int}/eV		0.05	
ε_v/eV		0.50	
ω_v/eV		0.17	
Γ/eV		0.04	
V/eV			-0.4
solvent parameter		**4a**	**4**
ε_{or}/eV	decalin	0.02	
	toluene	0.27	
	MeTHF	0.4	
	chloroform	0.7	

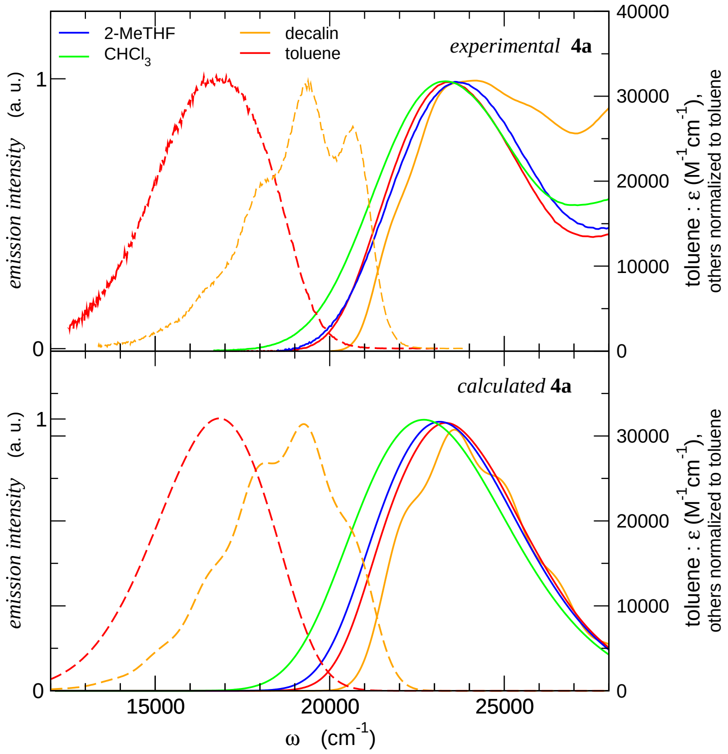

Figure 1.45: *Experimental (top) and calculated (bottom) absorption (right) and fluorescence (left) for fluorene* ***4a****. Parameters in tab. 1.15.*

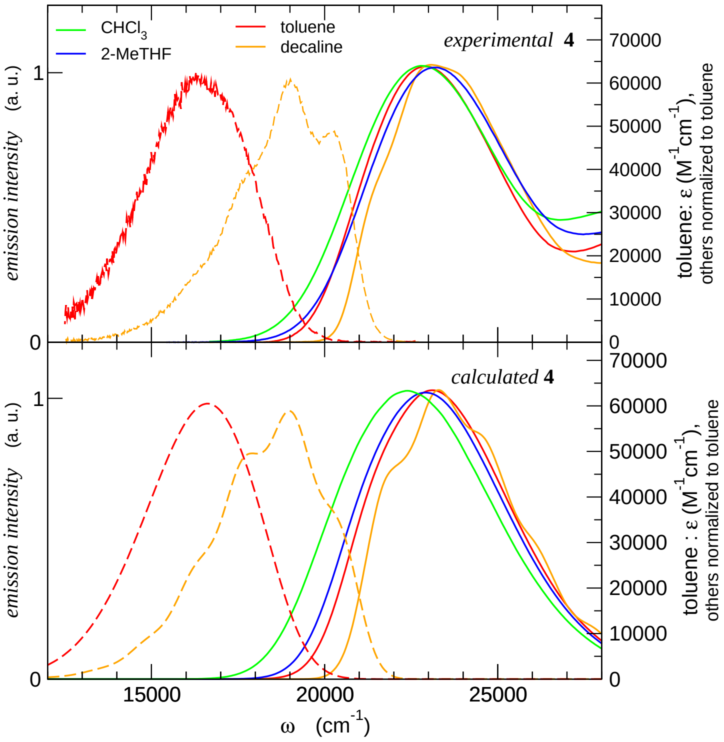

Figure 1.46: *Experimental (top) and calculated (bottom) absorption (right) and fluorescence (left) for spirobifluorene **4**. Parameters in tab. 1.15*

fluorescence results from the sum of both contributions. For **4** a small negative $V = -0.4$ eV is required to reproduce the red-shift of absorption and fluorescence bands when going from **4a** to **4**.

1.6.4 Fluorescence anisotropies, excitation and emission spectra in frozen solvent

To confirm the proposed model obtained from the analysis of absorbance and fluorescence spectra, fluorescence anisotropies on **1*** and **4*** were collected. The emission and the excitation anisotropies were measured in glassy solution of decaline at 200K and of 2-MeTHF (MeTHF) at 77K. The excitation and emission spectra together with the relative anisotropies are shown in several figures, according to the table below. Figures share experimental (upper panel) and calculated spectra (lower panel).

1a (exc. and em.) in decaline	: fig. 1.47
1a (exc. and em.) in MeTHF	: fig. 1.48
1 (excitation) in decaline	: fig. 1.49
1 (emission) in decaline	: fig. 1.50
1 (excitation) in MeTHF	: fig. 1.51
1 (emission) in MeTHF	: fig. 1.52
4a (exc. and em.) in decaline	:fig. 1.53
4a (exc. and em.) in MeTHF	:fig. 1.54
4 (excitation) in decaline	:fig. 1.55
4 (emission) in decaline	:fig. 1.56
4 (excitation) in MeTHF	:fig. 1.57
4 (emission) in MeTHF	:fig. 1.58

The polar fluorenes **1a** and **4a** show the expected behaviour for a push-pull chromophore. Their anisotropy is about 0.4, both in excitation and in emission, irrespective of the selected excitation and emission wavelength, and of solvents. A value something less than 0.4 ($r \sim 0.3$) is obtained for **4a** in decaline.

A more interesting behaviour is observed for the excitation anisotropy of the related spiro compounds **1** and **4**. For both compounds in frozen MeTHF the anisotropy start from a value close to 0.4 at the red edge of the excitation band, and then decreases until approximately vanishes at the blue edge of the same band. In the less polar solvent, decalin, a similar behaviour is observed with r decreasing from ~ 0.2 at the red edge down to ~ 0.1 at the blue edge.

Fluorescence excitation and emission anisotropy were calculated for **1*** and **4*** using the same model developed for absorption and fluorescence spectra. The calculation of the fluorescence anisotropy in frozen solvent in presence of the two internal conformational coordinates leads to a subtle problem. In fact the f_x and f_y distributions are frozen in glassy solutions, but u_1 and u_2 does relax after excitation. The relevant sampling of the grid for the spirobifluorenes is actually six-dimensional $\left(f_x, f_y, u_1^{(g)}, u_2^{(g)}, u_1^{(e)}, u_2^{(e)}\right)$, where $u^{(g)}$ and $u^{(e)}$ refer to the ground and excited state sampled internal coordinates. The computational cost become then fairly high and to save computational time is important to adopt operative criteria to minimiza the sampling. The detailed procedure to calculate anisotropy spectra in the presence of internal coordinates is described in the appendix B (see sect. B.3.2 in particular). A very large number of phonons is in general required to get stable results for anisotropy, that, being a difference of two spectra is particularly sensitive to small perturbations. The oscillations present in the calculated anisotropy spectra (lower panels of fig. from 1.47 to 1.58), can be due to some extent to the non-complete convergency of the calculated anisotropies.

Since measurements in decalin are performed at 200K, where solvent is considered a supercooled liquid with reduced molecular mobilites, we set $T = 200$K in the calculation.

On the opposite, measurements in MeTHF are performed at 77K. Since the liquid to glass transition is expected to occur at 90K, the solvent molecules are actually frozen at this thermodinamic temperature. We then set the temperature for the calculated properties in glassy MeTHF equal to 90K.

The refractive index of the solvent depends on the temperature. Since the fast degree of freedom are treated in the antiadiabatic approximation, this affects mainly the z_0 parameter [19]. We then adjust the z_0 value for $T = 90$ K calculations to 1.15 eV (vs. z_0 =1.28 eV at high temperature) for **1*** to 1.27 eV (vs. z_0 =1.20 eV at high temperature) for **4***. All other model parameters are the ones listed in the tables 1.14 and 1.15.

Fig. 1.47 - 1.52 and 1.53 - 1.57 report the experimental (upper panel) and the calculated (bottom panel), anisotropies for compounds **1*** and **4*** respectively. For all molecules calculated spectra agree very well with experimental spectra. Low temperature excitation and emission bandshapes and even vibrational structure are in most cases completely reproduced.

The excitation and emission anisotropy for dipolar molecules, as *DA* fluorenes **1a** and **4a**, is expected to be equal to 0.4, because the CT excitation and emission transition dipole moment are necessarily coinciding. Indeed, all our calculated anisotropy with the two state model are exactly equal to 0.4. However, in experimental measurements it is common to obtain anisotropies that are slightly less than 0.4. This occurs for the anisotropy excitation of **4a** in decaline, where a value around 0.3 is obtained also because decalin is not strictly glassy in the experimental condition. However, the value is completely constant inside the bands, confirming the validity of our approach.

We notice that, at variance with results obtained for liquid solutions, calculated excitation and emission spectra in frozen solvents for **1** ($V = 0$) are not identical to the monomer **1a** spectra multiplied by a factor 2. This puzzling result will be explained in the next section, where we also address the phenomenon called *red edge effect*. This name is used in the literature to describe the fact that for some chromophore the anisotropy smoothly increases inside the excitation band moving toward the red edge, where r reaches the limiting 0.4 value [68, 69, 70].

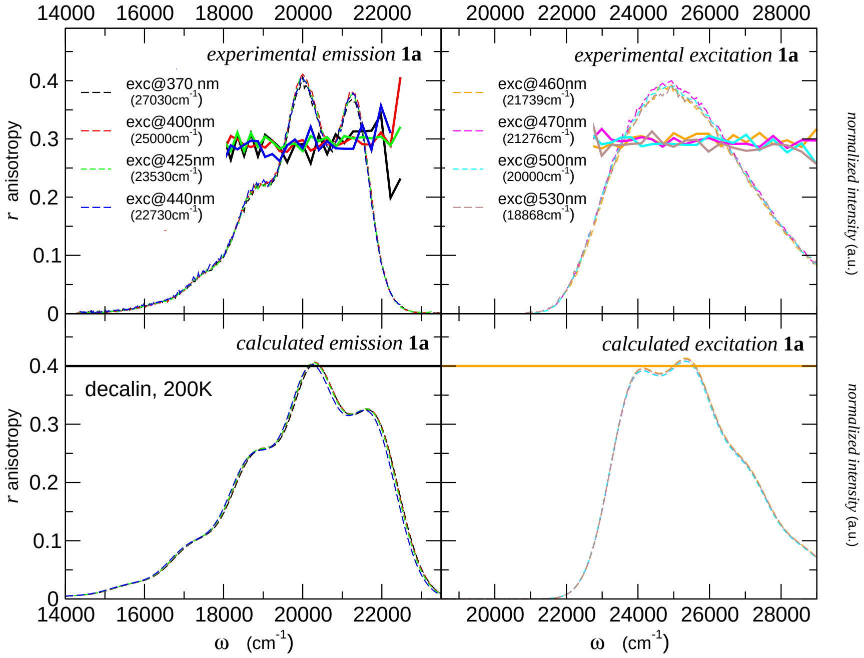

Figure 1.47: *Experimental (top) and calculated (bottom) excitation (right) and emission (left) spectra (dashed lines) and anisotropies (cont. thick lines) of* ***1a****in decalin. Parameters for calculated spectra in tab. 1.14.*

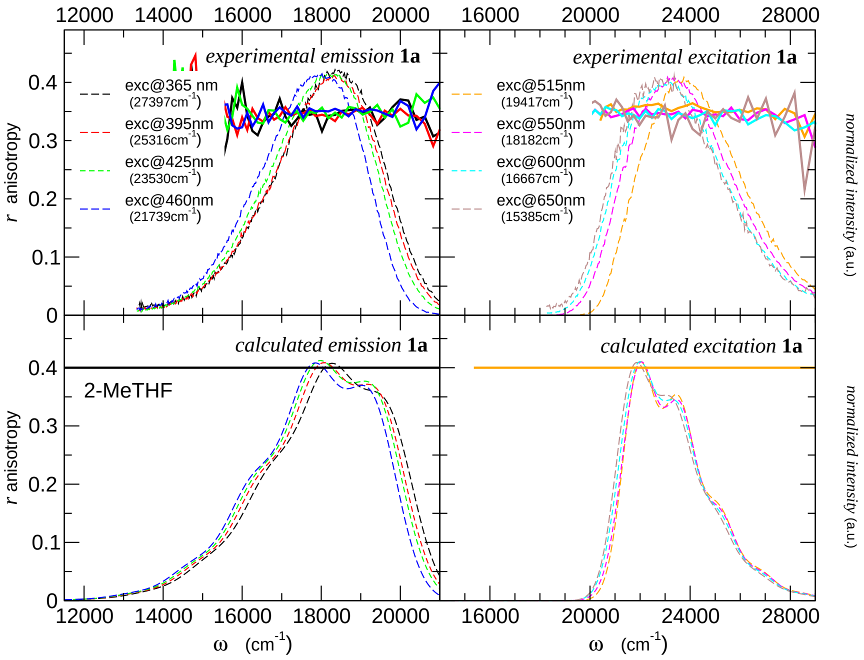

Figure 1.48: *Experimental (top) and calculated (bottom) excitation (right) and emission (left) spectra (dashed lines) and anisotropies (cont. thick lines) in 2-MeTHF of **1a**. Model parameters in tab. 1.14.*

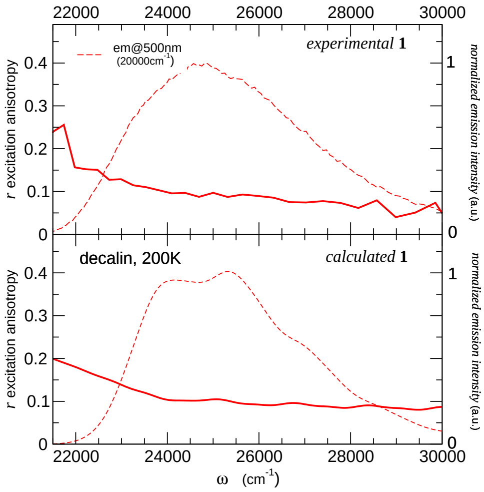

Figure 1.49: *Experimental (top) and calculated (bottom) excitation anisotropies (cont. thick lines) and excitation spectra (dashed lines) in decalin of **1**. Model parameters in tab. 1.14.*

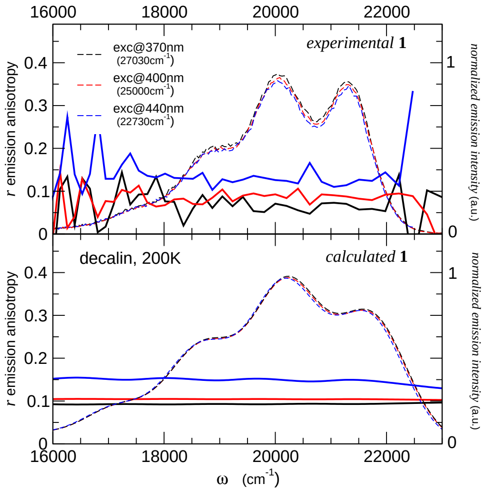

Figure 1.50: *Experimental (top) and calculated (bottom) emission anisotropies (cont. thick lines) and emission spectra (dashed lines) in decalin of **1**, at different excitation wavelength. Model parameters in tab. 1.14.*

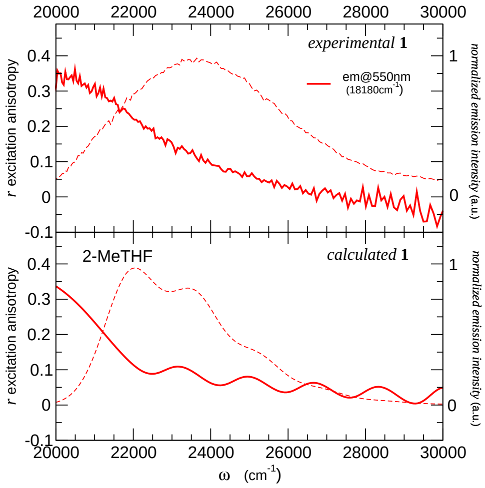

Figure 1.51: *Experimental (top) and calculated (bottom) excitation anisotropies (cont. thick lines) and excitation spectra (dashed lines) in 2-MeTHF of **1**. In the calculation the $T = 90$K. Model parameters in tab. 1.14.*

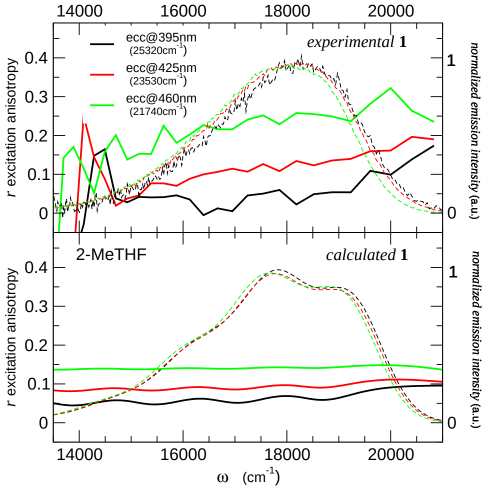

Figure 1.52: *Experimental (top) and calculated (bottom) emission anisotropies (cont. thick lines) and emission spectra (dashed lines) in 2-MeTHF of **1**. In the calculation $T = 90$K. Model parameters in tab. 1.14.*

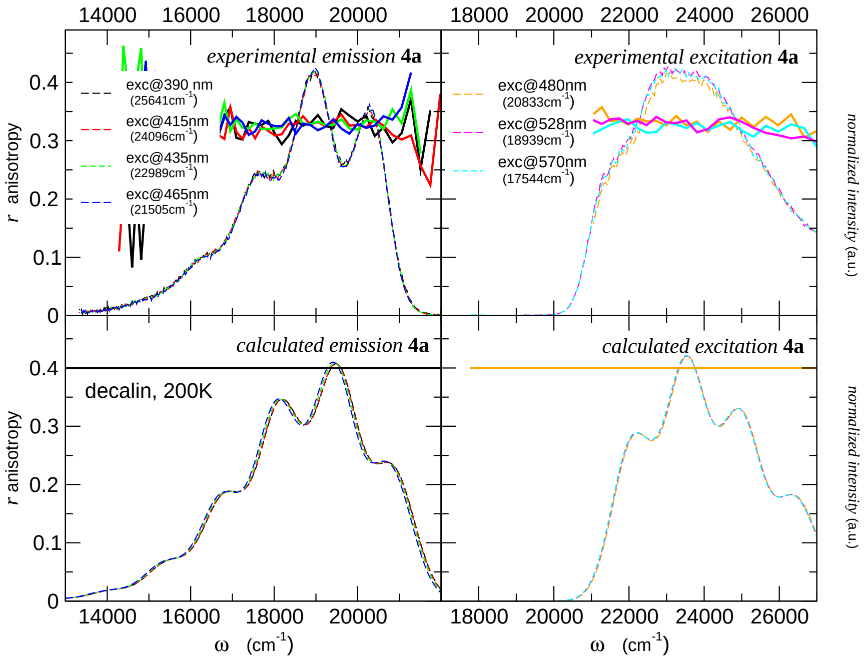

Figure 1.53: *Experimental (top) and calculated (bottom) excitation (right) and emission (left) spectra (dashed lines) and anisotropies (cont. thick lines) in decalin of **4a**. Model parameters in tab. 1.15.*

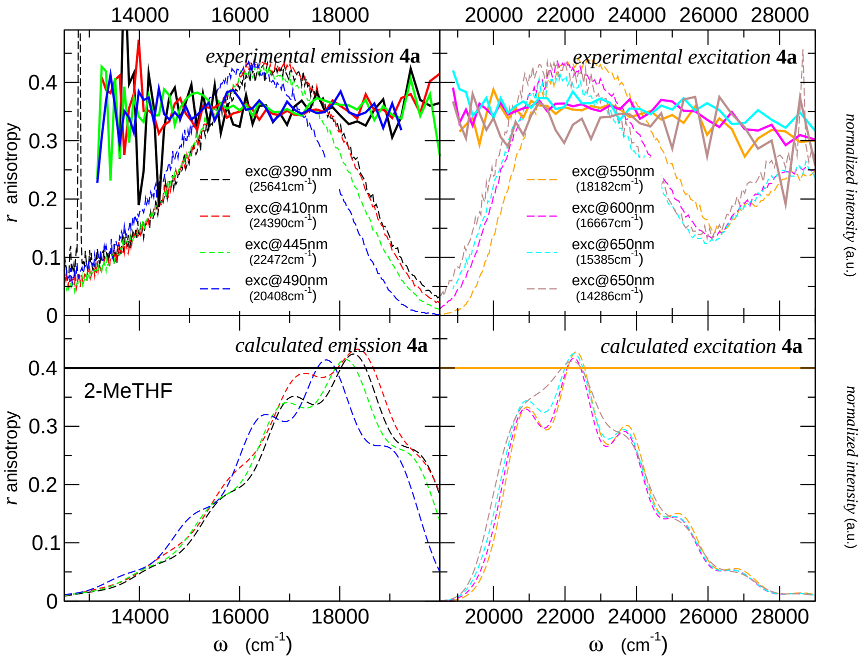

Figure 1.54: *Experimental (top) and calculated (bottom) excitation (right) and emission (left) spectra (dashed lines) and anisotropies (cont. thick lines) in 2-MeTHF of* ***4a****. Model parameters in tab. 1.15.*

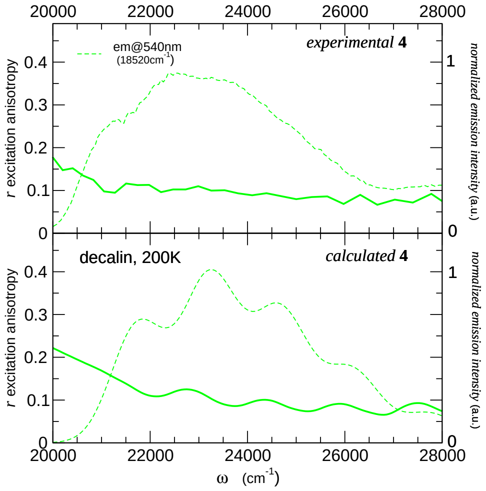

Figure 1.55: *Experimental (top) and calculated (bottom) excitation anisotropies (cont. thick lines) and excitation spectra (dashed lines) in decalin of* ***4****. Model parameters in tab. 1.15.*

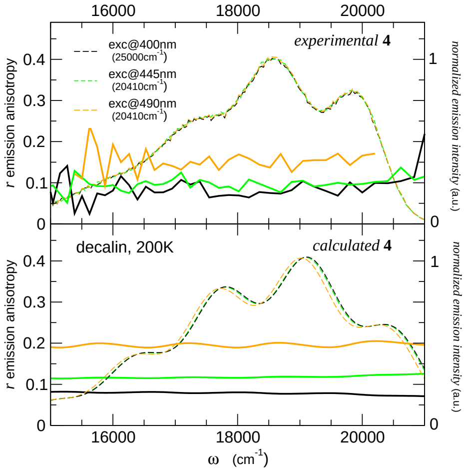

Figure 1.56: *Experimental (top) and calculated (bottom) emission anisotropies (cont. thick lines) and emission spectra (dashed lines) in decalin of* ***4****, at different excitation wavelength. Model parameters in tab. 1.15.*

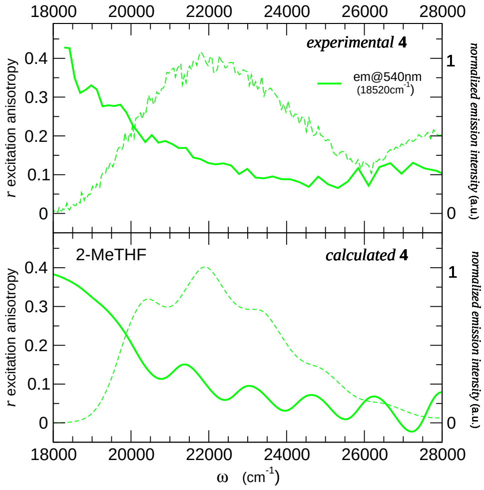

Figure 1.57: *Experimental (top) and calculated (bottom) excitation anisotropies (cont. thick lines) and excitation spectra (dashed lines) in MeTHF of* ***4****. In the calculation T = 90K. Model parameters in tab. 1.15.*

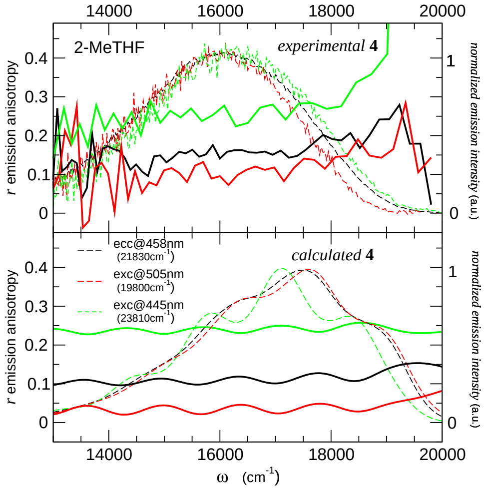

Figure 1.58: *Experimental (top) and calculated (bottom) emission anisotropies (cont. thick lines) and emission spectra (dashed lines) in MeTHF of* ***4****. In the calculation T = 90K. Model parameters in tab. 1.15.*

1.6.5 Understanding the red edge effect

In the frame of our model we can describe the "red edge" effect, i. e. the sistematic increase of r towards the limiting 0.4 value when moving towards the red-edge of the absorption band. To understand the behaviour we first discuss a pure electronic model ($\varepsilon_{or} = 0.0$ and $\varepsilon_{int} = 0.0$, and no vibrations). The exciton splitting produces a decreasing trend for the excitation anisotropy when moving away from the red-edge of the absorption band. Indeed if there is a non-degenerate exciton pair ($V \neq 0$), an excitation in the red edge limit of the absorption band will always produce the re-emission from the same state: absorbance and fluorescence dipoles are aligned and r =0.4. Moving the excitation toward the blue excites higher energy states that trasfer their energy to lower energy fluorescent states. The absorbing and emitting specie do not coincide and r can be lower than 0.4. Since the spirobifluorene has a perpendicular orientation, for a pure electronic model we predict two limit values for the anisotropy, 0.4 in red edge and -0.2 in the blue edge ($\varepsilon_{or} = 0.0$ and $\varepsilon_{int} = 0.0$). The smoothness of such decrease (i.e. how marked is the step between $+0.4$ and -0.2) depends on the relative extent of V compared to the intrinsic width of the transition Γ. However, when vibrations are introduced, the excitation anisotropy becomes more complex, because of the appearance of vibronic structure, and a smoother trend is observed, with r approaching the average value $r \sim 0.1$. The average is complete when orientational degrees of freedom are introduced ($\varepsilon_{int} \neq 0$) and at this point, regardless of the strength of the interaction V, a flat anisotropy is observed ($r = 0.1$). The value 0.1 is expected for the average of two orthogonal excitations, as in spirobifluorene ($r = 0.1$ when the angle between excitation and emission dipole moment is 45°, see eq. A.8 in appendix C).

We now introduce the solvent. In frozen solutions the solvent degree of freedom are not free to relax and the solvent configuration is fixed to that relevant to the ground state electronic distribution of the solute. The low-energy portion of the absoption spectrum is associated with a tail in the reaction field distribution $f_{x,y}$ and to the lowest energy excitations relevant to this tail in the distribution. There are no lower energy state to which is possible to transfer the energy, so that emission occurs most probably from the same states that have been excited leading to $r \sim 0.4$. When exciting at higher energy we excite both states relevant to the "red-tail" portion of the distribution, as well as states that are relevant to other portions of the distributions. Therefore, at fixed reaction field there is in general the possibility to transfer energy from higher to lower excited states, and, depending on the relative orientation of relevant transition dipole moment, value of $r < 0.4$ are expected.

We observe that spectra in frozen solvents for non-interacting ($V = 0$) chromophores are *not* the sum of the spectra of the two monomers, just in view of this red-edge effect. In fact, the degeneracy of the two one-exciton states is removed by the reaction field when $f_x \neq f_y$. For each point in the (f_x, f_y) grid when $f_x \neq f_y$ energy transfer is possible towards the lower excitation, leading to $r < 0.4$, apart from the very red-edge tail of the absorption band where $r = 0.4$, as discussed above.

Non-frozen conformational coordinates do not produce the red-edge effect, because after the excitation the slow degrees of freedom relax and fluorescence occurs from the relaxed state, lowering r. In fact the anisotropy calculated for $V = 0$ and $\varepsilon_{or} = 0$ is a flat line at $r = 0.1$. Small ε_{or}, as relevant to experimental data (decaline) for pair **1*** ($V = 0$), lead for **1** to excitation anisotropy values increasing smoothly from $r \sim 0.1$ to $r \sim 0.2$ when approaching the red-tail region.

With a model that describe two type of slow degree of freedom, we succeed in interpretating the observed red edge behaviour, and rationalizing the fully non-trivial mechanisms involved. The two coordinates respond to a very different physics in the anisotropy experiment, because the solvent effective coordinates are frozen and then the photoselection effects (see appendix B.3.1) that occurs in the excitation and de-excitaion processes in frozen solvent produces "anisotropic" results.

1.7 Conclusion

In this chapter an extensive study is presented of optical spectra of several *DA* chromophores and bichromophores in solution. Essential state models for *DA* chromophores were already developed in the host laboratory [18, 19, 39, 31, 33] and successfully applied to many systems [21, 22, 34, 35, 36, 20, 23, 32]. Here special emphasis is put on specific DA chromophores whose spectral behaviour calls for some extension of the basic model, to account for the presence of several low-energy excitations and/or for additional slow degrees of freedom. The detailed analysis of linear and non-linear optical spectra of relevant chromophores allows for the definition of reliable essential state models that properly account for electron-vibration coupling and for polar solvation and hence quite accurately reproduce the complex spectral behaviour of these dyes, including their important solvatochromism. Explicitly accounting for polar solvation, essential state models lead to define solvent-independent molecular models that represent the basic ingredient to describe interacting chromophore in multichromophoric systems. This bottom-up modelling strategy has been successfully applied here to several bichromophoric systems. Extended models for complex chromophores and/or for multichromophoric systems require an extensive validation against experimental data. The technique of fluorescence anisotropy, recently implemented in the host laboratory, proved extremely successful in this context. The theoretical modelization of fluorescence anisotropy spectra results in a very challenging task, that however provides very stringent tests for theoretical models.

Chapter 2

Mixed valence systems and bistability

The family of *DA* chromophores represents a wide group of chemical systems with interesting properties. Different donor and acceptor groups can be linked by different bridges leading to a large tunability of the molecular properties. In particular the donor and/or acceptor unit itself can be chosen to have specific properties, resulting in multifunctional *DA* systems.

Bistability is an emerging property of materials based on *DA* molecules. Bistable materials can be found in two stable states with different properties. The possibility to drive the system toward one of the two stable states by applying specific perturbations opens the way to molecular switches and/or memories. In the search for bistable molecular materials, *DA* molecules with a low energy gap between the neutral and the zwitterionic forms are particularly interesting.

Therefore, interesting donor groups for bistable materials have low ionization energy. Metallorganic unit(s) with many possible oxidation states are good candidate as (multi)donor group. *Mixed valence* systems are a well known family of compounds where a metal ion can be found in different electronic states, included formal intermediate oxidation states [71, 72, 73, 74]. Organic radicals represent interesting candidates as *D* o *A* groups because they can easily accept or release electrons to be reduced/oxidized. In these systems the presence of unpaired electrons is another element of interest in view of magnetic applications.

In this chapter we present work done in collaboration with the group of professor Veciana (ICMAB, Barcelona) that has a well recognized expertise in the synthesis and characterization of multifunctional molecular materials. The perchlorotriphenylmethyl (PTM) radical has been selected as an interesting acceptor group in view of its high stability and persistence [75, 76, 77]. The PTM ability to be reduced to the anion PTM$^-$, makes this system really promising to work as an acceptor in *DA* molecules. Moreover, PTM is a paramagnetic group and has stable αH derivative (PTMH) and is therefore an excellent candidate as building block for functional molecular materials. We will describe the properties of mixed valence compounds combining the PTM acceptor with ferrocene based donor units: ferrocene–PTM (FcPTM) and nonamethylferrocene–PTM (FcMe$_9$PTM) (see fig. 2.1). While the former exhibits intriguing bistable properties in the solid states, the second gives us the opportunity to understand the role played by bridge states in our essential state description. Bistability has been observed in crystal of ionic *DA*$^+$ species [78] and we present relevant models. Finally, preliminary results on a PTM derivative with tetrathiafulvalene (TTF) as donor, will be shortly addressed.

2.1 FcPTM and FcMe$_9$PTM: from solution spectra to bistability in molecular crystals

In this section we describe the properties of two compounds: ferrocene-perchlorothriphenylmethyl (FcPTM) and its nonamethylated derivative (FcMe$_9$PTM) in fig. 2.1, synthesized and characterized by the group of Prof. Veciana [79, 80]. These two molecules were designed as interesting valence tautomeric compounds with large non-linear optical responses, electrochemical switchability and good optical and thermal stability [81, 82]. Moreover, the presence of an unpaired electron makes these molecules interesting from a magnetic point of view, making them very promising for multifunctional applications.

Both species show a CT absorption in the NIR spectral region (see fig. 2.2) with a well pronounced solvatochromism, pointing to a largely neutral nature of both molecules in solutions. However, crystals of FcPTM show a quite intriguing behavior, as evidenced by Mössbauer spectra [80]. In fact at room temperature both the neutral and zwitterionic forms of FcPTM (shown in fig. 2.3) are found with similar concentration. By lowering T, the percentage of zwitterionic molecules decreases until at very low T ($\sim$ 4K) only the neutral specie is found.

We rationalize this intriguing behavior in terms of bistability induced by electrostatic intermolecular interactions in crystals of *DA* chromophores [38].

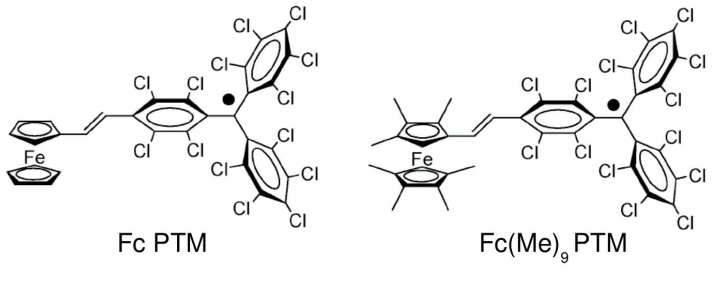

Figure 2.1: *Ferrocene–perchlorotriphenylmethyl (FcPTM) and the nonamethylated derivative (FcMe$_9$PTM)*

The work starts from the analysis of optical spectra of the two chromophores in solution to obtain reliable two-state models to be used, in a bottom-up strategy, to define a model for interacting chromophores in the crystal. Then we discuss bistability in FcPTM crystal based on a mean-field treatment of electrostatic interactions. To qualitatively compare with experimental data we need reliable estimates of electrostatic interactions: to such an aim we make resort to an original implementation of quantum chemical calculations [24].

While the description of optical properties of FcPTM in solution and the subsequent study of Mössbauer spectra of FcPTM crystals is very successful, optical spectra of FcMe$_9$PTM suggest the need to extend the essential state model to account for bridge states. This analysis leads not only to a better description of solution spectra of FcMe$_9$PTM (and FcPTM), but offers the opportunity to discuss and generalize the role of bridge states in *DA* chromophores [83], rationalizing some well-known discrepancies in the standard treatment of valence-tautomeric compounds. Finally the bistability model is extended to model interacting *DA* chromophores described in terms of three-state models, as to demonstrate the robustness of the proposed bistability mechanism.

2.1.1 Solution spectra and two state model

Figures 2.2 show absorbance spectra in the Vis-NIR of FcPTM and FcMe$_9$PTM in solvents of different polarity. The same spectra in the NIR window are shown in fig. 2.4 (upper panels). The absorption band located at $\sim$ 10000 cm^{-1} ($\sim$ 1000 nm) for FcPTM and at $\sim$ 7000 cm^{-1} ($\sim$ 1700 nm) for FcMe$_9$PTM corresponds to the CT absorption and shows, for both compounds, a weak solvatochromism,

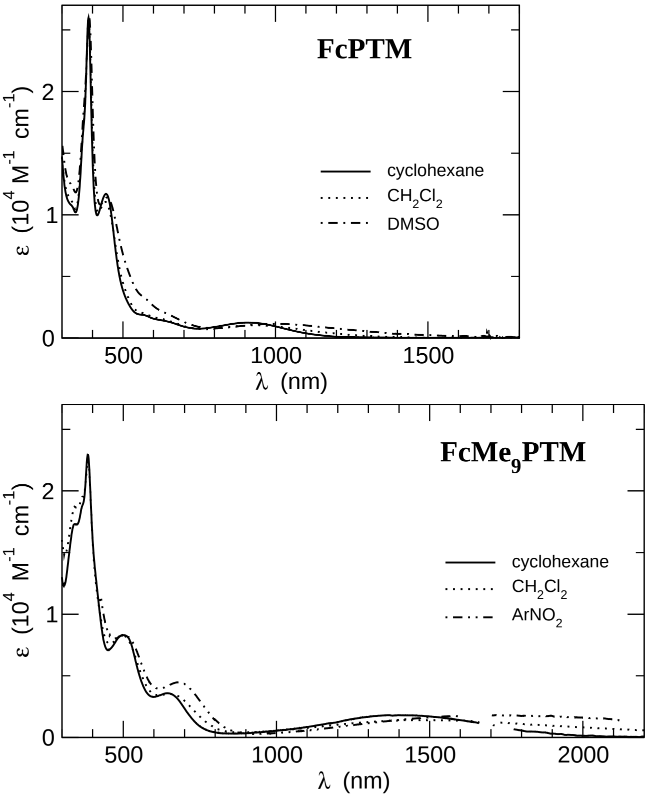

Figure 2.2: *Optical spectra of FcPTM (top) and FcMe$_9$PTM (bottom) in different solvents.*

as typically observed for largely neutral molecules.

The low-energy physics of FcPTM is governed by the charge resonance shown in figure 2.3. In close analogy with closed shell *DA* chromophores, we describe the FcPTM and FcMe$_9$PTM radicals in terms of a minimal model that accounts for two essential electronic states, $|DA\rangle$ and $|D^+A^-\rangle$, corresponding to the two resonating structures $DA^\bullet \longleftrightarrow D^{+\bullet}A^-$. The electronic Hamiltonian, as well as the coupling with molecular vibrations and solvent effects are the same as in section 1.1, and the complete Hamiltonian is: $\hat{h} = 2z_0\hat{\rho} - \tau\hat{\sigma} + \frac{{\omega_v}^2}{2}\left(q^2 + p^2\right) - g\sqrt{2\omega_v}q$, (see eq. 1.11, where $\hat{h} \equiv \mathscr{H}$). Here however we adopt an adiabatic treatment of molecular vibrations. First, we diagonalize the two state electronic Hamiltonian for fixed q and f to calculate the potential energy surfaces (PES) for the ground and the excited state. The different equilibrium position for the vibrational coordinate, q, in the ground and excited state accounts for the change in

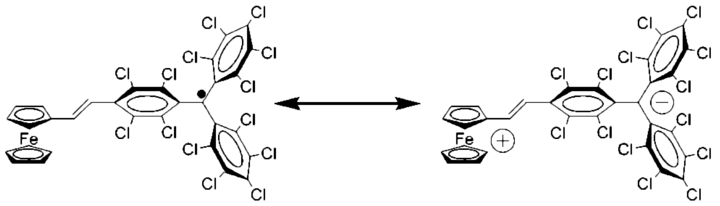

Figure 2.3: *FcPTM neutral and zwitterionic resonance*

the molecular geometry that accompanies the CT process, and is responsible for the Franck-Condon structure in absorption spectra. The adiabatic PES are anharmonic, but for a not too strong anharmonicity, the absorption spectrum can be calculated in the local harmonic approximation [84, 85] setting the vibrational frequency of the ground and excited state to the same value ω_v. Details about the calculation of optical spectra can be found in the appendix (see sect. B.1.2).

Spectra calculated for FcPTM and FcMe$_9$PTM based on the two state model of eq. 1.11 are reported in lower panels of figure 2.4. The spectra have been obtained for the molecular parameters at the top of table 2.1, while adjusting ε_{or} for each solvent as reported in the bottom part of table 2.1. Both compounds present a largely neutral ground state, as confirmed by the positive solvatochromism typical of *DA* chromophores with a neutral ground state: we estimate $\rho \sim 0.07$ for FcPTM and $\rho \sim$ 0.10-0.13 for FcMe$_9$PTM. The evolution with the solvent polarity of the main CT band of both compounds is well reproduced and is obtained by varying ε_{or}, while keeping fixed all molecular parameters. As already pointed out in the previous chapter, ε_{or} vanishes in nonpolar solvents and increases with the solvent polarity. The smaller ε_{or} values estimated for the methylated compound are in line with the larger cavity required to accommodate the bulkier methylated solute [18, 19]. The lower ionization energy of FcMe$_9$PTM with respect to FcPTM is well explained by an inductive effect of the methyl groups on Fc, resulting in a stronger donor character of the FcMe$_9$ group. The spectra do not show a resolved vibronic structure, hindering a precise estimate of the vibrational frequencies ω_v and of the intrinsic linewidths Γ. The vibrational relaxation energy ε_v, similar in the two compounds, are small if compared to the values relevant to closed-shell organic *DA* chromophore [18, 19, 86, 33, 84]. This can be rationalized since in closed-shell organic *DA* molecules the CT results in a change of the bond order alternation, that has no counterpart in open-shell systems like FcPTM and FcMe$_9$PTM.

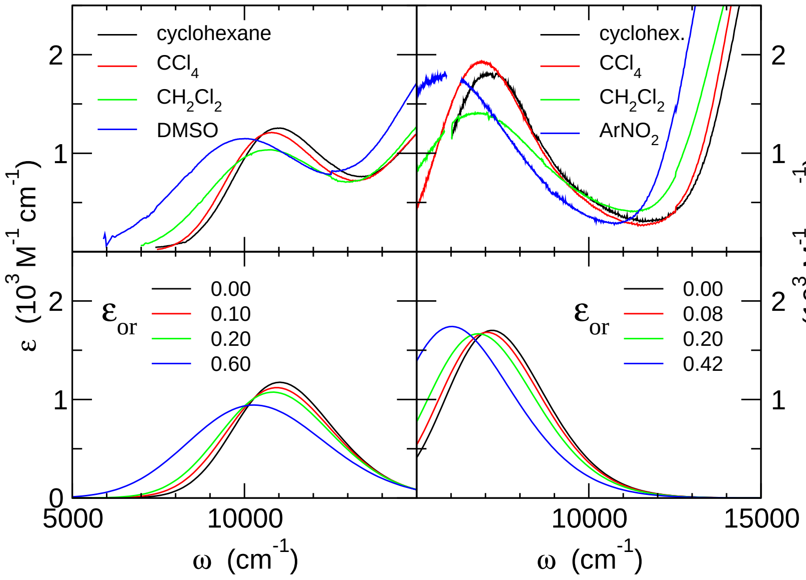

Figure 2.4: *Experimental (top panels) and calculated (bottom panels) spectra with the two-state model for FcPTM (left column) and FcMe$_9$PTM (right column). Calculated spectra are obtained with molecular parameters in table 2.1 and the ε_{or} values in the legend. The intrinsic bandwidth is set to $\sigma = 0.07$ eV in all calculated spectra.*

Table 2.1: *Molecular parameters and solvent relaxation energies for FcPTM and $FcMe_9PTM$ described in the two-state model.*

molecular parameter		FcPTM	$FcMe_9PTM$
z / eV		0.61	0.36
τ / eV		0.35	0.30
μ_0 / D		7.5	8.5
ε_v / eV		0.10	0.12
ω_v / eV		0.18	0.18
Γ / eV		0.17	0.17
solvent parameter		FcPTM	$FcMe_9PTM$
ε_{or} / eV	cyclohexane	0.0	0.0
	CCl_4	0.20	0.25
	dichloromethane	0.45	0.38
	$ArNo_2$		0.65
	DMSO	0.80	

The parameter μ_0, measuring the dipole moment of the zwitterionic D^+A^- specie, fixes the absolute intensity scale of absorption spectra, while it is irrelevant for band shapes and frequencies. The μ_0 values in table 2.1 are set to reproduce the experimental extinction coefficients. They correspond to dipole lengths of 1.56 and 1.77 Å for FcPTM and $FcMe_9PTM$, respectively. These values are unreasonably small if compared with geometrical *D–A* distances (the distance from the Fe atom and the central C atom of PTM is 9.5 and 9.7 Å for FcPTM and $FcMe_9PTM$ respectively, from crystallographic data [80]. It is very well known that the spectroscopic estimate of μ_0, based on the two-state model, usually lead to shorter dipole lengths to the one expected on geometrical basis [46, 87, 88, 89, 90, 91, 84]. We will face this issue in section 2.1.7.

2.1.2 Bistability in FcPTM crystal: the electronic model

To investigate the intriguing bistable behavior shown by FcPTM crystals we adopt the same bottom up modeling procedure, applied in chapter 1 to describe optical spectra of multichromophoric species. In this approach the Hamiltonian describing a crystals of molecules interacting via electrostatic forces is [92, 93]:

$$H = \sum_i \hat{h}_i + \frac{1}{2}\sum_{i,j} \hat{V}_{ij} \tag{2.1}$$

where the sums run on molecular sites, $\hat{h}_i$ is the Hamiltonian of the i-th molecule, and $\hat{V}_{ij}$ is the operator that describes the interaction between molecules at i and j sites. The above Hamiltonian neglects any overlap between orbitals located in different chromophores and hence applies to systems where intermolecular distances are larger that the sum of Van der Waals radii.

The heart of the bottom-up approach lies in recognizing that the molecular Hamiltonian $\hat{h}_i$ is the same that describes the molecule in solution and can therefore be extracted from the analysis of solution spectra [32, 20, 25, 16]. In the specific case of FcPTM crystals, the h_i is the molecular Hamiltonian defined in the previous section, for the analysis of solution spectra.

If the molecular units are modeled by the two-state electronic Hamiltonian (see eq. 1.2), the charge distribution on each molecule is fully described by the operator $\hat{\rho}$, and the electrostatic intermolecular interaction term in in equation (2.1) can be written as

$$\hat{V}_{ij} = V_{ij}\ \hat{\rho}_i \hat{\rho}_j \tag{2.2}$$

where V_{ij} is the interaction energy between the i-th and j-th molecules both in the zwitterionic $|D^+A^-\rangle$ state [92, 93, 25].

For simplicity we start our analysis accounting just for the electronic Hamiltonian: $\hat{h}_i = 2z_0\rho - \tau\hat{\sigma}$. The role of molecular vibrations will be discussed later. To start with, we first consider the $\tau = 0$ limit. For $\tau = 0$, there is no mixing between the basis state, an each molecule can be either in the $|DA\rangle$ ($\rho = 0$) or in the $|D^+A^-\rangle$ state ($\rho = 1$). The energy required to switch the N molecules in the crystal from the $|DA\rangle$ to the $|D^+A^-\rangle$ is simply $2N(z + \mathscr{M})$, where $\mathscr{M}$ is (half) Madelung energy of a crystal of zwitterions:

$$\mathscr{M} = \frac{1}{2N}\sum_i V_{ij} \tag{2.3}$$

When $(z_0 + \mathscr{M}) > 0$ the ground state of the crystal corresponds to a collection of neutral molecules, but for $(z_0 + \mathscr{M}) < 0$ it describes a collection of fully ionic molecules.

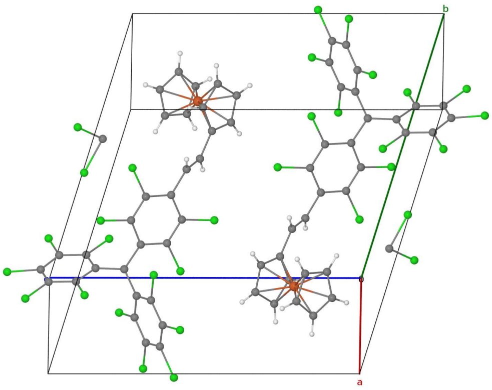

Figure 2.5: *Crystal structure for FcPTM, from [80]. Two molecule of solvent (CH_2Cl_2) per cell are cocrystallized.*

Moving away from the $\tau = 0$ limit opens the way to states with intermediate ionicity, but inevitably leads to a more complex problem. The Hamiltonian (2.1) with electrostatic interactions expressed in equation (2.2) can be diagonalized exactly on clusters of N molecules, [92, 93] but, since the basis dimension increases as 2^N, it is impossible to obtain exact results on large enough three dimensional clusters as required to properly model long-range electrostatic interactions. We therefore adopt the mean field (mf) approximation, a good and powerful approximation to describe the ground-state properties of clusters of interacting DA molecules [92, 93].

The ionicity of each molecule is written as the sum of a mean value plus a value accounting for the fluctuations: $\rho_i = \langle\rho\rangle + \delta_i$, where we impose that the average ionicity $\langle\rho\rangle$ is the same on all molecules in the crystal. In the mf approximation, all non-linear terms in the fluctuation are neglected, and the interaction can be rewritten:

$$\frac{1}{2}\sum_{ij} V_{ij}\hat{\rho}_i\hat{\rho}_j \approx \frac{1}{2}\sum_{ij} V_{ij}\left[-\langle\rho\rangle^2 + \langle\rho\rangle\left(\hat{\rho}_i + \hat{\rho}_j\right)\right] \tag{2.4}$$

and with the definition of eq. 2.3 we get:

$$\frac{1}{2}\sum_{ij} V_{ij}\hat{\rho}_i\hat{\rho}_j = -N\langle\rho\rangle^2\mathscr{M} + 2\langle\rho\rangle\mathscr{M}\sum_j \hat{\rho}_j \tag{2.5}$$

The total Hamiltonian in eq. 2.1 with ($\hat{h}_i \equiv \mathscr{H}$, $\mathscr{H}$ from eq. 1.1), therefore reads:

$$H_{\mathrm{mf}} = \sum_i \left[2\left(z + \mathscr{M}\rho\right)\hat{\rho}_i \; - \; \tau\,\hat{\sigma}_i\,\right] - N\mathscr{M}\rho^2 \tag{2.6}$$

where the first term defines an effective molecular Hamiltonian $\hat{h}_{i,\mathrm{eff}} = 2(z_0 + \mathscr{M}\rho)\hat{\rho}_i - \tau\hat{\sigma}$ that describes a molecule in the crystal. This effective molecular Hamiltonian is actually the same two state Hamiltonian in equation 1.1 with a renormalized ionization energy: $z_{\mathrm{eff}} = z_0 + \mathscr{M}\rho$. In other terms, the energy required to promote the electron transfer on a *DA* molecule is $2z_0$ for isolated molecules (more precisely for molecules in a nonpolar environment) but in the crystal this energy becomes $2z_{\mathrm{eff}}$, and it depends on the charge distribution of surrounding molecules, ρ.

We are now in the position to investigate the role of the intermolecular electrostatic interactions in crystals of FcPTM. We fix $z_0 = 0.61$ eV and $\tau = 0.35$ eV, as relevant for FcPTM. Fig. 1.1, presented in sect. 1.1 can be updated to describe the effect of $\mathscr{M}$ on the $\rho(z)$ curve dependence. The solution of the problem is self-consistent: from the universal $\rho(z_{\mathrm{eff}})$ in eq. 1.5, for each $\mathscr{M}$ value we extract $z_0 = z_{\mathrm{eff}} - \mathscr{M}\rho$. The $\rho(z)$ curves at three different values of $\mathscr{M}$ for attractive interactions are shown in fig. 2.6. For not too-large $|\mathscr{M}|$ a smooth crossover is observed from a largely neutral regime ($\rho \sim 0$) to a largely ionic regime ($\rho \sim 1$): in other terms, for small $|\mathscr{M}|$ a region is found where the hybridization energy, τ, is large enough to stabilize states with $\rho \sim 0.5$. On

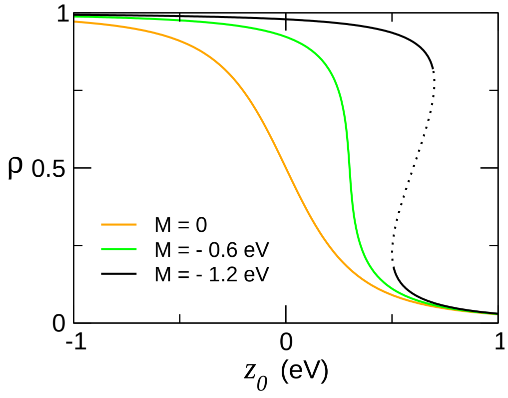

Figure 2.6: *$\rho(z)$ curves calculated for τ = 0.35 eV and different $\mathscr{M}$. Green, orange and black curves refer to M = 0, -0.6, and -1.2 eV, respectively. For $\mathscr{M}$ = -1.2 the region of the $\rho(z)$ curve with positive slope (marked by the dotted line) corresponds to unstable solutions*

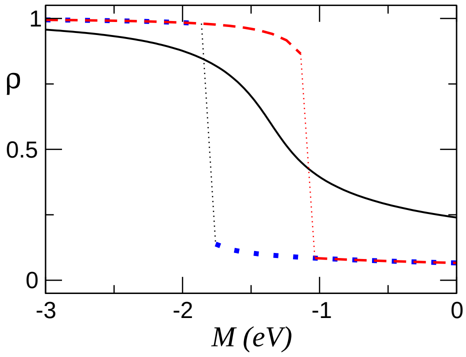

Figure 2.7: *$\mathscr{M}$-dependence of ρ for a crystal of DA molecules described by the mf Hamiltonian (2.6). The black continuous line refers to $z = 0.61$ eV and $\tau = 1$ eV. Dashed and dotted lines refer to $z = 0.61$ eV and $\tau = 0.35$ eV (as relevant for FcPTM). Blue dotted lines are obtained setting the initial guess for the self-consistent solution of the mf Hamiltonian as $\rho \approx 0$, while red dashed lines are obtained with the starting choice $\rho \approx 1$. The dotted thin lines are drawn as guide to the eyes.*

the opposite, when $|\mathscr{M}| \gg \tau$ the hybridization energy is never dominant, and states with $\rho \sim 0.5$ are not accessible: the charge crossover becomes discontinuous [37, 38, 16, 56, 94]. This is illustrated by the $\mathscr{M}$ = -1.2 eV curve in fig. 2.6 where the portion of the $\rho(z_0)$ curve with positive slope corresponds to unstable states. For large and attractive $\mathscr{M}$ value states with intermediate ionicities ($0.2 \lesssim \rho \lesssim 0.8$) are forbidden. More interesting for our discussion is however the appearance of a *bistability region* where, for each z_0 value, two different stable states with $\rho \sim 0$ and $\rho \sim 1$ are found. This bistability, induced by electrostatic intermolecular interactions, is the key to explain experimental observations on FcPTM crystals, and we will enter the detail afterward.

The same behavior can be understood with reference to the $\rho(\mathscr{M})$ curves, calculated for a crystal of molecules with $z_0 = 0.61$ eV (as relevant for FcPTM) and two different values of τ, as reported in figure 2.7. Only attractive interactions ($\mathscr{M} < 0$) are considered. In these case the self-consistent problem is solved imposing an initial guess for ρ to define the mf Hamiltonian in eq. 2.6 that is then diagonalized to obtain an updated ρ value. The procedure is repeated until convergence. For $\tau = 1$ *eV* (black continuous line) an unique solution is find irrespective of the starting guess for ρ: ρ increases smoothly from 0.25 in the limit of non-interacting molecules ($\mathscr{M} = 0$), to $\rho \sim 1$: attractive interactions push the system towards ionic states. Notice that the system moves from neutral to ionic regime at about $\mathscr{M} = 2z_0$, that is $z_{\text{eff}} \approx 0$.

More interesting is the case of smaller $\tau = 0.35\ eV$, as relevant for FcPTM. In fact, in this case, *two stable solutions* are found in the proximity of the interface, depending on the initial guess for ρ (see caption of fig. 2.7). The region, $-1.8 < \mathscr{M} < -1.1$, where the two results do not coincide defines the bistability region where a neutral and an ionic solution coexist for the same model parameters.

2.1.3 Bistability in FcPTM crystals: the complete model

We now introduce the coupling between electronic and vibrational degrees of freedom. In the two state model (discussed in the sect. 1.1, and shortly reviewed in sect. 2.1.1), we describe molecular vibration and e-mv coupling accounting for a molecular vibrational coordinate. In the crystal the N coordinates relevant to each chromophore are combined to get N coordinates in the wavevector space. The relevant coordinate for our problem, where all the molecules behave in the same way, is the in-phase vibration of all the molecules of the crystal, Q. To simplify notation the new vibrational coordinate is defined in energy units as follows:

$$Q = \sqrt{\frac{2\varepsilon_v}{N}}\,\omega_v \sum_i q_i \tag{2.7}$$

With this definition, the adiabatic mf Hamiltonian becomes

$$H_{\text{mf}}(Q) = \sum_i \left[2\left(z_0 + \mathscr{M}\rho - \frac{q}{2} \right) \hat{\rho}_i \; - \; \tau\,\hat{\sigma}_i \right] - N\mathscr{M}\rho^2 + \; N\frac{Q^2}{4\varepsilon_v} \tag{2.8}$$

The mf Hamiltonian again coincides with the two-state Hamiltonian in equation (1.1) but with $z_{\text{eff}} = z_{+}\mathscr{M}\rho - Q/2$. By substituting Q with its equilibrium value $Q_{eq} = 2\varepsilon_v\rho$ (as derived by Hellmann-Feynman theorem) we get a simple expression for the effective ionization energy, $z_{\text{eff}} = z + (\mathscr{M} - \varepsilon_v)\rho$, accounting for both electrostatic intermolecular interactions and molecular vibrations. The coupling between electronic and vibrational degrees of freedom plays the same role as attractive electrostatic intermolecular interactions [95], and the $\rho(\mathscr{M})$ curves in figure 2.7 still apply in the presence of vibrational coupling, but with $\mathscr{M}$ replaced by $\mathscr{M} - \varepsilon_v$. For FcPTM $\varepsilon_v = 0.1\ eV$ and the vibrational contribution to $\mathscr{M}$ represents just a minor correction.

More interesting is the calculation of the Q-dependent ground state energy, obtained by the diagonalization of the Q-dependent mf Hamiltonian in equation (2.8). Panels **a-d** of figure 2.8 show the ground state potential energy surfaces

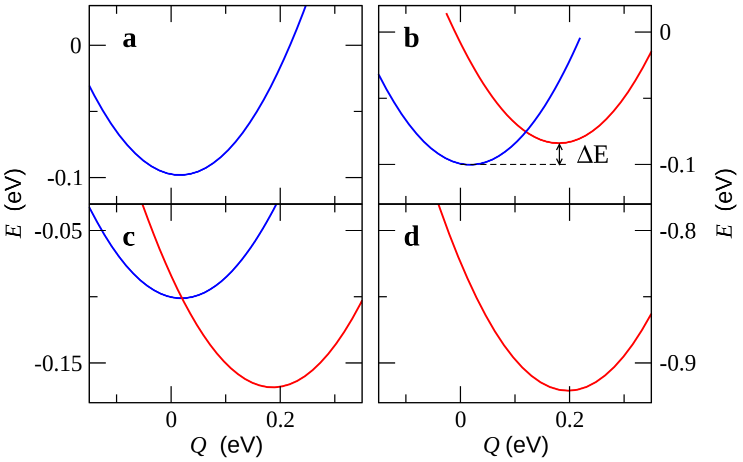

Figure 2.8: *Ground state PESs obtained from the diagonalization of mf Hamiltonian in equation (2.8), calculated for FcPTM molecular parameters in table 2.1, and* $\mathscr{M} = -0.8, -1.1, -1.2$ *and 2.0* eV*, in panels* **a**, **b**, **c** *and* **d** *respectively.*

(PES) calculated for a system with $z = 0.61$ eV, $\tau = 0.35$ eV, $\varepsilon_v = 0.1$ eV, as relevant for FcPTM, and different $\mathscr{M}$ values. For relatively weak interactions ($\mathscr{M} - \varepsilon_v = -0.9$ eV, corresponding to a large and negative z_{eff}), the $\rho(z)$ curve (not shown in figure 2.6) would lead to a single solution corresponding to a neutral ground state with $\rho(z) \approx 0.1$. The corresponding PES (panel **a** of figure 2.8) is almost harmonic with a minimum located at $q_{eq} = 0.01\ eV$. Similarly, for strong interactions ($\mathscr{M} - \varepsilon_v = -2.0\ eV$, corresponding to a large and negative z_{eff}) a single solution is found, corresponding to an ionic state with $\rho(z) \approx 1$. The relevant PES (panel **d** of figure 2.8) is centered at $q_{eq} = 0.2\ eV$. For $\mathscr{M} - \varepsilon_v$ within the bistability region, two stable states, with different ρ, are found. For $\mathscr{M} - \varepsilon_v = -1.2$ eV, a neutral ($\rho = 0.09$) and an ionic state ($\rho = 0.9$) are both stable. The corresponding PES in panel **b** of fig. 2.8 are almost harmonic with minima located at $q_{eq} = 0.018$ and 0.18 eV. Of course just one of the two states, the lowest energy one, is thermodynamically stable, while the other state is metastable. For $\mathscr{M} - \varepsilon_v = -1.3$ eV (cf. panel **c**, figure 2.8), again in the bistability region, the situation is reversed with the stable state corresponding to an ionic state ($\rho = 0.93$), while the metastable state corresponds to a neutral state ($\rho = 0.1$).

2.1.4 Bistability in FcPTM crystals: estimating the Madelung energy

Results presented in the previous section demonstrate that a discontinuous neutral to ionic crossover can be induced in crystals of DA chromophores by electrostatic intermolecular interactions. To support our hypothesis of electrostatically induced bistability in FcPTM crystals we need a reliable estimate of $\mathscr{M}$, defined in equation (2.3) as half the Madelung energy of a lattice of zwitterionic $|D^+A^-\rangle$ molecules. The crystal structure of FcPTM is known [80]. In the crudest approximation [92, 93, 25], $\mathscr{M}$ can then be estimated modeling the charge distribution on the zwitterionic FcPTM molecules in terms of a positive and a negative charge located at the center of the D and A groups, respectively. In this approximation, locating the charges at the positions of the Fe atom and of the central C-atom of the PTM, we estimate $\mathscr{M} = -0.72$ eV, an encouraging result.

An improved estimate of $\mathscr{M}$ can be obtained modeling the charge distribution on each molecule as a collection of point atomic charges as obtained by quantum chemical calculations [96]. The calculation is not trivial, however, because we need electrostatic interactions among FcPTM molecules in the $|D^+A^-\rangle$ form, and not in the almost neutral ground state that results from gas-phase calculations. To overcome this subtle problem we perform semiempirical calculations on a molecule subject to an external static electric field F, directed along the x-axis (that connects the central C-atom of the PTM to the Fe-atom of the Fc), in order to force the molecule in a zwitterionic form. The calculations are performed for different values of F, fixing the geometry to the experimental crystallographic geometry [80]. Restricted (open) Hartree-Fock calculations were performed with the semiempirical PM6 Hamiltonian [97], that provides parametrization for transition metals like Fe (MOPAC2007 package, [98]). Figure 2.9 summarizes the results in terms of dipole moment, molecular polarizability, and total charges on D or A unit.

The x-component of the molecular dipole moment, $\mu_x(F)$ is defined as $\mu_x = e\sum_p \mathrm{q}_p x_p$, where p runs on atoms, e is the electronic charge, x_p is the x-coordinate and q_p is the Coulson net atomic charge of the p-th atom, defined as [97]:

$$\mathrm{q}_p = Z_P - \sum_{\lambda \in p} P_{\lambda\lambda} \tag{2.9}$$

The S-shaped $\mu_x(F)$ curve in figure 2.9 confirms the two state assumption: two different regimes are clearly identified, a low and a high field regime separated by a narrow region at $F \approx 0.4\ V/\text{Å}$ where charges rearrange dramatically. Corresponding to this abrupt change in the electronic distribution the dielectric

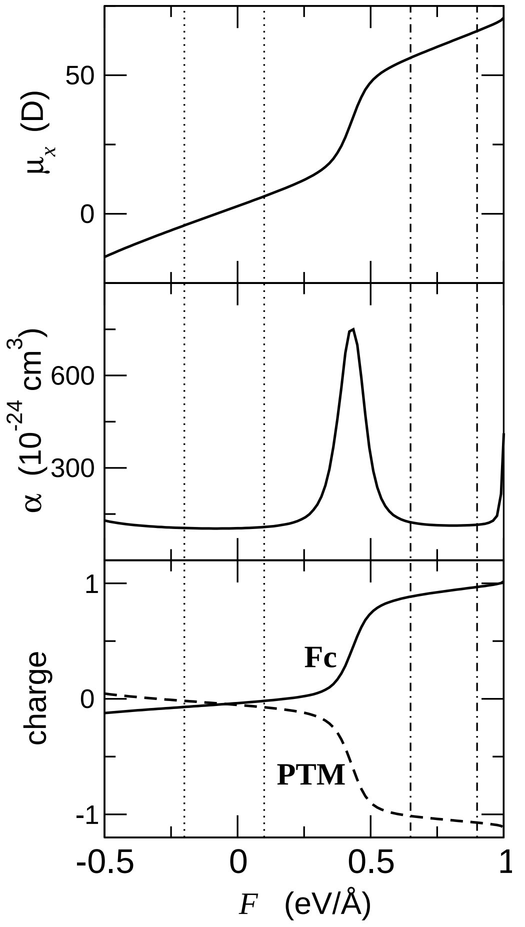

Figure 2.9: *Results of PM6 calculations for a FcPTM molecule with geometry fixed at the crystallographic structure under an external static electric field, F, oriented along the $D-A$ axis. F-dependence of the molecular dipole moment μ_x (top panel), molecular polarizability α (central panel), and total net charges (bottom panel) on the Fc (continuous line) and PTM (dashed line) units. Regions within dotted and dash-dotted vertical lines approximately mark the neutral and the ionic regimes, respectively, corresponding to regions of flat α.*

polarizability (in the central panel of figure 2.9), $\alpha \propto \frac{\partial \mu_x}{\partial F}$, shows a large peak. This allows to separate two regions of almost constant polarizability, whose boundaries in the figure are marked by dotted and dash-dotted vertical lines. These two regions correspond to two different regimes for FcPTM: an almost neutral regime where the ground state is largely dominated by the $|DA\rangle$ state and an ionic regime, dominated by the $|D^+A^-\rangle$ state.

To further support this interpretation, the bottom panel of figure 2.9 shows the total charges on the Fc unit (continuous line) and PTM unit (dotted line). The sum of the charges on the two units is approximately zero, confirming the picture of a charge transfer from D to A groups with an electrically neutral π-bridge. Moreover, in the small $|F|$ regime the net charge on each unit is is approximately zero, while the region of the second plateau corresponds to a system where one electron is transferred from Fc to PTM. A reasonable estimate of the charge distribution in the zwitterionic state of the FcPTM molecule is therefore given by the Coulson net point atomic charges, obtained with PM6 calculations on the FcPTM molecule in an electric field $0.65 < F < 0.9$ $V/\text{Å}$, corresponding to region delimited by dash-dotted lines in figure 2.9.

The change in the dipole moment μ_x going from the neutral to the ionic regime gives an independent estimate of μ_0, amounting to 50-60 D. This value corresponds to dipole length of about 10-12 Å, close to the crystallographic distance.

We can now estimate $\mathscr{M}$ relevant for the FcPTM crystal on the basis of the molecular charge distribution obtained for Fc-PTM in the ionic regime, as in fig. 2.9. The $\mathscr{M}$ calculation for this charge distribution has been performed summing up all interactions among ~19000 molecular sites ($17 \times 17 \times 33$ unit cells). According to the experimental crystal structure there are two molecules equivalent for symmetry. The two molecules per cell will be labeled with $l = 1, 2$, and each cell can be described by an index $I \equiv \{ijk\}$. Each atom belonging to the l molecule is described by an index σ. The expression for $\mathscr{M}$ is then the sum of the interaction between charges on atoms μ of a chosen molecule with the charges on atoms μ' on all other molecules in the crystal:

$$\begin{aligned} \mathscr{M} &= \frac{1}{2}\sum_{\mu}\sum_{\mu'\neq\mu}\frac{q_\mu q_{\mu'}}{r_{\mu\mu'}} \\ &= \frac{1}{2}\sum_{\mu} q_\mu \sum_{I\equiv\{ijk\}}^{n_a,n_b,n_c}\sum_{l}^{2}\sum_{\mu}\frac{q_{l,\sigma}}{|r_\mu - (iA + jB + kC + r_{l\sigma})|} \end{aligned} \tag{2.10}$$

the second line contain a more specific expression, being μ' explicitly identified in term of cell $\{ijk\}$, molecule l, and atom σ. A, B, C are the crystallographic axis and $r_{\sigma l}$ is the position of the atom in the unit cell.

For F values corresponding to the ionic regime (region within dash-dotted lines in figure 2.9) we estimate $\mathscr{M}$ ranging between -1.0 eV (for $F = 0.65\ V/\text{Å}$) to -1.5 eV(for $F = 0.9$ V/Å). This result safely locates FcPTM crystals in the bistability region of figure 2.7.

Additional information can be obtained using the expression 2.10 to calculate the electrostatic energies relevant to the charge distributions obtained for different F. Results are shown in fig. 2.10 for two molecular geometries extracted from the crystal structure. In the neutral regime (region within dotted lines) the electrostatic energy is < 0.05 eV, confirming that electrostatic interactions between fully neutral molecules are negligible. On the other hand, the electrostatic energy becomes large and negative in the zwitterionic region. The effects of molecular conformations are minor.

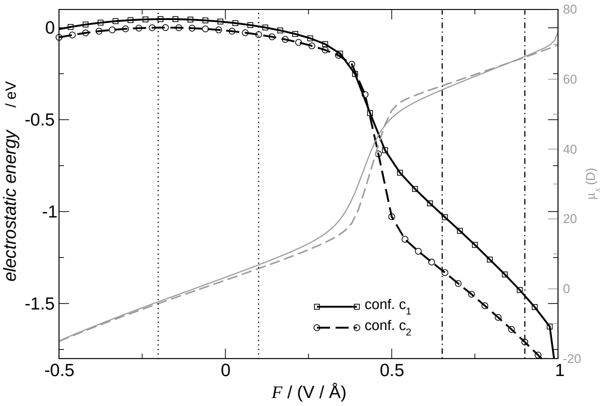

Figure 2.10: *Calculation of the electrostatic energy according to eq. 2.10 at different field F value (black lines, scale on the left) and dipole moments (gray lines, scale on the right), for configuration c_1 (cont. lines) and c_2 (dashed lines). As in fig. 2.9 region between dotted and dash-dotted vertical lines marks the neutral and ionic regimes, respectively.*

2.1.5 Bistability in FcPTM crystal: Mössbauer spectra

We now apply the model for bistability in FcPTM crystals to explain the T dependent Mössbauer spectra of FcPTM crystals. In the 4.2 K spectrum only the doublet assigned to the neutral Fc appears, indicating that the neutral $DA^\bullet$ form of FcPTM largely dominates at low temperature. With increasing temperature, an additional doublet appears in Mössbauer spectra, characteristic of the ferrocinium ion (Fc$^+$), signaling the presence of the $D^{+\bullet}A^-$ form of FcPTM. The intensity of the Fc$^+$ doublet increases with temperature at the expense of the Fc signal, suggesting an increasing population of the $D^{+\bullet}A^-$ form. At 293 K the relative intensity of the two signals is similar [80].

This behavior can be rationalized accounting for the thermal population on an ionic metastable state. Indeed Mössbauer spectra in figure 2.11 can be quantitatively reproduced in term of the Boltzmann population of an ionic metastable state separated from a neutral stable state by a temperature independent energy gap $\Delta E = 14$ meV ≈ 160 K. This energy gap is obtained with the mf Hamiltonian in equation (2.8), adopting FcPTM molecular parameters obtained from solution spectra and $\mathscr{M} = -1.1$ eV, consistent with estimates based on PM6 calculations (see panel **b** of figure 2.8). Experimental Mössbauer spectra in figure 2.11 are fitted as a Boltzmann-weighted sum of two couples of Lorentzian bands (for Fc and Fc$^+$ doublets) with adjustable positions and widths [99].

It is worthy to remind the most important approximations involved. We assume crystal structure fixed and identical to the structure experimental determined at 223 K. Some conformational disorder for the Fc rings and the π bridge is observed, and two molecular conformations are reported [80]. However, the $\mathscr{M}$ calculation performed on the two structures lead to similar results, within the uncertainty $\mathscr{M} \sim -1 \div -1.5$ (see fig. 2.10). In principle one expects a temperature dependent $\mathscr{M}$ and hence a temperature dependent energy gap between the two stable states. However, in the lack crystallographic data recorded at different T we impose temperature independent $\mathscr{M}$. In view of the many approximations involved in the model, the overall quality of the fit (red lines in figure 2.11) is very good.

The Ferrocinium ion itself, shows actually a twofold degeneracy in the electronic ground state [100, 101]. However, the reduced symmetry of the Fc unit in the FcPTM molecule most probably remove the degeneracy [102, 103]. Therefore we simulate some results considering a degeneracy factor $1 \leq d_{el} < 2$. The effect of degeneracy on calculated $\mathscr{M}$ spectra is however minor.

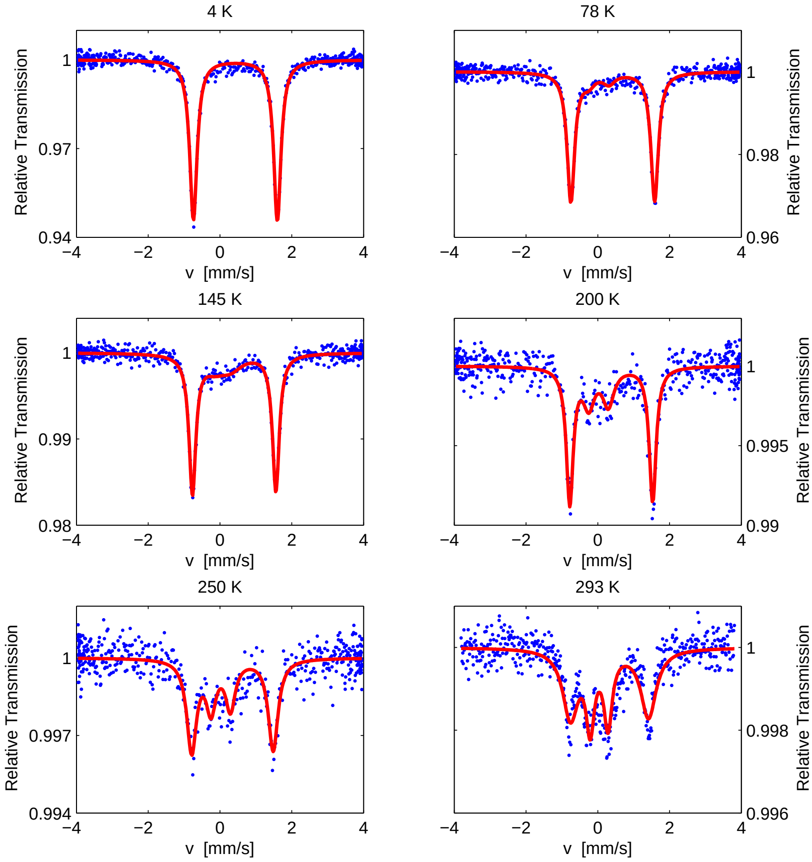

Figure 2.11: *Temperature dependence of Mössbauer spectra of FcPTM. Dots are experimental data from ref. [80]. Red lines are fittings of experimental data based on the proposed model for bistability.*

2.1.6 FcMe$_9$PTM in solution: the need for a three state model

A detailed analysis of FcMe$_9$PTM optical absorption spectra, reported in the right upper panel of figure 2.13, reveals the presence of a shoulder around 15000 cm^{-1}, that is assigned to a secondary CT absorption implying a π-bridge to A transition [79], in agreement with chemical intuition. This is further corroborated by the weak solvatochromism of this band. Similar features are observed for FcPTM around 15000-17000 cm^{-1} [79] (see left upper panel of figure 2.13), but in this case, the overlap with the localized absorption of the Fc unit makes the analysis delicate.

A three state model

To account for the secondary CT bands involving the π-bridge, at least the three resonating structures $D\pi A \longleftrightarrow D\pi^+A^- \longleftrightarrow D^+\pi A^-$, must be accounted for, where the first and the last structures (corresponding to the the DA and the D^+A^- structures of the previous section) largely dominate over the second one, that represents an higher energy state. The CT occurs through the bridge, and on the basis of the states, $|D\ \pi\ A\rangle$, $|D\ \pi^+A^-\rangle$ and $|D^+\pi\ A^-\rangle$, the electronic Hamiltonian reads [83]:

$$\hat{h}_{el}^{(3)} = 2\tilde{z}\ \hat{\rho}_D + 2\tilde{x}\ \hat{\rho}_\pi - \tilde{\tau}\ \hat{\sigma}_{(3)} \tag{2.11}$$

where the operators

$$\hat{\rho}_D = \begin{pmatrix} 0 & 0 & 0 \\ 0 & 0 & 0 \\ 0 & 0 & 1 \end{pmatrix} \quad \text{and} \quad \hat{\rho}_\pi = \begin{pmatrix} 0 & 0 & 0 \\ 0 & 1 & 0 \\ 0 & 0 & 0 \end{pmatrix} \tag{2.12}$$

measures the charge transferred from the D and from the π-bridge to A respectively, and

$$\hat{\sigma}_{(3)} = \begin{pmatrix} 0 & 1 & 0 \\ 1 & 0 & 1 \\ 0 & 1 & 0 \end{pmatrix} \tag{2.13}$$

accounts for the mixing between the $|D\ \pi\ A\rangle$ and the $|D^+\pi\ A^-\rangle$ states, mediated by the bridge state; $2\tilde{x}$ and $2\tilde{z}$ measure the energy of the states $|D\ \pi^+A^-\rangle$ and $|D^+\pi\ A^-\rangle$ respectively, having set to zero the energy of the $|D\ \pi\ A\rangle$ state (the tilde identifies the three-state model parameters with respect to the two-state model parameters in the previous section). As discussed above, the CT state involving the bridge is higher in energy that the main CT state, i.e. $\tilde{x} > \tilde{z}$.

A detailed parametrization of the three-state model is difficult, particularly because of the large overlap of the second absorption band with higher energy absorptions in both compounds. In the absence of additional data (like, e.g. the absorption from the first excited state) in order to avoid the proliferation of free parameters, the Hamiltonian matrix elements that describe the electron hopping from the bridge to the acceptor $\langle D\pi A|h^{(3)}|D\pi^+A^-\rangle = -\tilde{\tau}_\pi$ and from the donor to the bridge $\langle D^+\pi A|h^{(3)}|D\pi^+A^-\rangle = -\tilde{\tau}_D$, are set equal: $\tilde{\tau}_D = \tilde{\tau}_\pi = \tilde{\tau}$.

In close analogy with the two state model, the only relevant element of the dipole moment operator are the diagonal element for the CT states:

$$\hat{\mu}_{(3)} = \begin{pmatrix} 0 & 0 & 0 \\ 0 & \alpha\mu_0 & 0 \\ 0 & 0 & \mu_0 \end{pmatrix} \tag{2.14}$$

where $\tilde{\mu}_0$ is the dipole moment of the $|D^+A^-\rangle$ state. The dipole moment of the $|D\pi^+A^-\rangle$ state, $\alpha\mu_0$ is defined as a fraction of the first, and, again, to avoid too many parameters, is set to half μ_0, so $\alpha = \frac{1}{2}$. This choice locates the centroid of positive charge of the bridge state just halfway between the D and A centers.

As in the two-state model, the coupling to an effective molecular vibration is introduced assigning harmonic PESs with same frequency but different equilibrium geometries to the basis states, as shown in the left panels of figure 2.12. The description is made with a single vibrational coordinate q, corresponding to a single effective mode, that couples to the two electronic basis states. The Hamiltonian including the molecular vibration then reads:

$$\hat{h}^{(3)}_{el+ph} = 2\tilde{z}\;\hat{\rho}_D + 2\tilde{x}\;\hat{\rho}_\pi - \tilde{\tau}\;\hat{\sigma}_{(3)} - \omega_v\sqrt{2\tilde{\varepsilon}_v}\left(\hat{\rho}_D + a_\pi\hat{\rho}_\pi\right)q + \frac{1}{2}\omega_v^2 q^2 \tag{2.15}$$

where the a_π factor accounts for the possible different coupling of the $|D\pi^+A^-\rangle$ compared to the $|D^+\pi A^-\rangle$ state. Different geometries can occurs for each of the three basis states, leading to two independent vibrational relaxation energies for $D\pi^+A^-$ and $D^+\pi A^-$ states. However, getting reliable information on the vibrational coupling of the third state is difficult, and we impose the same geometry on the two charge-separated states (see figure 2.12, left panel), so that the same relaxation energy, $\tilde{\varepsilon}_v$, applies to both states (i.e. $a_\pi = 1$). Different choices are of course possible but do not alter main results.

Polar solvation is treated again in the framework of the reaction field model, with the reaction field proportional to the molecular dipole moment. Since the dipole moment of the third state is set to a fixed fraction of $\tilde{\mu}_0$, polar solvation is described by the single parameter $\tilde{\varepsilon}_{or}$. The total Hamiltonian, accounting for

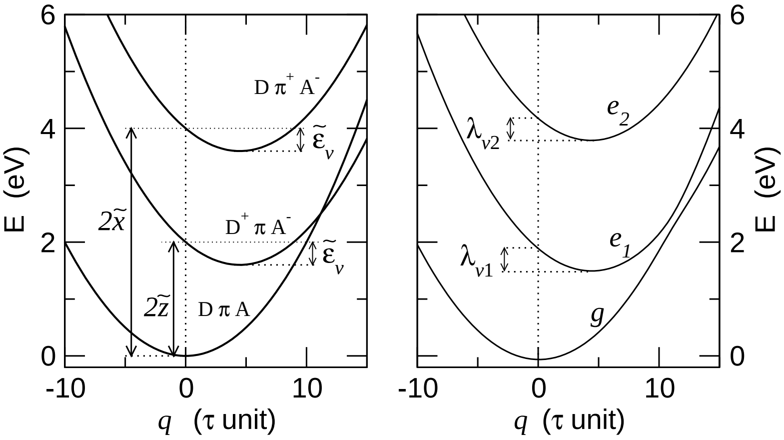

Figure 2.12: *Basis states (left panels) and eigenstate (right panel) PES for the three-state model in equation (2.16) with* $\tilde{z}$= 1 *eV,* $\tilde{x}$= 2 *eV,* $\tilde{\tau}$= 0.5 *eV* $\tilde{\omega}_v$= 0.2 *eV,* $\tilde{\varepsilon}_v$= 0.4 *eV and* $\tilde{\varepsilon}_{or}$= 0 *eV.*

both vibrational coupling and polar solvation, finally reads:

$$\begin{aligned} \hat{h}^{(3)}(q,f) \;=\; & \left(2\tilde{z} - \sqrt{2\tilde{\varepsilon}_v}\,\omega_v\, q - f\right)\hat{\rho}_D \\ & + \left(2\tilde{x} - \sqrt{2\tilde{\varepsilon}_v}\,\omega_v\, q - \frac{1}{2}f\right)\hat{\rho}_\pi \\ & - \tilde{\tau}\;\hat{\sigma}_{(3)} + \frac{1}{2}\tilde{\omega}_v q^2 + \frac{1}{4\tilde{\varepsilon}_{or}} f^2 \end{aligned} \tag{2.16}$$

where again the tilde marks symbols relevant to the three-state model. For each f, the diagonalization of the q-dependent Hamiltonian leads to three q-dependent eigenstates, that describe the PES relevant to the ground state, g, and to the first and second excited states, e_1 and e_2, respectively. The geometry of equilibrium for each adiabatic state is: $q_{eq,i} = \frac{\sqrt{2\tilde{\varepsilon}_v}}{\omega_v}\left(\langle\rho_D\rangle_i + \langle\rho_\pi\rangle_i\right)$ with $i = g, e_1, e_2$ The right panel of figure 2.12 shows the PES obtained for a specific set of parameters. The vibrational eigenstates are constructed on each PES in the harmonic approximation [84, 85] and optical spectra are finally calculated. The calculation is repeated for different f, and the spectra are obtained as Boltzmann averages with the same approach described for other compounds.

The proposed procedure to calculate spectra exploits the adiabatic approximation, as mentioned in sect. 1.1 for the two state model. The vibrational relaxation energy λ_{vi} is shown in the left panel of figure 2.12, and can be calculated at each f coordinate value. More details about spectra calculation can be

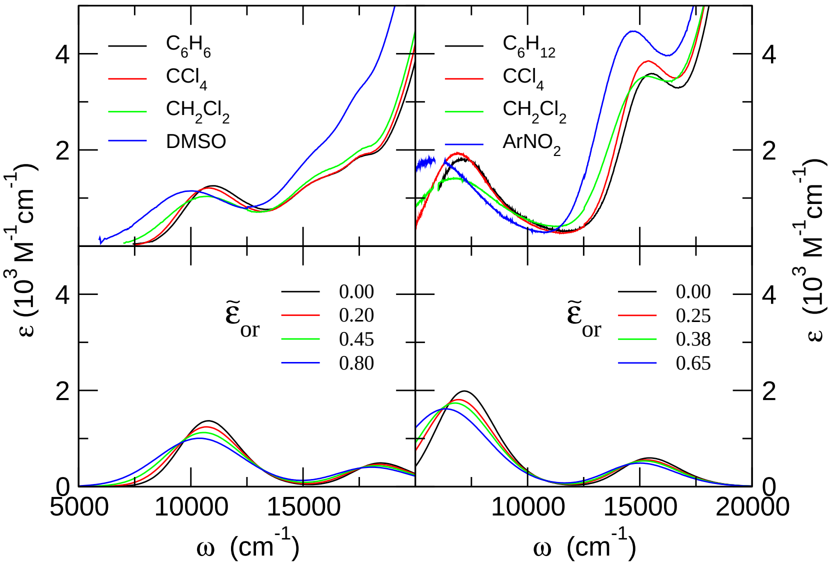

Figure 2.13: *Optical spectra of FcPTM (left panel) and Me$_9$FcPTM (right panel) in different solvents. Top panels: experimental spectra. Bottom panels: spectra calculated in the three state model with parameters of table 2.2, and setting the intrinsic bandwidth* $\Gamma = 0.07$ *eV.*

found in the appendix sect. B.1.2.

Results

Bottom panels of figure 2.13 show spectra calculated for the parameters in table 2.2. The vibrational frequencies and the intrinsic line width are set to the same values as in the two-state model. To facilitate the comparison, experimental spectra are reported in the upper panels of the same figure. As expected, the three-state model results in two absorption bands, which reproduce the experimental observation of two solvatochromic CT absorption bands. A detailed comparison of calculated and experimental spectra is hindered, particularly for FcPTM, by the overlap of the secondary CT band with nearby localized absorption bands. It is certainly possible to improve the quality of calculated spectra by increasing the number of parameters, like adopting two different τ for the two matrix elements (allowing for different τ_D and τ_π values.) However the basic role of bridge states is captured already in the simplest model.

From table 2.2, it turns out that $\tilde{x} > \tilde{z}$ for both compounds, as required on

Table 2.2: *Molecular parameters for FcPTM and FcMe$_9$PTM described in the three-state model.*

molecular parameter	FcPTM	FcMe$_9$PTM
$\tilde{z}$ / eV	0.78	0.50
$\tilde{x}$ / eV	0.87	0.69
$\tilde{\tau}$ / eV	0.47	0.47
$\tilde{\mu}_0$ / D	15.0	15.5
$\tilde{\varepsilon}_v$ / eV	0.06	0.07
$\tilde{\omega}_v$ / eV	0.18	0.18

solvent parameter		FcPTM	FcMe$_9$PTM
$\tilde{\varepsilon}_{or}$/ eV	cyclohexane	0.0	0.0
	CCl$_4$	0.10	0.08
	dichloromethane	0.20	0.20
	ArNo$_2$		0.42
	DMSO	0.65	

physical basis. Moreover $\tilde{\tau}$, which measures the direct charge hopping from either the D or the A site to the bridge, is larger than the bridge-mediated hopping, τ, in the two-state model (see table 2.1). The effective strength of the vibrational coupling is roughly halved in the three-state model, suggesting that the effective ε_v estimated in the two-state model is roughly the sum of the contributions from the two excited states. The values of the solvent relaxation energy in the three-state model are larger than the corresponding two-state model results (see table 2.1). This increase compensates for the reduction of the mesomeric dipole moment in the three-state model. The sizable weight of the $D\pi^+A^-$ in the first excited state in fact leads to a decrease of the relevant dipole moment with respect to the two-state model, so that larger solvent relaxation energies are required in the three-state model with respect to the two-state model to reproduce the same solvatochromism. While microscopic models relate the solvation relaxation energy to the solvent dielectric constant, refractive index and to the size and shape of the cavity occupied by the solute [27, 19, 33], this analysis demonstrates that ε_{or} is best treated as an adjustable parameter, whose specific value also depends on the model adopted to describe the solute electronic structure.

Finally the effective dipole lengths extracted in the three-state model, $\tilde{\mu}_0$ in table 2.2, are about twice the corresponding estimate in the two-state model

	basis states					energy	dipole
$\|N\rangle$	D	b_1	b_2	b_3	A	0	0
$\|3^+\rangle$	D	b_1	b_2	b_3^+	A^-	$2\tilde{x}$	$1/4\ \tilde{\mu}_0$
$\|2^+\rangle$	D	b_1	b_2^+	b_3	A^-	$2\tilde{x}$	$1/2\ \tilde{\mu}_0$
$\|1^+\rangle$	D	b_1^+	b_2	b_3	A^-	$2\tilde{x}$	$3/4\ \tilde{\mu}_0$
$\|Z\rangle$	D^+	b_1	b_2	b_3	A^-	$2\tilde{z}$	$\tilde{\mu}_0$

Figure 2.14: *Schematic representation of the basis state for a 5 state molecule (3 bridge states) with corresponding energies and dipole moments.*

(table 2.1) and correspond to a *DA* distance of 3.1 and 3.3 Å for FcPTM and FcMe$_9$PTM, respectively. These values are still small compared with the geometrical DA distance (9.5 and 9.7 Å for FcPTM and FcMe$_9$PTM), but they considerably improve over the corresponding estimates obtained in the two state approach, leading to a ratio between the geometrical and spectroscopic estimate of the *DA* distance in line with similar results for other *DA* molecules [46, 86, 33, 84, 87, 88, 89, 90, 91]. This result suggests to investigate in mode detail the role of the bridge state in effective models for *DA* chromophores.

2.1.7 The role of low energy bridge states

An electronic model to account for active bridge states

The increase of the estimated μ_0 by a factor ~ 2 when going from a two-state to a three-state model for either FcPTM and FcMe$_9$PTM suggests a way to solve a long-standing paradox in model for *DA* chromophores. It is well known in fact that dipole lengths estimated from the analysis of *DA* spectra always severely underestimate the *DA* distance [87, 88, 89, 90, 91]. To generalize the result we consider here a purely electronic model for a n-site molecule, where the electron is transferred from D to A via $n-1$ hops involving only adjacent $n-2$ bridge states [83]. The resulting n states are schematically shown in figure 2.14 for $n=5$. The same energy $2\tilde{x}$ is assigned to all bridge states, while the D^+A^- ($|Z\rangle$) state has energy $2\tilde{z} < 2\tilde{x}$. The same hopping integral $\tilde{\tau}$ describes the CT between all adjacent sites along the chain. The relevant Hamiltonian is a trivial extension of the three-state electronic Hamiltonian in equation (2.11):

$$\hat{h}_n = \begin{pmatrix} 0 & -\tilde{\tau} & 0 & 0 & \cdots & 0 & 0 \\ -\tilde{\tau} & 2\tilde{x} & -\tilde{\tau} & 0 & \cdots & 0 & 0 \\ 0 & -\tilde{\tau} & 2\tilde{x} & -\tilde{\tau} & \cdots & 0 & 0 \\ 0 & 0 & -\tilde{\tau} & 2\tilde{x} & \ddots & \vdots & \vdots \\ \vdots & \vdots & \vdots & \ddots & \ddots & -\tilde{\tau} & 0 \\ 0 & 0 & 0 & \cdots & -\tilde{\tau} & 2\tilde{x} & -\tilde{\tau} \\ 0 & 0 & 0 & \cdots & 0 & -\tilde{\tau} & 2\tilde{z} \end{pmatrix} \tag{2.17}$$

Consistent with the three-state model described in the previous section, the dipole moment of the $|Z\rangle$ state is set to $\tilde{\mu}_0$, while the dipole moments of bridge states are fractions of $\tilde{\mu}_0$, as relevant to a system with equally spaced sites (see figure 2.14), leading, for the general case in equation (2.17), to the following values:

$$\hat{\mu}_n = \begin{pmatrix} 0 & 0 & 0 & 0 & \cdots & 0 & 0 \\ 0 & \frac{\tilde{\mu}_0}{(n-1)} & 0 & 0 & \cdots & 0 & 0 \\ 0 & 0 & \frac{2\tilde{\mu}_0}{(n-1)} & 0 & \ddots & 0 & 0 \\ 0 & 0 & 0 & \frac{3\tilde{\mu}_0}{(n-1)} & \ddots & \vdots & \vdots \\ \vdots & \vdots & \vdots & \ddots & \ddots & 0 & 0 \\ 0 & 0 & 0 & \cdots & 0 & \frac{(n-2)\tilde{\mu}_0}{(n-1)} & 0 \\ 0 & 0 & 0 & \cdots & 0 & 0 & \tilde{\mu}_0 \end{pmatrix} \tag{2.18}$$

We limit our attention to a systems with an almost neutral ground state, in which bridge sites are weaker donors than D, so that $0 < \tilde{z} < \tilde{x}$. For $\tilde{x} - \tilde{z} \gg \tilde{\tau}$ bridge states become very high in energy and a perturbative treatment on $\tilde{\tau}/(2\tilde{x}-2\tilde{z})$ reduces the n-state model to an effective two-state model with $z_0 = \tilde{z}$, $\mu_0 = \tilde{\mu}_0$ and

$$\tau = \frac{\tilde{\tau}^{n-1}}{(2\tilde{x} - 2\tilde{z})^{n-2}} \tag{2.19}$$

where, as before, the tilde applies to symbols relevant to the n-state model, while bare symbols refer to the two-state model. n-site (or n-state) molecules have $n-1$ optical excitations whose energies and transition dipole moments are shown in figure 2.15 as a function of $\tilde{x}-\tilde{z}$ for systems with $n = 3$, 4, and 5 sites.

In all cases, model parameters have been chosen as to converge, in the large $\tilde{x}$ limit, to the two-state model with $z_0 = \tau = 1$, and $\mu_0 = 1$ (in this section, we work fixing τ as the energy unit and μ_0 as the unit dipole moment). With this

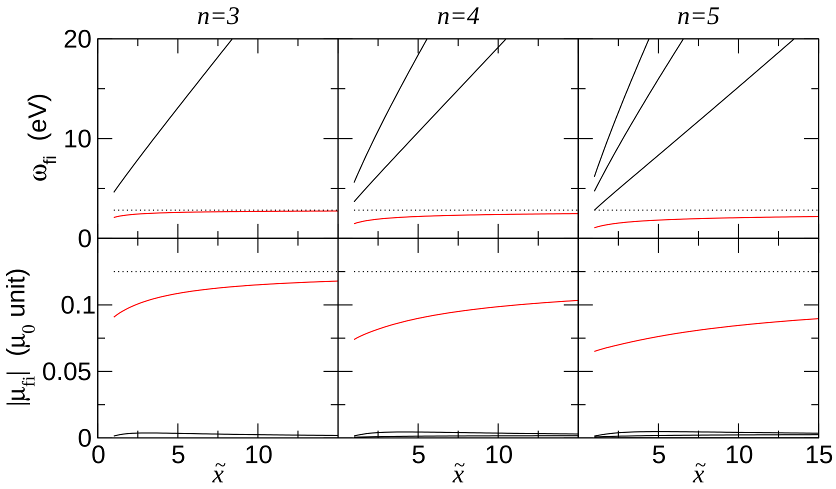

Figure 2.15: *Transition energies (top panels) and squared transition dipole moments (bottom panels) calculated for n = 3, 4 and 5 state models (panels from left to right) with* $\tilde{z}$= 1, $\tilde{\mu}_0$= 1, *variable* $\tilde{x}$ *and* $\tilde{\tau}= \left(\tau(2\tilde{x})^{n-2}\right)^{\frac{1}{n-1}}$. *Red lines refer to the lowest energy (main CT) transition. Dotted lines show the (*$\tilde{x}$*-independent) results relevant to the limiting two-state model (see text).*

choice, we expect convergence, in the large $\tilde{x}$ limit, to a two-state model with $\rho \approx 0.15$ (see equation 1.5). The corresponding limiting values of the transition frequency and squared transition dipole moments ($\omega_{CT} \approx 2.8$ and $\mu_{CT} \approx 0.13$) are shown as dotted lines in figure 2.15.

The lowest energy transition, corresponding to the main CT band (marked by red lines in figure 2.15) is well separated from higher energy transitions involving bridge states and has by far the largest intensity: the main CT transition dominates the low energy portion of the spectrum. The corresponding energies and transition dipole moments (red lines in figure 2.15) properly converge toward the two-state limit (dotted lines) for $\tilde{x} - \tilde{z} \rightarrow \infty$ (or equivalently $\tilde{x} \rightarrow \infty$). The convergence becomes slower with increasing n.

To investigate the effect of bridge states in the definition of an effective two-state model and in particular on the estimate of the relevant dipole length, we focus attention on the lowest energy, main CT absorption, disregarding higher energy transitions involving the bridge. Indeed, this is consistent with the treatment of experimental data, where we concentrate on the lowest energy transitions modeled in term of a two state model. In other terms, we analyze the data relevant to the main CT transition, obtained from the diagonalization of

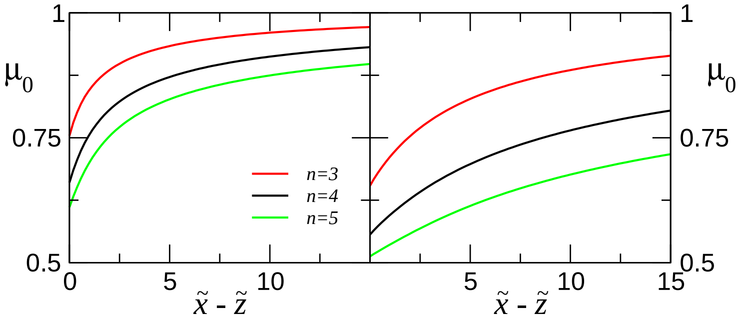

Figure 2.16: *Dipole length extracted from the two-state analysis of the main CT band of the n-state models described in figure 2.15. Left panel shows results obtained by extracting the two-state model parameters (x, τ and μ_0) from the frequency, the squared transition dipole moment and the mesomeric dipole moment; right panel shows similar results obtained using the ground state dipole moment instead of the mesomeric dipole moment.*

the n-state model, to extract an effective two-state model in an analogous way as usually done by analyzing experimental absorption spectra. In particular, the parameters of the effective two-state model, τ, z (or equivalently ρ), and μ_0, can be estimated from three spectral properties. Equations (1.8), (1.7) and (1.10) are therefore used to extract ρ, τ, and μ_0 out of the transition frequency, transition and mesomeric dipole moment (difference between ground and excited state dipoles, a quantity directly related to solvatochromism) calculated in the n-state model. If $d = \frac{\Delta\mu}{\mu_{ge}}$ it results:

$$\begin{aligned} \rho_\pm &= \frac{d^2+4\pm|d|\sqrt{d^2-4}}{2d^2+8} \qquad \mu_0 = \frac{\mu_{ge}}{\sqrt{\rho(1-\rho)}} \\ \tau &= \omega_{ge}\frac{\mu_{ge}}{\mu_0} \end{aligned} \tag{2.20}$$

The right panel of figure 2.16 shows the $(\tilde{x}-\tilde{z})$ dependence of the effective μ_0 estimated along these lines for the n =3, 4, and 5 state models in figure 2.15. In all cases the effective μ_0 converges toward the exact limit, $\mu_0 = 1$, for $\tilde{x} \to \infty$, but it is always underestimated for any finite $\tilde{x}$, i.e. when bridge states are closer in energy to the $D^+ \cdots A^-$ ($|Z\rangle$) state. It is worth noting that μ_0 deviates more from the limiting value with increasing the number of bridge state.

Different estimates of the effective two-state model parameters can be obtained if a different choice is made about the reference spectral properties, i.e.

the quantities that represent the set of experimentally accessible information. In fact, using equations (1.7), (1.8) and (1.9), the parameters of the effective two-state model can be extracted by reproducing the transition frequency, transition dipole moment and ground state dipole moment (instead of mesomeric dipole moment). In this case, the following equation for ρ stands:

$$\rho = \frac{1}{\left(\frac{\mu_{ge}}{\mu_g}\right)^2 + 1} \tag{2.21}$$

The effective μ_0 obtained according to this alternative procedure (right panel of figure 2.16) shows a qualitatively similar behavior to the previous one and even larger deviations from the limiting value than before.

This discussion clearly demonstrates that the unphysically small *D*–*A* distances, extracted from the two-state model analysis of optical spectra of *DA* molecules [87, 88, 89, 90, 91], results from the presence of low-lying bridge states, playing an active role in the *D* to *A* CT. The larger discrepancy between the geometrical and spectroscopic values of μ_0 obtained for FcPTM and Me$_9$FcPTM with respect to common organic *DA* chromophores, is then naturally explained by the presence of (at least) a secondary low-lying CT transition in the absorption spectra. Moreover this picture explains why this discrepancy is not observed in the μ_0 values obtained from the optical spectra of CT complexes and crystals. In CT complex and crystals, the intermolecular CT occurs trough space because of the direct overlap of frontier orbitals. Optical spectra of these systems can be described by the same two state model of DA molecules. However in these systems, where the *D* to *A* CT is not mediated by any virtual state, the dipole lengths obtained from the intensity of the CT bands are well comparable with geometrical distances. [104, 105, 106, 107]

2.1.8 Three-state models for bistability

In section 2.1.6 we introduced a three-state model for the description of the low energy physics of FcPTM and FcMe$_9$PTM. Following the bottom up modeling approach and in strict analogy with the model for a crystal of two-state molecules presented in section 2.1.2, we now present a model for a crystal of chromophores described in term of a three state model [41]. When molecular units are modeled by the three-state electronic Hamiltonian (eq. 2.11), the charge distribution on each molecule is described by the two operators $\hat{\rho}_D$ and $\hat{\rho}_\pi$, defined in equation (2.12). The electrostatic intermolecular interaction term in in equation (2.1) is:

$$\hat{V}_{ij} = V_{ij}\,\hat{\rho}_{D\,i}\hat{\rho}_{D\,j} + V'_{ij}\,\hat{\rho}_{\pi\,i}\hat{\rho}_{\pi\,j} + V''_{ij}\left(\hat{\rho}_{D\,i}\hat{\rho}_{\pi\,j} + \hat{\rho}_{\pi\,i}\hat{\rho}_{D\,j}\right) \tag{2.22}$$

where the coefficients measure the electrostatic interaction energy between i-th and j-th molecules with different charge distributions. Specifically, V_{ij} measures the interaction between the i-th and j-th molecules both in the $D^+\pi A^-$ state and coincides with the V_{ij} parameter introduced in equation (2.2) for the two-state model; V'_{ij} is instead the interaction between the i-th and j-th molecules both in the $D\pi^+A^-$ state, while V''_{ij} is a mixed term that describes the interaction between the i-th molecule in the $D^+\pi A^-$ state and the j-th molecule in the $D\pi^+A^-$ state or vice versa. We only account for electronic degrees of freedom, since, as discussed in section 2.1.2, molecular vibrations in FcPTM play only a marginal role, and can be implicitly considered by a renormalization of the interaction parameters.

In the mean field (mf) approximation the crystal Hamiltonian reduces to

$$\begin{aligned} H^{(3)}_{\mathrm{mf}} &= \sum_i \Big[2(\tilde{z} + \mathscr{M}\rho_D + \mathscr{M}''\rho_\pi)\hat{\rho}_{D\,i} + 2(\tilde{x} + \mathscr{M}'\rho_\pi + \mathscr{M}''\rho_D)\hat{\rho}_{\pi\,i} \\ &\quad - \tilde{\tau}\hat{\sigma}_{(3)}\Big] - N\left(\mathscr{M}(\rho_D)^2 + \mathscr{M}'(\rho_\pi)^2 + 2\mathscr{M}''\rho_D\rho_\pi\right) \end{aligned} \tag{2.23}$$

where $\mathscr{M}$ is half the Madelung energy, defined in equation (2.3), and

$$\mathscr{M}' = \frac{1}{2N}\sum_{i,j} V'_{ij} \tag{2.24}$$

is the interaction energy of a molecule in the $D\pi^+A^-$ state with the surrounding molecules in the same state, and similarly

$$\mathscr{M}'' = \frac{1}{2N}\sum_{i,j} V''_{ij} \tag{2.25}$$

is the interaction energy of a molecule in the $D\pi^+A^-$state with surrounding molecules in the $D^+\pi A^-$ state (or vice versa). As it is always the case, the mf Hamiltonian leads to a self consistent problem whose solution can be found iterating on the two parameters, ρ_D and ρ_π, corresponding to the ground state expectation values of the $\hat{\rho}_D$ and $\hat{\rho}_\pi$ operators, respectively.

The estimate of the generalized Madelung energies $\mathscr{M}'$ and $\mathscr{M}''$, entering the three-state mf Hamiltonian in equation (2.23) (or equivalently of the V'_{ij} and V''_{ij} terms entering the interaction Hamiltonian in equation (2.22)), is a delicate issue. In fact, it requires information about the charge distribution in the $D\pi^+A^-$ state. As discussed in section 2.1.4 we can force the FcPTM molecule into a $D^+\pi A^-$ state by applying a static electric field, but there is no numerical way to force the FcPTM molecule in the $D\pi^+A^-$ state. We therefore use the crudest approximation, and estimate the interactions accounting for unit charges located at the centroids of the D, A and π-bridge. Locating the centroids of the D group on the Fe atom and that of the A sites on the central C atom of PTM, one estimates $\mathscr{M} = -\ 0.72$ eV. Locating the π-bridge centroid midway between the D and A centroids, we get $\mathscr{M}' = -0.41$ eV and $\mathscr{M}'' = -0.41$ eV. These values of the generalized Madelung energies are very rough and probably represent a lower limit to the actual values. Therefore we use these values just to set the relative magnitude of the three energies as $\mathscr{M}' = \mathscr{M}'' = 0.6\mathscr{M}$. With these ratios fixed, we solve by iteration the self consistent mf Hamiltonian in equation (2.23) for the (electronic) molecular parameters obtained from the three-state analysis of the two CT bands of FcPTM, reported in table 2.2.

As described in detail in [41] a wide bistability region is found where a largely neutral and a largely ionic state are both accessible to the system. The width of the bistability window depends on the $\mathscr{M}'/\mathscr{M}$ and $\mathscr{M}''/\mathscr{M}$ ratios, and increases when the two ratios decrease. In any case, apart from quantitative aspects, bistability is a robust phenomenon, and survives reasonable choices of the generalized Madelung energies. As observed for the two-state model, bistability is suppressed by increasing the hybridization energy (see continuous curve in fig. 4 in [41]) .

2.2 $FcPyl^+$-based materials: extending the bistability model to ionic crystals

A temperature–dependence valence tautomerism, very similar to those observed for FcPTM, was recently observed by Kondo *et al.* in a ferrocenyl-oxodihydrodibenzochromenylium salt, $FcPyl^+$ X^-, with X^-=$TFSI^-$, PF_6^-, BF_4^- [78], where TFSI is the organic anion trifluoromethanesulphoneimide.

$FcPyl^+$ is a Fc-based DA molecular cation characterized by the charge resonance $FcPyl^+ \longleftrightarrow Fc^+Pyl$ (see fig. 2.17). Notice that $FcPyl^+$ has an even number

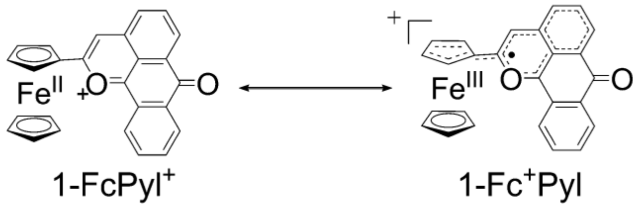

Figure 2.17: Molecule characterized in [78], and re-examined here.

of electrons, thus the structure on the left of fig. 2.17, DA^+, corresponds to a closed shell configuration, while the CT structure D^+A has a biradical character ($D^{\bullet +}A^{\bullet}$).

Quite interestingly, the solid state valence tautomerism of $FcPyl^+$, detected by Mössbauer spectroscopy, depends on the counterion. In particular, while with two counterions ($TFSI^-$ and PF_6^-) a growing intensity of the Fc^+ doublet is observed with increasing temperature (with a similar behavior as observed for FcPTM), Mössbauer spectra of the third compound (counterion BF_4^-) present only the Fc doublet at all the temperature. The counterion-dependent behavior suggests that also in this case electrostatic interactions play an important role. However, the model presented above for crystal of neutral DA molecules does not immediately apply to crystals of molecular ions. In fact, the molecular two-state model applies quite irrespective of the net molecular charge, but the treatment of intermolecular interactions in a crystal of molecular ions requires a specific model.

As for the molecular model, we adopt a (purely electronic) two state model, with 1-$FcPyl^+$ in fig. 2.17 playing the role of DA and 1-Fc^+Pyl playing the role of D^+A^-. Optical spectra of FcPyl in solution, reported in [78], show a CT absorption band at $\sim$ 10000 cm^{-1}, with molar extinction coefficient ϵ = 2.3 - 2.5 10^3

M^{-1} cm^{-1} at the maximum. On this basis we fix the two state model parameters as in table 2.3, neglecting both the coupling with the vibrations and with solvation coordinates. The parameters are similar to those obtained for FcPTM, and represent a reasonable preliminary estimate. Additional experimental data are needed to obtain more reliable estimates. However, the precise value of these parameters is not critical for our discussion.

Table 2.3: *Approximated values of the two state model parameters extracted on the basis of the optical spectra [78].* $\Gamma = 0.17$ *eV.*

z_0 / eV	0.57
τ / eV	0.30
μ_0 / D	13

2.2.1 The model for a molecular ion crystal

To address electrostatic interactions we simplify the notation defining the molecular cationic FcPyl unit as M^+, while X^- represents the counterion (either $TFSI^-$, PF_6^- or BF_4^-). The two crystals with PF_6^- and BF_4^- counterions are isostructural, and all three have four equivalent MX unit per cell, $Z = 4$. Unit cells are labeled as $I, J\dots$; the unit formulas MX within a cell are numbered as $l, m\dots$, and the atomic sites are labeled in this as $\mu \in M^+$, $\chi \in X^-$. The electrostatic interaction energy is:

$$\begin{aligned}
\mathscr{E} \;=\; & \sum_I \sum_l \Bigg\{ \sum_{\mu\chi} \frac{\mathrm{q}_\mu \mathrm{q}_\chi}{R^{\mu\chi}_{II,mm}} + \\
& + \frac{1}{2} \sum_J \sum_{\substack{J=I\,:\,m\neq l \\ J\neq I\,:\,m}}^{Z} \Bigg[\sum_{\mu\chi} \mathrm{q}_\mu \mathrm{q}_\chi \left(\frac{1}{R^{\mu\chi}_{IJ,lm}} + \frac{1}{R^{\chi\mu}_{IJ,lm}} \right) \\
& \sum_{\mu\mu'} \frac{\mathrm{q}_\mu \mathrm{q}_{\mu'}}{R^{\mu\mu'}_{IJ,,lm}} + \sum_{\chi\chi'} \frac{\mathrm{q}_\chi \mathrm{q}_{\chi'}}{R^{\chi\chi'}_{IJ,lm}} \Bigg] \Bigg\}
\end{aligned} \tag{2.26}$$

where q_μ and q_χ are the charges on the μ and χ atomic sites of the M^+ and X^- units and $R^{\mu\mu'}_{IJ,lm}$ is the distance between the μ atom of l molecule (ion) in the I cell and the μ' atom of the m molecule in the J cell.

To proceed we relate the charge distribution of M^+ to the ρ operator that describes the charge distribution in the two state model. We set:

$$\mathrm{q}_\mu = \mathrm{q}_\mu^0 + \delta_\mu \hat{\rho} \tag{2.27}$$

so that the charge on each atomic site is the charge residing on the site when the molecule is in the *DA* state (q_μ^0) plus a fraction ρ of δ_μ, that measures the variation of charge on the site when ρ goes from 0 to 1. By the way, the charge distribution on the anion X$^-$ is not affected by ρ (q_χ is constant). With this definition we rewrite the eq. 2.26, as follows:

$$\begin{aligned}
\mathscr{E} \;=\; & \sum_I \sum_l \Bigg\{ \mathscr{E}_0^{II}(\mathrm{q}_\mu^0 \mathrm{q}_\chi) \\
& + \sum_J \left[\mathscr{E}_0^{IJ}(\mathrm{q}_\mu^0 \mathrm{q}_{\mu'}^0) + \mathscr{E}_0^{IJ}(\mathrm{q}_\mu^0 \mathrm{q}_\chi) + \mathscr{E}_0^{IJ}(\mathrm{q}_\chi \mathrm{q}_\mu^0) + \mathscr{E}_0^{IJ}(\mathrm{q}_\chi \mathrm{q}_\chi) \right] \\
& + \hat{\rho} \left[\sum_{\mu\chi} \frac{\delta_\mu \mathrm{q}_\chi}{R_{II,ll}^{\mu\chi}} + \frac{1}{2} \sum_J \sum_{\substack{J=I\,:\,m\neq l \\ J\neq I\,:\,m}}^{Z} \left(\sum_{\mu\chi'} \frac{\delta_\mu \mathrm{q}_{\chi'}}{R_{IJ,lm}^{\mu\chi'}} \right.\right. \\
& \left.\left. + \sum_{\mu'\chi} \frac{\delta'_\mu \mathrm{q}_\chi}{R_{IJ,lm}^{\mu\chi}} + \sum_{\mu\mu'} \frac{\delta_\mu \mathrm{q}_{\mu'}^0 + \delta_{\mu'} \mathrm{q}_\mu^0}{R_{IJ,lm}^{\mu\mu'}} \right) \right] \\
& + \hat{\rho}\;\hat{\rho} \left[\frac{1}{2} \sum_J \sum_{\substack{J=I\,:\,m\neq l \\ J\neq I\,:\,m}}^{Z} \sum_{\mu\mu'} \frac{\delta_\mu \delta_{\mu'}}{R_{IJ,lm}^{\mu\mu'}} \right] \Bigg\}
\end{aligned} \tag{2.28}$$

Apart from the irrelevant constant terms on the first and on the second line, there are term proportional to $\hat{\rho}$ and terms proportional to $\hat{\rho}^2$. We notice that terms proportional to $\hat{\rho}$ have contributions from FcPyl–FcPyl interactions as well as from the FcPyl–anion interactions. These term proportional to $\hat{\rho}$ in eq. 2.28 do not have a counterpart in the treatment of crystals of neutral *DA* molecules and play a similar role as a crystal electrical field:

$$\begin{aligned}
\mathscr{F} \;=\; & \frac{1}{2} \left[\sum_{\mu\chi} \frac{\delta_\mu \mathrm{q}_\chi}{R_{ii}^{\mu\chi}} + \frac{1}{2} \sum_{j\neq i} \left(\sum_{\mu\chi'} \frac{\delta_\mu \mathrm{q}_{\chi'}}{R_{ij}^{\mu\chi'}} \right.\right. \\
& \left.\left. + \sum_{\mu'\chi} \frac{\delta'_\mu \mathrm{q}_\chi}{R_{ij}^{\mu\chi}} + \sum_{\mu\mu'} \frac{\delta_\mu \mathrm{q}_{\mu'}^0 + \delta_{\mu'} \mathrm{q}_\mu^0}{R_{ij}^{\mu\mu'}} \right) \right]
\end{aligned} \tag{2.29}$$

where we used a simplify notation in which i, j counts the unit formulas in the crystal. On the opposite, the term proportional to $\hat{\rho}^2$ in eq. 2.28, plays the same role as the $\mathscr{M}$ term in the treatment of crystal of *DA* molecules in sect. 2.1.2.

So we define:

$$\mathcal{M} = \frac{1}{2}\sum_{j\neq i}\sum_{\mu\mu'}\frac{\delta_\mu\delta_{\mu'}}{R_{ij}^{\mu\mu'}} \tag{2.30}$$

A mf treatment of the $\hat{\rho}^2$ interaction finally leads to the following mf Hamiltonian:

$$\begin{aligned} H_{\mathrm{mf}} &= \sum_i \left[\hat{h}_i + \mathcal{E}_0 + 2\mathcal{F}_i\hat{\rho}_i + 2\mathcal{M}_i\rho\hat{\rho}_i + \right] - N\mathcal{M}\rho^2 \\ &= \sum_i \left[2z_{\mathrm{eff}}\hat{\rho}_i\right] - N\mathcal{M}\rho^2 + N\mathcal{E}_0 \end{aligned} \tag{2.31}$$

where $z_{\mathrm{eff}} = z_0 + \mathcal{F} + \mathcal{M}\rho$, can be redefined as the effective energy separation in the two state model and $\mathcal{E}_0$ refer to constant term.

2.2.2 Results

FcPyl$^+$ X$^-$ crystals were characterized from the structural point of view with XRD single crystal analysis, as reported in the Kondo work [78]. The crystal structures are available at two different temperatures for FcPyl$^+$ PF_6^- and FcPyl$^+$ BF_4^-: 113K (LT) and 273K (HT). For X= TFSI only the HT structure is given. For the LT and HT structures of FcPyl$^+$ PF_6^- and FcPyl$^+$ BF_4^- two conformations have been mapped (c_1 and c_2). They are related to two orientation for the anion X. Indeed, conformational disorder can affect BF_4 and PF_6 units and in particular the rotation around the central atom is possible, resulting in two different sets of atomic coordinates for each anion. Figures 2.18 to 2.20 show the overall arrangement in the crystal structure.

Calculating $\mathcal{M}$ and $\mathcal{F}$ for FcPyl

To estimate $\mathcal{F}$ and $\mathcal{M}$ in eq. 2.29 and 2.30 we need to estimate the atomic charges on the molecular anion relevant to both the DA^+ and the D^+A structures of FcPyl as well as the distribution of charges in counterions. For counterions we run a standard PM6 [97] calculation and, neglecting the (minimal) polarizability of counterions, we assume that the resulting atomic charges q_χ do not change with the environment. To estimate atomic charges on FcPyl we follow a similar strategy as adopted for FcPTM. In particular we perform quantum chemical calculation on FcPyl under an applied electric field $\mathcal{F}$ as to drive the system from the DA^+ to the D^+A state.

Fig. 2.21 shows the properties of FcPyl as a function of an electric field oriented along the DA direction (from the Fe atom to the C atom in the carbonyl,

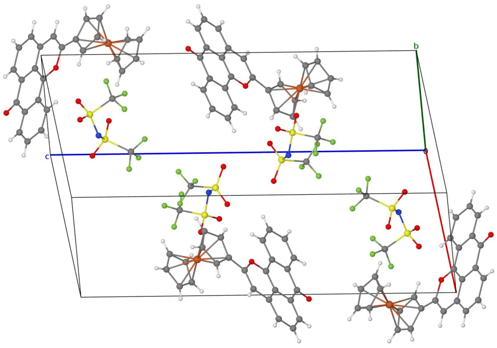

Figure 2.18: *Monoclinic crystal structure in the unit cell of FcPyl*$^+$ *TFSI*$^-$*, from [78].*

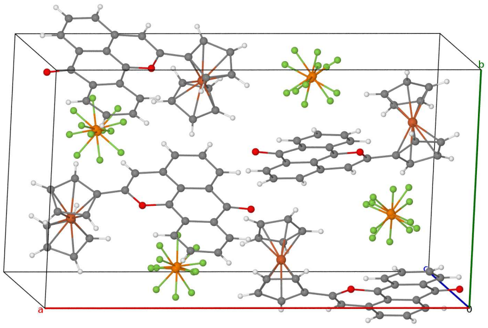

Figure 2.19: *Orthorhombic crystal structure in the unit cell of FcPyl*$^+$ *PF*$_6^-$ *(HT), from [78]. Both* c_1 *and* c_2 *are shown.*

linked to the external oxygen). The different curves are obtained adopting the FcPyl structure from the five crystal structures available. The results are very similar to those relevant to FcPTM. The region around $F = 0$ V/Å and $F = 1$ V/Å has almost flat polarizability, and we assume the charge distribution at $F = 0$ as $\{q^0\}$, while the charge distribution at $F = 1$ V/Å describes Fc$^+$Pyl state ($\{q(\rho = 1)\}$) . The calculation has been run on MOPAC2007 package, with PM6 model Hamiltonian, imposing the keyword `BIRADICAL`, that actual mixes four microstates to include an eventual biradicalic character (this keyword is actually redundant and corresponds to the combination of the keywords `MECI OPEN(2,2) SINGLET` in the MOPAC2007 package). It implies a C.I. calculation

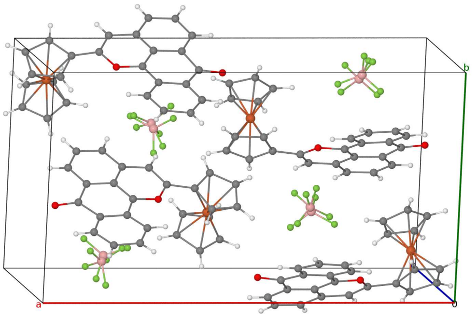

Figure 2.20: *Orthorhombic structure in the unit cell of FcPyl$^+$ BF$_4^-$ (HT), from [78]. Both c$_1$ and c$_2$ are shown.*

with the four configurations that arise considering the space of the HOMO and the LUMO.

As shown in the middle panel of fig. 2.21 the overall charge on the acceptor unit is close to 1 in the $F \sim 0$ region and close to 0 in the region assumed for the CT state ($F \sim 1$ V/Å), and vice versa on the donor Fc unit. The μ_0 value that can be extracted here is about 40 D, corresponding to a dipole length of about 8 Å. This is really close to the crystallographic distances from the donor center (Fe atom) and the considered acceptor center (C of carbonyl group), being 7.6 - 7.7 Å in the reported structures. Moreover, the sigmoid curves for the five structures are similar, with minor differences (curves corresponding to the X= BF$_4$ structure are smoother than the other curves). The information about atomic charges obtained from quantum chemical calculations is finally entered in eq. 2.29 and 2.30 to calculate $\mathscr{F}$ and $\mathscr{M}$ value: results are summarized in table 2.4 for the five crystal structures.

Table 2.4: *Calculated value for electrostatic energies*

anion X =	T / K	$\mathscr{F}$ / eV		$\mathscr{M}$ /eV
TFSI$^-$	273	-0.05		-1.04
BF$_4^-$ (LT)	113	0.04 (c$_1$)	-0.01 (c$_2$)	-0.91
BF$_4^-$ (HT)	273	-0.12 (c$_1$)	-0.26 (c$_2$)	-1.10
PF$_6^-$ (LT)	113	-0.05 (c$_1$)	-0.04 (c$_2$)	-0.95
PF$_6^-$ (HT)	273	-0.02 (c$_1$)	-0.07 (c$_2$)	-0.93

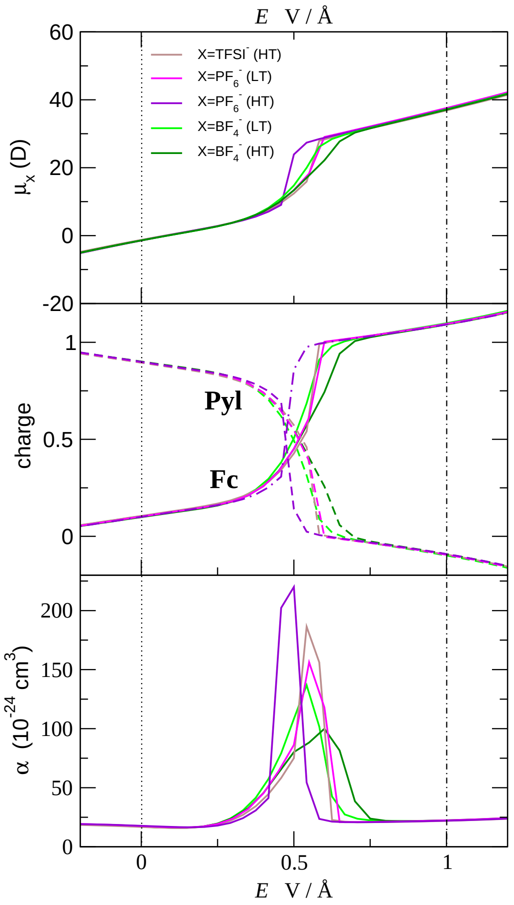

Figure 2.21: *Results of PM6 calculations for a FcPyl molecule with the crystallographic structures (see legend) under an external static electric field, F. F-dependence of the molecular dipole moment μ_x (top panel), molecular polarizability α (bottom panel), and total net charges (central panel) on the Fc (continuous line) and Pyl (dashed line) units. Dotted and dash-dotted vertical lines mark the DA$^+$ structure ($F = 0$) and the CT charge distribution, corresponding to flat regions of α.*

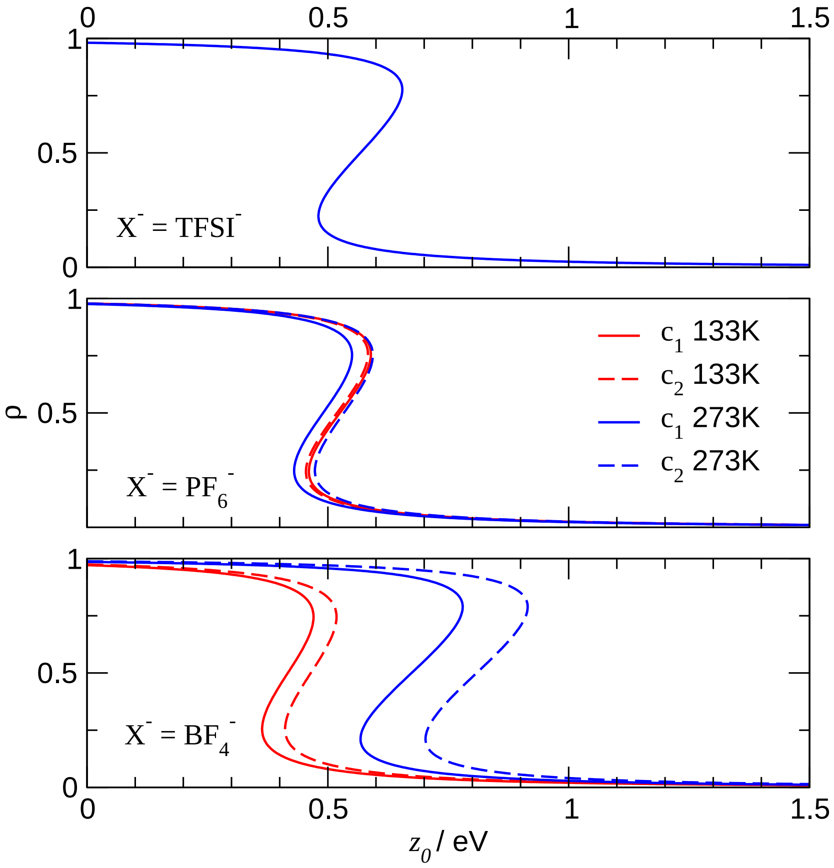

Figure 2.22: $\rho(z_0)$ *curves plotted for the* $\mathscr{M}$ *and* $\mathscr{F}$ *values calculated for each FcPylX structures (X= TFSI (top), X=* PF_6 *(middle), X =* BF_4 *(bottom)) as reported in tab. 2.4. Red lines and blue lines refer to low temperature (LT, 133K) and high temperature (HT, 273 K), respectively. Dashed lines refer to conformation* c_2*, where experimentally available.*

The solution of the mf Hamiltonian in eq. 2.31 leads to results in figure 2.22, that shows the $\rho(z_0)$ curves obtained for the $\mathscr{M}$ and $\mathscr{F}$ values in table 2.4; τ is set equal to 0.30 eV (see table 2.3). In all the cases a bistability region occurs. For X=TFSI and X $=\mathrm{PF}_6$ the bistability occurs at z_0 in the range $0.5 \div 0.6$ eV, a value compatible with the parameters estimated in table 2.3.

A more exhaustive analysis including the fit of Mössbauer spectra is deferred to a subsequent work. We notice, however, that temperature dependent structural data allows to calculate temperature dependent $\mathscr{F}$ and $\mathscr{M}$ values, suggesting a small increase of electrostatic interactions upon increasing temperature. This result can easily justify the experimental observation of $\mathrm{Fc}^+\mathrm{Pyl}$ / FcPyl^+ concentration ratios larger than 1 ah high T, as extracted from Mössbuaer spectra [80].

The analysis of results relevant to FcPyl BF_4 salt is more delicate. Remembering that for FcPyl^+ we estimate $0.5 \div 0.6$ eV, data in fig. 2.22 suggest that at low T only the FcPyl^+ species is present in the crystal, so that, in agreement with experimental data, only in the neutral Fc signal is seen in Mössbauer spectra. However the same data, would predict in the high T phase a complete transformation of FcPyl^+ to the $\mathrm{Fc}^+\mathrm{Pyl}$, in contrast with experimental results. While the delicate energy balance at the crossover and the fairly large uncertainties on molecular parameters and/or on electrostatic energies can explain this discrepancy, we also notice that the geometry of FcPyl^+ unit is different in the three salt, leading to slightly different molecular properties. In particular data in fig. 2.22 show the F-dependence of molecular properties as a function of the applied electric field. The results are different depending on the molecular geometry and in particular the results obtained for the geometry relevant to the $\mathrm{FcPylBF}_4$ salts are much smoother than for the two other salts. This suggests a larger conjugation between Fc and Pyl fragments, i. e. a larger τ in the two state model for the FcPyl unit in the BF_4 salt. This observation is also in line with results from TDDFT calculations in ref. [78], that obtain a larger HOMO-LUMO gap for the FcPyl molecule in the geometry for the $\mathrm{FcPylBF}_4$ salt than for other geometries. A larger HOMO-LUMO gap definitively implies a larger conjugation (or possibly a large z_0 value) and *not* a smaller conjugation as incorrectly suggested in ref. [78].

While we are not able to completely explain experimental observation for $\mathrm{FcPylBF}_4$ crystals, results in fig. 2.22 exclude bistable behavior for this salt, at variance with FcPylTFSI and PF_6 salts. The $\mathscr{M}$ energies are similar for the three salts. In fact only electrostatic interaction energies between the FcPyl units enter the $\mathscr{M}$ expression (see eq. 2.30), and in view of the similar crystal structures of the three salts, similar $\mathscr{M}$ values are calculated. The difference between the three salts is related to different $\mathscr{F}$ values. Interaction between FcPyl units and counterions explicitly enter the $\mathscr{F}$ expression (eq. 2.29), leading to a large variability of $\mathscr{F}$ with the counterion. This suggests that crystals of molecular ions, like DA^+ or DA^-, are particularly interesting for bistability. In these systems in fact a careful choice of the counterion offers a powerful tool to tune intermolecular electrostatic interactions as to guide the system towards bistability regions.

2.3 TTFPTM$^\bullet$ and related systems: bistability and aggregation phenomena

Another interesting $DA^\bullet$ molecule has been synthesized by the group of Professor Veciana attaching the well known TTF (tetrathiafulvalene) donor moiety to the PTM radical. TTF donor is widely used in the field of the organic functional materials, and in organic electronic in particular, for its ability to be oxidize to TTF^+ and TTF^{2+} and for the peculiar properties of TTF based CT crystals crystals [108, 109].

TTFPTM combines many properties at the same time. As FcPTM it is a radicalic *DA* molecule. TTF and PTM have low energy for the oxidation and the reduction, respectively, and stable derivative of the two species exist, like TTF^+, and TTF^{2+} or PTMH and PTM^-. This open the way to many possible derivatives of TTFPTM, with different chemical, optical and magnetic properties. Examples are TTFPTMH, TTF^+PTM (biradical), TTF^+PTMH, and so on. TTF^+ is also known to have the tendency to aggregate and dimerize [110, 111, 109], the interest for TTFPTM is then increased by the possibility to generate supramolecular structures [112], very important in view of the magnetic character of PTM.

The work is a results of a collaboration with the Prof. Veciana's group. Most of the experimental work has been done at ICMAB in Barcelona, partly during a short stage that I spent there (April - May 2009), and during a visit of a PhD student of Prof. Veciana group (Judit Guash) in our laboratory.

In this section two topics related to TTFPTM and derivatives will be considered. The first part is about the peculiar properties observed for TTFPTM radical in solution [113]. The second part concerns the study of the dimerization of TTFPTM (and its heterodimer with TTF^+PTM) and of the αH derivative TTF^+PTMH (and the heterodimer with TTFPTMH) [114].

2.3.1 TTFPTM: bistability in solution

Optical spectroscopy

The radicalic species TTFPTM$^\bullet$ (TTFPTM) resonate between neutral and charge separated (zwitterionic) structures, as shown in fig. 2.23. As for other *DA* systems we expect a CT transition in the low energy region of optical spectra.

Optical spectra have been recorded in Barcelona, at ICMAB. Special care has been taken to avoid aggregation for the TTFPTM, that in some solvent (CH_2Cl_2, for instance) produce noticeable change in the optical spectra. No

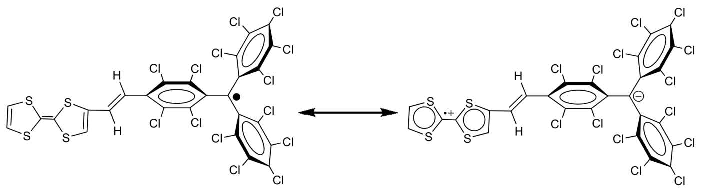

Figure 2.23: *Resonance for TTFPTM*

clear evidence of a CT band is observed, apart a weak and broad structure at 9000-11000 cm^{-1} that is seen in some solvents, as evidenced in fig. 2.24.

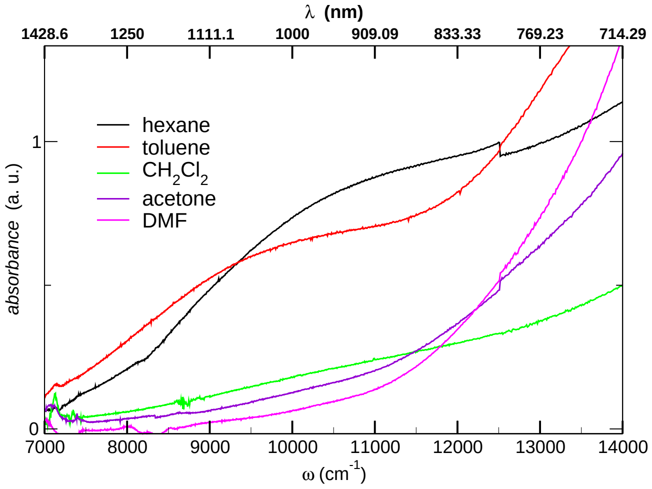

Figure 2.24: *Low energy NIR absorption spectra of TTFPTM in some solvents.*

Complete optical spectra in fig. 2.25 strongly depend on the solvent:

- in *apolar solvents* (like toluene, hexane, cyclohexane) the strongest absorption is the sharp peak at ∼ 390 nm, assigned to the PTM radical [76, 81]. A weak and broad band appears at 900-1200 nm that we tentatively assign as a CT band (see detail in fig. 2.24).

- in *strongly polar solvents* (acetone and DMF) the 390nm- peak of PTM radical is suppressed (it disappears in DMF) while a peak a 510 nm appears, assigned to PTM^- [115, 81]. At the same time, in these solvents the CT absorption at ∼1000 nm is not seen.

- spectra collected in intermediate polarity solvent, as dichloromethane, tetrahydrofurane (THF), chlorobenzene (PhCl) show intermediate behavior.

The solvatochromic trend is clearly readable in the series CH_2Cl_2, PhCN, acetone, dimethylformamide (DMF), as reported in fig. 2.26, left panel. The CT band is observed only in non-polar solvent, as a broad feature. In more polar solvent the CT transition is not seen and it is possibly hidden under the tail of higher energy transition. By the way, the overall spectra show changes at different wavelength going from one solvent to other, as a probable results of the solvation on the conformational degrees of freedom of TTFPTM.

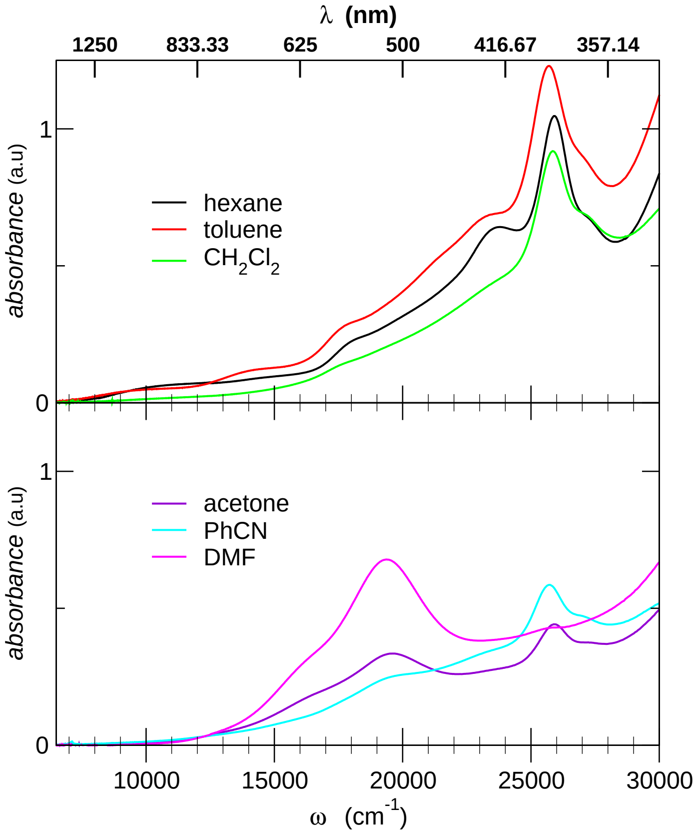

Figure 2.25: *Vis-NIR absorption spectra of TTFPTM in low polarity solvent (top panel) and in polar solvent (bottom panel).*

The observed behavior can be interpreted in terms of a valence tautomerism, where the molecule switches from the TTFPTM$^{\bullet}$ to the TTF$^{\bullet+}$PTM^{-} in polar solvents. The behavior is reversible (i.e. the spectral changes are not the results of a chemical reaction or decomposition), and has been verified in mixtures of solvents of different polarities (acetone and CH_2Cl_2 in varying proportions) observing intermediate spectral behavior. Increasing solvent polarity promotes the charge transfer and then the observation of the PTM^{-} anion spectral features in place of the radical ones, leading to bistable behavior already in solution. This results, that makes this molecule really promising for future studies, confirms the tendency of PTM derivatives to molecular bistability.

EPR results

EPR spectra were recorded in Barcelona on TTFPTM solutions in four solvent: CH_2Cl_2, PhCN, acetone, DMF. EPR spectra are shown on the right panel of fig. 2.26, together with absorption spectra in the Vis-NIR on the left.

EPR spectra of TTFPTM shows a two lines system (g=2.00253 for PTM$^{\bullet}$, coupling with the closest vinylene H, a_1= 1.61 G). However, room temperature spectra are often unresolved and a single broad signal (one EPR line) is observed. EPR spectra show a decrease of the PTM radical signal (one EPR line), increasing solvent polarity. On the other hand, no new signals appears in the region of the TTF radical, and the EPR intensity is strongly suppressed in polar solvents. This is a puzzling result, in fact if increasing the solvent polarity the system goes from the TTFPTM$^{\bullet}$ to the TTF$^{\bullet+}$PTM^{-} structure, as discussed above, we would expect an increase of the EPR signal related to the TTF^{+} specie.

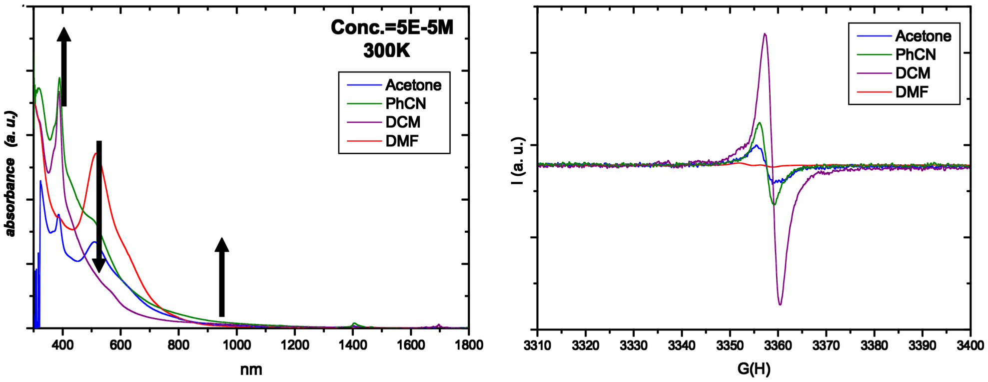

Figure 2.26: *Optical Vis-NIR spectra (left) and EPR spectra (right) in four solvents of medium and large polarities.*

Possible explanations rely on the diamagnetic coupling due to the formation of the dimer ($TTF^{\bullet +}PTM^{-}$)$_2$. However there are no spectroscopic signature of the dimer in optical spectra. Dynamic effects related to the rate of the equilibrium $DA^{\bullet} \leftrightharpoons D^{+\bullet}A^{-}$and/or to the high delocalization of the unpaired electrons in the $TTF^{\bullet +}PTM^{-}$ species can also contribute in broadening the EPR band. To better investigate this effect, some T dependent EPR measurements are in progress.

Understanding molecular intrinsic bistability

Experimental results on TTFPTM suggests an intriguing bistability at the molecular level. Even if further measurements are in order, we discuss the results in terms of an electronic two-state model, as presented in sect. 1.1 and applied in this chapter for this class of molecules (sect. 2.1.1).

In particular the experimental behavior of TTFPTM is expected in systems described by two state model in sect. 1.1, provided that the hybridization energy τ is small [41]. In these systems, the degree of mixing is very small (i.e. $\rho \rightarrow 0$ or $\rho \rightarrow 1$). If the external perturbation (like the reaction field of the polar solvent) is large compared to the energy separation ($2z_0$) then the system switches to the zwitterionic form in polar solvent. In these conditions we expect a low transition energy ω_{ge} (compared to push-pull dyes) as well as very weak CT band, and almost no solvatochromism (see eq. 1.7, 1.8 and 1.10 and their ρ dependencies), in agreement with the experimental data.

To support our picture, we perform calculation on the TTFPTM molecule subject to an electric field pointing along DA direction, as done for FcPTM (see sect. 2.1.4). Calculations were run with the MOPAC2007 package, adopting the PM6 Hamiltonian at the ROHF level of theory [98, 97]. However, for this molecule, the crystallographic experimental structure is not available. We then perform a preliminary geometry optimization with unrestricted DFT method (UDFT/B3LYP[1], basis set: 6-31G*) [116]. Semiempirical F dependent calculations were then run on the molecule either in this fixed structure (reported in fig. 2.27), or allowing for geometry relaxation at each F value. Center of D group was assigned to carbon C41 and center of the A group was assigned to atom C9 (see fig. 2.27).

Results shown in figure 2.28 are similar for fixed geometry or allowing for the geometry relaxation with the field, suggesting the minor effect of the e-mv coupling. The neutral to zwitterionic crossover is located at very low fields

---

[1] Unrestricted Density Functional Method. Functional: Becke-3-Parameter/HF+Slater+Becke88+VWN+LYP

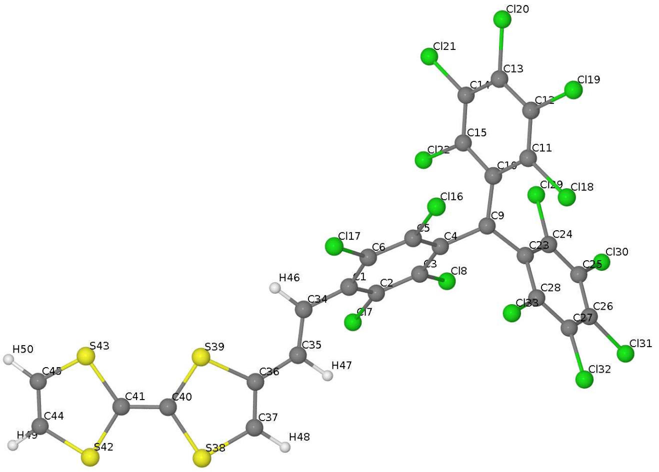

Figure 2.27: *Molecular structure optimized from UDFT calculation.*

(compare with results on FcPTM in fig. 2.9 and FcPyl in fig 2.21), confirming our idea of a very small energy differences between $DA^{\bullet}$ and $D^{+\bullet}A^{-}$ states (i.e. a small z_0 value). Moreover, the dipole moment dependence on the field F show a sharp jump in correspondence of the crossover. This sharp crossover supports our view of a small resonance integral τ. In correspondence of some field values, inside the ionic region, the system is driven back to a neutral electronic state, strongly suggesting an intrinsic molecular bistability: small perturbations can drive the system toward one form or the other.

2.3.2 Dimers of TTFPTM and derivatives

The cationic form of TTF (TTF^{+}) has a well known propensity to form dimers [110, 111]. The interest for dimer properties, and for supramolecular aggregates, is a key point in the study of multifunctional molecular materials. TTFPTM derivatives considered in this section are shown in fig. 2.29, and the following dimers can be investigated:

- TTF^{+}PTMH homodimer
- TTF^{+}PTMH – TTFPTMH heterodimer
- TTF^{+}PTM homodimer

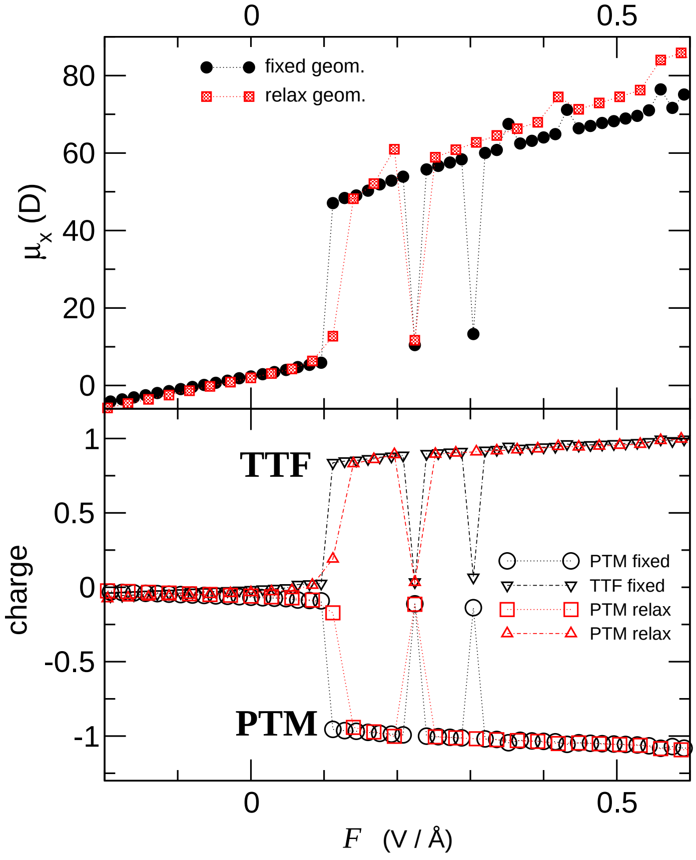

Figure 2.28: *Molecular dipole moment (upper panel) and charges on each unit (lower panel, empty symbols) calculated for a TTFPTM molecule placed in an electric field directed along DA direction. Black symbols refer to calculation at fixed geometry, red symbols refer to results obtained relaxing the molecular geometry at each F value.*

- TTF^+PTM – TTFPTM heterodimer (and TTF^+PTM – TTF^+PTM^- homodimer)

Temperature dependent EPR spectra of CH_2Cl_2 solutions of the different species were collected in Barcelona, whereas temperature-dependent optical Vis-NIR-IR spectra in solution were collected in our laboratory. Measurements in Parma were done using the cryostat described in the appendix A.3.1 combined with both the UV-Vis absorption instrument for the 300-800 nm region and with the FT-IR spectrophotometer for the NIR (and IR) region. More technical details about procedures and instruments can be found in the appendix sect A.1.2.

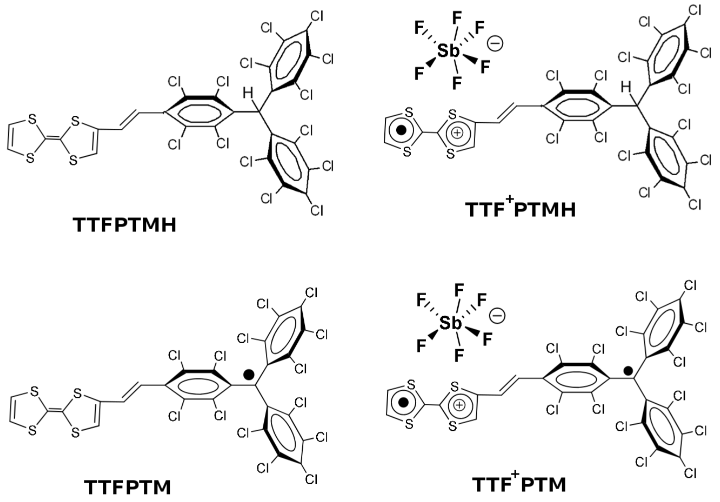

Figure 2.29: *Structures of the TTFPTM derivatives involved in the dimer formations: αH derivatives (top) and radical derivatives (bottom).*

The characteristic EPR signals at g = 2.00767 is typical for the $TTF^{\bullet+}$ radical, while the $PTM^\bullet$ radical signal is observed at g = 2.00253. From the optical point of view, characteristic bands are observed in the range of 600-800 nm for the $(TTF^+)_2$ dimers, and about 2000-3000 nm for the mixed valence $(TTF)_2^+$ specie.

The information extracted from optical and EPR spectra confirm the dimer formation. The quantitative study of the dimer formation with the temperature allows, in favorable cases, the definition of the thermodynamic quantities (ΔH e ΔS) that rule the equilibrium. Work is still in progress, and in some cases only qualitative results will be shown.

TTF^+PTMH homodimer

The tendency to self-dimerize of the TTF^+PTMH species can be detected thanks to optical (NIR absorption spectroscopy) and magnetic (EPR) techniques. We consider the dimerization equilibrium:

$$\mathrm{M} + \mathrm{M} = \mathrm{M}_2 \tag{2.32}$$

and define the nominal concentration $c = [\mathrm{M}] + 2[\mathrm{M}_2]$ and the monomer fraction $\alpha = \frac{[\mathrm{M}]}{[\mathrm{M}]+2[\mathrm{M}_2]}$. The T-dependence of α

$$\alpha(T) = \frac{-1 + \sqrt{1 + 8K(T)}}{4cK(T)} \tag{2.33}$$

is governed by the T-dependence of the equilibrium constant:

$$K(T) = \exp\left(-\frac{\Delta G}{RT}\right) = \exp\left(\frac{\Delta S}{R} - \frac{\Delta H}{RT}\right) \tag{2.34}$$

For what concern EPR results, the dimer (diamagnetic specie) is expected to be silent. On the opposite the monomer TTF^+PTMH is a paramagnetic specie with the unpaired electron on the TTF unit. Hence we expect to observe an EPR integrated signal (double integration of the actual EPR spectra, i.e. the correspondent area) proportional to the concentration of the monomer $[M]$:

$$S_{EPR} \propto [M] = \alpha\, c \tag{2.35}$$

The temperature dependence of the EPR intensity of eq. 2.35 can be then calculated in term of the equations 2.33 and 2.34:

$$S_{EPR}(T) \;=\; A\, \alpha(T)\, c \tag{2.36}$$

where A is a multiplicative factor. T dependent measurements of EPR area can be then fitted with the equation 2.36 to extract thermodynamic information.

EPR spectra were collected in the temperature range 180 ÷ 300K on solutions of TTF^+PTMH SbF_6^- at concentration of $\sim 10^{-3}$ M, and the T-dependence of the integrated areas are plotted together with the fitted curves in fig. 2.30, for two nominal concentration $c = 5.4 \cdot 10^{-3}$ and $c = 8.5 \cdot 10^{-3}$. Actually, the EPR intensity decreases with the expected behavior and the equilibrium model works pretty well. The values for the thermodynamic parameters extracted from fit of the temperature dependent results are:

ΔS (cal mol$^-$1 K^{-1})	-15.4
ΔH (cal mol$^-$1)	-4420
K(298K)	~ 0.5
K(180K)	$\sim 10^4$

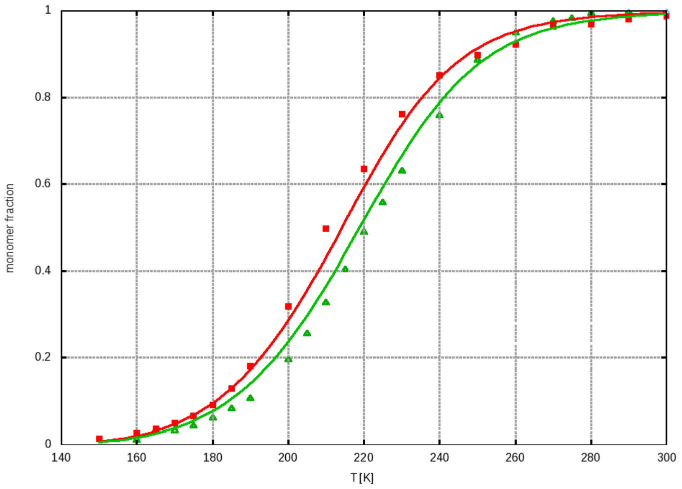

Figure 2.30: *Temperature dependent EPR monomer fraction from experimental area (symbols) and calculated from fit with eq. 2.36 (curves) at two concentration level* $c = 5.4 \cdot 10^{-3}$ *M (red) and* $8.5 \cdot 10^{-3}$ *M (green).*

For the optical measurements a similar analysis of the temperature dependence of the signals can be done. Since the area of a band (deconvoluted when necessary) is proportional to the concentration of the absorbing specie, we have:

$$S_{abs,M}(T) = M_M[\mathrm{M}](T) = M_M\ c\ \alpha(T) \tag{2.37}$$

$$S_{abs,D}(T) = M_D[\mathrm{M}](T) = M_D\ \frac{1}{2}\ c\ (1-\alpha(T)) \tag{2.38}$$

The $\alpha(T)$ relation in eq. 2.33 allow us to extract T dependent thermodynamic information from the area of absorption bands. The low temperature measurements recorded in the Vis-NIR region are shown in fig. 2.31. These results confirm the interpretation of EPR data. The 800 nm (12500 cm^{-1}) band, assigned to the homodimer [110] increases its intensity with decreasing temperature and increasing nominal concentration. It is interesting to observe that in the low concentration solution the band at 670 nm ($\sim$ 15000 cm^{-1}), assigned to the monomer specie [110] decreases in intensity (the same band is too intense to be observed in the high concentration sample).

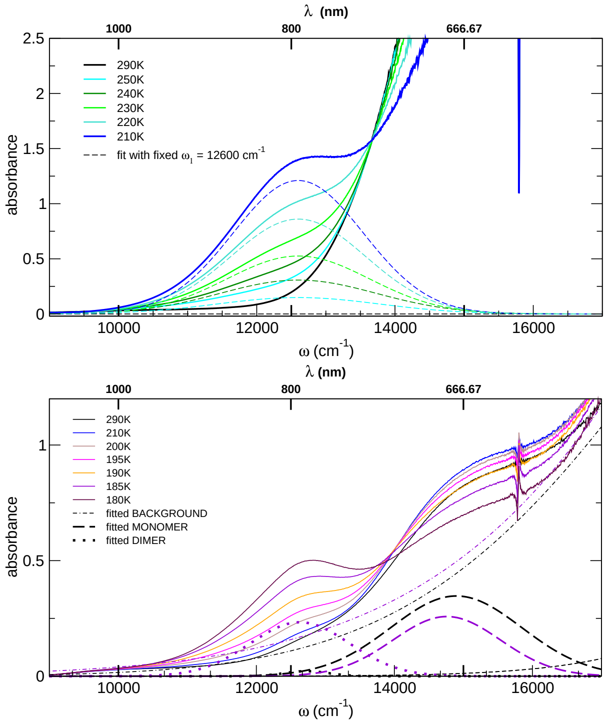

Figure 2.31: *Temperature dependent Vis-NIR absorption spectra of TTF*$^+$*PTMH (and the related dimer) recorded at* $c = 2.8 \cdot 10^{-3}$ *M (upper panel) and* $c = 4.0 \cdot 10^{-3}$ *M (lower panel). In dotted lines the fitted band at some temperature, with Gaussian function. Baseline of experimental data was corrected.*

TTF$^+$PTMH and TTFPTMH heterodimer

The formation of the TTF$^+$PTMH – TTFPTMH mixed valence heterodimer is detected by the appearance of a CT band in the NIR region. The equilibrium is:

$$\mathrm{A} + \mathrm{B} = \mathrm{AB} \tag{2.39}$$

and the concentrations:

$$[\mathrm{A}] = c_A - [\mathrm{AB}] \qquad [\mathrm{B}] = c_B - [\mathrm{AB}] \tag{2.40}$$

where $c_{A,B}$ is the nominal concentration of A, B. The concentration of the mixed valence specie AB is then:

$$[\mathrm{AB}](T) = \frac{(c_A + c_B)K(T) + 1 - \sqrt{(c_A - c_B)^2[K(T)]^2 + c(c_A + c_B)K(T) + 1}}{4K(T)} \tag{2.41}$$

Then, assuming the same T dependence for the equilibrium constant K as in eq. 2.34 we can express the dependence of the intensity (area) of the CT band as:

$$S_{abs,AB}(T) = M_{AB}\ [\mathrm{AB}](T) \tag{2.42}$$

where M_{AB} is a multiplicative factor.

Optical spectra, shown in fig. 2.32 in the CT region were recorded at two different ratios for the TTFPTMH and the TTF$^+$PTMH: 1:5 and 1:10. In both cases the nominal concentration of TTF$^+$PTMH is $7.3 \cdot 10^{-5}$. The spectral region in fig. 2.32 is particularly critical because of the presence of absorptions due to the solvent (overtones of vibrational modes). The data in fig. 2.32 have been treated to remove solvent peaks. A broad band at about 3000 nm (~5500 cm^{-1}) appears very clearly. Its fit with a Gaussian function is also shown in fig 2.32 (dashed lines). This fit is necessary to obtain a reliable integrated areas. Then

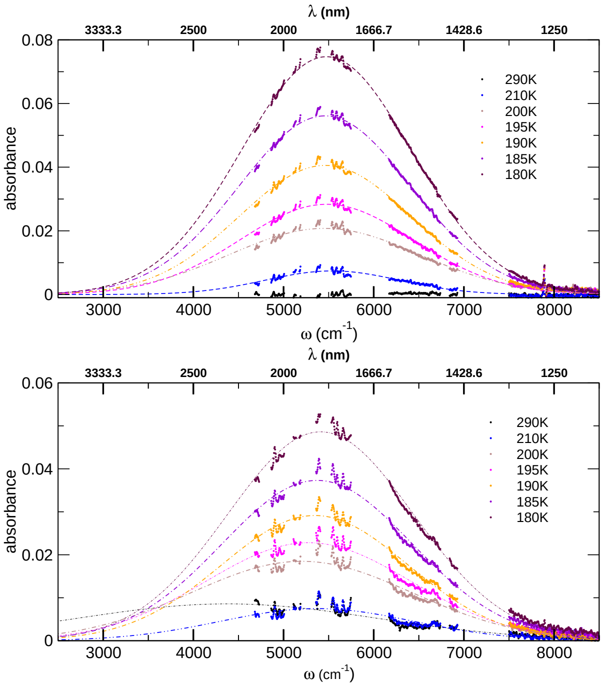

Figure 2.32: *Temperature dependent NIR absorption spectra recorded at two different ratio of concentration for TTF$^+$PTMH and TTFPTMH, respectively, 1:10 (upper panels) and 1:5 (lower panels). In both cases concentration of TTF$^+$PTM is equal to $7 \cdot 10^{-5}$. In dotted lines are show the fitted band with a Gaussian function with three adjustable parameter. Baseline was corrected.*

the two series of temperature dependent area have been fitted with the function in eq. 2.42 to obtain the following estimation of thermodynamic parameters:

ΔS (cal mol^{-}1 K^{-1})	-24
ΔH (cal mol^{-}1)	$-7{\cdot}10^3$
K(298K)	~ 0.8
K(180K)	$\sim 10^3$

However, these estimates are effected by large uncertainties, because the absorption bands are very weak. Further measurements are in order for more reliable results.

TTF$^+$PTM homodimer and TTF$^+$PTM – TTFPTM dimer

TTF$^+$PTM is a biradical and the analysis of its EPR spectra is difficult. In fact one expects a doublet related to the PTM radical, that becomes a triplet upon dimer formation. Moreover, one expects a 7-line multiplet due to the TTF radical. The two signals partly overlap, and the shape of the signal changes with the formation of the dimer. In particular the TTF$^+$ signal should disappear in the homodimer. EPR spectra essentially confirm this picture, as shown in the T dependent spectra of fig 2.33. While the quantitative analysis of EPR data is still in progress, optical spectra in fig. 2.34 are reasonably clear and suggest dimer formation. The CT band of the dimer is observed at 800 nm as shown in fig. 2.34.

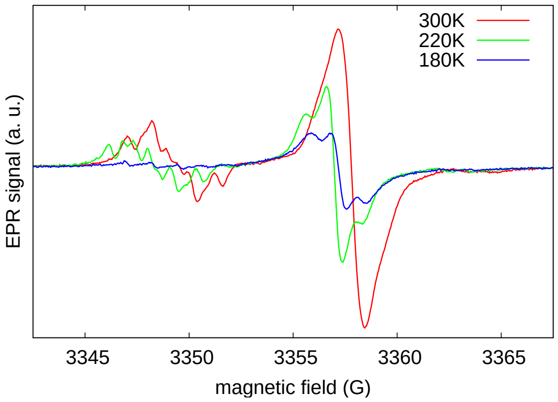

Figure 2.33: *EPR spectra of TTF$^+$PTM (and the related dimer) in CH_2Cl_2 at* $c = 9.3 \cdot 10^{-4}$ *M, at three different temperatures.*

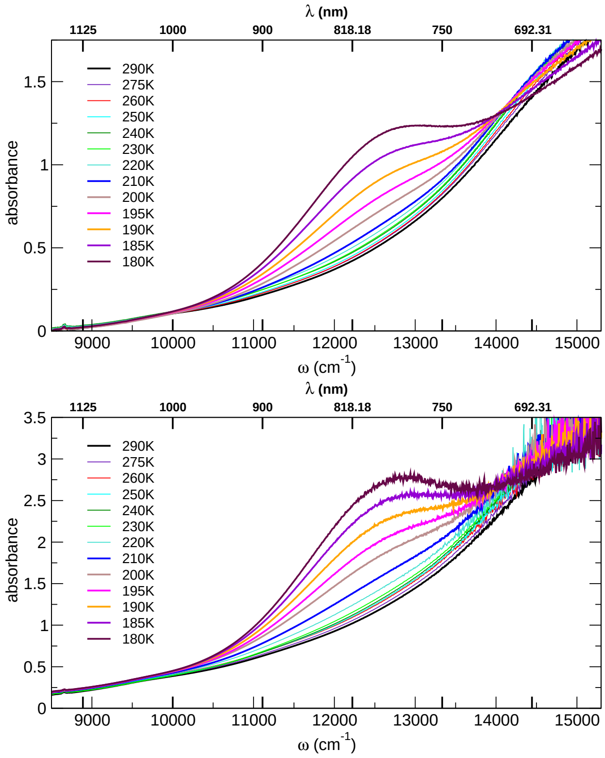

Figure 2.34: *Temperature dependent NIR absorption spectra recorded at two different concentration of TTF$^+$PTM, c =1.1·10^{-3} M (upper panels) and c =2.3·10^{-3} M (lower panels). Baseline was corrected.*

For the mixed-valence TTF$^+$PTM –TTFPTM the picture is even more complex because of the mesomeric properties of TTFPTM itself, that is subject to the valence tautomerism driven by the solvent polarity discussed in sect. 2.3.1. Then the analysis of the T dependent data is cumbersome. If TTFPTM is quantitatively present in the zwitterionic form (TTF$^+$PTM$^-$) the resulting dimer can form an homodimer, since the two TTF$^+$ moieties are both in the cationic form. In optical spectra a weak and broad absorption band assigned to the dimer is observed, suggesting the formation of aggregates rather than a dimerization (data not shown). On the other hand, the hypothesis of dimerization is well compatible with EPR results at room T.

Interestingly, mixed valence dimer (as detected in NIR spectroscopy) occurs in solution only when TTFPTM$^\bullet$ and TTF$^+$PTM$^\bullet$ are obtained *in situ*, via chemical oxidation with NOSbF$_6$ (from the anion TTFPTM−). For this sample NIR absorption as a function of T are shown in figure 2.35. A mixed-valence dimer absorption band appear at $\sim$ 5000 cm^{-1}, when decreasing the T. Sample prepared in this way has measured with EPR, confirming the mixed valence dimer (5-lines signal for the TTF radical).

Therefore, the possibility to form both homodimer and mixed-valence dimer depends on T, on the concentration, on the nature of the solvent and on the method used for the chemical oxidation, leading to a very complex phenomenology.

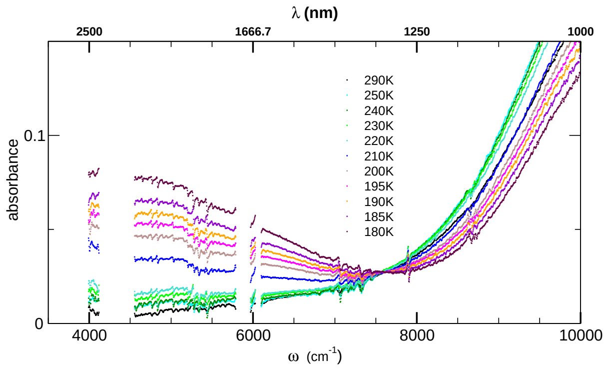

Figure 2.35: *Temperature dependent NIR absorption spectra of TTF$^+$PTM and TTFPTM generated in situ, concentrations are* $\sim 5.0\cdot10^{-4}$ *each. Baseline was corrected.*

2.4 Conclusion

In this chapter we have investigated several *DA* molecules characterized by a fairly small conjugation between the *D* and the *A* moieties, i. e. characterized by a small τ. This results in low-energy CT absorption bands, usually in the NIR region, with low intensity and minor solvatochromism. These molecules are particularly promising for bistability [24, 41]. Most of the work discussed here was devoted to FcPTM (and related) molecules. These radical *DA* species show intriguing temperature dependent Mössbauer spectra that can be quantitatively explained in terms of bistability induced in crystals of *DA* molecules by intramolecular electrostatic interactions [24]. Optical spectra of FcPTM and related molecules have been discussed based on effective three-state model. This simple expansion of the two-state model to account for the role of the bridge state allowed us to rationalize a long standing problem in the description of optical spectra of *DA* molecules. In fact we were able to demonstrate that the dipole moment associated with the D^+A^- specie as extracted from the analysis of optical spectra is always underestimated with respect to its geometrical value and we were able to assign this discrepancy to the active role of bridge state [83]. We demonstrate that the bistability model is robust and applies also to model of crystals of *DA* molecules when the molecule are described in term of a three-state model [41].

A recent work appeared in the literature [78] on $\mathrm{FcPyl^+X^-}$ crystals ($\mathrm{X^-}$ = $\mathrm{TFSI^-}$, $\mathrm{BF_4^-}$, $\mathrm{PF_6^-}$) allowed us to extend the model for bistability in crystals of *DA* molecules to DA^+X^- salts. The presence of counterions modifies the model for electrostatic interactions, leading in the mf to a new term not present in crystals of *DA* molecules. This makes DA^+X^- (or DA^-X^+) crystals interesting and promising systems to build bistable molecular materials.

Finally, we discussed a series of *DA* molecules based on the TTF donor and the PTM acceptor. Several species can be obtained depending on the chemical nature of PTM radical that can be easily protonated, and/or reduced. Moreover the TTF moiety undergoes to interesting dimerization processes leading to a rich behavior. While a complete discussion of the rich physics of these systems is deferred to subsequent work, here we underline just the interesting behavior of the TTFPTM molecules that changes from a neutral structure in non polar solvent to a zwitterionic structure in polar solvents, suggesting bistable behavior in solution.

Chapter 3

Electron-phonon coupling in molecular organic semiconductors

Molecular organic semiconductors are nowadays object of relevant interest due to their application in a new generation of (opto)-electronic devices, that are cheap and offer the advantage of flexibility and large-area integration. Indeed, charge transport properties of molecular semiconductor, with intrinsic mobilities of the order of 10-100 cm^2/Vs [117], already allow their exploitation in commercial devices, like organic light-emitting diodes, solar cells, or field-effect transistors [118, 119, 120, 121].

Classical theory of charge transport in inorganic semiconductors (Si, representing a typical example) is based on a simple tight binding Hamiltonian:

$$\mathscr{H} = \sum_r \epsilon_r a_r^+ a_r + \sum_{r \neq s} t_{rs} a_r^+ a_s \tag{3.1}$$

Here, a_r^+ and a_r are the creation and annihilation operators, respectively, for an electron on molecular site r, ϵ_r is the site energy. t_{rs} is the transfer integral (intersite electronic coupling), which leads to the bands involved in the charge transport.

In Si or Ge-based semiconductors, one deals with atomic sites, bounded by chemical bonds, while in organic semiconductors one has molecular sites kept together by weak Van der Waals forces. As a consequence, in organics t_{rs} is small, and the bands are narrow, of the order of a few tenths of eV. The charge mean-free path is then comparable to intermolecular distances, and ordinary band theory is inadequate to explain the mobility. On the other hand, a site-to-site hopping cannot account for the observed room temperature mobilities and the corresponding evolution with T: a detailed understanding of the leading mechanism of the charge-transport in organic semiconductors is still an important research challenge [122].

Molecular crystals have a high number of vibrational degrees of freedom (phonons), and their coupling with the charge carrier (electron or hole) plays a very important role in the charge transport mechanism [123, 124, 125]. Considering the two energetic terms in the Hamiltonian 3.1, two different types of coupling of the carrier with the phonons can be considered, the Holstein coupling and Peierls coupling. The former operates *on site*, and is expressed by the change in the electronic energy ϵ_r. In molecular crystals ϵ_r can be assimilated with the HOMO (LUMO) orbital energy for the holes (electron)). Instead, the Peierls coupling is related to the modulation by the phonons of the transfer integral t_{rs}.

In this chapter a new approach to characterize the Holstein and Peierls coupling constant is developed, and applied to a well known organic semiconductors, rubrene. The application of the same methodology on pentacene is in progress. This work has been done in collaboration with the group ”Physical Chemistry of the Solid State”, Prof. Brillante, Della Valle and Venuti of Bologna University. They have mainly developed the procedure to characterize the phonon structure (frequencies and eigenvectors) of molecular crystals (see sect. 3.1.1), a necessary prerequisite for the deployment of our method.

3.1 The calculation of carrier-phonon coupling constants in organic semiconductors

One of the most common approximations adopted in dealing with the complex phonon structure of molecular crystals is to separate intra-molecular vibrations from inter-molecular, or lattice, phonons. The latter correspond to translations and rotations of the rigid molecules. Within this approximation, called RMA (rigid molecule approximation), and in the framework of a molecular orbital (MO) description of the electronic structure, it is natural to associate the Peierls coupling, i.e., the modulation of inter-molecular hopping integrals, to lattice phonons. In the same spirit, intra-molecular vibrations are expected to modulate only on-site energies, giving rise to local, or Holstein, carrier-phonon coupling. The RMA approximation and corresponding separation of Holstein and Peierls coupling constitutes the approach most commonly adopted for molecular semiconductors. However, the approach fails when dealing with large molecules, where low-frequency intra-molecular phonons can mix with the molecular rotational and translational motions. We have developed a method that goes beyond the RMA approximation, and treat the Holstein and Peierls coupling on the same footing.

3.1.1 Phonon structure

The methodology adopted to characterize the phonon structure of molecular crystals has been developed by the Bologna group [126]. The RMA is used as a starting point, where intra- and inter-molecular vibrations are calculated separately Intra-molecular phonons are calculated by standard DFT methods (B3LYP functional, 631G(d) basis set) for the isolated (gas phase) molecule, whereas the lattice phonons are calculated by adopting an empirical, atom-atom intermolecular potential, Φ_{inter} of the type:

$$\Phi_{\text{inter}} = \frac{1}{2}\sum_{\alpha\beta}\left[A_{\alpha\beta}\exp(-B_{\alpha\beta}\; r_{\alpha\beta}) - \frac{C_{\alpha\beta}}{r_{\alpha\beta}^6} + \frac{q_\alpha q_\beta}{r_{\alpha\beta}}\right] \tag{3.2}$$

where the sum is extended to all distances $r_{\alpha\beta}$ between pairs α,β of atoms in *different* molecules. The $A_{\alpha\beta}, B_{\alpha\beta}, C_{\alpha\beta}$ empirical parameters are taken from literature [127]. Charges q_α, q_β in the Coulomb term are the electrostatic potential (ESP) atomic charges [128], fitted to the electrostatic potential obtained in the above DFT calculations of the isolated molecule. Given an initial lattice structure, one computes Φ_{inter} and its second derivatives with respect to the displacements of the molecular coordinates. The second derivatives form the dynamical matrix, which is numerically diagonalized to obtain the phonon frequencies $\omega_{\mathbf{k}i}$ and the corresponding eigenvectors.

The structure as a function of p and T is then determined by the QHLD (Quasi Harmonic Lattice Dynamics) method [129]. This method is based on the vibrational contribution to the Gibbs energy $G(p,T)$ of the crystal at pressure p and temperature T:

$$\begin{aligned} G(p,T) &= \Phi_{\text{inter}} + pV + \sum_{\mathbf{k}l}\frac{\hbar\omega_{\mathbf{k}l}}{2} \\ &\quad + k_B T\,\sum_{\mathbf{k}l}\ln\left[1-\exp\left(-\frac{\hbar\omega_{\mathbf{k}l}}{k_B T}\right)\right] \end{aligned} \tag{3.3}$$

where Φ_{inter} is the inter-molecular potential in eq. 3.2, pV is the pressure-volume term, $\sum_{\mathbf{k}l}\hbar\omega_{\mathbf{k}l}/2$ is the zero-point energy, and the last term is the entropic contribution. The sums are extended to all phonon modes of wavevector $\vec{\mathbf{k}}$ and frequency $\omega_{\mathbf{k}l}$. The frequencies calculated as second derivative of the potential in eq. 3.2 are introduced in eq. 3.3, and $G(p,t)$ is minimized self-consistently with respect to lattice parameters, molecular positions and orientations.

At this point, the RMA approximation is relaxed and the coupling between inter-molecular and intra-molecular coordinates is introduced perturbatively through Φ_{inter}, a function of inter-atomic distances. Since the distances depend on the Cartesian coordinates of the atoms, the derivatives of Φ_{inter} can be directly computed in terms of the Cartesian coordinates, and then converted to molecular coordinates. The displacements corresponding to rigid translations and rotations of the molecules can be derived by simple geometric arguments, whereas the displacements associated to the intra-molecular degrees of freedom are the Cartesian eigenvectors of the normal modes of the isolated molecule, as calculated by DFT. The atomic displacements, together with the inter-molecular potential model, determine the coupling between intra-molecular and lattice modes.

3.1.2 Electronic structure

The Holstein and Peierls couplings are connected to the modulation of the on-site energy and the transfer integral, respectively. Having relaxed the RMA, we calculate both types of coupling for *all* the phonons in the crystal. Within the tight binding approximation the on-site energy and transfer integral, are given by :

$$\epsilon_r = \langle \varphi_r | \mathbf{h} | \varphi_r \rangle \tag{3.4}$$

$$t_{rs} = \langle \varphi_r | \mathbf{h} | \varphi_s \rangle \tag{3.5}$$

where $\mathbf{h}$ is the one-particle electronic Hamiltonian, and $\varphi_{r,s}$ is the relevant frontier orbital (HOMO for hole transport, LUMO for electron transport) of the molecule at site r,s. Calculating the modulation of these quantities by all phonons is exceedingly onerous, so we have chosen the a semi-empirical approach based on the INDO Hamiltonian with the Zerner spectroscopic parametrization (INDO/S) [130]. In appendix C we summarize shortly the MO-HF method and INDO/S approximations and parametrizations.

Calculating electronic integrals

While the energy of the frontier orbital ϵ_r is obtained from the INDO/S calculation, the calculation of the transfer integral t_{rs} requires some comment. Of course, t_{rs} refers to a pairs of molecules (a dimer): depending on the crystal structure the number of different (symmetry non-equivalent) interacting pair of molecules can vary.

One common approach to evaluate the transfer integral is the so-called "energy splitting in the dimer" (ESD) model. The ESD model consider the energy splitting of the two HOMO (or LUMO) orbitals in the dimer with respect to the isolated molecule. The energy separation between the HOMO-1 and HOMO (LUMO and LUMO+1) of the dimer is twice the transfer integrals between the two molecules for the considered orbital:

$$\Delta\varepsilon = 2\,|t_{rs}| \tag{3.6}$$

However, the approach is only valid where the two molecules in the dimer are equivalent by symmetry, and, for subsequent applications to the calculation of Peierls coupling constant, it is also required that the two molecules remain equivalent also during a vibration. The latter condition is clearly inapplicable to non-totally symmetric modes [124]. Moreover, this approach cannot determine the sign of t_{rs}, which instead can be important when comparing the t_{rs} of different dimers within the crystal.

We therefore propose an alternative method that directly considers the interacting matrix element between the frontier orbitals of the two molecules within the dimer. First, we perform the calculation for the two isolated molecules:

$$\mathbf{f}^r\,\varphi_r^0 = \epsilon_r\varphi_r^0 \qquad \mathbf{f}^s\,\varphi_s^0 = \epsilon_s\varphi_s^0 \tag{3.7}$$

where $\mathbf{f}^{r,s}$ is the Fock operator for the r,s molecule of the dimer and $\varphi_{r,s}^0$ are the corresponding HOMO or LUMO with energy $\epsilon_{r,s}$. Next we repeat the calculation for the dimer:

$$\mathbf{f}^{rs}\,\varphi_{rs} = \epsilon_{rs}\,\varphi_{rs} \tag{3.8}$$

The transfer integral is then given by:

$$t_{rs} = \langle\varphi_r^0|\mathbf{f}^{rs}|\varphi_s^0\rangle \tag{3.9}$$

Hence, from a computational point of view, for a given geometry and for a chosen dimer, it is necessary to run three calculations: one for each of the two isolated molecule r and s, and then one for the dimer rs. In the INDO/S method the MO wavefunctions $\varphi_{r,s}$ of eq. 3.9 are expressed as a linear combination of molecular orbitals $\chi_{\sigma,\mu}$:

$$\varphi_r^0 = \sum_\sigma c_{r\sigma}\chi_\sigma \qquad \varphi_s^0 = \sum_\mu c_{s\mu}\chi_\mu \tag{3.10}$$

and eq. 3.9 can be rewritten as:

$$t_{rs} = \sum_\sigma \sum_\mu c_{r\sigma} c_{s\mu} \langle \chi_\sigma | \mathbf{f}^{rs} | \chi_\mu \rangle \tag{3.11}$$

where the $\langle \chi_\sigma | \mathbf{f}^{rs} | \chi_\mu \rangle$ is the Fock matrix element on the dimer AO basis. The above equation is easily implemented in programs written on purpose and interfaced with the main INDO/S program (see appendix sect. C.3).

To determine the relative sign of t involving different dimers in the crystal it is important to force the phase (sign) of the coefficient sets ($c_{r\sigma}$, $c_{s\mu}$) obtained from the single molecule calculation to be coherent in the calculation of different t_{rs}, because independent diagonalizations can randomly produce different signs of the eigenvectors. The simplest way to overcome this problem is to check the sign of a sizeable coefficient of an s orbital, that is independent of molecular rotations and translations. The phase correction is then determined in order that two s orbital coefficient of the HOMO (LUMO) belonging to equivalent atoms in the two molecule have the same sign. However, this procedure may not work when HOMO (LUMO) orbitals has a dominant π character, or when a dimer is formed by non-equivalent molecules, and other computational strategies have to be developed to ensure the phase agreement.

3.1.3 Carrier-phonon coupling

The strength of carrier-phonon coupling can be expressed in a variety of ways, and computed by different methods [122]. Here we shall follow the nomenclature and procedure adopted by our laboratory since in studies on electron-phonon coupling in organic charge-transfer crystals [131, 107]

We define the linear Holstein and Peierls coupling constants as follows:

$$g_H(r;\mathbf{k}m) = \left(\frac{\partial \epsilon_r}{\partial q_{\mathbf{k}m}}\right) = \sqrt{\frac{\hbar}{2\omega_{\mathbf{k}m}}}\left(\frac{\partial \epsilon_r}{\partial Q_{\mathbf{k}m}}\right) \tag{3.12}$$

$$g_P(rs;\mathbf{k}l) = \left(\frac{\partial t_{rs}}{\partial q_{\mathbf{k}l}}\right) = \sqrt{\frac{\hbar}{2\omega_{\mathbf{k}l}}}\left(\frac{\partial t_{rs}}{\partial Q_{\mathbf{k}l}}\right) \tag{3.13}$$

where ϵ_r is the HOMO (or LUMO) energy of the molecule at site r, and t_{rs} is the transfer integral between the HOMOs (or the LUMOs) of two molecules at site r and s. Moreover, $q_{\mathbf{k}m,l}$ and $Q_{\mathbf{k}m,l}$ are the dimensionless and dimensional (spectroscopic) normal coordinates of mode m, l of wavevector **k** and frequency $\omega_{\mathbf{k}m,l}$. With this definition, g_H and g_P are both expressed in energy units, at variance with other current definitions [122].

In the following we consider only optical ($\mathbf{k} = 0$) phonons, with the reasonable assumption that the coupling constants do not vary considerably with **k**. Consistently with this approximation, we disregard the coupling to acoustic phonons, although the coupling at the zone edges may be of the same order of magnitude as that of the optical phonons [132]. Therefore we will drop the index **k**, as well as the index r, because it's implicit.

The strength of the Holstein and Peierls couplings is expressed by the small polaron binding energy, ε_{sp}, and by the lattice distortion energy, ε_d, respectively, defined as [131, 107]:

$$\varepsilon_{sp} = \sum_l \varepsilon_{sp}(l) = \sum_l \frac{g_H^2(l)}{\omega_l} \tag{3.14}$$

$$\varepsilon_d = \sum_{sl} \varepsilon_d(s;l) = \sum_{sl} \frac{g_P^2(s;l)}{\omega_l} \tag{3.15}$$

where the sums run over all optical modes of the crystal (both intra- and intermolecular modes) and over all the non-equivalent transfer integrals. If one assumes that the normal modes of the neutral and ionized molecule are equal, a reasonable assumption when considering all the modes together, the small polaron binding energy is also defined as λ, the reorganization (or relaxation) energy.

Computational details

The actual calculation of the derivative as expressed in eq. 3.13 needs some technical notes. A few words concern the units in which the derivatives are expressed. The introduction a multiplicative factor $\sqrt{\frac{\hbar}{2\omega}}$ as in eq. 3.13 is useful to get the derivative expressed in energy units (like t and ϵ). Since normal modes are usually express in Å$\sqrt{u}$, where u is the atomic mass unit (Dalton, Da), the factor $\sqrt{\frac{\hbar}{2\omega}}$ is introduced to render the normal coordinates dimensionless. If we multiply by $\frac{1}{\sqrt{2}} \frac{1}{2\pi} \frac{1}{\sqrt{\tilde{\nu_p} \,/\, cm^{-1}}} \sqrt{\frac{h N_A \, \mathring{A}^2 u}{10^{-21} c}}$ we obtain $4.1058 \cdot \sqrt{\mathring{A}^2 u} \, \frac{1}{\sqrt{\tilde{\nu_p} \,/\, cm^{-1}}}$ where c is the light velocity and N_A the Avogadro number. $\tilde{\nu}_p$ is the phonon wavenumber for the considered mode (in cm^{-1}). Thus using the 4.1058 multiplicative factor we obtain coupling constants in meV.

To actually calculate the numerical derivative for each normal mode, 9 steps of calculation along the normal mode deformation are done. The covered range is 0.4 Å$\sqrt{u}$, with an elementary step (h) of 0.05 Å$\sqrt{u}$. The derivative is then calculated with the *nine point stencil method*, that approximates the first derivative as an algebraic expression of the difference:

$$\Delta y_{\pm i} = y(x_0 + i\mathrm{h}) - y(x_0 - i\mathrm{h}) \tag{3.16}$$

where y can be ϵ or t_s, and $i = 1..4$, to finally obtain:

$$y'(x_0) = \frac{-3\Delta y_{\pm 4} + 32\Delta y_{\pm 3} - 168\Delta y_{\pm 2} + 672\Delta y_{\pm 1}}{840\mathrm{h}} \tag{3.17}$$

3.2 The rubrene crystal

The above procedure is applied to a complex organic semiconductor, rubrene (5,6,11,12-tetraphenyltetracene). The choice of rubrene is dictated by its importance in the field: Rubrene in fact shows one of the highest carrier mobilities among organic semiconductors and interesting optoelectronic properties as well [133]. On the other hand, the rubrene crystal also represents an interesting test system for our computational method. In particular the relaxation of the RMA is compulsory in rubrene, as the isolated rubrene molecule possesses several very low-frequency vibrations [134], that mix with lattice phonons when the molecules are embedded in the crystal [135].

In addition, computations at the DFT level for the isolated rubrene molecule predict that about one third of the Holstein coupling strength is associated with low-frequency vibrations [134]. Finally, analogous calculations on the naphthalene crystal have produced the rather unexpected result of a strong Peierls coupling by high-frequency ($\sim$ 1600 cm^{-1}) intra-molecular vibrations [136]. Therefore we have decided to investigate the consequences of the relaxation of the RMA on the Peierls coupling, and the relative importance of Peierls and Holstein carrier-phonon coupling, by calculating both couplings for *all* the optical phonons of the rubrene crystal. The comparison with other theoretical approaches applied to rubrene and with the experimental results will be described in section 3.2.3.

3.2.1 The crystal structure of rubrene

The most commonly encountered rubrene phase is orthorhombic, space group *Cmca* (D_{2h}^{18}) with four molecules per unit cell [137, 135]. The conventional cell is non-primitive (*C* face centered), with two molecules exchanged by a roto-translation and two more molecules obtained by a non-primitive translation.

The primitive unit cell contains two molecules, which have C_{2h} symmetry and lie on sites with symmetry $2/m$. The uncommon high symmetry of the rubrene crystal simplifies the computational problem.

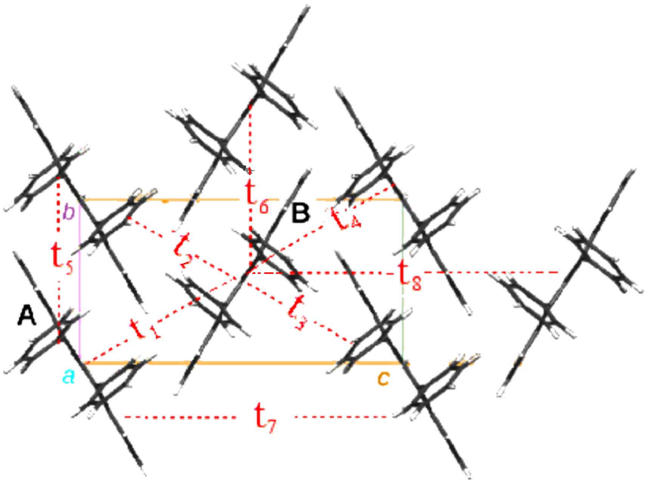

Figure 3.1: *Crystal structure of orthorhombic rubrene. The two independent molecules (A, B) within the primitive cell and the eight nearest-neighbor transfer integrals are evidenced.*

Due to the symmetry the number of different (nearest neighbor) dimers that can be generated with two molecules per cell is 8, defined through the displacement vector (in cell units) for each of the two molecule in the unit cell A and B, as reported in table 3.1. Fig. 3.1 shows the crystal structure of orthorhombic rubrene. A and B label the two independent molecules within the primitive unit cell, and t_1 to t_8 indicate the nearest-neighbor transfer integrals.

3.2.2 Rubrene transfer integrals and coupling constants

As it can be noticed the transfer integrals t_1 to t_4 are all equal by symmetry. The same applies to t_5 and t_6 integrals, and to t_7 and t_8. The INDO/S values for the HOMO and LUMO t are listed in the table 3.2. Because t_5, t_6 are much larger than all other t the electronic structure of orthorhombic rubrene is anisotropic, with the hopping probability strongly directed along the b crystal axis.

Table 3.1: *Dimers obtained for the crystal structure of Rubrene [137], according to the equivalent position in the crystal occupied by the A and B molecule and the displacement along the* b, c *axis.*

D**1**.	A(1 0 0)	B(0 0 0)	$-\vec{R}(b+c)$
D**2**.	A(0 1 0)	B(0 0 0)	$\vec{R}(b-c)$
D**3**.	A(1 0 1)	B(0 0 0)	$-\vec{R}(b-c)$
D**4**.	A(0 1 1)	B(0 0 0)	$\vec{R}(b+c)$
D**5**.	A(0 0 0)	A(-1 1 0)	$\vec{R}(b)$
D**6**.	B(0 0 0)	B(-1 1 0)	$\vec{R}(b)$
D**7**.	A(0 0 0)	A(0 0 1)	$\vec{R}(c)$
D**8**.	B(0 0 0)	B(0 0 1)	$\vec{R}(c)$

Table 3.2: *INDO/S hopping integral value for the eight dimer D**1** to D**8** defined in table 3.1.*

transfer integral	HOMO (eV)	LUMO (eV)
t_1, t_2, t_3, t_4	-0.006	0.004
t_5, t_6	0.125	-0.70
t_7, t_8	0	0

Holstein coupling

We first analyze the Holstein coupling. For the isolated molecule, only totally symmetric (a_g) modes can have g_H different from zero. The top panel of fig. 3.2 reports the small polaron binding energies, $\varepsilon_{sp}(m)$, for each mode in the isolated molecule, as calculated for the rubrene HOMOs by the INDO/S method. When the molecule is embedded in the crystal, the a_g modes of the two molecules in the primitive unit cell couple in-phase and out-of-phase, yielding phonons of A_g and B_{3g} crystalline symmetry, respectively [135]. In addition, we have the lattice phonons, which mix with the low-frequency molecular phonons (table 3.3).

The calculated small polaron binding energies are reported in the bottom panel of fig. 3.2, in blue line. The comparison between top and bottom panels by the figure immediately shows that the Holstein coupling strength of the lowest frequency a_g molecular mode, at 21 cm^{-1}, is essentially washed out when

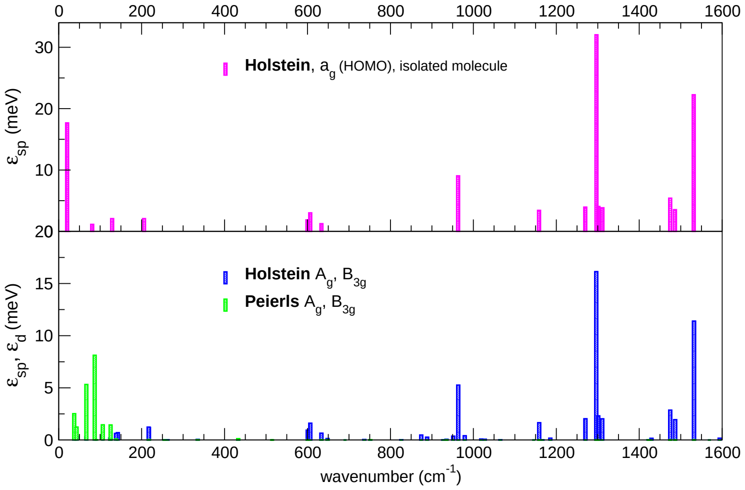

Figure 3.2: *Small polaron binding energy for the isolated molecule (top) and small polaron binding energy and lattice distortion energy for a rubrene molecule embedded in the crystal, relative to holes (HOMO orbitals).*

the molecule is embedded in the crystal. Due to the mixing with the lattice modes, the coupling strength of the mode is indeed distributed over several phonons. In addition, the packing inside the crystal makes the molecule more rigid (higher frequencies of the modes), again contributing to a reduction of the coupling strength. The calculated total small polaron binding energy of the rubrene molecule in the crystal is 99 meV, slightly smaller than for the isolated molecule (about 110 meV).

The numerical values of the coupling constants are reported in the fifth and six column of Table 3.3, for HOMO and LUMO respectively, for the low-frequency modes. In the same table 3.3 the intermolecular contribution is also reported for each mode: obviously this information is important only for low frequency modes, that can exhibit a significant mixing with lattice phonons. Since other high energy modes have ≈ 100% of intramolecular contribution, these are considered as purely intra-molecular modes, and are reported in table 3.4.

The figures 3.5 and 3.7 in the upper panels show the overall Holstein coupling for low frequency modes, and for intramolecular modes, while fig. 3.6 and in 3.8 the upper panels show the small polaron binding energy.

Clearly, the coupling of the high–frequency modes dominates, and in particular the strongest coupling is associated to the phonons at 1532, 1296, and 963

cm^{-1} phonons. Fig. 3.3 shows the eigenvectors of the these three most strongly coupled Holstein modes for the HOMO. All three modes imply CC stretching vibrations of the tetracene skeleton, as it might have been expected since the HOMO is mostly localized on the tetracene rings. Only the 963 cm^{-1} mode has some contribution of the ring breathing of the phenyl groups, but the modulation of the HOMO energy in any case results from the vibrations of the tetracene unit.

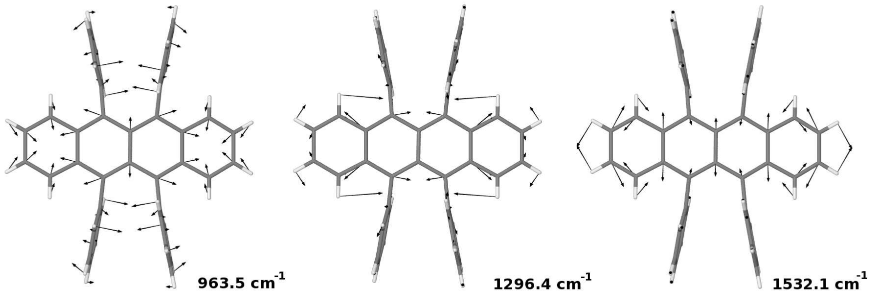

Figure 3.3: *The strongly coupled Holstein phonons*

Table 3.3: *Holstein HOMO and LUMO coupling constants of low-frequency phonons in the orthorhombic rubrene crystal. Frequencies ($\overline{\nu}$) in cm^{-1}, coupling constants in meV. For the B_{3g} modes the sign of the coupling constant for the second molecule is opposite. The ab-initio intramolecular frequencies are scaled for a factor* 0.9413

	$\overline{\nu}$ calc.	% intra	$\overline{\nu}$ exp.	g_H (HOMO)	g_H (LUMO)
A_g	37.4	46.8	35.5	−0.9	0.6
	66.6	78.5	75.3	−1.6	−1.4
	106.3	81.1	104.8	0	0.1
	125.1	94.5	118.6	1.4	2.0
	142.6	99.2	139.6	3.5	− 1.4
	217.7	100.0	220.2	−5.7	− 3.0
	253.5	99.9	–	0.1	−1.3
	261.8	100.0	–	0.9	−2.2
	334.9	100.0	–	−1.5	−10.5
B_{3g}	43.1	61.2	35.5	1.3	0.3
	86.7	48.4	75.3	−0.6	0.9
	90.6	95.7	87.4	0.1	−0.7
	123.9	96.1	104.0	1.7	−2.3
	138.2	98.7	139.2	3.3	0.2
	216.8	100.0	–	−5.8	−2.9
	254.8	99.9	–	0.8	−2.6
	262.7	100.0	–	0.7	−0.4
	335.5	100.0	–	−1.6	10.5

Table 3.4: *A_g and B_{3g} Holstein coupling constants of pure intra-molecular modes in the orthorhombic rubrene crystal. Frequencies ($\overline{\nu}$) in cm^{-1}, coupling constants in meV. Only modes with $g_H \geq 5.0$ meV are reported. A_g and B_{3g} modes have the same frequency and coupling constants, so only a single value is shown.*

$\overline{\nu}$ calc.	g_H (HOMO)	g_H (LUMO)
514.6	0.1	5.9
600.3	8.4	2.8
606.8	−11.0	−0.8
633.6	−7.2	−9.4
751.4	−0.7	−6.1
874.3	7.2	10.3
951.3	6.6	−1.8
963.5	25.1	−10.4
979.1	7.0	2.2
1158.7	−15.4	15.3
1185.7	5.1	12.9
1270.3	−17.9	18.8
1296.4	50.9	−48.6
1301.2	19.3	−18.2
1310.8	−18.1	15.6
1422.5	−2.4	23.1
1429.5	5.3	3.2
1474.6	22.9	−15.7
1486.5	−19.0	3.1
1532.1	−46.5	35.2
1593.9	5.7	8.2

Peierls coupling

We now turn our attention to Peierls coupling. A simple symmetry analysis indicates that phonons belonging to the B_{1g}, B_{2g}, A_u, and B_{3u} crystal symmetry species cannot modulate the transfer integrals. The B_{1u} and B_{2u} phonons modulate the t_{1-4} integrals, but the coupling is negligibly small (less than 1 meV), since the integrals themselves are small. The A_g and B_{3g} phonons can couple both to the t_{1-4} and to the $t_{5,6}$ transfer integrals, but only the latter are appreciably different from zero. The sign of $g_P(5;l)$ and $g_P(6;l)$ is the same for the A_g phonons, and opposite for the B_{3g} ones.

The values of the Peierls coupling constants relevant to t_5 are reported for low frequency modes in Table 3.5, and for high frequency fully intra-molecular modes in Table 3.6. The lattice distortion energy of individual phonons is compared with the corresponding small polaron binding energy in the bottom panel of fig. 3.2. Lattice distortion energies for low frequency and high frequency modes are reported as well in Fig. 3.6 and 3.8, while the Peierls coupling constants for the same modes are reported in Fig. 3.5 and 3.7.

From the tables and the figures it is immediately evident that only the low-frequency phonons exhibiting some component of inter-molecular displacement are able to appreciably modulate the transfer integrals. The most strongly coupled phonons are the second lowest frequency of each symmetry species, namely, the A_g mode at 66.6 cm^{-1} and the B_{3g} mode at 86.7 cm^{-1}. Among purely intra-molecular vibrations, only the modes at 633, 648 and 751 cm^{-1} show a weak coupling to the transfer integrals, but given their high frequency they yield negligible contributions to ε_d. The total lattice relaxation energy is calculated to be about 20 meV.

Despite the mixing between intra- and inter-molecular modes, particularly strong in rubrene due to the presence of the heavy phenyl groups, a rather sharp separation persists between Holstein and Peierls-coupled phonons. The former are indeed high-frequency, fully intra-molecular modes, and the latter are low-frequency modes, with clear inter-molecular character (as it can be noticed in Fig. 3.2, bottom), or looking at the different scales in the upper and bottom panels for low and high frequency modes. Very few phonons exhibit both types of coupling.

The eigenvectors of the four most strongly coupled Peierls modes are reported in Fig. 3.4. The A_g and B_{3g} modes at 67 and 87 cm^{-1} are rather similar, both implying the relative displacements of the tetracene skeletons of the molecules aligned along the b axis. On the other hand, the A_g modes at 37 cm^{-1} and at 106, and the pair of A_g and B_{3g} phonons around 120 cm^{-1} (the

Table 3.5: *Peierls HOMO and LUMO coupling constants (for the dimer 5) of low-frequency phonons in the orthorhombic rubrene crystal. Frequencies ($\overline{\nu}$) in cm^{-1}, coupling constants in meV. For the B_{3g} modes the sign of the coupling constant for the second molecule is opposite. The ab-initio intramolecular frequencies are scaled by a factor* 0.9413.

	$\overline{\nu}$ calc.	% intra	$\overline{\nu}$ exp.	$g_P(5,l)$ (HOMO)	$g_P(5;l)$ (LUMO)
A_g	37.4	46.8	35.5	3.4	-2.2
	66.6	78.5	75.3	-6.6	4.5
	106.3	81.1	104.8	-4.4	3.0
	125.1	94.5	118.6	-4.8	2.8
	142.6	99.2	139.6	0.0	-0.3
	217.7	100.0	220.2	1.1	-0.3
	253.5	99.9	–	0.2	-0.6
	261.8	100.0	–	0.0	0.2
	334.9	100.0	–	1.0	-0.4
B_{3g}	43.1	61.2	35.5	-2.6	1.7
	86.7	48.4	75.3	-9.3	6.1
	90.6	95.7	87.4	0.4	-0.4
	123.9	96.1	104.0	-1.1	0.7
	138.2	98.7	139.2	-1.3	0.5
	216.8	100.0	–	1.0	-0.2
	254.8	99.9	–	0.5	-0.5
	262.7	100.0	–	-0.0	0.5
	335.5	100.0	–	0.9	-0.4

latter not reported in the Figure) mostly involve the lateral phenyl group. A more detailed analysis of the eigenvectors shows that the lowest frequency a_g mode of the isolated molecule, calculated at 20 cm^{-1} (top of fig. 3.2), in the crystal redistributes mainly over four phonons, A_g at 37.4 and 66.6 cm^{-1}, and B_{3g} at 43.1 and 86.7 cm^{-1}.

Table 3.6: *A_g and B_{3g} Peierls coupling constants of pure intra-molecular modes in the orthorhombic rubrene crystal. Frequencies ($\overline{\nu}$) in cm^{-1}, coupling constants in meV. Only modes with $g_P \geq 1.0$ meV are reported. A_g and B_{3g} modes have the same frequency and coupling constants, so only a single value is shown.*

$\overline{\nu}$ calc.	$g_P(5;l)$ (HOMO)	$g_P(5;l)$ (LUMO)
633.6	1.3	−0.8
648.4	1.6	−0.2
751.4	1.4	−1.4
1422.5	−0.8	1.9

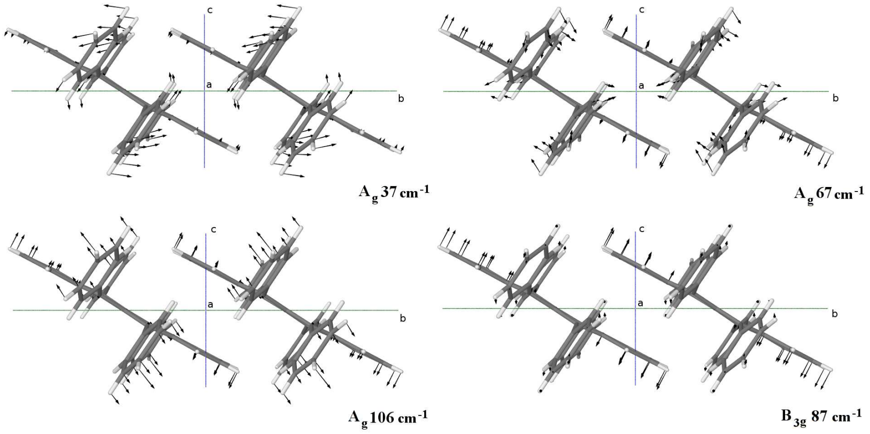

Figure 3.4: *Four examples of strongly coupled Peierls phonons.*

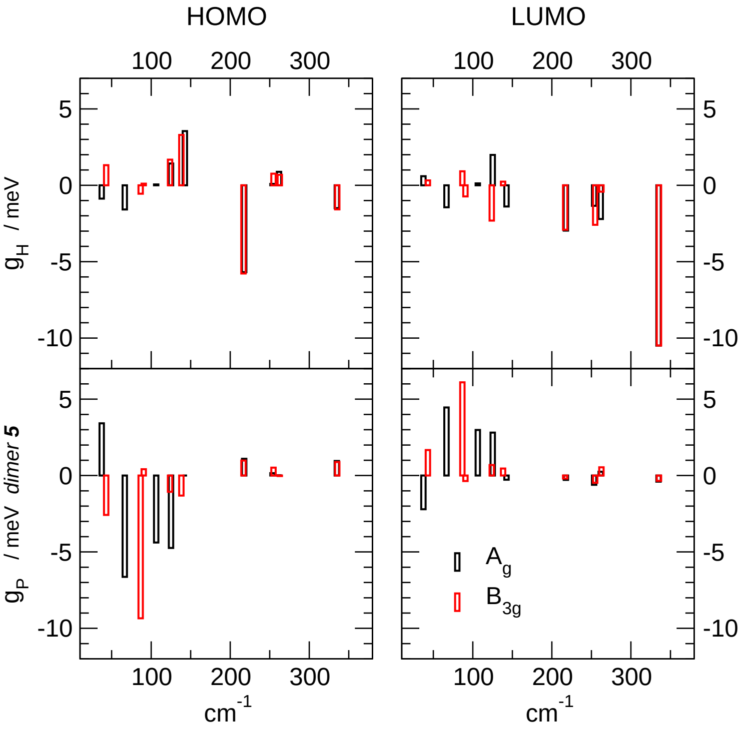

Figure 3.5: *Holstein (upper panels) and Peierls (lower panels) coupling constants for low frequency modes respect to HOMO (left) or LUMO (right) orbitals.*

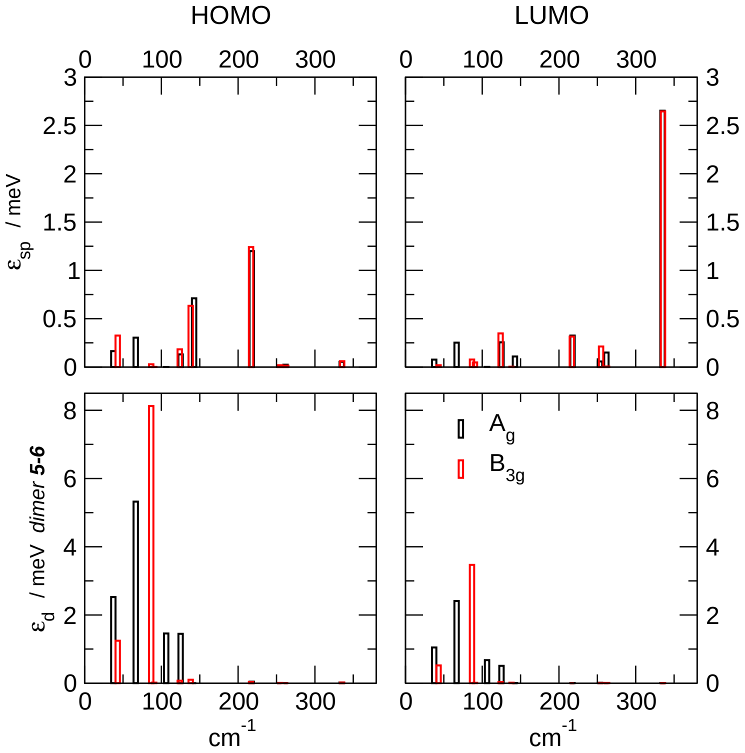

Figure 3.6: *Small polaron binding energy (top) and lattice distortion energy (bottom) for low frequency modes respect to HOMO and LUMO orbitals. Notice the different scale in the energy, because of the larger contribution coming from the Peierls coupling.*

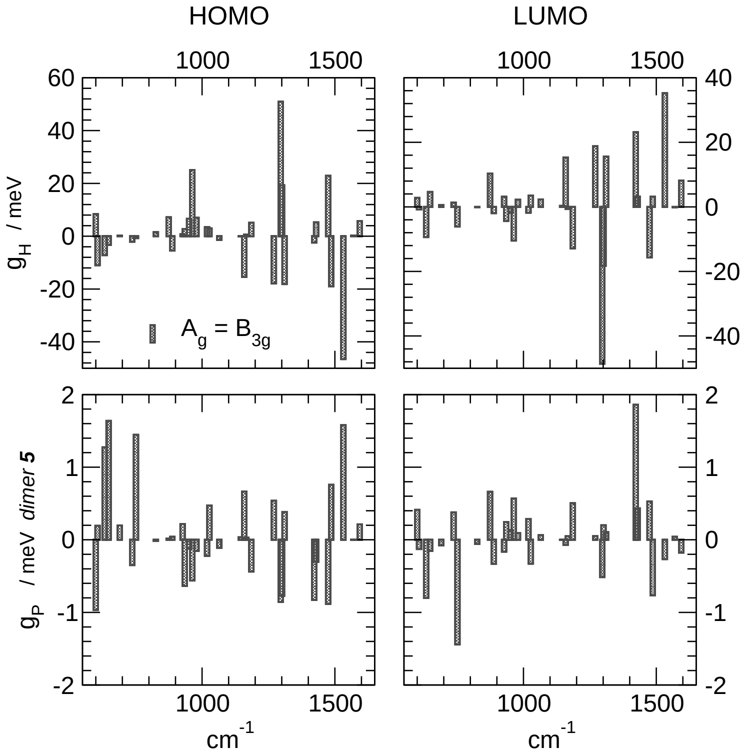

Figure 3.7: *Holstein and Peierls coupling constants for high frequency fully intramolecular modes, for HOMO and LUMO orbitals*

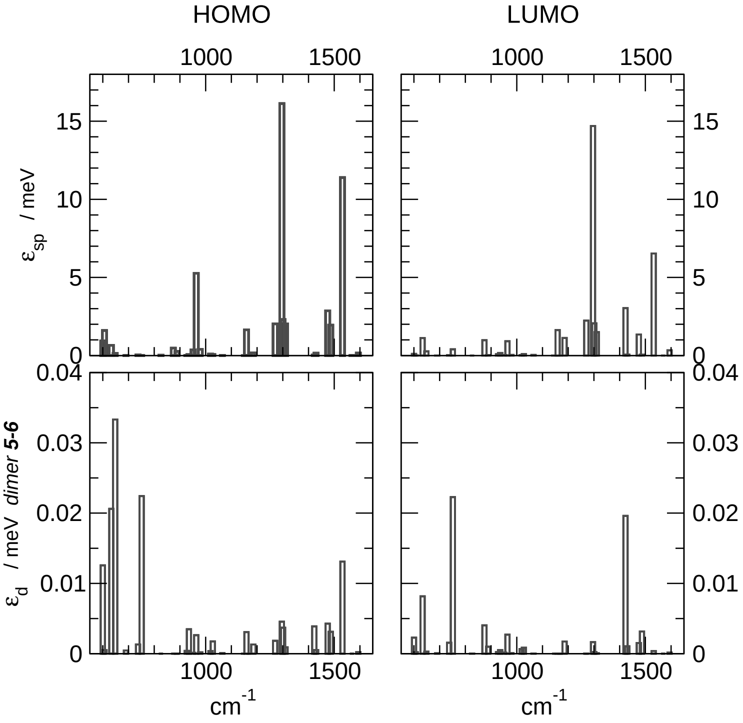

Figure 3.8: *Small polaron binding energy and lattice distortion energy for high frequency fully intra-molecular modes. Notice the very different energy scales because of the much larger* ε_{sp}.

3.2.3 Discussion

Since rubrene (like the great majority of organics) is a hole semiconductor, we will limit ourselves to discuss results relevant to the HOMO (valence band). The Holstein coupling strength of the isolated rubrene molecule has been calculated by DFT methods [134, 138], with some interesting result of a strong coupling by very low frequency (below 100 cm^{-1}) vibrations. We have already seen that the Holstein coupling of the low-frequency mode of the isolated molecules are washed out when the molecule is embedded in the crystal. A part from this, our values of the individual $\varepsilon_{sp}(m)$ are somewhat higher than those obtained by DFT, but the *relative* values show the same trend.

An important contribution in the field has been given by Troisi [124]. He has been able to predict rubrene absolute mobility and its temperature dependence (between 200 and 350 K) by looking at the thermal fluctuations of the transfer integrals. The idea of Troisi [124] is based on the analysis of the time-dependent fluctuations of the transfer integrals, obtained by classical molecular dynamics and INDO/S. Since this approach is somehow complementary to ours, it is instructive to compare the results. The top of fig. 3.9 reports the Fourier transform of the autocorrelation function of the time-dependent transfer integrals along the rubrene b axis, (adapted from [124]). The peaks correspond to the frequencies of phonons that most strongly modulate the transfer integrals, corresponding to phonons with the strongest Peierls coupling constants. The middle panel of the Figure shows the absolute values of the Peierls coupling constants in Table 3.5, multiplied by the relevant phonon density of states (PDOS), calculated as:

$$PDOS(\omega) = \sum_{l} \int \frac{1}{\frac{d\omega_l(\mathbf{k})}{d\mathbf{k}}} \tag{3.18}$$

The PDOS of rubrene shows a relatively small dispersion of the optical phonons, that somehow justify our assumption of disregarding the wavevector dependence of the coupling constants (see sect. 3.1.3). The Troisi function is less peaked than ours, with a broad band centered at about around 50 cm^{-1}, whereas in our case the most important peaks occur at higher frequencies. On the other hand, our calculations appears to be completely compatible with the experimental Raman spectra, reported in the bottom panel of fig. 3.9.

In many approaches the idea is that the mobility does not depends on the details of the carrier-phonon coupling. According to this in the Troisi's model the mobility is computed on the basis of only one effective phonon per type (Holstein and Peierls), with coupling strength taken as twice ε_{sp} and ε_d. The

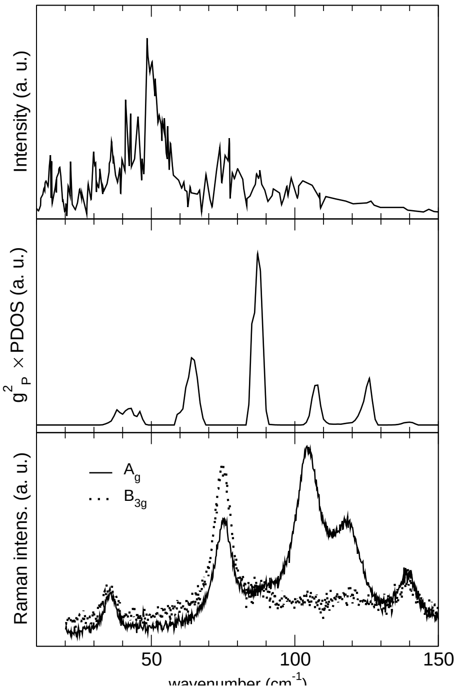

Figure 3.9: *Top panel: Frequency analysis of the nuclear motions that modulate more strongly the transfer integral along the b axis (adapted from Ref. [124]). Middle panel: Peierls coupling constant multiplied by the phonon density of states (PDOS). Bottom panel: Raman spectrum reporting the* A_g *and* B_{3g} *phonons (adapted from Fig. 1 of Ref. [135].)*

effective phonons frequency is roughly set equal to the frequency of the most strongly coupled mode [124].

Our calculated total Holstein and Peierls coupling strengths (99 and 20 meV, respectively) have the same ratio as the reorganization energies used in ref. [124]. For the frequency of the effective phonons, we use the weighted average of the coupled frequencies:

$$\omega_{\text{eff}} = \frac{\sum_j \omega_j \varepsilon_j}{\sum_j \varepsilon_j} \tag{3.19}$$

where ω_j are the frequencies of either the Holstein or Peierls coupled modes, with small polaron binding energy or lattice distortion energy ε_j. We obtain an effective frequency of the same magnitude of the one obtained by Troisi. Two different approaches give comparable parameters, in terms of which the rubrene mobility around room temperature is satisfactorily reproduced.

3.3 Conclusions and further developments

In this chapter we have illustrated the method developed to calculate the e-ph constants of organic semiconductor, with application to rubrene.

We have obtained a detailed description of phonons and of their local and non-local coupling with the holes in the valence and conduction bands. Of course, we cannot trust the absolute value of the coupling constants, but the relative magnitude of Holstein and Peierls coupling strengths is correctly considered. Indeed, having adopted a unified method of calculation, and that properly accounts for the change in the phonon description when the rubrene molecule is embedded into the crystal, we can confidently state that the overall coupling strength of the Peierls coupling (ε_d) is about one fifth of the strength of the Holstein coupling (ε_{sp}).

One key ingredient of our method is to allow interaction and mixing of the inter- and intra-molecular phonons. This has been done within the QHLD method, that provides the complete phonon structure, in a semiempirical frame based on ab initio molecular vibrations. The mixing of inter- and intramolecular vibrations is fundamental in accounting for the phonon related properties of the crystal [132]. The possibility to mix such contributions is expected to be important in a flexible molecule like rubrene. Due to the presence of heavy lateral phenyl group, isolated (gas phase) rubrene has several low-frequencies vibrations, some of which show strong Holstein coupling to the charge carrier [134, 138]. However, we have put in evidence that embedding the rubrene molecule in the crystal strongly attenuate the Holstein coupling of low-frequency phonons and the overall Holstein coupling strength is slightly decreased in the crystal. Calculation of both Holstein and Peierls coupling constants for *all* phonons in the rubrene crystal shows that despite the mixing between inter- and intramolecular phonons, a rather clear separation remains between low-frequency phonons, which mostly modulate the transfer integral, and high frequency phonons modulating the on-site energies (fig. 3.8)

It is worthy to remind the approximations we adopt in our calculations: for instance, we calculate the coupling constants only for the optical phonons at the zone center ($\mathbf{k} = 0$ assumption). This is normally done in the field of the transport properties calculation, and it is a reasonable approximation (as discussed in 3.2.3). Relaxing this approximation will offer an interesting procedure to eventually consider other source of the couplings, but is computationally very costly. In addition, we disregard the anharmonicity, which in the case of low-frequency phonons might have important effects on the physical properties above 100 - 150 K. However, it is known that macroscopic properties such as mobility do not depend strongly on the details of the carrier-phonon coupling. Indeed, models aimed at reproducing the temperature dependence of the mobility of organic semiconductors use single effective phonons as model parameters.

The approach adopted is semi-empirical, as well as the calculation performed with INDO/S (Zerner parametrization), that lead to reasonable results in term of the estimated coupling constant and relaxation energies, that are compatible with the state of the art. The model proposed is general and can be easily extended and applied to many other molecular crystal of medium and large molecular size, because of the rather low computational cost. In these respect, within a collaboration with the same group in Bologna, an application of the same approach on pentacene molecular crystal to extract coupling constants is in progress. Pentacene shows large mobilities, comparable with inorganic semiconductor, even at high temperature. The relation between structure and electronic and charge transport properties it is even more intriguing by virtue of the presence of two polymorph (H and C phases) of the pentacene crystal [139].

The extension of this study to other organic semiconductors will be helpful in validating the presented computational protocol. The application of the model to different systems will provide parameters for the local and non-local carrier-phonon coupling, in order to check if the differences in term of mobility in different systems are correctly rationalized and accounted for.

Chapter 4

Resonant energy transfer and chromophore excitation interactions

Energy transfer is a widespread process in nature: it plays a key role in life science processes like photosynthesis, or bioluminescence [11, 140]. At the same time, with the idea to mimic the nature operations, energy transfer is very important in designing new materials for the energy storage and transport [141, 142, 143, 144], as well as organic solar cells [145] and organic light-emitting devices [146].

Basically, the process describe the transfer of energy from an excited donor molecule D to an acceptor molecule A:

$$\mathsf{D}^* + \mathsf{A}^0 \rightarrow \mathsf{D}^0 + \mathsf{A}^* \tag{4.1}$$

where starred symbols refer to molecules in an excited state, while the zeroed symbols refer to the ground state. In a more general sense, D and A can be supramolecular entities, such as proteins, or semiconductor nanocrystal, like quantum dots or nanorod.

Depending on the D–A distance, three mechanisms govern energy transfer. At large distance the acceptor molecule can absorb a photon emitted by the excited donor. This non-coherent process requires a finite overlap between the fluorescence spectrum of the donor and the absorption spectrum of the acceptor and an intermolecular distance larger than the wavelength of the exchanged photon. At very short distances, when the overlap between the frontier orbitals of the D and of the A molecules become sizeable ($d_{\mathrm{DA}} \lesssim$ 3-4 Å), the energy transfer can be mediated by the exchange of electrons, in the so-called Dexter mechanism [147, 148]. Here we discuss the resonant energy transfer (RET) as relevant to intermediate distances, where RET is driven by electrostatic intermolecular interactions and can be described as the exchange of a *virtual photon*.

A general quantum description of RET, valid in perturbative limit, can be done through the Fermi Golden Rule for the transfer rate:

$$k_{ET} = \frac{2\pi}{\hbar} |\langle \Psi_{\mathrm{D^*A^0}} | \hat{\mathbb{V}} | \Psi_{\mathrm{D^0A^*}} \rangle|^2 \delta \left(\omega_{\mathrm{D^0D^*}} - \omega_{\mathrm{A^0A^*}} \right) \tag{4.2}$$

where $\hbar = \frac{h}{2\pi}$, $\Psi_{\mathrm{D^*A^0}}$ and $\Psi_{\mathrm{D^0A^*}}$ are the basis state wavefunctions relevant to the donor – acceptor system with either D or A excited, respectively. $\hat{\mathbb{V}}$ is the operator for the interactions responsible for the transfer process. The Dirac delta imposes energy conservation enforcing equal energies for the $\mathrm{D}^* \rightarrow \mathrm{D}^0$ and $\mathrm{A}^0 \rightarrow \mathrm{A}^*$ processes. Equation 4.2 clearly points to two important ingredients for the ET: the presence of some kind of *interaction* (the matrix element $\mathbb{V}_{\mathrm{D^*D^0,A^0A^*}}$, later on simply $\mathbb{V}$) between the two molecular unit involved in RET; and the *conservation* of energy. From the spectroscopic point of view, energy conservation is guaranteed by the presence of a spectral overlap between the emission spectrum of the D and the absorption spectrum of A. Hence the last factor of eq. 4.2 can be generalized, accounting for finite bandwidths:

$$\delta \left(\omega_{\mathrm{D^0D^*}} - \omega_{\mathrm{A^0A^*}} \right) \longrightarrow \int_0^\infty S_{\mathrm{D}}^{em}(\omega) S_{\mathrm{A}}^{abs}(\omega) \, \mathrm{d}\omega \tag{4.3}$$

where $S_{\mathrm{D}}^{em}(\omega)$ and $S_{\mathrm{A}}^{abs}(\omega)$ refer to emission spectra of the donor and the absorption spectra of the acceptor.

In this chapter we discuss some theoretical aspect of resonant energy transfer. In particular we will introduce an original approach to estimate $\mathbb{V}$, based on semiempirical computational methods. We show preliminary results on selected molecular systems. This work is due to a collaboration with Prof. Pati group of JNCASR (Bangalore, India), in the frame of an Indo-Italian project, financed by the Foreign Affair Ministry. A consistent part of the work has been done in Bangalore during a short research period (April 2010).

4.1 Common theoretical treatment for resonance energy transfer

4.1.1 The transition densities approach

Assuming a perturbative approach, the exciton states involved in the ET process can be expressed as a product of the wave functions of the isolated acceptor A and donor D unit:

$$\begin{aligned} |\Psi_{\mathrm{D}^*\mathrm{A}^0}\rangle &\approx |\psi_{\mathrm{D}^*}\rangle|\psi_{\mathrm{A}^0}\rangle \equiv |\psi_{\mathrm{D}^*}\psi_{\mathrm{A}^0}\rangle \\ |\Psi_{\mathrm{D}^0\mathrm{A}^*}\rangle &\approx |\psi_{\mathrm{D}^0}\rangle|\psi_{\mathrm{A}^*}\rangle \equiv |\psi_{\mathrm{D}^0}\psi_{\mathrm{A}^*}\rangle \end{aligned} \qquad (4.4)$$

If we consider Coulombic interactions the explicit expansion for $\mathbb{V}$ reads:

$$\begin{aligned} \mathbb{V} = \langle \Psi_{\mathrm{D}^*\mathrm{A}^0}|\mathbb{V}|\Psi_{\mathrm{D}^0\mathrm{A}^*}\rangle &\approx \langle \psi_{\mathrm{D}^*}\psi_{\mathrm{A}^0}|\mathbb{V}|\psi_{\mathrm{D}^0}\psi_{\mathrm{A}^*}\rangle \\ &= \langle \psi_{\mathrm{D}^*}\psi_{\mathrm{A}^0}|\sum_{d,a}\frac{1}{|\mathbf{r}_d - \mathbf{r}_a|}|\psi_{\mathrm{D}^0}\psi_{\mathrm{A}^*}\rangle \end{aligned} \qquad (4.5)$$

where $\mathbf{r}_D$ and $\mathbf{r}_A$ are the electronic coordinates of donor and acceptor, respectively; the sum runs over d and a electrons belonging to D and A, respectively. In line with the perturbative treatment, these equations do not account for D A electron exchange and nor for relaxation of the wavefunction due to the D A interactions. At this stage it is useful to introduce the transition densities, for the donor and the acceptor units:

$$\varrho_{\mathrm{D}}(\mathbf{r}_d) = \psi_{\mathrm{D}^0}(\mathbf{r}_d)\psi_{\mathrm{D}^*}(\mathbf{r}_d) \qquad (4.6)$$

$$\varrho_{\mathrm{A}}(\mathbf{r}_a) = \psi_{\mathrm{A}^0}(\mathbf{r}_a)\psi_{\mathrm{A}^*}(\mathbf{r}_a) \qquad (4.7)$$

Then eq. 4.5 can be rewritten integrating the Coulomb interaction between transition densities of D and A:

$$\mathbb{V} = \iint \varrho_{\mathrm{D}}(\mathbf{r}_d)\frac{1}{|\mathbf{r}_d - \mathbf{r}_a|}\varrho_{\mathrm{A}}(\mathbf{r}_a)d\mathbf{r}_d d\mathbf{r}_a \qquad (4.8)$$

Time dependent density functional theory (TDDFT) method, as well as ab-initio approaches, can produce accurate transition densities, and hence are extensively used to calculate RET interaction energies [142].

4.1.2 The dipolar approximation and experimentally accessible information

When intermolecular distances are much larger than the molecular dimensions the charge distribution on the D and A molecules can be described in the dipolar approximation. In this approximation one regains eq. 4.8 but with the electronic transition densities ϱ_{D} and ϱ_{A} substituted by transition dipoles moments, $\boldsymbol{\mu}_{\mathrm{D}}$ and $\boldsymbol{\mu}_{\mathrm{A}}$. The interaction between point dipoles reads:

$$\mathbb{V} \approx \mathbb{V}_{dd} = \frac{\boldsymbol{\mu}_{\mathrm{D}}\boldsymbol{\mu}_{\mathrm{A}}}{R^3} - \frac{3\left(\boldsymbol{\mu}_{\mathrm{D}} \cdot \mathbf{R}\right)\left(\boldsymbol{\mu}_{\mathrm{A}} \cdot \mathbf{R}\right)}{R^5} \tag{4.9}$$

where the dot implies a scalar product between vectors. $\mathbf{R} = \mathbf{r}_d - \mathbf{r}_a$ represents the vector oriented along the D–A centers direction, and obviously $R = |\mathbf{R}|$. We rewrite this expression in a more readable form, with the definition of a geometrical parameter κ :

$$\kappa = \check{\boldsymbol{\mu}}_{\mathrm{D}} \cdot \check{\boldsymbol{\mu}}_{\mathrm{D}} - 3\left(\check{\boldsymbol{\mu}}_{\mathrm{D}} \cdot \check{\mathbf{R}}\right)\left(\check{\boldsymbol{\mu}}_{\mathrm{A}} \cdot \check{\mathbf{R}}\right) \tag{4.10}$$

$$\mathbb{V}_{dd} = \kappa\,\frac{\mu_{\mathrm{D}}\mu_{\mathrm{A}}}{R^3} \tag{4.11}$$

where the unit vectors for dipoles are defined in these way $\check{\boldsymbol{\mu}}_{\mathrm{D}} = \frac{\boldsymbol{\mu}_{\mathrm{D}}}{|\boldsymbol{\mu}_{\mathrm{D}}|}$, and the same relations stands for A. The orientational factor κ depends on two angles defined in fig. 4.1:

$$\kappa = \cos\theta_{\mathrm{DA}} - 3\cos\theta_{\mathrm{D}}\cos\theta_{\mathrm{A}} \tag{4.12}$$

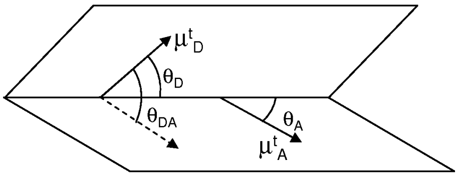

Figure 4.1: *Definition of angles for the calculation of the orientational factor κ.*

The main advantage of the dipolar approximation is that all quantities entering eq. 4.9 are experimentally accessible, as originally recognized by Förster [149, 150, 151, 152]. Indeed, the transition dipole moment of the donor μ_{D} is related to the fluorescence process and can be estimated from D fluorescence quantum yield and excited-state lifetime in the absence of transfer (i.e. in the absence of the acceptor). μ_{A} can be measured instead from the integral of the A absorption spectrum (oscillator strengths). The orientational factor κ can be easily calculated. For example, if energy transfer is measured in solution, donor and acceptor molecules are randomly oriented and the transition dipole moments of the donor and of the acceptor can explore all possible orientations during the lifetime of a possible ET process: the orientational factor is averaged over all possible orientations, and $\langle k^2 \rangle = 2/3$. Different is the case of a solute in a rigid matrix, where the orientation of transition dipole moments is random, but they are constrained in a fixed position during the emission process, so that $\langle k \rangle^2 = 0.476$.

The rate of RET k_{RET} in eq. 4.2 is usually rewritten as

$$k_{RET} = \frac{2\pi}{\hbar} |\mathbb{V}_{dd}|^2 J = \frac{1}{\tau_D} \left(\frac{r_0}{R} \right)^6 \tag{4.13}$$

where J represent the spectral overlap of the formula 4.3, τ^0_{D} represents the characteristic time of the decay of the donor excited state and r_0 is the Förster radius, at which energy transfer and spontaneous decay of the excited donor are equally probable. The energy-transfer efficiency is given by:

$$\phi_{RET} = \frac{k_{RET}}{\frac{1}{\tau^0_{\mathbf{D}}} + k_{RET}} = \frac{1}{1 + \left(\frac{R}{r_0} \right)^6} \tag{4.14}$$

All these expressions involve quantities that can easily accessed experimentally and the Förster approach (i.e. the RET description based on dipolar approximation) has been extensively adopted. The R^{-6} dependence is a typical feature of this approximation, and has been in used to determine distance between interacting D and A, using RET as a “spectroscopic ruler”.

However the dipolar approximation works only if the distance between dipoles is larger than the molecular size. In multichromophoric assemblies, for instance, interchromophores distances can be very small, and the dipolar approximation becomes inadequate to describe interactions responsible for energy transfer. Relaxing the dipolar approximation allows to calculate in a more rigorous way the interaction between molecules, but, even more interestingly, it may open new channels for energy transfer, which are strictly forbidden when the dipolar approximation is adopted. Of particular interest is the case of electronic dark state (i.e. optically inactive), that can interact by non dipolar mechanism, and it will be discussed later.

4.2 Semiempirical MO-CIS approaches to energy transfer

We adopt an INDO/S MO description, extensively discussed in appendix C, to directly calculate the interaction $\mathbb{V}$ involved in the RET, through the estimate of the configuration interaction (CI) matrix elements without making any reference to transition densities. Results obtained in this original approach will be compared with results obtained with the transition density method.

Actually, the method presented in this section, applies more generally to HF–CI calculations, irrespectively of the model Hamiltonian assumed for the description, either INDO/S or ab-initio Hamiltonians, and can be adapted to different basis. It can also be extended to double CI (CISD) scheme. However we will explicitly refer to INDO/S – CIS.

The idea is that the non-interacting "dimer", the supermolecule formed by D and A, can be considered as the basis for the evaluation of the interaction $\mathbb{V}$. Then a perturbative frame is implicitly adopted, but the form of the interaction operator is fully defined by the Hamiltonian of the chosen method. No other approximations will be done.

In the computational procedure a delicate step is to identify the transitions that are relevant to the energy transfer process, i. e. the D excitation and the A de-excitation. In this respect a knowledge of the experimental spectroscopic properties of the D and A molecules, is helpful in order to select the low energy excitation of the proper energy and intensity, among the calculated ones. Here we only address the evaluation of the $\mathbb{V}$ element. The experimentalist must choose with care the D and the A molecules in order to ensure the proper spectral overlap between relevant transitions.

4.2.1 Frozen orbitals MO-CIS evaluation of $\mathbb{V}$ with INDO/S Hamiltonian

The first calculation refer to the D A pair ideally "prepared" placing the two molecules at a very large distance, $R > 100$ Å, as to neglect any intermolecular interaction. This calculation defines the non-interacting reference states that will be adopted as the basis for the perturbative treatment of the interaction. We will refer to this calculation as the *infinite distance* calculation, and we label all quantities obtained in this limit with the ∞ index or apex.

If a method to compute the excitations, like a configuration interaction (CI), is applied to the supermolecule DA at infinite distance, the calculated electronic transitions will only involve MO localized on either the D or A unit. Therefore, it is easy to select the two states responsible for the for the RET process, nominally the D excited state (when A is in the ground state) and the A excited state (when D is in the ground state configuration); respectively written as $|\mathrm{D}^*\mathrm{A}^0\rangle$ and $|\mathrm{D}^0\mathrm{A}^*\rangle$. In the CI approach these are expressed as as linear combination of single excited configurations (compare with equation C.7):

$$\begin{aligned} |\mathrm{D}^*\mathrm{A}^0\rangle_\infty &= \sum_{i,r} C^{\infty}_{\mathrm{D}\,i,r} \Psi_{i\to r} && (4.15) \\ |\mathrm{D}^0\mathrm{A}^*\rangle_\infty &= \sum_{i,r} C^{\infty}_{\mathrm{A}\,i,r} \Psi_{i\to r} && (4.16) \end{aligned}$$

where $C^{\infty}_{\mathrm{D}i,r}$ ($C^{\infty}_{\mathrm{A}i,r}$) are the CI coefficients relevant to the $|D^*A^0\rangle$ ($|D^0A^*\rangle$) state described at infinite distance, and $\Psi_{i\to r}$ is the configuration obtained promoting an electron from the i-th occupied MO towards the r-th virtual MO. Here and in the following we will adopt the *frozen orbital* approach, and whenever MO are introduced they refer to infinite distance.

The interaction $\mathbb{V}$ is then calculated (according to its perturbative definition), on the basis of these frozen MOs referring to infinite distance, but actually using the finite distance Hamiltonian H^d. According to this scheme, the relevant matrix element for RET interaction then reads:

$$\mathbb{V} = _\infty\langle \mathrm{D}^*\mathrm{A}^0|\hat{H}^d|\mathrm{D}^0\mathrm{A}^*\rangle_\infty = \sum_{ir,js} C^{\infty}_{\mathrm{D}\,i,r} C^{\infty}_{\mathrm{A}\,j,s} \langle \Psi_{i\to r}|\hat{F}^d|\Psi_{j\to s}\rangle = \sum_{ir,js} C^{\infty}_{i,r} C^{\infty}_{j,s} H^d_{ir,js} \qquad (4.17)$$

where $\hat{F}^d$ is the Fock matrix operator for the pair of molecules at distance d.

The approach is expected to apply when d is small enough for the two molecules to feel each other, and large enough to neglect any intermolecular charge-transfer. According to eq. 4.17 the calculation of the RET matrix elements is possible provided that we have expressions for the coefficient of the CI expansion of basis (infinite distance) states ($C^{\infty}_{i,r}$ and related in eq. 4.15 and 4.16) and the elements of the CI matrix, $\mathbf{H}^d$ calculated at finite distance on the basis of the frozen orbitals.

The calculation of $H^d_{ir,js}$

To find explicit expression for the CI matrix elements on the frozen orbital basis we work in second quantization and label occupied and virtual orbitals of the D molecules with the i and the r indexes, respectively. Symbols j and s refer to occupied and virtual orbitals of the A molecule. The matrix elements relevant to RET, $H^d_{ir,js}$ in eq. 4.17, have $i \neq j$ and $r \neq s$. The general molecular Hamiltonian, on the basis of the MO, can be written as:

$$H = \sum_{k,l,\sigma} h_{kl} a^{\dagger}_{k,\sigma} a_{l,\sigma} + \frac{1}{2} \sum_{klmn,\sigma,\mu} (kn|lm) a^{\dagger}_{k,\sigma} a^{\dagger}_{l,\mu} a_{m,\mu} a_{n,\mu} \tag{4.18}$$

where Greek letters refer to AO, h_{kl} are the matrix elements of the one-electron Hamiltonian and $(kn|lm)$ are the bielectronic repulsion terms. Moreover:

$$\begin{aligned} \Phi_{i \to r} &= \frac{1}{\sqrt{2}} [a^{\dagger}_{1,\alpha} a^{\dagger}_{1,\beta} \dots a^{\dagger}_{i,\alpha} \dots a^{\dagger}_{r,\beta} \\ &\quad - a^{\dagger}_{1,\alpha} a^{\dagger}_{1,\beta} \dots a^{\dagger}_{i,\beta} \dots a^{\dagger}_{r,\alpha}] |0\rangle \qquad (4.19) \\ \Phi_{j \to s} &= \frac{1}{\sqrt{2}} [a^{\dagger}_{1,\alpha} a^{\dagger}_{1,\beta} \dots a^{\dagger}_{j,\alpha} \dots a^{\dagger}_{s,\beta} \\ &\quad - a^{\dagger}_{1,\alpha} a^{\dagger}_{1,\beta} \dots a^{\dagger}_{j,\beta} \dots a^{\dagger}_{s,\alpha}] |0\rangle \qquad (4.20) \end{aligned}$$

For the CIS matrix elements of interest for RET ($i \neq j$ and $r \neq s$) only bielectronic terms are relevant and the resulting expression, derived from equation 4.17, actually coincides with the standard expression built with Slater's rule (p. 236 in [153]), and then:

$$H^{d}_{ir,js} = 2(ri|js) - (rs|ji) \tag{4.21}$$

The equivalence of eq. 4.21 with the standard expression was not granted from the beginning. Indeed the standard expression for the CIS Hamiltonian is written on the basis of determinants that are built with MOs that diagonalize the Fock matrix. The MO that appear in eq 4.17 do not diagonalize the Fock matrix at distance d, while they diagonalize the Fock matrix at infinite distance. The formal equivalence is related to the fact that the only matrix elements of H^{d} in the RET refer to the non diagonal elements that mix the configurations coming from the D excitations with the one from A. The same equivalence does not apply to diagonal elements of the CI matrix. The four-center integrals that enter the equation 4.21 are the same that enter a regular CIS calculation, and then can be calculated in the INDO/S approach, according to the approximations and the expressions reported in the appendix sect. C.3.2, and imposing frozen orbitals.

Therefore, to calculate $\mathbb{V}$ within this INDO/S MO–CIS formulation, the calculation has to be run for the pair D and A first at very large distance, to calculate relevant MO, select relevant excitations, and obtain single excited configuration coefficients $C^{\infty}_{\mathrm{D}\ i,r\ ;\ \mathrm{A}\ j,s}$ of eq. 4.15 and the frozen MOs. Thereafter, a calculation is run at finite d distance, without diagonalizing any Fock or CIS matrix, but simply evaluating $H^{d}_{ir,js}$ according to eq. 4.21. This information enters eq. 4.17 to get the required RET matrix element. Thus, no diagonalizations at finite distance are required: only bielectronic integrals $(ri|js)$ and $(rs|ji)$ have to be calculated at finite d for the calculation of selected matrix elements of the CI matrix, in number of $2\mathrm{N}_C$, in N_C is the number of configurations that are basis for the CI. The calculation of four center integrals, even if approximated in the INDO/S Hamiltonian, is actually computationally demanding when the complete CIS is needed, as required for the calculation of excitation at infinite distance. Actually the infinite distance calculation can be optimized by performing the calculation on the two molecules separately and diagonalizing the Fock and CIS matrix for the D and A separately, obtaining the relevant MO and excitations. Then the AO basis for the supermolecule can be constructed by simply queuing A AOs after D AOs. The MOs and the CIS matrix for the supermolecule can be easily rewritten on the composite basis, filling with zeroes. Then the calculation of $H^{d}_{ir,js}$ can be performed normally. In these calculation at finite distance d, only the specific CI matrix elements entering the expression for $\mathbb{V}$ (eq. 4.17) have to be calculated, representing just a minimal fraction of the full CI matrix. For the calculation of $\mathbb{V}(d)$ we have modified an available INDO/S code [130], (see appendix C.3).

4.2.2 From transition densities to point atomic charge densities in the INDO/S

For the sake of comparison we elaborate on the transition density approach described in sect. 4.1.1 and discuss how it applies to INDO/S Hamiltonian. In particular, as in other semiempirical approaches, in INDO/S the basis wavefunctions are not fully defined (i.e. they do not have an explicit space coordinate dependence), so that the transition densities as defined in eq. 4.6 and 4.7 cannot be calculated. Transition densities in fact collapses in INDO-like approaches into a distribution of transition charges located at atomic sites. Then we define point transition charges, located at the atomic position. For a single configuration we will refer to the $i \rightarrow r$ excited configuration for D and $j \rightarrow s$ for A unit in the way that the configuration transition densities are:

$$\mathrm{q}^{i\rightarrow r}{}_{d} = \sum_{\delta\in d} c_{i\delta} c_{r\delta} \tag{4.22}$$

$$\mathrm{q}^{j\rightarrow s}{}_{a} = \sum_{\alpha\in a} c_{j\alpha} c_{s\alpha} \tag{4.23}$$

where the first equation stand for the D molecule and δ refers to all the AO centered on the atom d, while the second equation stands for the molecule A (α is the AO for a atom). The coefficients in equation 4.22 are the MO coefficients.

Once the transition is defined as a linear combination of single CI (see appendix eq. C.8, and also 4.15), the point transition charge density results:

$$\tilde{\mathrm{q}}_{d\ \mathrm{D}^*\mathrm{A}^0} = \sum_{(i,r)} C_{\mathrm{D}\ i,r} \mathrm{q}^{i\to r}{}_d \tag{4.24}$$

$$\tilde{\mathrm{q}}_{a\ \mathrm{D}^0\mathrm{A}^*} = \sum_{(j,s)} C_{\mathrm{A}\ j,s} \mathrm{q}^{j\to s}{}_a \tag{4.25}$$

where again the first line refer to the transition charge at the atom d for an excitation localized on the donor and the second line refer to the localized acceptor excitation. The above expressions for the charge densities refer to the non-interacting D − A pair. The calculation, that involve extensive CIS, can be conveniently performed separately on D and on A.

In this approximation the RET interaction energy in 4.8 reads:

$$\mathbb{V} = \sum_d \sum_a \tilde{\mathrm{q}}_{d\ \mathrm{D}^*\mathrm{A}^0} \tilde{\mathrm{q}}_{a\ \mathrm{D}^0\mathrm{A}^*} \frac{1}{|\mathbf{r}_d - \mathbf{r}_a|} \tag{4.26}$$

4.3 Extended dipole methods in essential state models

We finally mention an approach to the calculation of V based on essential state model [154]. As discussed on chap. 1 and chap. 2 essential state models proved very successful to describe electrostatic interactions between different CT chromophores, and, in this respect, they are expected to provide a reliable description of RET occurring between CT chromophores. In the examples studied, the donor molecule is a dipolar *DA* chromophore, that can be described based on a two-state model (sect. 1.1), while the acceptor A can be a dipolar, a quadrupolar and an octupolar molecule, described in terms of two, three, or four state models, respectively. For each model the basis states are defined considering the neutral state plus a zwitterionic state for each arm. In essential state models the charge distribution on CT chromophores is approximated to point charges at the center of the *D* and *A* groups. The calculation of relevant $\mathbb{V}$ interaction is described in [154] and will not be addressed here.

4.4 Results

To test the proposed approach to the calculation of $\mathbb{V}$ we consider two *DA* pairs. In both cases the D species is a commercial laser dye, LD390 (**L** in the following). In the first pair we consider a dipolar acceptor, cumarine C480 (**C**), while in the second pair the acceptor is the quadrupolar chromophore trans,trans-bis(dimethylamino)styril-tetrafluorobenzene. (**Q**).

For each D – A pair an INDO/S calculation is performed, in order to calculate $\mathbb{V}$ with the direct matrix element evaluation (eq. 4.17), or via the charge density approach (eq. 4.26). Results are compared with the dipolar approximation $\mathbb{V}_{dd}$ (eq. 4.9). Results are obtained running a properly adapted version of INDO/S program on molecular structures, optimized at DFT B3LYP level using Gaussian package (Prof. Pati Group) [154]. Geometry optimization refer to the ground state for the acceptor molecule, while the D geometry is optimized with reference to the emitting state. Interactions are always reported in absolute value.

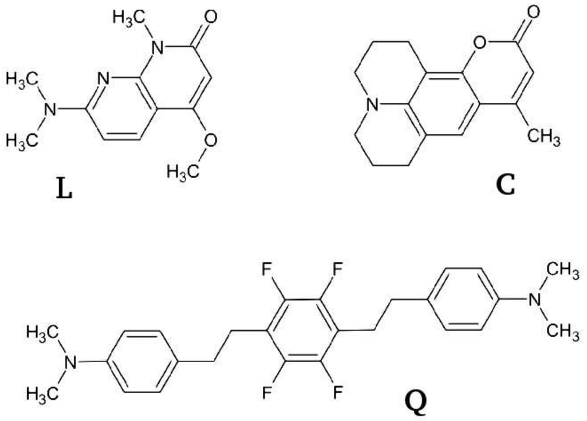

Figure 4.2: *Molecular structure of studied molecules.*

We now concentrate on the first pair of dipolar molecules: LD390 (**L**) that works as the donor, and the coumarine C480 (**C**) that work as an acceptor. The molecular structure are reported in fig. 4.2. For both molecules the lowest energy transition is optically allowed with large oscillator strength and CT character. Relevant transition energies and oscillator strength are reported in table 4.1.

The absolute values of the calculated $\mathbb{V}$ are reported in fig. 4.3 and 4.4 for two different geometry of the donor-acceptor pair. In particular ***A1*** and ***A2*** in fig. 4.3 refer to a "face to face" geometry with R measuring the interplanar distance. In ***B1*** and ***B2*** in fig. 4.4 the molecule are instead aligned and R measures the distance between the centers of the charge distributions. ***A*** geometry

Table 4.1: *Properties of the computed transition at INDO/S level (full CIS) for* **L** *as* Donor*, and* ***C*** *and* **Q** *as* Acceptor*.*

		energy (cm^{-1})	trans. dip. moment (D)	osc. strength
L:	$\lvert D^{*}A^{0}\rangle_{\infty}$	26850	6.8	0.59
C:	$\lvert D^{0}A^{*}\rangle_{\infty}$	25720	7.1	0.60
Q(1):	$\lvert D^{0}A^{*}\rangle_{\infty}$	24010	13.4	2.04
Q(2):	$\lvert D^{0}A^{*}\rangle_{\infty}$	29930	0.0	0.00

leads to larger RET interactions, about doubled compared to the ***B*** geometry. Results obtained in the dipolar approximation (continuous line) in fig. 4.3 and 4.4 represent the limiting results at large R of the two other approaches. Deviations from the dipolar limit are in general sizeable. The direct calculation of the interaction via the calculation of relevant matrix element of the CI matrix yields in general to a large $\mathbb{V}$ value than the method based on transition charges.

We now turn attention to the interaction between the polar dye **L** and the quadrupolar dye **Q**. According to the essential state analysis for a quadrupolar dye we expect an optically allowed lowest excitation and a second excited state optically forbidden [21]. Both states have a strong CT character. The two lowest excitation calculated for **Q** confirm this general picture, as shown in the table 4.1.

Five different geometries are considered for the **L** – **Q** pair. For the two face to face geometries ***A*** and ***C*** of fig. 4.5, R measures the interplanar distance. For the T-shaped geometry ***B*** of fig. 4.5 R is the distance between the **Q** plane and the center of charge distribution of **L**. Finally for the two aligned geometries of fig. 4.6, R measures the distance between the centers of charge distributions.

Here we calculate $\mathbb{V}$ from the excited **L** towards either the first or a second excited state of **Q**, **Q(1)** and **Q(2)**, respectively. In particular we notice that in the dipolar approximation the optically forbidden (dark) **Q(2)** state would be totally inactive in RET and the relevant $\mathbb{V}$ should vanish. The most striking result is that in most cases the $\mathbb{V}$ interaction involving the dark state is of the same order of magnitude as the interaction involving the allowed state **Q(1)**, demonstrating the failure of the dipolar approximation. Interestingly, in geometry ***B*** the RET interaction is larger for the **L** – **Q(2)** interaction than for the **L** – **Q(1)**, which almost vanishes. This is related to the different symmetry of the two excited state of **Q**, with respect to the orthogonal orientation of the dipolar

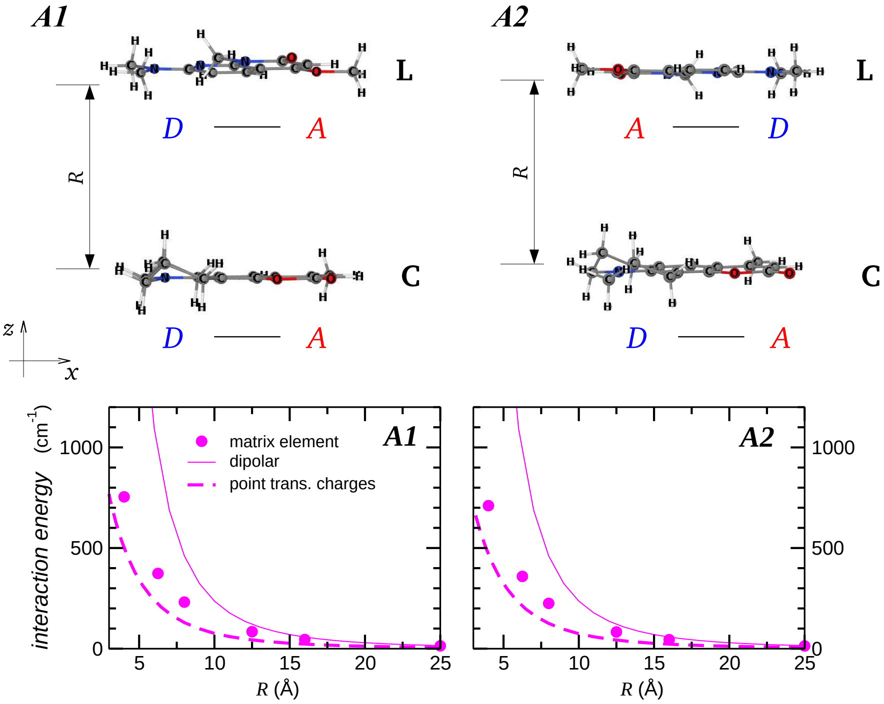

Figure 4.3: *Results of the INDO/S calculation on the pair* **L** *–* **C** *at different distance, with the three methods: direct evaluation of matrix elements (symbols), dipolar approximation, atomic point transition charges (dotted thick line). As represented in the upper scheme in the geometry on the right the* **L** *molecule is rotated of 180° around the z axis.*

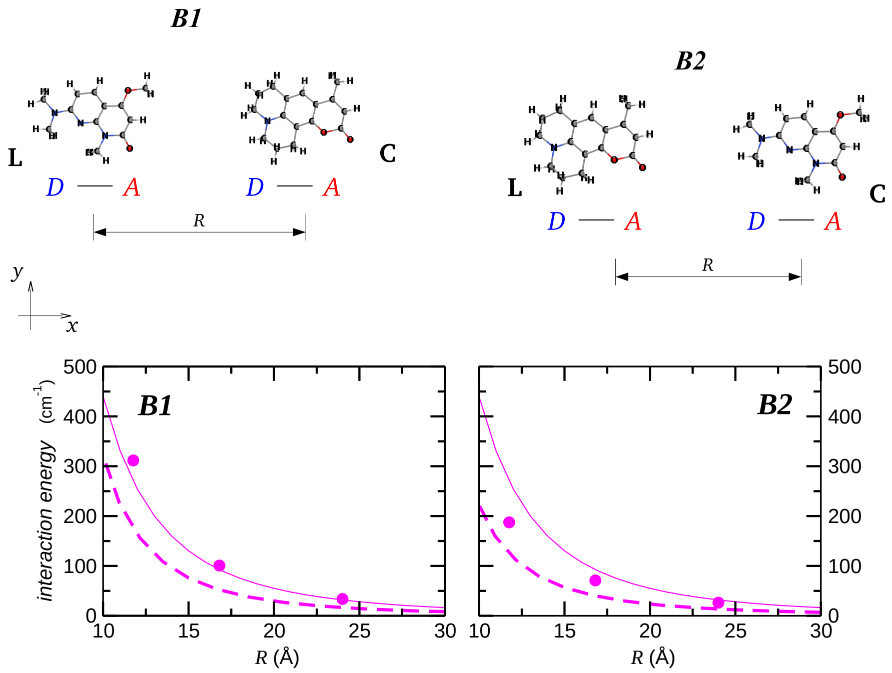

Figure 4.4: *Results of the INDO/S calculation on the pair* **L** *–* **C***at different distance in the "aligned" geometry, with the three methods: direct evaluation of matrix elements (symbols), dipolar approximation, atomic point transition charges (dotted thick line). As sketched at the top geometry on the left refer to the two molecules when approaching the A group of the* D *molecule and the D group of the* A *molecule, while vice versa on the left.*

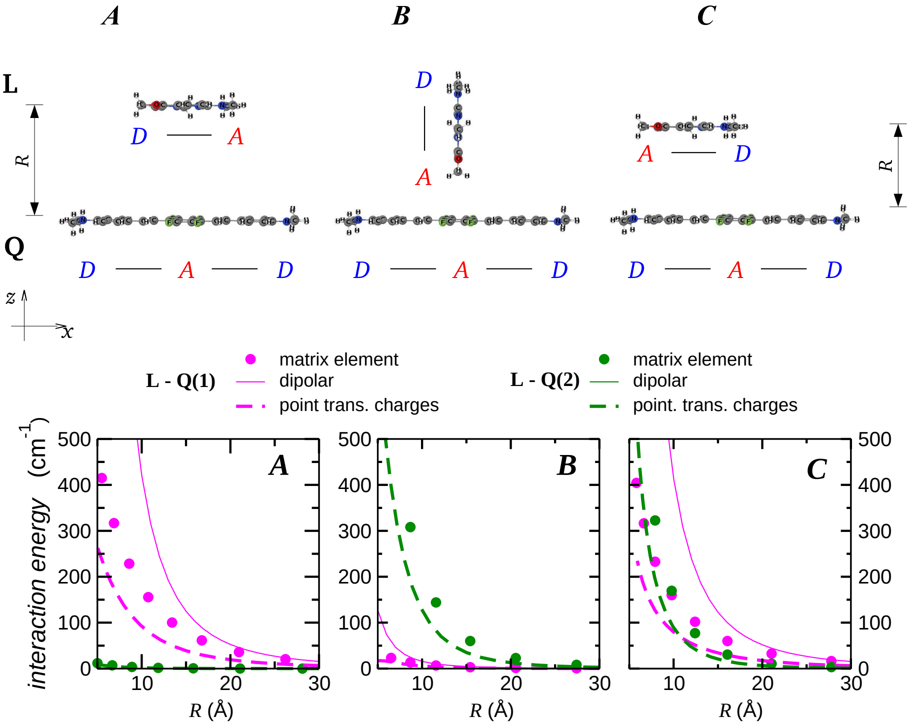

Figure 4.5: *Results of the INDO/S calculation on the pair* **L** – **Q** *at different distance, with the three methods: direct evaluation of matrix elements (symbols), dipolar approximation (line), atomic point transition charges (dotted thick line). The calculation has been performed in three different geometry, as sketched in the top scheme (view on the xz plane). Different color correspond to the choice of two different excited state in for the* **Q** *molecule, expressed as Q(1) (pink lines and symbols) and Q(2) (green lines and symbols).*

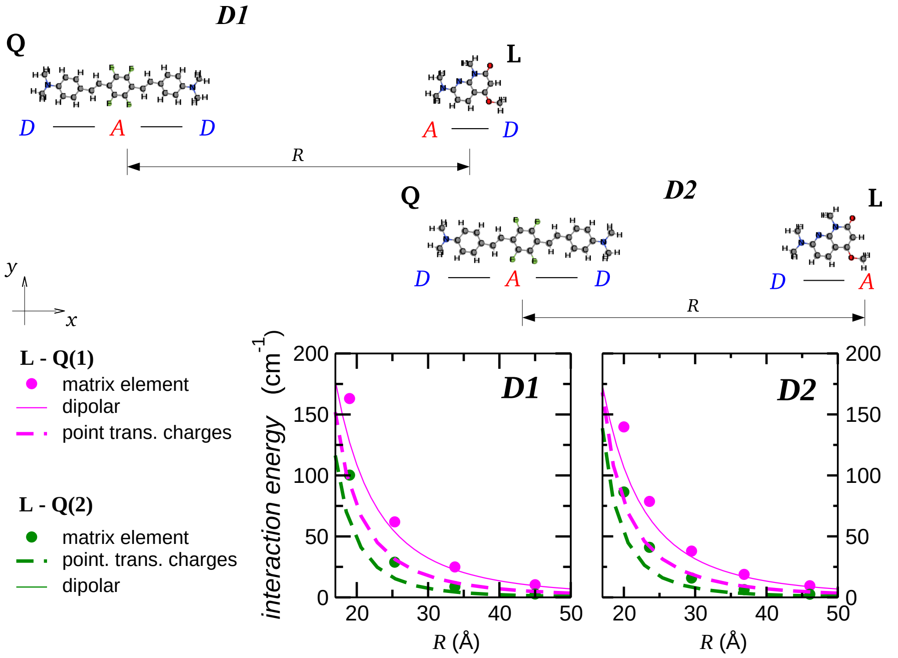

Figure 4.6: *Results of the INDO/S calculation on the pair* **L** *–* **Q** *at different distance in the "aligned" geometry, with the three methods: direct evaluation of matrix elements (symbols), dipolar approximation (line), atomic point transition charges (dotted thick line). The calculation has been performed in two different geometry, as sketched in the top scheme. Different color correspond to the choice of two different excited state in for the* **Q** *molecule, expressed as Q(1) (pink lines and symbols) and Q(2) (green lines and symbols).*

molecule **L** [154]. At the same time, in ***C*** geometry, the **L – Q(2)** contribution is larger than the **L – Q(1)** at short distances.

A proper investigation of the R dependence of $\mathbb{V}$ is an important issue to understand the physical mechanism of the interaction. The dipolar approximation always gives the classical $\mathbb{V}(R) \sim R^{-3}$ dependence, but the R-dependence is different and more complex in other geometries.

4.5 Conclusion and further developments

We presented a novel computational scheme to evaluated RET interaction energy. The method is general and applies irrespective of the choice of the model Hamiltonian and of the basis set, as well the number and level of CI will affect the global quality of the results. In particular the approach can be extended to doubly excited configurations, and applies quite naturally to TD-DFT scheme as well (work is in progress along these line in collaboration with Prof. Pati).

For both the **L–C** and **L–Q** pairs the results unambiguously point to the failure of the dipolar approximation at distances $\sim$ 20 Å and below. Particularly striking in this respect are the results obtained for RET involving the dark state of **Q**: this transfer, forbidden in the dipolar approximation, is instead allowed with $\mathbb{V}$ values that, depending on the supramolecular arrangement of the D and A pair, can be even larger than those calculated for the allowed **Q** transition. Results obtained using the transition density approach (that within INDO/S reduces to transition charges approach) and via the direct calculation of the CI matrix elements are in good qualitative agreement in all cases but always lead to large $\mathbb{V}$ for the direct calculation with respect to transition density calculations.

While the dipolar approximation fails at short distances, both the transition densities and the direct CI calculation lead to similar results, with the CI approach leading to larger estimates of $\mathbb{V}$ than the transition density approach. This discrepancy can have two origins. First, in the empirical INDO/S approach effective models for electron-electron interaction are adopted to account for the screening of electronic charges from core electrons as well as from other effects, so that the interaction Hamiltonian does not coincide with the simple $\frac{1}{r}$ expression entering eq. 4.5 (as in the standard INDO/S [130] we adopt a modification of the Mataga-Nishimoto parametrization, in eq. C.16 in the appendix). The other possible reason for discrepancy is the “exchange term” (the first contribution in right side of eq. 4.21) that enters the $\mathbb{V}$ expression calculated in the

CI approach, but that is totally silent in the transition density approach. Further studies are in order to evaluate the relative importance of these two effects.

Conclusion and perspectives

This thesis discusses a wide range topics related to the spectroscopic characterization and to the theoretical modeling of molecular functional materials. The work implied (a) spectroscopic measurements mainly in solution; (b) the development, implementation and exploitation of essential state models for spectral properties of chromophores and multichromophores assemblies in solution and for molecular crystals; (c) the implementation of original numerical algorithms in semiempirical quantum chemical calculations (mainly INDO codes).

Most of the work was devoted to DA chromophores whose low energy physics is governed the charge resonance between DA and D^+A^- states. Essential state models are presented to describe the rich phenomenology associated to these chromophores and to related materials. In particular we obtain a very detailed description of low-energy spectral properties including linear and non-linear spectra, solvatochromism, excitonic effects in spectra of multichromophoric assemblies. Central issues in this work are electron-vibration coupling, treated either in the adiabatic approximation or in truly non-adiabatic approaches, the description of polar solvation and of internal conformational degrees of freedom, and the role of electrostatic interchromophore interactions. Fluorescence anisotropy spectroscopy, a technique recently implemented in the host laboratory, proved extremely useful to extend the range of available experimental data yielding further support to theoretical models.

Essential state models are also central to the description of valence tautomerism in DA chromophores with reduced DA delocalization and of bistability driven by electrostatic intermolecular interactions in molecular crystals of DA chromophores. In this context, a mean field treatment of electrostatic intermolecular interactions leads to a sound understanding of the complex phenomenon of bistability, that requires a precise balance between inter and intramolecular energies. In crystals of ionic DA^+ dyes the electrostatic interaction between the molecular ion and the counterion can be adjusted by changing the counterion, offering a powerful tool to drive the system in the bistability regime.

The comparison with experimental system is done in a bottom-up modeling strategy: the molecular model is obtained from the analysis of optical spectra of the *DA* chromophore in solution, while an ad hoc implementation of quantum chemical calculations is developed to estimate electrostatic intermolecular interactions. Along these lines the T dependence of Mössbauer spectra of a *DA* crystal is quantitatively reproduced in terms of T dependent population of the metastable state in the bistability region.

Electron-vibration coupling, central to properly understand optical spectra of CT chromophores in solution also plays an important role to understand charge-transport in organic semiconductors. Here we developed an original implementation of the INDO/S code and apply it to estimate the strength of Holstein and Peierls coupling in crystals of rubrene, a widely investigated organic semiconductor.

Electrostatic interchromophore interactions have been investigated to model excitonic effects in optical spectra of multichromophoric system, as well as to understand bistability in crystals of *DA* chromophores. The same interactions are responsible for the phenomenon of resonant energy transfer (RET). RET is a wide spread phenomenon in nature with important technological applications in fields ranging from organic light emitting diods to organic solar cells to biosensing, etc. . The widespread Förster model for RET dates back to the 40's [149]: it works pretty well for many systems, but its limitations in many systems of interest for applications (including large chromophores and/or multichromophoric assemblies) are known. The main limitation is related to the dipolar approximation enforced in the Förster description of RET. Here we propose an original approach to the calculation of electrostatic interchromophore interactions responsible for RET that fully relaxes the dipolar approximation. The approach is based on the calculation of CI matrix elements in an HF-SCF approach on the basis of frozen MO calculated for the chromophores at infinite distance. This extremely promising approach, implemented in the INDO/S code, was applied to a few systems.

Some of the topic discussed in this work are now fairly mature. Essential state models for chromophores and multichromophores, as an example, represents now a well tested and reliable tool. Models for bistability are similarly mature, but much work is needed to develop new materials showing bistable behavior. Our models offer a guide for this ambitious goal. In spite of extensive work done in the last decades on charge-transport in organic semiconductors, a reliable a coherent model is still missing, and our work on electron-vibration coupling just represents a step towards a better understanding of the delicate interplay of molecular vibrations and lattice modes with mobile electron. The importance of RET is hardly emphasized. Our original approach for the calculation of interaction energies relevant to the RET processes is extremely promising and does not require any specific approximation on electrostatic interaction beyond those introduced in the definition of the adopted quantum chemical model. The approach implemented here within the INDO/S model should be applicable to large chromophores. It applies as such to other HF-SCF scheme at the CIS level, but it can be extended to double CI as well. Particularly simple (and promising) is the extension of the model to TD-DFT codes, and work in this direction is presently in progress.

Appendix A

Experimental techniques

A.1 Absorption and Fluorescence

Absorption spectra were collected using a Lambda650 Perkin-Elmer instrument. A Jobin-Yvon FluoroMax3 fluorometer was used for emission measurements. Unless otherwise specified spectra are obtained with concentration $\sim 10^{-5}$ M for absorption and $\sim 10^{-6}$ for fluorescence. We verify the Lambert-Beer law in absorption spectra, by comparing spectra at different concentration. When measuring the molar extinction coefficient, absorption measurements are collected at 4-6 levels of concentration, in the range $10^{-6} \div 10^{-4}$ M. A linear regression is then performed with the concentration and the absorption at the band maximum. The slope of the least square line is the molar extinction coefficient. Unless otherwise specified, experimental error in the extinction coefficient are within the 10%.

A.1.1 Measurement of fluorescence quantum yields (FQY)

By definition, the fluorescence quantum yield, ϕ, measures the portion of excited molecules that deactivate by emitting a photon, corresponding to the ratio of the number of emitted photons to the number of absorbed photon per time unit [155]. Fluorescence quantum yield is related to the radiative (k_r) and nonradiative (k_{nr}) rate constants of deactivation by the relationship:

$$\phi = \frac{k_r}{k_r + k_{nr}} \tag{A.1}$$

The measurement of *absolute* quantum yield requires special equipments, such as integrating spheres. For measurements in solution, the *relative* quantum yield is usually determined. The fluorescence efficiency of a sample is related to the fluorescence of a standard reference compound by the equation:

$$\phi_x = \frac{A_s}{A_x} \frac{I_x}{I_s} \frac{n_x^2}{n_s^2} \phi_s \tag{A.2}$$

where x, s refer to the sample and the standard, respectively. A is the absorbance of the solution at the excitation wavelength and accounts for absorbed photons, I is the integrated area of the fluorescence spectrum (in wavelengths) that accounts for emitted photons, and n is the refractive index of the solvent. To avoid internal filter effects, optically diluted solutions must be used, with $A < 0.1$.

The integrated area of fluorescence spectra is calculated considering the corrected spectra. Gratings, detectors and other spectrometer components have characteristic responses that vary as a function of the wavelength. In a fluorometer, two correction curves have to be accounted for:

1. the correction for the emission channel (grating and detector) allows to get a reliable bandshape of the fluorescence spectrum, and as a consequence, a reliable integrated area.

2. the source in a fluorometer is usually a halogen lamp, that emits in the visible range. and which intensity emitted depends on the wavelength. For fluorescence quantum yield measurements, if the sample and the standard are excited at different wavelengths, fluorescence spectra has to be divided by the intensity of the lamp at the excitation wavelength. Moreover, the response of the detector that monitors the intensity of the lamp is a function of the wavelength, and its signal response has to be corrected.

If not otherwise specified emission spectra are collected exciting the sample at the maximum of the absorption band. Moreover, the standard fluorophore used for fluorescence quantum yield measurements is Fluorescein in NaOH 0.1M ($\phi_s = 0.9$), excited at 470nm. Its fluorescence quantum yield was tested using different standards, such as Rhodamine101 in EtOH ($\phi_s = 1$) and Quinine Bisulfate in H_2SO_4 0.05M ($\phi_s = 0.56$). Since emission intensity is sensitive to temperature, fluorescence spectra were collected on thermostated solutions, at 23°C, when not differently specified.

The error in the determination of fluorescence quantum yield, adopting the procedure described above, does not exceed 10% - 15%.

A.1.2 *T* dependent optical Vis-NIR-MIR measurements

T dependent spectra in solution are collected using the cryostat described in sect. A.3.1 in this appendix, combined with a spectrophotometer FT-IR Bruker IF66 for the Vis-NIR-IR region or with the instrument Lambda650 Perkin-Elmer for the Vis region.

For these measurements solutions were cooled and not frozen. Once the temperature in the temperature controller was stable, the measures has been recorded after 15-20 minutes in order to left the sample to reach the thermal equilibrium.

In the FT-IR Bruker IF66 spectrophotometer different experimental setup can be adopted depending on the spectral range of interest. In particular we combined

- the source: Globar (MIR, 400-8000 cm^{-1}) or halogen (NIR-Vis),
- the detector: DTGS (MIR: 4000-13000 cm^{-1}), Ge (NIR: 5000-14000 cm^{-1}) and Si (Vis: 10000-22000 cm^{-1}) and
- the beamsplitter: KBr (MIR) and CaF_2 based (NIR-Vis).

Measurements were collected in transmission, recording the series of *T* dependent spectra for the reference (the solvent), and then collecting the *T* dependent measurements for the sample (solution), working in the same experimental conditions.

A.2 Two photon absorption (TPA) and two-photon excited fluorescence (TPEF)

Two-photon absorption is a third-order nonlinear process in which two photons are absorbed simultaneously by the sample (coherent process). The two-photon absorption data reported in this thesis (chap. 1) were measured using the two-photon excited fluorescence (TPEF) technique. TPEF measures the fluorescence signal induced by the simultaneous absorption of two photons. The two-photon absorption cross section, $\sigma_2(\omega)$, is derived by comparison to a reference compound based on the fluorescence quantum yield (ϕ) of the sample. Assuming that ϕ is the same when the sample is excited by one or two photons, the fluorescence signal F induced by two-photon absorption is:

$$F \propto cP^2K\sigma_2\phi \tag{A.3}$$

where c is the concentration of the active species, P is the incident power, K is the detection efficiency. The detection efficiency is expressed as follows:

$$K = \frac{f}{n^2} \tag{A.4}$$

where f is the correction factor, taking into account the wavelength dispersion of the response function, and n is the refractive index of the medium [156]. The ratio of the function F/P^2 measured on the sample and on the reference $(F/P^2)_R$ is proportional to the two-photon absorption cross section σ_2:

$$\frac{F}{P^2}\left(\frac{F}{P^2}\right)_R^{-1} = \frac{cK\sigma_2\phi}{c_R K_R(\sigma_2\phi)_R} \tag{A.5}$$

From Equations A.4 and A.5, the TPEF cross section of the molecule of interest, multiplied by ϕ, is given by the following expression:

$$\sigma_2\phi = (\sigma_2\phi)_R \frac{f_R}{f}\frac{c_R}{c}\frac{n^2}{n_r^2}\frac{F}{P^2}\left(\frac{F}{P^2}\right)^{-1} \tag{A.6}$$

The direct outputs of the measurements are the signals $\frac{F}{P^2}$ of the sample and of the reference compound. The dependence of such signals on P must be constant, i.e. the fluorescence signals must have a quadratic dependence on the incident power. The quadratic dependence of the fluorescence signal on P is always tested for each wavelength, to rule out the occurrence of photodegradation or saturation phenomena [156].

The excitation source is a Ti:sapphire femtosecond laser system, delivering pulses of ca 150fs duration and 76MHz repetition rate. This laser supplies photons in the 700-980nm spectral range. The experimental setup at University of Padova, Italy, (Prof. C. Ferrante) collects the fluorescence signal at 90° with respect to excitation.

In the CGS system, the TPA cross section has the following units: $\mathrm{cm}^4 \cdot \mathrm{s} \cdot \mathrm{photon}^{-1}$. Practical units commonly adopted are the Göppert-Mayer (GM) defined as: $1\mathrm{GM}=10^{-50} \cdot \mathrm{cm}^{4} \cdot \mathrm{s} \cdot \mathrm{photon}^{-1}$ [156].

If not specified the experimental uncertainties in the TPA cross section reported in chap.1 are around the 15%.

A.3 Cryogenic measurements on solutions

Low-temperature measurements give hints about important phenomena related to solvation of CT-dyes. As previously discussed, molecules of polar solvents arrange according to the electric field created by the polar solute, originating the so-called reaction field. Inhomogeneous broadening is related to the disorder of the system caused by a thermal distribution of the orientational component of the reaction field around its equilibrium value. Being governed by thermal distribution, inhomogeneous broadening is affected by temperature. Moreover, if the temperature is sufficiently low to immobilize the solvent molecules (glass or solid transition, depending on the solvent and the cooling speed), the relaxation of the solvent around the excited solute molecule is hindered.

Low-temperature measurements in glassy solvents set the basis for emission and excitation anisotropy, discussed in the next section.

A.3.1 Cryostat and experimental setup

Experimental measurements at low temperature were performed using the liquid-nitrogen cooled cryostat OptistatDN (Oxford Instruments), equipped with the temperature controller ITC601 (speed of cooling $\sim$ 20°C/minute). Figure A.1 shows a schematic diagram of the OptistatDN cryostat. Liquid nitrogen is stored in a reservoir, that surrounds the central sample access tube, but is thermally isolated from it. Liquid nitrogen is supplied to the heat exchanger in the sample space through a capillary tube. The flow of liquid nitrogen is aided by gravity, but the flow rate is controlled by the exhaust valve at the top of the sample space. A platinum resistor and heater are fitted to the sample space heat exchanger and a temperature controller is used to supply the required amount of heat to balance the cooling power and set the required temperature. The sample is positioned inside the window block, which is just below the sample space heat exchanger, and three quartz windows give optical access to the sample. The sample chamber is pumped with a rotatory pump, to evacuate air and especially water vapor, and the sample space is filled with dry helium, that, thanks to its good thermal conductivity, ensures good heat exchange to the sample. The reservoir and sample space are thermally isolated from the room temperature surroundings by the outer vacuum chamber (OVC). This space is pumped to a high vacuum before the cryostat is cooled down, and the vacuum is maintained by a small sorption pump fitted to the reservoir. This continuously pumps the residual gases from the OVC to maintain good thermal isolation. A heater has been fitted to the sorb, and is used to drive the absorbed gases out of the activated charcoal when the system is at room temperature [157].

The sample is contained in special quartz cuvettes for cryogenic applications. They are constituted by a single piece, because glue usually has a different coefficient of thermal expansion with respect to quartz. Alternatively, the faces of the cells are sealed with special glues for cryogenics.

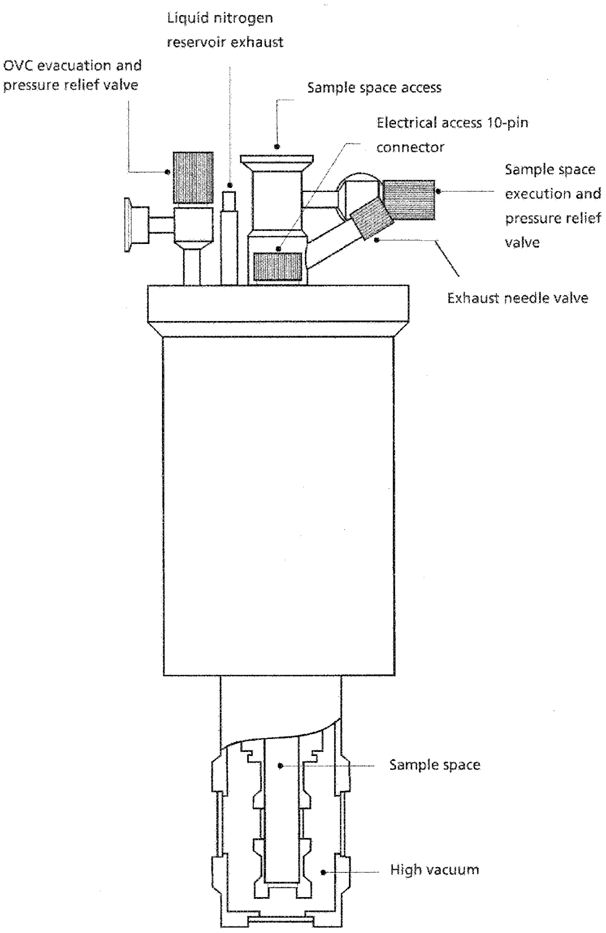

Figure A.1: *Schematic diagram of the OptistatDN cryostat.*

A.3.2 Glassy solution measurements

All measurements are performed on diluted solutions, with absorbance < 0.1 ($\sim 10^{-6}$M), to avoid inner filter effects. Particular attention is paid to the choice of solvents for measurements at low temperature. Solvents that show a glass transition (instead of the more common crystallization transition) are preferred, to avoid light scattering in crystalline environment. Many solvents are reported in the literature to have a glass transition, but the glass transition strongly depends on the cooling speed. Using the cryostat described previously, we were able to obtain glasses from 2-methyltetrahydrofuran (2-MeTHF or MeTHF), propylene glycol (PrG) and decalin.

Properties of solvents, such as the refractive index and the dielectric constant, strongly depend on temperature. In particular, for organic solvents, the refractive index increases when temperature decreases [158]. The dielectric constant increases as well when temperature decreases, so that solvents become more polar when decreasing the temperature.

Propylene glycol (PrG) is a polar solvent. Glassy PrG solution can be obtained directly from purchased solvent without any further purification. Best experimental condition to achieve the glassy state are obtained cooling PrG solution to 190K $\div$ 200K [55]. The experimental measurements performed on glassy solution of PrG presented in chap. 1 (see sect. 1.4.2) have been collected at 200K.

Decalin is an apolar solvent. Measurements in decalin (see sect. 1.6.3) has been performed at 200K. The melting point for decalin is 233K (for the mixture of cis and trans decalin), and at $T \approx 200$K the solvent can be considered a supercooled liquid with reduced molecular mobilities.

2Me-THF at room temperature is a solvent of intermediate polarity, with dielectric constant $\epsilon = 6.97$. The T_g temperature for MeTHF is 91K. The glass is prepared from solution that has been stored under molecular sieves for 12-24 hours before the experiment. The whole series of anisotropy measurements reported in MeTHF (see sect. 1.6.3 and 1.4.2) has been performed at 77K, i.e. when the solvent is a transparent glass. Range of temperature like 77K $\div$ 150K are not explored since 2Me-THF crystallizes at 137K and approaching the temperature of crystallization is dangerous because the glass to crystal transitions often results in the sample cell breaking.

A.4 Fluorescence anisotropy

Fluorescence anisotropy is a spectroscopic technique based on the principle that upon excitation with polarized light, many samples also emit polarized light. The origin of this phenomenon is related to the presence of transition dipole moments for absorption and emission, which lie along specific molecular axes. In solution, fluorophores are randomly oriented. When exposed to polarized light, molecules with the absorption transition dipole moment oriented along the direction of polarization of the incident light are preferentially excited. Hence, the excited state population is not randomly oriented. Anisotropy measures the change in orientation of the transition dipole moment relevant to emission with respect to absorption (excitation).

Depolarization of emission originates from a number of different phenomena. One of the most common reason of depolarization is rotational diffusion. Since anisotropy measures the angular displacement between the absorption and emission transition dipole moments, if the rate of diffusion is faster then the rate of the emission, fluorescence is completely depolarized. The rate of diffusive motion depends both on the viscosity of the solvent, and on the shape and the dimension of the fluorophore. Small molecules are characterized by a fast diffusion rate. On the contrary, diffusion is hindered in viscous solvents, or in glassy matrices. This is one of the reasons why we were interested in low temperature measurements (presented in the previous section).

Fluorescence anisotropy finds interesting applications in biochemistry. The timescale of rotational diffusion of biomolecules is comparable to the decay time of many fluorophores. Hence, all factors that alter the rotational correlation time, also affect anisotropy. Fluorescence anisotropy is used for example to quantify protein denaturation, or to study the internal dynamics of proteins. [55]

Our interest in fluorescence anisotropy is instead related to the possibility to obtain information about angle formed between the transition dipole moments of absorptions and emission processes. This information, particularly interesting for multibranched systems, requires measurements in frozen (glassy) solutions.

A.4.1 Fundamental aspects and experimental setup for anisotropy measurements

The experimental setup for fluorescence anisotropy measurements is schematically illustrated in Figure A.2. The sample is excited with polarized light, and

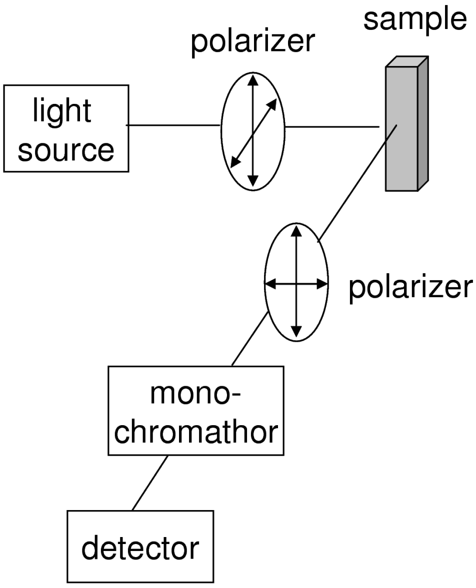

Figure A.2: *Sketch of experimental setup for anisotropy measurements.*

emission is detected through another polarizer. Anisotropy is defined as:

$$r = \frac{I_{\parallel} - I_{\perp}}{I_{\parallel} + 2I_{\perp}} \tag{A.7}$$

where $I_{\parallel}$ is the intensity of emission measured when the polarizer before the detector (analyzer) is parallel to the excitation polarizer, while $I_{\perp}$ is the intensity of the emission when the analyzer is perpendicular to the excitation polarizer. Anisotropy is a dimensionless quantity, because the difference between the intensity of light emitted parallel and perpendicularly to the excitation $(I_{\parallel} - I_{\perp})$, is normalized by the total intensity of emitted light $(I_{\parallel} + 2I_{\perp})$ [55].

The fundamental anisotropy of a sample of molecules in frozen random orientation in absence of broadening effect is:

$$r_0 = \frac{2}{5}\left(\frac{3cos^2\beta - 1}{2}\right) \tag{A.8}$$

where β is the angle between transition dipole moments relevant to emission and absorption processes. The term r_0 is used to refer to anisotropy observed in the absence of other depolarizing process such as rotational diffusion. Equation

Table A.1: *Relationship between the angular displacement of transition moments β and the fundamental anisotropy r_0 for a sample of randomly oriented fluorophores.*

β (deg)	r_0
0	0.4
45	0.1
54.7	0
90	-0.2

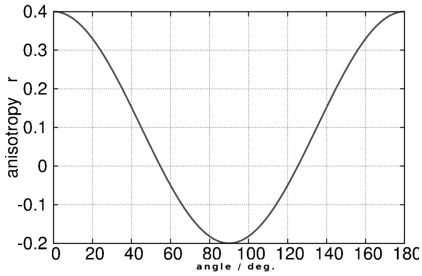

Figure A.3: *Relation between angle β and anisotropy value r_0.*

A.8 is derived in Ref. [55]. The relation expressed by eq. A.8 is plotted in fig. A.3. Table A.1 lists the values of the fundamental anisotropy for different values of β. The maximum value for anisotropy is 0.4, when the absorption and emission transition dipole moments are aligned. Anisotropy is 0 at the magic angle (54.7°), and the lowest value, $r_0 = -0.2$, is obtained when the two dipole moments are perpendicular. Anisotropy is 0 also when some depolarization effect occurs.

Measurements of the fundamental anisotropy r_0 require special conditions. In order to avoid rotational diffusion, the samples are examined in solvents forming transparent glasses (see sect. A.3.2). Since the matrix is rigid, photoselection plays a main role, as it will be discussed in the B.3.1. Moreover, solutions must be optically diluted (absorbance < 0.1) to avoid depolarization processes due to internal absorption and subsequent emission of photons, or due to energy transfer.

Two methods are commonly used to measure anisotropy: the L-format method, in which a single emission channel is used, and the T-format where both the parallel and perpendicular components are simultaneously detected, through separate channels [55]. Only the first one is described, corresponding to the setup available in the FluoroMax Instrument. In particular after excitation with polarized light, emission is collected after a monochromator (see Figure A.2). The monochromator has a different transmission coefficient for vertically and horizontally polarized light, and, as a consequence, the rotation of the polarizer causes a change in the detected intensity even if emission is unpolarized. The G-factor takes into account the sensitivity of the detection system for vertically and horizontally polarized light:

$$G = \frac{I_{HV}}{I_{HH}} \tag{A.9}$$

where I_{HV} is the emission intensity when the excitation wavelength is polarized horizontally (H), while the analyzer is polarized vertically (V) and I_{HH} is the emission intensity when both the polarizer and the analyzer are horizontal. Consequently, anisotropy is defined as follows:

$$R = \frac{I_{VV} - GI_{VH}}{I_{VV} + 2GI_{VH}} \tag{A.10}$$

The excitation anisotropy spectrum is a plot of anisotropy detected at a fixed wavelength, as a function of the excitation wavelength. According to the Kasha's rule, the lowest singlet state is responsible for emission, independently of excitation. Since the detected wavelength is fixed, the emission dipole moment remains the same. On the other hand, the transition dipole moment relevant to absorption changes for different excited states, so that the anisotropy is different for different absorption bands.

The emission anisotropy spectrum is measured exciting the sample at a fixed wavelength and detecting the emission anisotropy at frequencies covering the whole emission band. The main difference with respect to the excitation anisotropy spectrum, is that in this case only two excited states are involved: the lowest singlet excited state, responsible for emission, and the state that absorbs the excitation wavelength (obviously, they can be the same state). Consequently, in the lack of spectral features, the emission anisotropy spectrum is a flat line across the whole emission band.

Appendix B

Computational details for the calculation of optical spectra

All calculation of spectra, with the computational methodologies presented in this appendix, has been performed with codes written on purposes in Fortran 90-95, with GNU/GCC or Lahey Fortran Compiler.

B.1 Calculation of absorption and fluorescence spectra

B.1.1 Spectra calculation in the non-adiabatic approach

Depending on the system at hand, as described in the main text, we introduce a variable number of components of the reaction field: one component is enough for linear molecules, two are needed for planar chromophores, or for bichromophoric species. For each component f_i of the reaction field we define a grid of values and on each point of the grid we solve the coupled electron-vibration problem via a numerically exact diagonalization algorithm. Specifically, for each f_i, the total Hamiltonian is written on the basis obtained as the direct product of the electronic basis states times the product of the eigenstates of the of the relevant number of harmonic oscillators, depending of the number of vibrational coordinates introduced in the considered model. The vibrational basis is truncated to a number of states large enough as not to affect relevant results (the number of vibrational states required for convergence, depends on the molecular properties of interest, and increases for strong electron-phonon coupling; typical values are 10 states for each oscillator). The resulting Hamiltonian matrix is diagonalized numerically to get vibronic eigenstates. A Gaussian bandshape with half-width $\sigma = \frac{\Gamma}{\sqrt{2ln2}}$ (wavenumber or energy units) is assigned to each vibronic transition, where Γ is the half-width at half-maximum for a corresponding Lorentzian band. Then the molar extinction coefficient (ϵ) and fluorescence spectrum (I) are calculated as a function of the wavenumber, $\tilde{\nu}$ (expressed in $\text{cm}^{-}1$), as follows:

$$\epsilon(\tilde{\nu}) = \frac{10\pi N_A \tilde{\nu}}{3ln10\hbar c\epsilon_0} \frac{1}{\sqrt{2\pi}\sigma} \sum_n \mu_{gn}^2 \exp\left[-\frac{1}{2}\left(\frac{\tilde{\nu}_{gn} - \tilde{\nu}}{\sigma}\right)^2\right] \tag{B.1}$$

$$I(\tilde{\nu}) \propto \tilde{\nu}^3 \frac{1}{\sqrt{2\pi}\sigma} \sum_n \mu_{en}^2 \exp\left[-\frac{1}{2}\left(\frac{\tilde{\nu}_{en} - \tilde{\nu}}{\sigma}\right)^2\right] \tag{B.2}$$

In Equation B.1, N_A is the Avogadro number, c is the speed of light, ϵ_0 is the vacuum permittivity, $\tilde{\nu}_{gn}$ and μ_{gn} are the transition wavenumber and dipole moment respectively, for the $g \rightarrow n$ transition from the ground (g) to the generic excited state (n), and summation runs over all (vibronic) excited states. In Equation B.2, referring to fluorescence, $\tilde{\nu}_{fn}$ and μ_{fn} are the transition wavenumber and dipole moment, respectively, for the $e \rightarrow n$ transition from the fluorescent state (e) to the generic lower-energy state (n), and summation runs over all states having lower energy with respect to the fluorescent state, e. Selection of the emissive states is a tricky process and must be optimized for each system.

The calculation of linear spectra is repeated in all point of the f-grid values and the total spectra are obtained summing up the contributions at different f_i weighted by the relevant Boltzmann population.

B.1.2 Spectra calculation in the adiabatic approximation

While simpler in principle the adiabatic approximation calculation of optical spectra is computationally more complex than the direct non-adiabatic approach. We underline that slightly different model parameters are in general obtained when adiabatic or non-adiabatic approaches are adopted for the calculation of optical spectra.

As in non-adiabatic calculation the adiabatic approach implies a calculation on a grid of f values. On each point of the grid value the following relevant spectroscopic quantities have to be evaluated in order to calculate the f dependent absorption spectrum: the vibrational relaxation energy λ_{vi}, the Huang-Rhys factors S_i, the Franck Condon factors and the frequencies of the vibronic transitions ω_{0n}. Here we shortly present how these quantities are calculated, as relevant for the sections where adiabatic calculation are adopted (sect. 2.1). In particular for the two-state model, the electronic excited state index $i = 1$ (as relevant for sect. 2.1.1) , while for the three-state model, the electronic excited state index $i = 1, 2$ (as relevant for sect. 2.1.6).

To ensure some physical requisite, like the coincidence of the 0-0 transition in the absorption process and in the emission, the $\lambda_{v,i}$ is defined as:

$$\lambda_{v,i} = \frac{1}{2}\left[\left(E_{ei}(q_{eq,g}) - E_g(q_{eq,g})\right) - \left(E_{ei}(q_{eq,ei}) - E_g(q_{eq,ei})\right)\right] \tag{B.3}$$

corresponding to the average of the difference between the vertical and the 0-0 energies in absorption and in emission. In eq. B.3 $i = 1, 2$ (two excited states) q_{eq} and E are the equilibrium value for the vibrational coordinate and the adiabatic energy respectively, for the considered state (as labeled in the index). Eq. B.3 applies under the assumption of the same frequency for the ground and excited states and a single relaxation energy stands for a given transition process $g \rightarrow e_1$ or $g \rightarrow e_2$. The resulting frequency ω_{00} for the 0–0 transition results as

$$\omega_{00} = \omega_{g,ei}^{abs} - \lambda_{v,ei} = E_{ei}(q_{eq,g}) - E_g(q_{eq,g}) - \lambda_{v,ei} \tag{B.4}$$

(with $\hbar = 1$), while the energy for the $0 - n$ vibronic transition is:

$$\omega_{0n} = \omega_{00} + n\omega_v \tag{B.5}$$

The Huang-Rhys factors S^2 are defined as:

$$S_i^2 = \lambda_{v,i}/(\omega_v) \tag{B.6}$$

where $i = 1, 2$. The corresponding Franck-Condon factors then are:

$$\left|\langle 0|n\rangle\right|_i^2 = \frac{1}{n!} S_i{}^{-n} e^{-S_i} \tag{B.7}$$

The absorption spectra are calculated in the local harmonic approximation [84, 85]. For the sake of simplicity we set the vibrational frequency of the ground and excited state to the same value ω_v. A more rigorous choice does not provide appreciable differences in the calculated electronic spectra.

The absorption spectra are then calculate as follow:

$$\epsilon(\tilde{v}) = \frac{10\pi N_A}{3ln10\hbar c\epsilon_0}\,\tilde{v}\sum_i \left|\mu_{ge_i}\right|^2 \sum_n |\langle 0|n\rangle|_i{}^2 \exp\left[-\frac{\left(\tilde{v} - \tilde{v}_{0n_i}\right)^2}{2\sigma^2}\right] \tag{B.8}$$

where σ is the intrinsic linewidth of the Gaussian shape assigned to each vibronic line $\sigma = \frac{\Gamma}{\sqrt{2\ln 2}}$. $\tilde{v}$ is the frequency (wavenumber) expressed in cm^{-1}.

The constants entering the prefactors are the same defined for eq. B.1. The summations in eq. B.8 refer to electronic states i and to excited state vibrational state n, respectively. The spectra in eq. B.8 are calculated at each f value and multiplied by the f dependent Boltzmann probability, that weights the average with all the other spectra determining the overall spectra.

The presented approach concerns absorption spectra, as needed for model in chap. 2. However, analogous quantities can be defined for the fluorescence spectra, and the same procedure apply to calculate the adiabatic fluorescence spectra.

The adiabatic approximation, with the separation of electronic and vibrational degree of freedom, can produce more readable and easily rationalizable results: the specification of the emitting state is trivial in this approach, at variance with the non-adiabatic case. On the other hand, when there are more than two electronic states and several vibrational modes, the adiabatic approach becomes rather complex.

B.2 Calculation of the two-photon absorption spectra

The calculation of two photon absorption spectra goes along similar lines as the calculation of linear absorption spectra. Once vibronic eigenstate are obtained on each point of the f_i grid the two-photon absorption cross section (in GM) is calculated according to the following expression [156]:

$$\sigma_2(\omega) = 10^{58}\frac{\hbar\omega^2}{4\epsilon_0^2 c^2} Im\langle\gamma_{ijkl}(-\omega;\omega,\omega,-\omega)\rangle_{IJKL} \tag{B.9}$$

where c is the speed of light, and $\langle\gamma\rangle$ the orientationally averaged second hyperpolarizability ($IJKL$ indexes run on the laboratory axis; $ijkl$ run on the axis of the molecular reference system). Tensor elements $\gamma_{ijkl}(-\omega;\omega,\omega,-\omega)$ are given by the following sum-over-states expressions [159]:

$$\begin{aligned}\gamma_{ijkl}(-\omega;\omega,\omega,-\omega) \;=\;& \frac{1}{\hbar^3}\sum_{lmn}\left\{\frac{\langle g|\mu_i|l\rangle\langle l|\bar{\mu}_j|m\rangle\langle m|\bar{\mu}_k|n\rangle\langle n|\mu_l|g\rangle}{(\Omega_{lg}-\omega)(\Omega_{mg}-2\omega)(\Omega_{ng}-\omega)}+\right.\\ & \frac{\langle g|\mu_j|l\rangle\langle l|\bar{\mu}_i|m\rangle\langle m|\bar{\mu}_k|n\rangle\langle n|\mu_l|g\rangle}{(\Omega^*_{lg}-\omega)(\Omega_{mg}-2\omega)(\Omega_{ng}-\omega)}+\\ & \frac{\langle g|\mu_i|l\rangle\langle l|\bar{\mu}_j|m\rangle\langle m|\bar{\mu}_l|n\rangle\langle n|\mu_k|g\rangle}{(\Omega_{lg}-\omega)(\Omega_{mg}-2\omega)(\Omega_{ng}-\omega)}+\\ & \left.\frac{\langle g|\mu_j|l\rangle\langle l|\bar{\mu}_i|m\rangle\langle m|\bar{\mu}_l|n\rangle\langle n|\mu_k|g\rangle}{(\Omega^*_{lg}-\omega)(\Omega_{mg}-2\omega)(\Omega_{ng}-\omega)}\right\}\end{aligned} \tag{B.10}$$

where only two-photon resonant terms have been retained; g is the ground state and summations run over all vibronic excited states; $\Omega_{lg} = \omega_{lg} - i\Gamma_{lg}$ (we set $\Gamma_{lg} = \Gamma$, the width of the Gaussian bandshape defined above, for all transitions) and $\bar{\mu} = \mu - \langle g|\hat{\mu}|g\rangle$.

For linear molecules (dipolar chromophores and linear quadrupolar chromophores), the only tensor element different from zero is the γ_{xxxx} term, where x is the molecular axis. The orientationally-averaged second hyperpolarizability is thus given by $\langle\gamma\rangle_{XXXX} = 1/5\gamma_{xxxx}$. More generally, for a bidimensional system:

$$\langle\gamma\rangle \equiv \langle\gamma\rangle_{XXXX} = \frac{1}{5}\sum_{i}^{x,y}\gamma_{iiii} + \frac{1}{15}\sum_{i\neq j}^{x,y}\left(\gamma_{iijj}+\gamma_{ijji}+\gamma_{ijij}\right) \tag{B.11}$$

As for OPA, the calculation of TPA spectra is repeated on the f_i grid and the overall spectrum is obtained summing up the TPA spectra weighted by the Boltzmann population.

B.3 Calculation of emission and excitation anisotropy

B.3.1 Calculation of anisotropy spectra

Excitation and emission anisotropy spectra of (multi)polar chromophores can be calculated using essential-state models. The calculation of anisotropy spectra is not trivial, and in particular two tricky problems have to be considered:

1. Experimental spectra are collected in a glassy matrix at low temperature. This experimental condition has major consequences on inhomogeneous broadening and on the Stokes shift. The excitation wavelength preferentially excites a subset of molecules out of the inhomogeneous distribution

(those absorbing at the specific wavelength). The same molecules are responsible for emission. Since the matrix is rigid, the relaxation along the solvation coordinate is hindered, and only vibrational relaxation takes place before fluorescence. Therefore the emitting state is specific of the photo-selected molecules. This phenomenon is called *energy photoselection*.

2. When exciting with a polarized light beam, molecules with the absorption transition dipole moment oriented along the direction of polarization are preferentially excited. This phenomenon is called *polarization photoselection*. Moreover, since anisotropy is measured in solutions of randomly oriented molecules, an appropriate averaging over all possible orientations has to be performed.

The first problem related to energy photoselection is solved considering the probability of each molecule to absorb the incident monochromatic photons, according to the ground-state energy distribution. In particular, the same ground state Boltzmann distribution is assumed for both the ground state and for the excited state responsible for emission, because the solvent molecule are frozen in the configuration they have around the solute molecule in the ground state: solvent relaxation is hindered in the glassy matrix. The relevant Boltzmann distribution for strictly glassy solvent (like MeTHF) is that related to the glass-transition temperature; while for supercooled solvents (like decalin and propylenic glycol) it corresponds to the measurement temperature.

The second problem is related to the orientational photoselection. The following expressions allow to estimate the fluorescence intensity, when the polarizers are parallel ($I_{\|}$) or perpendicular ($I_{\perp}$), for a sample of randomly oriented molecules in frozen solutions [160]:

$$I_{\|} = \frac{|\vec{\mu}_{em}|^2 \cdot |\vec{\mu}_{abs}|^2 + 2(\vec{\mu}_{em} \cdot \vec{\mu}_{abs})^2}{15} \tag{B.12}$$

$$I_{\perp} = \frac{2|\vec{\mu}_{em}|^2 \cdot |\vec{\mu}_{abs}|^2 - (\vec{\mu}_{em} \cdot \vec{\mu}_{abs})^2}{15} \tag{B.13}$$

These two terms have to be weighted separately for the relevant Boltzmann distribution, to take into account the effects related to inhomogeneous broadening. This is a key point: $I_{\|}$ and $I_{\perp}$ are the experimental results of two separated measurements, while anisotropy comes from a processing of these data [161]. Hence, the Boltzmann distribution has to be associated to these two terms, and not to the final anisotropy. The previous expressions of Equations B.12 and B.13, weighted for the Boltzmann distribution of the ground state, allow to calculate anisotropy using Equation A.7. Of course when applied a strictly 1D systems or more precisely to systems when the dipole moment has a single component the expressions above lead to $r = 0.4$.

B.3.2 Anisotropy calculation with orientational degree of freedom

A more delicate issue is the anisotropy calculation in the presence of two sources of broadening, where one of them does not freeze, like for instance an internal conformational degrees of freedom (u). In these condition two Boltzmann distributions can be defined. One is relevant for the excitation process, where all the slow coordinates are centered around the ground state (g) minimum and corresponds to a probability $p_g(f,u)$, where $f \equiv \{f_i\}$ refer to all the relevant solvation coordinates and $u \equiv \{u_i\}$ refer to conformational coordinates, (or more generally to other slow non frozen coordinates). A second distribution is relevant to emission processes, that take place from the fluorescent state e. In these processes the solvent coordinates are still frozen, while the orientational coordinates are relaxed in the excited state configuration. This probability is the one relevant to the calculation of fluorescence in frozen solution and not $p_e(f,u)$, which instead measures the probability distribution around the excited solute when all degrees of freedom are relaxed.

Calculation goes along these steps:

1. the Hamiltonian is diagonalized on the (f,u) grid and, based on the ground state energy, the $p_g(f,u)$ distribution is fixed. On the same grid the energy of the emissive state leads to the definition of the distribution $p_e(f,u)$.
2. to account for the fact that the solvent is frozen at the equilibrium around the gs, we integrate (sum) the distribution $p_g(f,g)$ over the u grid to obtain the integrated probability $\tilde{p}_g(f)$
3. The probability distribution for the excited state in the frozen solvent is finally obtained as $p_g(f,u)p_e(f,u)\tilde{p}_g(f)$. The first product $p_g p_e$ accounts for the fact that at each f, a point in the u ground state configuration can arrive at any u-point in the excited state configuration (the product of probabilities correspond to independent events). For each f this joint probability is multiplied by the probability of the f configuration in the gs $\tilde{p}(f)$, independent of u.

The calculation is cumbersome and it is important to reduce computational effort by a careful choice of sampling criteria. The calculations of $p_g(f,u)$ and

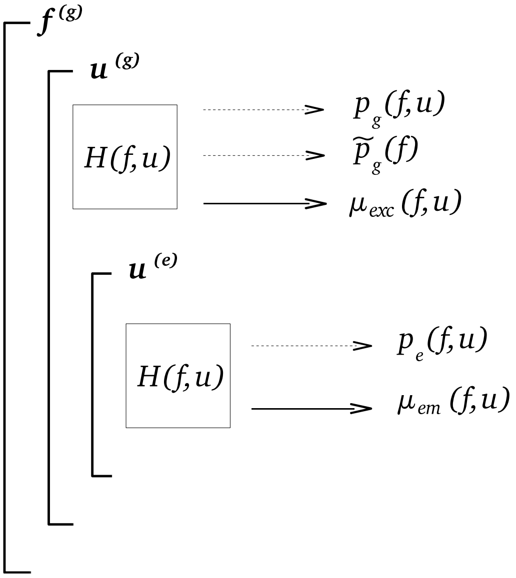

Figure B.1: *Schematic diagram of the computational procedure for the calculation of spectra with both frozen coordinate(s) f and non-frozen coordinate(s) u. μ_{exc} and μ_{em} refer to excitation and emission dipole moments, that as well as probabilities resulted from the diagonalization of the $H(f,u)$ Hamiltonian (see text).*

$p_e(f,u)$ are done on the same grid for f centered around the ground state equilibrium, and on two grids of u centered around the equilibrium position for u relevant to ground and excited state, respectively, as sketched in fig. B.1.

Appendix C

The MO-CIS approach for excited state description and the INDO/S semiempirical method

C.1 HF-MO frame

In the general HF approach the electronic problem is expressed in term of the Fock operator:

$$\hat{f}(1) = \hat{h}(1) + \sum_{a} 2\hat{J}_a(1) - \hat{K}_a(1) \tag{C.1}$$

where $\hat{h}$ is the one-electron operator and $\hat{J}$ and the $\hat{K}$ are the Coulomb and exchange operator, and sum runs over occupied spatial wavefunctions. The molecular orbital (MO) ϕ_i eigenstate of eq. C.1, are expressed as the sum of N basis functions χ_μ:

$$\phi_i = \sum_{\mu=1}^{N} c_{\mu i} \chi_\mu \tag{C.2}$$

Adopting HF-MO-LCAO approach, the basis functions χ_μ are atomic orbitals. On this basis the Fock matrix reads:

$$F_{\mu\nu} = H_{\mu\nu}^{core} + \sum_{a}^{occ} \sum_{\lambda\sigma} c_{\lambda a} c_{\sigma a} \left[2\left(\mu\nu|\sigma\lambda\right) - \left(\mu\lambda|\sigma\nu\right) \right]] \tag{C.3}$$

The matrix elements of the core Hamiltonian, $H^{core}_{\mu\nu}$, are the sum of the kinetic plus nuclear attraction integrals:

$$\begin{aligned} H^{core}_{\mu\nu} &= T_{\mu\nu} + V^{nucl}_{\mu\nu} \\ &= \int d\mathbf{r}_1 \chi^*_\mu(1) \left[-\frac{1}{2}\nabla^2_1 \right] \chi_\nu(1) \\ &\quad + \int d\mathbf{r}_1 \chi^*_\mu(1) - \left[\sum_A \frac{Z_A}{|\mathbf{r}_1 - \mathbf{R}_A|} \right] \chi_\nu(1) \end{aligned} \tag{C.4}$$

The two electron terms can be written in this form:

$$(\mu\nu|\sigma\lambda) = \int d\mathbf{r}_1 d\mathbf{r}_2 \chi^*_\mu(1)\chi_\nu(1) \left[\frac{1}{r_{12}} \right] \chi^*_\lambda(2)\chi_\sigma(2) \tag{C.5}$$

The evaluation of these integrals is computationally demanding. While the the core Hamiltonian term $\mathbf{H}^{core}$ is constant, i .e. it does not depend on the coefficients and it can be evaluated at once, the full Fock matrix $\mathbf{F}$ depends on the coefficients $\{c_{\mu i}\}$ themselves and has to be solved in self consistent way:

$$\mathbf{F}(\mathbf{C})\mathbf{C} = \mathbf{SC}\boldsymbol{\epsilon} \tag{C.6}$$

If the basis is orthonormal: $\mathbf{S} = \mathbf{1}$. The resulting set of eigenvectors, i.e. the coefficients $c_{\mu i}$, fully define the MO, according to eq. C.2, while the eigenvalues ϵ_i represent the orbital energies.

C.2 CIS: the simplest approach for excited states

One of the first developed methods to describe exited states is the single excited configuration interaction (CIS). We consider a closed shell molecule represented by a restricted determinant $|\Psi_0\rangle$, defined filling up the first N spin orbital out of the set of $2K$ spin orbitals. A large number of N-electron determinants can be obtained promoting electron from the set of N occupied orbitals to the $2K - N$ virtual spin orbitals. If we restrict the treatment to the single excitation we can express the CI single (CIS) wave function for a generic excited state Φ_1 as a linear combination of single excited determinants:

$$|\Phi_1\rangle = \sum_{ar} C^r_a |\Psi^r_a\rangle \tag{C.7}$$

where $|\Psi^r_a\rangle$ represent a single excited determinant, corresponding to the formal excitation of an electron from the occupied a spin orbital to the r virtual orbitals. There are $\binom{N}{1}\binom{2K-N}{1} = N(2K - N)$ single excited determinants. The problem is formulated over the single excited determinants (i.e. over the configurations) basis and can be written in matrix form. By Slater rules, the CIS matrix element between two single excited determinants is:

$$\langle {}^1\Psi_a^r | \mathscr{H} - E_0 | {}^1\Psi_b^s \rangle = \left(\epsilon_r - \epsilon_a\right) \delta_{rs}\delta_{ab} - (rs|ba) + 2(ra|bs) \tag{C.8}$$

where the ground state energy is subtracted because we are treating excited state and we consider only singlet states. The first term of the equation, is only present in diagonal element of the CIS matrix. Diagonalizing the CIS matrix we obtain the coefficients of the CIS expansion C_a^r in eq. C.7.

C.3 Semiempirical method: INDO/S

The semiempirical method INDO/S is presented in its basic version: d orbital are not included, and the description stands for singlet excitation and for closed shell molecule.

Since the original INDO/S (ZINDO) code is not in the public domain, we have updated and modified a Fortran version of the code from the CINDO QCPE program described in J. A. Pople and D. L. Beveridge, [162] The parameterization has been taken from the original papers by the Zerner group [130], and checked against those found in the ArgusLab program files [54].

C.3.1 Zerner INDO/S approximations and expressions

INDO/S method is a spectroscopical parameterization of the INDO/1 (Intermediate Neglect of Differential Overlap, [163]) method. The detailed parameterization of INDO/S, also known as “ZINDO”, is explained in the detail of the Zerner work [130] and review [164]. Here we just summarize the main features.

For a closed shell configuration and assuming an orthonormal basis set ($\boldsymbol{S} = \mathbf{1}$) the solution of the eigenvalue problem

$$\mathbf{F}\mathbf{c}_i = \epsilon_i \mathbf{c}_\mathrm{i} \tag{C.9}$$

gives the energy and the AO composition for the i-th MO.

In the INDO/S approach the diagonal terms of the Fock matrix are written as follow:

$$F_{\mu\mu} = U_{\mu\mu} + \sum_{\sigma}^{A} P_{\sigma\sigma} \left[(\mu\mu|\sigma\sigma) - \frac{1}{2}(\mu\sigma|\mu\sigma) \right] + \sum_{B \neq A} (P_{BB} - Z_B)\gamma_{AB} \tag{C.10}$$

$$\mu \in A$$

where the core integral are derived as:

$$U_{\mu\mu} \equiv (\mu| - \frac{1}{2}\nabla^2 - \frac{Z_A}{R_A} + V|\mu) \tag{C.11}$$

$$= \begin{cases} I_\mu - (Z_A -)F^0(ss) + \frac{1}{6}mG^1(sp) & s \text{ AO} \\ I_\mu - (Z_A -)F^0(ss) + \frac{1}{6}lG^1(sp) + \frac{2}{25}(m-1)F^2(pp) & p \text{ AO} \end{cases} \tag{C.12}$$

with μ centered on the atom A, V representing a pseudo-potential accommodating the neglected inner shells. I_μ is the ionization potential for the process $s^l p^m \rightarrow s^{l-1} + p^m + (s)$ or $s^l p^m \rightarrow s^l + p^{m-1} + (p)$, and $G^1(sp)$ and $F^2(pp)$ are the Slater-Condon factors [165].

The off-diagonal term of the Fock Matrix are:

$$F_{\mu\nu} = \begin{cases} \frac{3}{2}P_{\mu\nu}(\mu\nu|\mu\nu) - \frac{1}{2}P_{\mu\nu}(\mu\mu|\nu\nu) & \mu,\nu \in A \\ \bar{S}_{\mu\nu}\frac{\beta_A+\beta_B}{2} - \frac{P_{\mu\nu}\gamma_{AB}}{2} & \mu \in A, \nu \in B \end{cases} \tag{C.13}$$

where the first line refer to AO on the same atom and the second to AO on different atoms A, B. The density matrix of eq. C.10 and C.13 are defined as:

$$P_{\mu\nu} = 2\sum_{i}^{MO} c_{\mu i} c_{\nu i} \tag{C.14}$$

while the atomic density matrix element of eq. C.10 are:

$$P_{AA} = \sum_{\mu \in A} P_{\mu\mu} \tag{C.15}$$

In the INDO/S model the Coulombian two-electron, two-center integral that enter the Fock matrix element (eq.C.13 and eq. C.10) are parametrized following a modification of the Mataga-Nishimoto recipe:

$$\gamma_{AB} = \frac{f_\gamma}{\frac{2f_\gamma}{\gamma_{AA}+\gamma_{BB}} + R_{AB}} \tag{C.16}$$

where R_{AB} is the distance between the two centers (Bohr radius unit) and the parameter f_γ is set equal to 1.2. The one-center, two-electron integral γ_{AA} entering the above equation are parametrized following the Pariser's equation:

$$\gamma_{AA} = F^0(AA) = I_A - A_A \tag{C.17}$$

where $F^0(AA) = F^0(ss) = F^0$ (see also eq. C.18). One center Coulombian $(\mu\nu|\mu\nu)$ and exchange $(\mu\mu|\nu\nu)$ integrals of eq. C.10 and in the first line of eq.

C.13 for an s or p block element are five and can be estimated by Slater-Condon factors [165]:

$$
\begin{aligned}
(ss|ss) &= F^0 && \text{(C.18)}\\
(ss|pp) &= F^0 && \text{(C.19)}\\
(sp|sp) &= \frac{1}{3}G^1(sp) && \text{(C.20)}\\
(p_xp_x|p_xp_x) &= F^0(pp)+\frac{4}{25}F^2(pp) && \text{(C.21)}\\
(p_xp_x|p_yp_y) &= F^0(pp)-\frac{2}{25}F^2(pp) && \text{(C.22)}\\
(p_xp_y|p_xp_y) &= \frac{3}{25}F^2(pp) && \text{(C.23)}
\end{aligned}
$$

Finally, in the two center Fock elements of eq. C.13 $F_{\mu\nu} = \bar{S}_{\mu\nu}(\beta_A+\beta_B)/2 - \frac{P_{\mu\nu}\gamma_{AB}}{2}$ the β_A refer to the Huckel bonding parameter for the atom A, while the modified overlap $\bar{S}$ are defined as:

$$
\begin{aligned}
\bar{S}_{msns} &= S_{msns} && \text{(C.24)}\\
\bar{S}_{msnp} &= S_{msnp} && \text{(C.25)}\\
\bar{S}_{mpnp} &= f_\sigma G_\sigma S_{mp_\sigma np_\sigma} + f_\pi G_\pi S_{mp_\pi np_\pi} && \text{(C.26)}
\end{aligned}
$$

where the G_σ and G_π are the appropriate geometric factor necessary to rotate the overlap form the local diatomic system to the molecular system and $f_\sigma = 0.585$ and $f_\pi = 1.266$, are justified by experimental and ab-initio results.

C.3.2 INDO/S and CIS method

Rule to build the CIS matrix inside the INDO/S frame for singlet – singlet transition, can be found in [130, 166]. Shortly, the diagonal and off-diagonal element of the CIS matrix in the INDO/S method read:

$$
\begin{aligned}
\langle {}^1\Psi_{i\to r}|\mathscr{H}|{}^1\Psi_{i\to r}\rangle &= \Delta E_{ir} = \epsilon_r - \epsilon_i - (rr|ii) + 2(ri|ir) && \text{(C.27)}\\
\langle {}^1\Psi_{i\to r}|\mathscr{H}|{}^1\Psi_{j\to s}\rangle &= 2(ri|js) - (rs|ij) && \text{(C.28)}
\end{aligned}
$$

The general integral over MOs is (Greek letters refer to AO, $\alpha \in A, \beta \in B\gamma \in C, \delta \in D$, small roman to MOs):

$$
\begin{aligned}
(ij|kl) &= \int \phi_i^*(1)\phi_j(1)\phi_k^*(2)\phi_l(2)\frac{1}{r_{12}}d\mathbf{r}_1 d\mathbf{r}_2\\
&= \sum_{\alpha\beta\gamma\delta} c_{i\alpha}c_{j\beta}c_{k\gamma}c_{l\delta}(\alpha\beta|\gamma\delta) && \text{(C.29)}
\end{aligned}
$$

is here approximated retaining only the element rising from two center:

$$\begin{aligned}(ij|kl) &= \sum_{\substack{\alpha\neq\beta\\ \gamma\neq\delta}} c_{i\alpha}c_{j\beta}c_{k\gamma}c_{l\delta}(\alpha\beta|\gamma\delta)\delta^{AB}\delta^{CD}\delta^{AC}\\ &\quad +\sum_{\alpha\gamma} c_{i\alpha}c_{j\alpha}c_{k\gamma}c_{l\gamma}\delta^{AC}\left[(\alpha\alpha|\gamma\gamma)-F^{0}(\alpha\gamma)\right]\\ &\quad +(ij|kl)_{CNDO} \qquad \text{(C.30)}\end{aligned}$$

where the first term applies when all α, β, γ, δ are all the same center A, the following refer to the case when α and γ are on the same center. The actual parametrized expressions of the one-center atomic orbital integrals $(\alpha\beta|\gamma\delta)$ are reported in the figure C.1, (from the appendix of the paper [130]) in term of the Slater-Condon factors. The last line in equation C.30 refer to when α and γ are on the two center and it is the nonzero term in the CNDO approach:

$$(ij|kl)_{CNDO} = \sum_{\alpha\gamma} c_{i\alpha}c_{j\alpha}c_{k\gamma}c_{l\gamma}(\alpha\alpha|\gamma\gamma) \qquad \text{(C.31)}$$

where $(\alpha\alpha|\gamma\gamma) = \gamma_{\alpha\gamma}$ (i.e. the two-center Coulombian integral), vanishing if one orbital is p and the other is s. Other integral involving three or four centers are neglected in the INDO approximation (one-electron product $\chi_{\mu}(1)\chi_{\nu}(1)$ are retained only *in one center integrals*, i. e. $\mu \in A, \nu \in A$) [163].

C.3.3 INDO/S transition and permanent dipole moment

In our implementation of the INDO/S code the transition dipole moment were calculating following [167, 164, 168]. Slater rules [153] are adopted to evaluate a matrix element between two determinants, as here for the dipole moment $\hat{\mu} = -e\hat{r}$.

The transition dipole moment is:

$$\begin{aligned}\mu_{GE} &= \langle\Phi_G\left|\hat{\mu}\right|\Phi_E\rangle = \sum_{ar}\sum C_a^r\langle\phi_a\left|\hat{\mu}\right|\phi_r\rangle\\ &= \sum_{ar}\sum_{a\mu}\sum_{r\nu} c_{a\mu}c_{r\nu}\left[-\delta^{AB}\delta^{\mu\nu}R_A - \delta^{AB}(\mu|\hat{r}|\nu)\right] \qquad \text{(C.32)}\end{aligned}$$

the first term $(\delta^{AB}\delta^{\mu\nu})$ is the point-charge contribution (diagonal) and refer to the case where $\mu = \nu$ (same AO in the same atom), where the R_A is the position of the A nucleus. The second term is the sp-polarization (off-diagonal) term and refer to the different AO, centered on the same atom ($\mu \neq \nu$, $\mu, \nu \in A$).

The expectation value for the last integral $(\mu|\hat{r}|\nu)$ is calculated with the recipes found in [167], where $\hat{r} = \sum_{i=1}^{3}\hat{x}_i$. Here we only show the results

$$
\begin{aligned}
\text{Correction} = {} & \Sigma C_{i\alpha} C_{j\beta} C_{k\gamma} C_{l\delta} (\alpha\beta|\gamma\delta) \\
& [\alpha, \beta, \gamma, \delta] \in A \\
& \alpha \neq \beta \\
& \gamma \neq \delta \\
= {} & \{[C_{ix} C_{js} + C_{is} C_{jx}][C_{kx} C_{ls} + C_{ks} C_{lx}] \\
& + [C_{iy} C_{js} + C_{is} C_{jy}][C_{ky} C_{ls} + C_{ks} C_{ly}] \\
& + [C_{iz} C_{js} + C_{is} C_{jz}][C_{kz} C_{ls} + C_{ks} C_{lz}]\} \frac{G^1}{3} \\
& + \{[C_{ix} C_{jy} + C_{iy} C_{jx}][C_{kx} C_{ly} + C_{ky} C_{lx}] \\
& + [C_{ix} C_{jz} + C_{iz} C_{jx}][C_{kx} C_{lz} + C_{kz} C_{lx}] \\
& + [C_{iy} C_{jz} + C_{iz} C_{jy}][C_{ky} C_{lz} + C_{kz} C_{ly}]\} \frac{3}{25} F^2 \\
& + \{C_{ix} C_{jx} C_{kx} C_{lx} + C_{iy} C_{jy} C_{ky} C_{ly} + C_{iz} C_{jz} C_{kz} C_{lz}\} \frac{4}{25} F^2 \\
& - \{[C_{ix} C_{jx} C_{ky} C_{ly} + C_{iy} C_{jy} C_{kx} C_{lx}] \\
& + [C_{ix} C_{jx} C_{kz} C_{lz} + C_{iz} C_{jz} C_{kx} C_{lx}] \\
& + [C_{iy} C_{jy} C_{kz} C_{lz} + C_{iz} C_{jz} C_{ky} C_{ly}]\} \frac{2}{25} F^2
\end{aligned}
$$

Figure C.1: *Orbital integrals $(\alpha\beta|\gamma\delta)$ when of eq. C.30, from [130].*

for the integral between an s and a p orbitals on the same atom. In this case the only non vanishing term for the integral $(\mu|\hat{x}_i|\nu)$ has $\mu = ns$ and $\nu = np_i$ (with $i = 1, 2, 3$), equal to $a_0 \frac{(2n+1)2^{2n+1}(\xi_s \xi_p)^{n+\frac{1}{2}}}{\sqrt{3}(\xi_s+\xi_p)^{2n+2}}$, where a_0 is the Bohr radius, and the $\xi_{s,p}$ is the Slater exponent of the of the s, p orbitals.

We calculate the permanent dipole moment of the excited state E as:

$$
\begin{aligned}
\mu_{EE} &= \langle \Phi_E | \hat{\mu} | \Phi_E \rangle \\
&= \sum_{ar} |C_a^r|^2 \{ \sum_{\nu,\mu} \left[\left(P_{\mu\nu} \right)_G + c_{a\mu} c_{a\nu} - c_{r\mu} c_{r\nu} \right] (\mu|\hat{\mu}|\nu) \qquad \text{(C.33)}
\end{aligned}
$$

where in the above equation $\left(P_{\mu\nu} \right)_G = 2 \sum_j^N c_{\nu j} c_{\mu,j}$ is the density matrix for the ground state closed shell configuration and the integral $(\mu|\hat{\mu}|\nu)$ is calculated according to the above expressions for $\hat{\mu}$.

Acknowledgments

I wish to express my deep gratitude to my supervisor Prof. Anna Painelli for the presence, guidance and constant support during these years. I wish to thanks also Prof. Alberto Girlando for the essential support and all people of the research team for their help and for the interesting and useful discussions: Dr. Francesca Terenziani, Dr. Matteo Masino, Dr. Cristina Sissa. and Dr. Gabriele D'Avino (now in University of Bologna). They all have contributed to make this PhD a very important formative and scientific experience.

I also wish to thank all people I have collaborated with:

- Prof. Camilla Ferrante of University of Padova (Italy), and people working there;
- Prof. Dominique Roberto of University of Milano and Dr. Silvio Quici of CNR of Milan (Italy), and people working in their research groups;
- Prof. Ivano Brillante, Raffaele Della Valle and Elisabetta Venuti of University of Bologna (Italy);
- Prof. Swapan Pati, Dr. Ershaad Ahamed Bashir, Dr. Arun Manna, Dr. Prakash Parida of JNCASR of Bangalore (India);
- Prof. Jaume Veciana, Prof. Imma Ratera and Dr. Judit Guasch of ICMAB in Barcelona (Spain).

This work was supported by the INSTM and the European Union through NoE-MAGMANet, by the Italian Ministry for Education, through PRIN-2006031511, and by Foreign Affair Ministry with the Indo-Italian programme of scientific and technological co-operation (2008-2010).

This thesis is dedicated to all people working in Italian Public Universities, that thanks to their work and their constant effort contribute to the progress of scientific research, in spite of government cuts and the law obstacles.

Bibliography

[1] J. R. Heath and M. A. Ratner, *Physics Today*, **2003**, *56*, 43.

[2] E. Vogel, *Nature Nanotechnologies*, **2007**, *2*, 25.

[3] H. Friend, R. W. Gymer, A. B. Holmes, J. H. Burroghes, R. N. Marks, C. Taliani, D. D. C. Bradley, D. A. Dos Santos, J.-L. Brédas, M. Lögdlund, and W. R. Salaneck, *Nature*, **1999**, *397*, 121.

[4] S. K. Sahoo, S. Parveen, and J. J. Panda, *Nanomedicine*, **2007**, *3*, 20.

[5] W. Zhou, S. M. Kuebler, K. L. Braun, T. Yu, J. K. Cammack, C. K. Ober, J. W. Perry, and S. R. Marder, *Science*, **2002**, *296*, 1106.

[6] B. H. Cumpston, S. P. Ananthavel, S. Barlow, D. L. Dyer, J. E. Ehrlich, L. L. Erskine, A. A. Heikal, S. M. Kuebler, I. Y. S. Lee, D. McCord-Maughon, J. Q. Qin, H. Rockel, M. Rumi, X. L. Wu, S. R. Marder, and J. W. Perry, *Nature*, **1999**, *398*, 51.

[7] C. N. La Fratta, J. T. Fourkas, T. Baldacchini, and R. A. Farrer, *Angew. Chem. Int. Ed.*, **2007**, *46*, 6238.

[8] Y. N. Konan, R. Gurny, and E. Alleman, *J. Photochem. Photobiol. B*, **2002**, *66*, 89.

[9] P. K. Frederiksen, M. Jorgensen, and P. R. Ogilby, *J. Am. Chem. Soc.*, **2001**, *123*, 1215.

[10] T. Breitenbach, M. K. Kuimova, P. Gbur, S. Hatz, N. B. Schack, B. W. Pedersen, J. D. C. Lamber, L. Poulsen, and P. R. Ogilby, *Photochem. Photobiol. Sci.*, **2009**, *8*, 442.

[11] V. Sundström, *Annu. Rev. Phys. Chem.*, **2008**, *59*, 53.

[12] T. Pulleritis and V. Sundström, *Acc. Chem. Res.*, **1996**, *29*, 381.

[13] A. C. Benniston and A. Harriman, *Materials Today*, **2008**, *11*, 27.

[14] Z. G. Soos, D. Mukhopadhyay, A. Painelli, and A. Girlando; Marcell Dekker, 1998; page 165.

[15] J.-L. Brédas, J. Cornil, D. Beljonne, and F. Meyers; Marcell Dekker, 1998; page 1.

[16] A. Painelli and F. Terenziani; Springer, 2006; page 251.

[17] S. R. Marder, B. Kippelen, A. K.-J. Jen, and N. Peyghambarian, *Nature*, **1997**, *388*, 845.

[18] A. Painelli, *Chem. Phys. Lett.*, **1998**, *285*, 352.

[19] A. Painelli, *Chem. Phys.*, **1999**, *245*, 185–197.

[20] A. Painelli, F. Terenziani, L. Angiolini, T. Benelli, and L. Giorgini, *Chem. Eur. J.*, **2005**, *11*, 6053.

[21] F. Terenziani, A. Painelli, C. Katan, M. Charlot, and M. Blanchard-Desce, *J. Am. Chem. Soc.*, **2006**, *128*, 15755.

[22] F. Terenziani, C. Sissa, and A. Painelli, *J. Phys. Chem. B*, **2008**, *112*, 5079–5087.

[23] C. Sissa, F. Terenziani, A. Painelli, A. Abbotto, L. Bellotto, C. Marinzi, E. Garbin, C. Ferrante, and R. Bozio, *J. Phys. Chem. B*, **2010**, *114*, 882–893.

[24] G. D'Avino, L. Grisanti, J. Guasch, I. Ratera, J. Veciana, and A. Painelli, *J. Am. Chem. Soc.*, **2008**, *130*, 12064.

[25] F. Terenziani, G. D'Avino, and A. Painelli, *ChemPhysChem*, **2007**, *8*, 2433.

[26] D. R. Kanis, M. A. Ratner, and T. J. Marks, *Chem. Rev.*, **1994**, *94*, 195.

[27] C. Reichardt, *Chem. Rev.*, **1994**, *94*, 2319.

[28] M. Albota, D. Beljonne, J.-L. Brédas, J. E. Ehrlich, J.-Y. Fu, A. A. Heikal, S. E. Hess, T. Kogej, M. D. Levin, S. R. Marder, D. McCord-Maughon, J. W. Pery, H. Röckel, M. Rumi, G. Subramaniam, W. W. Webb, X.-L. Wu, and C. Xu, *Science*, **1998**, *281*, 1653.

[29] O. Mongin, L. Porrès, M. Charlot, C. Katan, and M. Blanchard-Desce, *Chem. Eur. J.*, **2007**, *13*, 1481.

[30] D. Beljonne, W. Wenseleers, E. Zojer, Z. Shuai, H. Vogel, S. J. K. Pond, J. W. Perry, S. R. Marder, and J.-L. Brédas, *Adv. Funct. Mater.*, **2002**, *12*, 631.

[31] F. Terenziani, A. Painelli, and D. Comoretto, *J. Phys. Chem. A*, **2000**, *104*, 11049.

[32] F. Terenziani, A. Painelli, A. Girlando, and R. M. Metzger, *J. Phys. Chem. B*, **2004**, *108*, 10743.

[33] B. Boldrini, E. Cavalli, F. Terenziani, and A. Painelli, *J. Phys. Chem. A*, **2002**, *106*, 6286.

[34] C. Sissa, V. Parthasarathy, D. Drouin-Kucma, M. H. V. Werts, M. Blanchard-Desce, and F. Terenziani, *Phys. Chem. Chem. Phys.*, **2010**, *12*, 11715–11727.

[35] F. Terenziani, O. V. Przhonska, S. Webster, L. A. Padilha, Y. L. Slominsky, I. G. Davydenko, A. O. Gerasov, Y. P. Kovtun, M. P. Shandura, A. D. Kachkovski, D. J. Hagan, E. W. Van Stryland, and A. Painelli, *J. Phys. Chem. Lett.*, **2010**, *1*, 1800–1804.

[36] J. Campo, A. Painelli, F. Terenziani, T. Van Regemorter, D. Beljonne, E. Goovaerts, and W. Wenseleers, *J. Am. Chem. Soc.*, **2010**, *132*, 16467–16478.

[37] F. Terenziani and A. Painelli, *J. Am. Chem. Soc.*, **2003**, *125*, 5624.

[38] F. Terenziani and A. Painelli, *Phys. Rev. B*, **2003**, *68*, 165405.

[39] F. Terenziani and A. Painelli, *J. Phys. Chem. A*, **2000**, *104*, 11041.

[40] R. S. Mulliken, *J. Am. Chem. Soc.*, **1952**, *74*, 811.

[41] G. D'Avino, L. Grisanti, A. Painelli, J. Guasch, I. Ratera, and J. Veciana, *CrystEngComm*, **2009**, *11*, 2040.

[42] R. A. Marcus, *Rev. Mod. Phys.*, **1993**, *65*, 599.

[43] N. S. Hush, *Prog. Inorg. Chem.*, **1967**, *8*, 2264.

[44] N. S. Hush, *Coord. Chem. Rev.*, **1985**, *8*, 391.

[45] N. H. Hush and J. R. Reimers, *Chem. Rev.*, **2000**, *100*, 775.

[46] M. Bixon and J. Jortner, *Adv. Chem. Phys.*, **1999**, *106*, 35.

[47] L. Grisanti, C. Sissa, F. Terenziani, A. Painelli, D. Roberto, F. Tessore, R. Ugo, S. Quici, I. Fortunati, E. Garbin, C. Ferrante, and R. Bozio, *Phys. Chem. Chem. Phys.*, **2009**, *11*, 9450.

[48] G. Hübener, A. Lambacher, and P. Fromherz, *J. Phys. Chem B.*, **2003**, *107*, 7896–7902.

[49] V. Calabrese, S. Quici, E. Rossi, E. Cariati, C. Dragonetti, D. Roberto, E. Tordin, F. De Angelis, and S. Fantacci, *Chem. Commun.*, **2010**, *46*, 8374–8376.

[50] D. Patra R. M. Moustafa, J. A. Degheili and B. R. Kaafarani, *J. Chem. Phys. A*, **2009**, *113*, 1235–1243, Note: the behaviour we observed for azachrysene luminescence is very similar to the one presented here, even if here refers to other species.

[51] Z. R. Grabowski, K. Rotkiewicz, W. Rubaszewska, and E. Kirkor-Kamińska, *Acta Physica Polonica*, **1978**, *A54*, 767–776.

[52] Z. R. Grabowski, K. Rotkiewicz, and W. Rettig, *Chem. Rev.*, **2003**, *103*, 3899–4031.

[53] K. A. Zachariasse, T. von der Haar, A. Hebecker, U. Leinhos, and W. Kühnle, *Pure Appl. Chem,*, **1993**, *65*, 1745–1750.

[54] M. A. Thompson; *ArgusLab* - Planaria Software LLC, Seattle, WA; `http://www.arguslab.com`.

[55] J. R. Lakowicz; Kluwer Academic/Plenum Publisher, 2006; chapter Fluorescence Anisotropy, page 291.

[56] A. Painelli, F. Terenziani, and Z. Soos, *Theor. Chem. Acc.*, **2007**, *117*, 915.

[57] F. Todescato, I. Fortunati, S. Carlotto, C. Ferrante, L. Grisanti, C. Sissa, A. Painelli, A. Colombo, C. Dragonetti, and D. Roberto, **2010**, *submitted*.

[58] L. A. Summer; The bipyridines; In *Adv. Heterocycl. Chem.*, Vol. 35, pages 281–374. 1984.

[59] M Bourgault, T. Renouard, B. Lognoné, C. Mountassir, and H. Le Bozec, *Can. J. Chem.*, **1997**, *75*, 318–325.

[60] H. Dürr and R. Gleiter, *Angew. Chem. Int. Ed. Engl.*, **1978**, *17*, 559–569.

[61] T. P. I. Sarag, T. Sspehr, A. Sibert, T. Fuhrmann-Lieker, and J. Slabeck, *Chem. Rev.*, **2007**, *107*, 1011–1065.

[62] N. A. van Dantzig, D. H. Levy, C. Vgo, and P. Piotrowiak, *J. Chem. Phys.*, **1995**, *103*, 4894–4906.

[63] C. M. Brendel, F.B. Dias, T.P.I. Saragi, A. P. Monkman, and J. Salbeck, *Phis. Status Solidi A*, **2009**, pages 1–8.

[64] W. Ken-Tsung, K. Sung-Yu, C. Yi-Ming, L. Xiauo-Yun, H. Ying-Yueh, P. Shih-Chieh, C. Pi-Tai, L. Gene-Hsiang, and P. Shie-Ming, *J. Org. Chem.*, **2006**, *71*, 456–465.

[65] P. Palmieri and S. Samorí, *J. Am. Chem. Soc.*, **1981**, *103*, 6818–6823.

[66] S. Y. Kim, M. Lee, and B. H. Boo, *J. Chem. Phys.*, **1998**, *109*, 2593–2595.

[67] Rizzi et al., *Eur. J. Org. Chem.*, **2010**, pages 4004–4016.

[68] A. P. Demchenko, *Luminescence*, **2002**, *17*, 19–42.

[69] B. Valeur and G. Weber, *J. Chem. Phys.*, **1978**, *69*, 2393–2400.

[70] G. Weber and M. Shinitzky, *Proc. Natl. Acad. Sci. USA*, **1970**, *65*, 823–830.

[71] C. Creutz and N. Sutin, *Chem. Soc. Rev.*, **2002**, *31*, 168–184.

[72] A. Dei, D. Gatteschi, C. Sangregorio, and L. Sorace, *Acc. Chem. Res.*, **2004**, *37*, 827.

[73] M. E. Itkis, X. Chi, A. W. Cordes, and R. Haddon, *Science*, **2002**, *296*, 1443–1145.

[74] C. Joachim, J. K. Gimzewski, and A. Aviram, *Nature*, **2000**, *408*, 541–548.

[75] M. Ballester, J. Riera, J. Castaner, and A. Rodriguez, *Tetrahedron Lett.*, **1971**, page 2079.

[76] M Ballester, *Acc. Chem. Res.*, **1985**, *297*, 131.

[77] O. Armet, J. Veciana, C. Rovira, J. Riera, J. Castaner, E. Molins, J. Rius, C. Miravitlles, S. Olivella, and J. Brichfeus, *J. Phys. Chem.*, **1987**, *91*, 5608.

[78] M. Kondo, M. Uchikawa, K. Namiki, W.-W. Zhang, S. Kume, E. Nishibori, H. Suwa, S. Aoyagi, M. Sakata, M. Murata, Y. Kobayashi, and H. Nishihara, *J. Am. Chem. Soc.*, **2009**, *131*, 12112.

[79] I. Ratera, C. Sporer, D. Ruiz-Molina, N. Ventosa, J. Baggerman, A. Brouwer, C. Rovira, and J. Veciana, *J. Am. Chem. Soc.*, **2007**, *129*, 6117.

[80] I. Ratera, D. Ruiz-Molina, F. Renz, J. Ensling, K. Wurst, C. Rovira, P. Gütlich, and J. Veciana, *J. Am. Chem. Soc.*, **2003**, *125*, 1462.

[81] C. Sporer, I. Ratera, D. Ruiz-Molina, Y. Zhao, K. Wurst, P. Jaitner, J. Vidal-Gancedo, K. Clays, P. Persoons, C. Rovira, and J. Veciana, *Angew. Chem., Int. Ed.*, **2004**, *43*, 5266.

[82] C. Sporer, I. Ratera, K. Wurst, J. Vidal-Gancedo, D. Ruiz-Molina, C. Rovira, and J. Veciana, *ArkiVoc*, **2005**, *ix*, 104.

[83] L. Grisanti, G. D'Avino, A. Painelli, J. Guasch, I. Ratera, and J. Veciana, *J. Phys. Chem. B*, **2009**, *113*, 4718–4725.

[84] A. Painelli and F. Terenziani, *Chem. Phys. Lett.*, **1999**, *312*, 211.

[85] L. Del Freo and A. Painelli, *Chem. Phys. Lett.*, **2001**, *338*, 208.

[86] A. Painelli and F. Terenziani, *J. Phys. Chem. A*, **2000**, *104*, 11041.

[87] R. J. Cave and M. D. Newton, *Chem. Phys. Lett.*, **1996**, *249*, 15.

[88] S. F. Nelsen and M. D. Newton, *J. Chem. Phys. A*, **2000**, *104*, 10023.

[89] L.-T. Zhang and M. J. Ondrechen, *Inorg. Chem Acta*, **1994**, *226*, 43.

[90] V. Coropceanu, J. M. Andre, M. Malagoli, and J. L. Bredas, *Theor. Chem. Acc.*, **2003**, *110*, 59.

[91] V. Coropceanu, N. E. Gruhn, S. Barlow, C. Lambert, J. C. Durivage, T. G. Bill, G. Noll, S. R. Marder, and J.-L. Bredas, *J. Am. Chem. Soc.*, **2004**, *126*, 2727.

[92] F. Terenziani and A. Painelli, *Phys. Rev. B*, **2003**, *68*, 165405.

[93] A. Painelli and F. Terenziani, *J. Am. Chem. Soc.*, **2003**, *125*, 5624.

[94] Z. G. Soos, H. J. Keller, W. Moroni, and D. Nothe, *Ann. N.Y. Acad. Sci.*, **1978**, *313*, 442.

[95] A. Painelli and A. Girlando, *Phys. Rev. B*, **1988**, *37*, 5748.

[96] E. V. Tsiper and Z. G. Soos, *Phys. Rev. B*, **2001**, *64*, 195124.

[97] J. P. Stewart, *J. Mol. Model.*, **2007**, *13*, 1173.

[98] James J. P. Stewart; *MOPAC2007*, Stewart Computational Chemistry, Colorado Springs, CO, USA; `http://OpenMOPAC.net`, now MOPAC2009.

[99] G. D'Avino; *Cooperativity from charge transfer, phonons and electrostatic interactions in functional molecular materials;* PhD thesis, Dottorato in Scienza e Tecnologia dei Materiali Innovativi, **2009;** p. 112 (see table 2.2). Note: The fit procedure is the same as in the supporting information of [24] but the fit were improved and the parameter updated.

[100] A. Stebler, A. Furrer, and J. H. Ammeter, *Inorg. Chem.*, **1984**, *23*, 3493–3500.

[101] Y.S. Sohn, D. N. Henrickson, and H. B. Gray, *J. Am. Chem. Soc.*, **1971**, *93*, 3603–3612.

[102] A. Boccia, A. G. marriani, S. Stranges, R. Zanoni, M. Alagia, M. Cossi, and M. F. Iozzi, *J. Chem. Phys.*, **2008**, *128*, 154315.

[103] J. H. Ammeter, L. Zoller, J. Bauchmann, P. Baltzer, E. Gamp, R. Bucher, and E. Deiss, *Helv. Chim. Acta*, **1981**, *99*, 1063–1082.

[104] M. Tanaka, *Bull. Chem. Soc. Jpn.*, **1977**, *50*, 2881.

[105] C. S. Jacobsen and J. B. Torrance, *J. Chem. Phys.*, **1983**, *78*, 112.

[106] K. Yakushi and H. Kuroda, *Chem. Phys. Lett.*, **1984**, *111*, 165.

[107] A. Painelli and A. Girlando, *J. Chem. Phys.*, **1986**, *84*, 5655, Note: misprint in footnote 24, which should read: $q_R = Q\sqrt{2\omega/\hbar}$.

[108] D. Canevet, M. Sallé, G. Zhang, D. Zhang, and D. Zhu, *ChemComm*, **2009**, pages 2245–2269.

[109] J. B. Torrance, B. A. Scott, B. Welber, F. B. Kaufman, and P. E. Seiden, *Phys. Rev. B*, **1979**, *19*, 730–741.

[110] S. V. Rosokha and J. K . Kochi, *J. Am. Chem. Soc.*, **2007**, *129*, 828–838.

[111] R. Bozio, I. Zanon, A. Girlando, and C. Pecile, *J. Chem. Phys.*, **1979**, *71*, 2282–2293.

[112] J. M. Spruell, A. Coskun, D. C. Friedman, R. S. Forgan, A. A. Sarjeant, A. Trabolsi, A. C. Fahrenbach, G. Barin, W. F. Paxton, and *et al.* S. K. Dey, *Nature Chem.*, **2010**, *2*, 870–879.

[113] J. Veciana *et. al.*, **2011**, *in preparation*.

[114] J. Veciana *et. al.*, **2011**, *in preparation*.

[115] M. Ballester, I. Pascual, J. Riera, and J. Castañer, *J. Org. Chem.*, **1991**, *56*, 217.

[116] *Jaguar* package - Schrödinger, LLC; `http://www.schrodinger.com/`.

[117] M. E. Gershenson, V. Podzorov, and A. F. Morpurgo, *Rev. Mod. Phys.*, **2006**, *78*, 973.

[118] J. Y. Kim, K. Lee, N. E. Coates, D. Moses, T. Q. Nguyen, M. Dante, and A. J. Heeger, *Science*, **2007**, *317*, 222.

[119] M. C. Scharber, D. Wuhlbacher, M. Koppe, P. Denk, C. Waldauf, A. J. Heeger, and C. L. Brabec, *Adv. Mater.*, **2006**, *18*, 789.

[120] C. W. Tang and S. A. Vanslyke, *Appl. Phys. Lett.*, **1987**, *51*, 913.

[121] H. E. Katz, A. J. Lovinger, J. Johnson, C. Kloc, T. Slegrist, W. Li, Y. Y. Lin, and A. Dodabalapur, *Nature*, **2000**, *404*, 478.

[122] V. Coropceanu, J. Cornil, D. da Silva Filho, Y. Olivier, R. Silbey, , and J. L. Brédas, *Chem. Rev.*, **2007**, *107*, 926.

[123] A. Troisi and G. Orlandi, *Phys. Rev. Lett.*, **2006**, *96*, 086601.

[124] A. Troisi, *Adv. Mat.*, **2007**, *19*, 2000–2004.

[125] J. J. Kwiatkowski, J. M. Frost, J. Kirkpatrick, and J. J. Nelson, *J. Phys. Chem. A*, **2008**, *112*, 9113.

[126] A. Girlando, L. Grisanti, M. Masino, I. Bilotti, A. Brillante, R. G. Della Valle, and E. Venuti, *Phys. Rev. B*, **2010**, *82*, 035208.

[127] D. E. Williams, *J. Mol. Struct.*, **1984**, *486*, 321.

[128] M. J. Frisch *et. al*; *Gaussian03* - Gaussian Inc., Wallingford, CT, 2004 .

[129] Raffaele G. Della Valle and Elisabetta Venuti, *Phys. Rev. B*, **1998**, *58*, 206.

[130] J. Rydley and M. Zerner, *Theor. Chim. Acta*, **1973**, *32*, 111–134.

[131] A. Girlando, M. Masino, G. Visentini, R. G. Della Valle, A. Brillante, and E. Venuti, *Phys. Rev. B*, **2000**, *62*, 14476.

[132] A. Girlando, M. Masino, A. Brillante, R. G. Della Valle, and E. Venuti, *Phys. Rev. B*, **2002**, *66*, 100507.

[133] V.C. Sundar, J. Zaumseil, V. Pozdorov, E. Menard, R. Willett, T. Someya, M. Gershenson, and J.A. Rogers, *Science*, **2004**, *303*, 1644.

[134] D. da Silva Filho, E-G. Kim, and J. L. Brédas, *Adv. Mat.*, **2005**, *17*, 1072.

[135] E. Venuti, I. Bilotti, R. G. Della Valle, A. Brillante, P. Ranzieri, M. Masino, and A. Girlando, *J. Phys. Chem. C*, **2008**, *112*, 17416.

[136] V. Coropceanu, R. Sánchez-Carrera, P. Paramonov, G. M. Day, and J.L. Brédas, *J. Phys. Chem. C*, **2009**, *113*, 4679.

[137] O. D. Jurchescu, A. Meetsma, and T. T. M. Palstra, *Acta Cryst. B*, **2006**, *330*, 62.

[138] G. Nan, X. Yang, L. Wang, Z. Shuai, and Y. Zhao, *Phys. Rev. B*, **2009**, *79*, 115203.

[139] A. Brillante R. G. Della Valle, L. Farina, E. Venuti, M. Masino, and A. Girlando, *Mol. Cryst. Liq. Cryst.*, **2004**, *416*, 145–154.

[140] T. Wilson and J. W. Hastings, *Annu. Rev. Cell. Dev. Biol.*, **1998**, *14*, 197.

[141] D. Beljonne, C. Curutchet, G. D. Scholes, and R. J. Silbey, *J. Phys. Chem B*, **2009**, *113*, 6583.

[142] G. D. Scholes, *Ann. Rev. Phys. Chem.*, **2003**, *54*, 57.

[143] S. Saini, G. Srinivas, and B. Bagchi, *J. Phys. Chem. B*, **2009**, *113*, 1817.

[144] M. R. Wasielewki, *Chem. Rev.*, **1992**, *92*, 435.

[145] B. E. Hardin, E. T. Hoke, P. B. Armstrong, J.-H. Yum, P. comte, T. Torres, J. M. J. Frechet, M. K. Nazeeruddin, M. Grätzel, and M. D. McGehee, *Nature Photonics*, **2009**, *3*, 406.

[146] M. A. Baldo, M. E. Thompson, and S. R. Forrest, *Nature*, **2000**, *403*, 750.

[147] B. Valeur, *Molecular Fluorescence: Principles and Applications;* Wiley-VCH, 2001.

[148] T. Renger, *Photosynth Res*, **2009**, *102*, 471.

[149] T. Förster, *Ann. Phys.*, **1948**, *437*, 55.

[150] T. Förster, *Disc. Far. Soc.*, **1959**, *27*, 7.

[151] T. Förster, *Radiation Res. Supp.*, **1960**, *2*, 326.

[152] T. Förster; Academic Press, 1965; page 93.

[153] A. Szabo and N. S. Ostlund, *Modern Quantum Chemistry;* Dover Publications, 1982.

[154] C. Sissa, A. Manna, F. Terenziani, A. Painelli, and S. Pati, **2011**, *submitted*.

[155] S. Fery-Forgues and D. Lavabre, *J. Chem. Ed.*, **1999**, *76*, 1260.

[156] F. Terenziani, C. Katan, M. Blanchard-Desce, E. Badeva, and S. Tretiak, *Adv. Mater.*, **2008**, *20*, 4641.

[157] Oxford Instruments; *Operator's Handbook OptistatDN*, **2006**.

[158] Á.Pineiro, P. Brocos, A. Amigo, M. Pintos, R. Bravo, and A. Glines, *J. Solution Chem.*, **2002**, *31*, 369.

[159] B. J. Orr and J. F. Ward, *Mol. Phys.*, **1971**, *20*, 513.

[160] S. S. Andrews, *JCE*, **2004**, *81*, 877.

[161] F. Terenziani *et. al.*, **2011**, *in preparation*.

[162] J. A. Pople and D. L. Beveridge, *Approximate Molecular Orbital Theory;* McGraw-Hill, 1970.

[163] J. A. Pople, D. L. Beveridge, and P. A. Dobosh, *J. Chem. Phys.*, **1967**, *47*, 2026–2033.

[164] M. Zerner; Semiemiprical molecular orbitals methods; In *Review in computational chemistry*, Vol. 4, pages 313–365. 1984.

[165] H. H. Hinze, J. Jaffé, *J. Chem. Phys.*, **1963**, *38*, 1834.

[166] J. Rydley and M. Zerner, *Theor. Chim. Acta*, **1976**, *42*, 223–236.

[167] James J. P. Stewart; *MOPAC 2000 V1.3 User's Manual;* FUJITSU, **2000**.

[168] R. L. Ellis, G. Kuehnlenz, and H. H. Jaffé, *Theor. Chim. Acta*, **1972**, *26*, 131–140.

List of Publications

- F. Todescato, I. Fortunati, S. Carlotto, C. Ferrante, L. Grisanti, C. Sissa, A. Painelli, A. Colombo, C. Dragonetti, D. Roberto *Dimers of polar chromophores in solution: role of excitonic interactions on one- and two-photon absorption properties*, submitted

- A. Girlando, L. Grisanti, M. Masino, I. Bilotti, A. Brillante, R. G. Della Valle, and E. Venuti *Peierls and Holstein carrier-phonon coupling in crystalline rubrene* Phys. Rev. B **2010** *82* 035208

- L. Grisanti, C. Sissa, F. Terenziani, A. Painelli, D. Roberto, F. Tessore, R. Ugo, S. Quici, I. Fortunati, E. Garbin, C. Ferrante, R. Bozio, *Enhancing the Efficiency of Two-Photon Absorption by Metal Coordination: Theoretical Evidence of the Role of a Virtual Charge Transfer*, Phys. Chem. Chem. Phys. **2009** *11* 9450-9457

- G. D'Avino, L. Grisanti, A. Painelli, J. Guasch, I. Ratera and J. Veciana, *Cooperativity from electrostatic interactions: understanding bistability in molecular crystals*, CrystEngComm **2009** *11* 2040

- L. Grisanti, G. D'Avino, A. Painelli, J. Guasch, I. Ratera and J. Veciana, *Essential State Models for Solvatochromism in Donor-Acceptor Molecules: The Role of the Bridge*, J. Phys. Chem. B **2009** *14* 113

- G. D'Avino, L. Grisanti, J. Guasch, I. Ratera, J. Veciana and A. Painelli, *Bistability in Fc-PTM Crystals: The Role of Intermolecular Electrostatic Interactions*, J. Am. Chem. Soc. **2008** *13* 12064

Luca Grisanti
`luca.grisanti@gmail.com`

printed in Parma (Italy)
January 25, 2011